UNIVERSITÁ DEGLI STUDI DI PADOVA

Sede Amministrativa: Università degli studi di Padova

Dipartimento di Scienze Chimiche

SCUOLA DI DOTTORATO IN

SCIENZA ED INGEGNERIA DEI MATERIALI

INDIRIZZO XXI CICLO

Multifunctional organic semiconductors as active materials in electronic and opto-electronic devices

Direttore della scuola: Ch.mo Prof. Gaetano Granozzi

Supervisore: Ch.mo Prof. Renato Bozio

Dott Michele Muccini

Dottorando: Stefano Toffanin

Dedicated to my grandparents
and to the 5-year-old myself

I’ve been waiting for a guide to come and take me by the hand,
Could these sensations make me feel the pleasures of a normal man?

Disorder, Joy Division

Come on girl it's alright
Come on girl it's alright now
Come on girl it's gonna be alright now
…
Come on girl it's too late
Come on girl it's too late now
Come on girl let it all go
Come on girl it's too late now
Come on girl it's gonna be alright
Come on girl it's never gonna be alright

Mirrorball, Everything But The Girl

Index

Introduction

Since the first discovery of the photoelectric effect in anthracene by the Italian scientist Pochettino [1], organic compounds have been studied as multi-functional materials because of their capability of showing a variety of properties such as charge transport, light absorption/emission, photoconductivity, electroluminescence and superconductivity.

The peculiar properties of these materials reside in their chemical structure. This is essentially based on π-conjugated double bonds in a skeleton of carbon atoms. The wavefunctions that describe the π-conjugated orbitals are highly delocalized over the carbon atoms of the molecule, creating an electronic structure suitable for semiconducting properties.

Moreover, organic materials offer the possibility of tailoring the chemical structure to change the chemical-physical properties thereby adapting the material functionality and improving key properties such as thermal and environmental stability.

The rapid growth in the interest for π-conjugated materials in general and organic semiconductors in particular is due to both academia and industry. On the basic research side, π-conjugated materials are fascinating systems whose functional properties are strictly connected to the interplay between their π-electronic structure and their molecular structure [2]. On the applied research side, they are not going to replace silicon-based technologies, organic semiconductors promise the advent of fully flexible devices for applications including organic field-effect transistors (OFETs) [3], light-emitting diodes (OLEDs) [4], photovoltaic cells [5], sensors [6], and radio frequency identification (RF-ID) tags [7].

Charge transport in *molecular* materials has been investigated in a number of conjugated molecules that can be grown in the form of reasonably large single crystals by vacuum sublimation techniques under controlled conditions. Well-defined structures with a limited number of impurities can be obtained through repeated sublimation steps [8]. Such crystals provide an ideal test bed to investigate the fundamental parameters affecting charge mobility. However, their slow growth and lack of processability prevent them from being integrated in industrial processes. For industrial applications, cost-effective

approaches are sought after, based in particular on solution processing of (substituted) molecules or on the deposition of polycrystalline or amorphous films by vacuum sublimation.

In both cases, the efficiency of organic field-effect transistors is determined by the field-effect mobility of the charge carriers in the organic semiconductor layer and by the efficiency of the injection and extraction of carriers at the source and drain contacts. For virtually all classes of organic semiconductors the intrinsic carrier mobility depends critically on the degree of molecular ordering and on the extent of the π–π stacking in the material [9].

Despite their different chemical structures, materials showing highest mobility values in OFET device structures have in common the unidimensionality of their elemental unit, which results in anisotropic charge transport and optical properties. An important consequence of this anisotropy is that the realization of efficient electronic or photonic devices requires a precise control of the material organization for guaranteeing the *proper* overlap between molecular orbitals.

In addition to the tight molecular packing and strong intermolecular interactions needed to reach a high charge-carrier mobility, efficient control of the orientation of the conjugated chains on the substrate is imperative to obtain optimal charge transport in the desired direction.

So in order to enhance the performance of opto-electronic devices based on thin-film, it is of great interest to understand at the micro- and nano-scale which morphological features are detrimental for charge transport or energy transfer. Whereas it has been demonstrated that the molecular properties can be tuned by chemical tailoring, morphology and supramolecular arrangement are generally more difficult to control, and this appears to be one of the next challenges in the field of organic π–conjugated materials.

Photoluminescence spectroscopy has proven to be a powerful and highly sensitive technique to probe how the electronic structure and energy transport processes in conjugated molecules are modulated by aggregation in solid state thin-film [10,11]. The transfer of the exciton energy within the electronic manifold, which occurs upon charge recombination in opto-electronic devices, is highly sensitive to the local molecular environment [12]. Therefore, luminescence eventually depends on how the molecules pack in the solid into aggregates, rather than being exclusively an intrinsic property of the molecule [13]. So cross correlating PL spectroscopy with morphological probing tools such as confocal laser scanning microscopy (CLSM) and atomic force microscopy (AFM)

allows to gain fundamental information on the thin-film supra-molecular organization, and provides feedback to the deposition conditions (i.e. deposition rate, substrate temperature,..) for improving device electrical and light-emission properties.

In alternative to the control of the molecular orientation and interactions in π–conjugated oligomers essentially by physical processes, which are likely to complicate device fabbrication, molecular engineering and synthetic chemistry can be implemented to solve the problems related to the *unidimensionality* of linear π–conjugated systems. Indeed, the development of organic semiconductors with higher dimensionality (2D and 3D) could represent an exciting alternative strategy to allow for the realization of electronic or photonic devices without any constrain in terms of the control over the molecular orientation. Due to the lack of directionality in the charge transport and optical properties, homogeneous amorphous material based on 3D conjugated architectures as active material in solution-processed opto-electronic have been extensively implemented [14].

Among all the organic materials showing semiconducting properties, thiophene derivatives have always attracted attention since the implementation of linear α-conjugated thiophene-based oligomers as active materials in the first field-effect transistors [15].
The versatility of thiophene chemistry allows a great diversity of thiophene-based chemical structures. Thiophene can be functionalized in positions α and β to sulphur or at the sulphur atom itself [16], regioregular oligomers and polymers with extremely varied functionalizations can be prepared, oligomers can be linear, branched, or star-shaped, and even-all thiophene dendrimers can be prepared [17]. The driving force behind the continuous creation of new thiophene-based structures is that they allow fine-tuning of charge-transport and light-emission properties and, more importantly, that understanding of the structure-property relationship is still dramatically scarce, particularly in the solid state.

Given the multi-functional properties of many classes of organic compounds, the full explanation of these properties requires the realizion of devices that are able to integrate electronic functions (e.g., transistors) with optical functions (e.g., light sources and light detectors). Light-emitting field-effect transistors (LET) provide a very simple integration scheme for combining the switching properties of transistors with the emission properties of light-emitting diodes.

Organic semiconductors are ideal candidates for light emission applications since many small molecule and conjugated polymer semiconductors show very high photoluminescence and electroluminescence efficiencies over the whole visible spectrum coupled to charge transport properties, that allowed the realization of efficient light-emitting diodes [18].

In recent years, many research groups have worked to achieve light emission from organic field-effect transistors. Ambipolar OFETs can provide an effective pn-junction within the transistor channel that allows exciton formation and radiative recombination [19].

With respect to light-emitting diodes, LETs present some intriguing characteristics which overcome many physical and technical withdraws in the realization of nano-scale integrated electro-optical devices. In particular, these characteristics include: control over the position of the emission zone, emission far away from injecting metal electrodes, high current densities, low charge concentration within the emission zone, and perfectly balanced hole and electron currents.

So, LET planar structure is not only a convenient platform for investigating charge carrier recombination processes in organic semiconductors with spatially resolving probes, but it is also attractive for the realization of integrated electro-optical switches and, potentially, electrically pumped lasers.

Electrically pumped organic laser is considered the most promising next-generation technologies in organic opto-electronics. Apart from obstacles related to the device configuration choice [20], there are many intrinsic aspects of the photophysics of organic semiconductors that are relevant to laser realization.

First, the fact that organic materials strongly absorb light in very short distances means that very strong gain is also possible, given that stimulated emission is closely related to absorption.

The fluorescence spectra of organic semiconductors are broad so that laser emission can be tuned over a significant spectral range (from near ultraviolet to infrared) [21]. Moreover the broad spectral width implies that organic semiconductor lasers are capable of short pulse generation [22] and broad-band optical amplification [23].

Considerable effort has gone into increasing the photoluminescence efficiency of thin films of organic materials. In particular, a range of strategies, including the dispersion of laser dyes in a host matrix, have been developed to control intermolecular interactions and prevent light emission quenching.

The thesis is organized as follows:

In Chapter 1 a general description of the two main classes in which the organic semiconductors are grouped (small molecules and polymers) is introduced. Optical properties of organic are then described in more detail introducing the concept of exciton and describing its properties in the case of physical dimers, single crystals and thin film. The nature of stimulated and spontaneous emission in a two-level system together with the mirrorless lasing properties in organic semiconductors is described.
The charge transport processes in organic semiconductors are introduced and a brief overview of the opto-electronic devices with particular attention to the organic filed-effect transistors (structure, working principles and main components) is given.

In Chapter 2 the experimental setups used are described. In particular, CLSM and AFM are presented in detail as probing tools for morphological characterization. Time-resolved spectro-microscopy is outlined, which gives the possibility of correlating morphology and photophysical properties at the nanoscale.
The setups we used for opto-electronic measurements on organic field-effect transistors are also described. Particular attention is given to highlight possible spurious effects that can drastically affect the measurements.

Chapter 3 introduces oligothiophenes as a class of organic compounds displaying multifunctional properties. In particular we present linear oligothiophenes with chain substituents suitable to be used as active materials in single-layer OFET. We show that implementing a morphological study for optimizing proper growth conditions, state-of-the-art electron and hole mobility values are achieved.
In the second part of the chapter we present a brand-new family of branched all-thiophenes molecules, named *spider-like* oligothiophenes, in which linear π–conjugation is displayed on different branches in a 3D architecture. After performing a detailed photoluminescence spectroscopy study on all the molecules dispersed in dilute solution, we instigated how the molecular spectroscopic features are modified by the solid-state aggregation in thin-films. A morphological study on the thin-films has been carried out as well.
OFET devices based on the most promising spider-like oligothiophene were also prepared.

In Chapter 4 we report on the characteristics of a host-guest lasing system obtained by co-evaporation of an oligo(9,9-diarylfluorene) derivative (host) with a well-known red-emitter dye (guest). The blend satisfies the necessary conditions for an efficient Förster energy transfer to take place from host matrix to guest molecules. We performed a detailed

spectroscopic study on the system by systematically varying the guest concentration in the matrix.

We found out that this host-guest system presents very competitive mirrorless lasing properties with respect to most-frequently used molecular binary host-guest system.

Finally in Chapter 5 we present vertical tri-layer heterojunction approach for realizing organic light-emitting transistor. The specificity of the presented tri-layer based OLET is the intrinsic separation of the charge transport region from the exciton formation region thus preventing completely the exciton-carrier quenching.

Each layer is devoted to a single functionality and can be optimised by controlling the growth of the different organic/organic, organic/metal and organic/dielectric interfaces. The first layer and third layer are optimized for field-effect charge (electrons and holes) transport. The second layer is formed by a host-guest matrix with high optical performance and showing amplified spontaneous emission under optical pumping.

We realized devices changing substrates, dielectric, the active materials and their growing conditions. Moreover we can correlate the OLET electrical characteristics to the exciton formation and recombination processes by a simple and effective theoretical model.

The deep comprehension of the charge transport and light emission mechanisms allow the realization of a tri-layer heterojunction with balanced electron and hole mobility ($\sim 10^{-1}$-10^{-2} cm^2/Vs), high charge carrier density in correspondence of the maximum EL signal (~ 1 KA/cm^2) and intense light emission.

In conclusion a brief summary of the results and the possible future developments of the tri-layer heterojunction is given.

References

[1] A. Pochettino, *Atti della R. Accademia di Lincei. Rendiconti della classe di scienze fisiche, matematiche e naturali*, **1906**, 15, 355.

[2] W. P. Su, J. R. Schrieffer, A. J. Heeger, *Phys. Rev. Lett.* **1979**, 42, 1698.

[3] G. Horowitz, *Adv. Mater.* **1998**, 10, 365.

[4] J. H. Burroughes, D. D. C. Bradley, A. R. Brown, R. N. Marks, K. Mackay, R. H. Friend, P. L. Burns, A. B. Holmes, *Nature* **1990**, 347, 539.

[5] C. J. Brabec, N. S. Sariciftci, J. C. Hummelen, *Adv. Funct. Mater.*, **2001**, 11, 15.

[6] B. Crone, A. Dodabalapur, A. Gelperin, L. Torsi, H. E. Katz, A. J. Lovinger, Z. Bao, *Appl. Phys. Lett.*, **2001**, 78, 2229.

[7] A. R. Brown, A. Pomp, , Hart, C. M., Deleeuw, D. M., *Science*, **1995**, 270, 972.

[8] Jurchescu, O. D., Baas J., Palstra, T. T. M., *App. Phys. Lett.*, **2004**, 84, 3061.

[9] D. J. Gundlach, Y. Y. Lin, T. N. Jackson, S. F. Nelson, D. G. Scholm, *IEEE Electron Device Lett.*, **1997**, 18, 87.

[10] R. Kersting, U. Lemmer, R. F. Mahrt, K. Leo, H. Kurz, H. Bässler, O. Göbel, *Phys. Rev. Lett.*, **1993**, 70, 3820.

[11] R. N. Marks, R. H. Michel, W. Gebauer, R. Zamboni, C. Taliani, R. F. Mahrt, and M. Hopmeier, *J. Phys. Chem. B*, **1998**, 102, 7563.

[12] H. Sirringhaus, N. Tessler, R. H. Friend, *Science*, **1998**, 280**,** 1741.

[13] A. Hepp, H. Heil, W. Weise, M. Ahles, R. Schmechel, H. von Seggern. *Phys. Rev. Lett*., **2003**, 91**,** 157406.

[14] J. Roncali, P. Leriche, A. Cravino, *Adv. Mater.*, **2007**, 19, 2045.

[15] D. Fichou, *Handbook of Oligo- and Polythiophenes*, (New York, Wiley-VCH, 1998).

[16] G. Barbarella, L. Favaretto, G. Sotgiu, M. Zambianchi, A. Bongioni, C. Arbizzani, M. Mastragostino, M. Anni, G. Gigli, R. Cingolati, *J. Am. Chem. Soc.*, **2000**, 122, 11971.

[17] Y. Shirota, *J. Mater. Chem.*, **2000**, 10, 1.

[18] C. W. Tang, S. A. Vanslyke, *Appl. Phys. Lett.* **1987**, 51, 913.

[19] A. Dodabalapur, H. E. Katz, L. Torsi, *Adv. Mater.* **1996**, 8, 853.

[20] M. A. Baldo, R. J. Holmes, S. R. Forrest, *Phys. Rev. B*, **2002**, 66, 035321.

[21] R. D. Xia, G. Heliotis, D. D. C. Bradley, *Appl. Phys. Lett.*, **2003**, 82, 3599.

[22] M. Goossens, A. Ruseckas, G. A. Turnbull, I. D. W. Samuel, *Appl. Phys. Lett.*, **2004**, 85, 31.

[23] M. Goossens, G. Heliotis, G. A. Turnbull, A. Ruseckas, J. R. Lawrence, R. Xia,; D. D. C. Bradley, I. D. W. Samuel, In *Organic Light-Emitting Materials and Devices IX*; Z. H. Kafafi, , P. A. Lane, Eds.; Proceedings of SPIE, The International Society for Optical Engineering, Vol. 5937; Society of Photo-Optical Instrumentation Engineers: Bellingham, WA, **2005**; 593706.

Chapter 1

Optically active organic semiconductors

1.1 π conjugated materials

The name organic semiconductor denotes a class of materials based on carbon, that display semiconducting properties. Most attractive opto-electronic properties of these materials arise from the carbon atom features. In its ground state, the carbon atom has this classic electronic structure: $1s^2 2s^2 2p_x^1 2p_y^1$. This means that carbon has two electrons in orbital 1s, two in orbital 2s and 2 in orbitals 2p (Fig. 1). Since the s orbitals are totally filled, an atom carbon should form only two bonds involving the two unpaired electrons in 2p orbitals.

Instead, it is well known that carbon is tetravalent and forms four bonds. This can be explained using the valance bond theory [1].

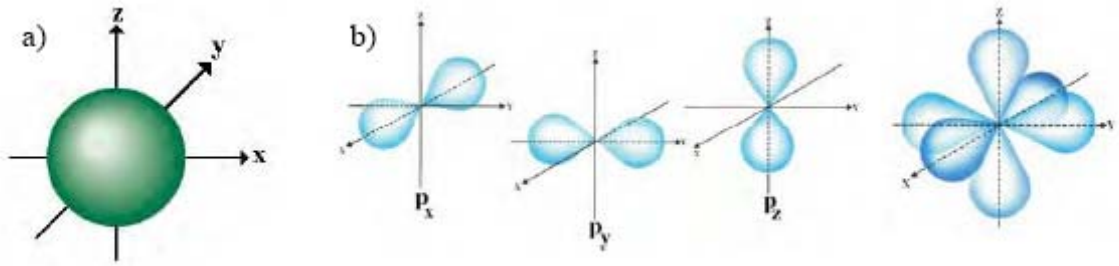

Figure 1. a) Spherical shape of *s* orbital. b) Representation of the three p orbitals (p_x, p_y and p_z) and of their spatial combination.

This theory asserts that a chemical bond is formed by the overlapping of the atomic orbitals which contain the electrons participating in the bond, in order to lower the total energy of the system. Since the atomic orbitals are the wave functions solving the Schrödinger equation for an atom, the overlapping between atomic orbitals corresponds to the combination of the wave functions describing the two electrons involved in the bond.

The overall normalized wave function describing a molecular system (*molecular orbital*) can be expressed as:

$$\Psi = \sum_i a_1 \varphi_i \qquad \text{with} \qquad \sum_i a_1^2 = 1$$

in which φ_i are the solutions of the atomic Schrödinger equation, i.e. one-electron functions centered on the nuclei of the component atoms of the molecule. So the molecular orbital Ψ is the linear combination of n atomic orbitals φ_i (LCAO), each multiplied by a corresponding coefficient a_i. The coefficients are weights of the contribution of n atomic orbitals to the molecular orbital. The molecular orbital is expressed as linear combination of basis functions. By minimizing the total energy of the system an appropriate set of the linear combinations is determined.

In the case of carbon atom the linear combination can be between *2s* orbital and one, two or three 2p orbitals and is properly denominated *hybridazation* [2].

If the mix occurs between the 2s orbital and all the 2p orbitals, we obtain four degenerate sp^3 hybrid orbitals lying in a tetrahedral geometry around the central carbon atom (109,47° between bond axes). This hybridization is the one found in diamond, in which every carbon atom is bonded to another four carbons.

Mixing can also occur between 2s orbital and one 2p orbital to form 2 equivalent sp orbitals. These are on the same plane passing through the nucleus, and lie at 180° from one each other. The 2 pure p remaining orbitals lie in a plane which is perpendicular to the former. In the case of the sp^2 hybridization, the 2s orbital is mixed with two 2p orbitals, for example the $2p_x$ and the $2p_y$ in Fig. 1. Three new hybrid states are formed that lie in the XY plane, leaving the 2pz orbital unchanged as it can be seen in Fig. 2.

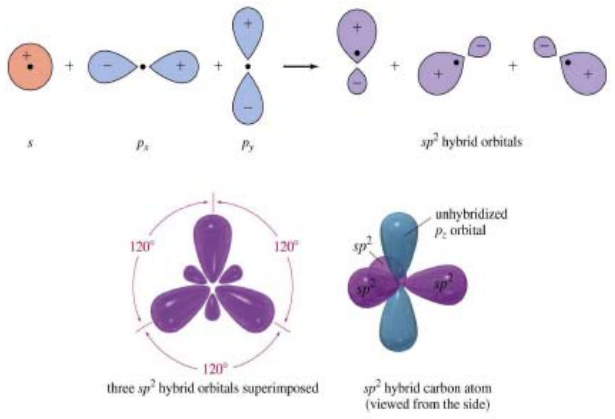

Figure 2. sp^2 hybridization of atomic orbitals s and p_x and p_y in a carbon atom.

In the top view of the hybridized atom (Fig. 2), it is possible to see that all the hybrid orbitals lye in the same plane at an angle of 120^{o} to each other. This configuration is the one in which the electron pairs are further apart, thus being energetically the most favourable.

The first bond that occurs between two hybridized atoms is of the σ type. In this bond, the electron density lies between the nuclei, and one pair of electrons is shared. In order to form a second bond, the p_z orbitals from both atoms overlap laterally (i.e. sideways) and form a π bond. This lateral bonding is therefore weaker than the highly directional σ bond. One double bond consists of a σ bond and a π bond, both of them having one pair of electrons shared.

Since the electronic distribution in the π bond is less spatially localised that that of the σ bond, the energy difference between the ground state (*bonding*) and the excited state (*antibonding*) is smaller than for the σ case. The two possible configurations are shown in Fig. 3.

One important point to highlight, is that single bonds, allow rotations along the σ bond axis, but double bonds, since they must have a π bond, do not allow any kind of rotation. In a way, double bonds induce more rigidity and hindrance in the molecular geometry that cannot be released unless the bond is broken.

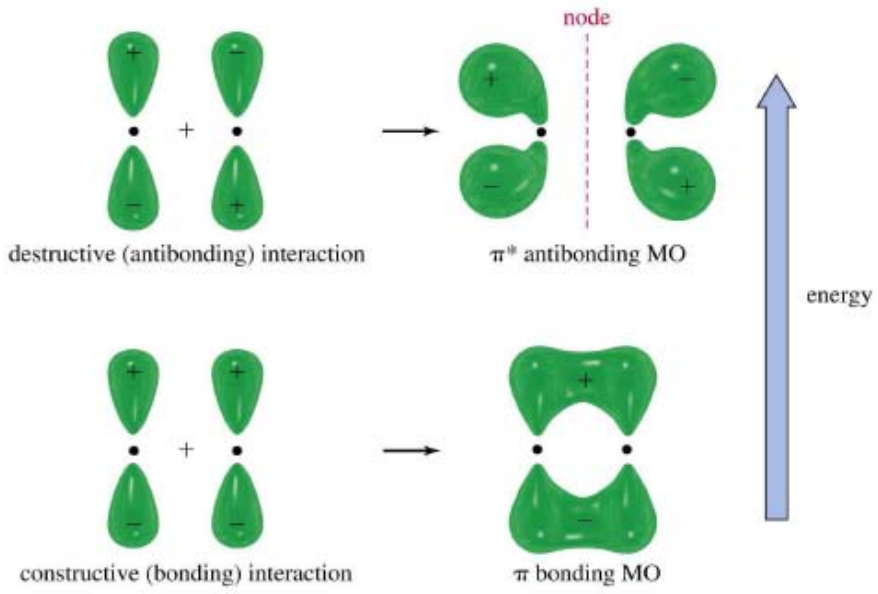

Figure 3. The two possible configurations of π bond due to p_z orbitals.

Therefore π electrons are not confined between the nuclei, rather they form an electron density cloud above and below the plane of the σ bond. This cloud creates an electron system ideally delocalized over the entire molecule or polymer. In real cases, this delocalization can be confined in only a part of the molecule [3]. As a matter of fact, conjugation exists, and it largely determines the electron energy structure of the organic materials.

Indeed in organic semiconductors, which are a class of materials based on carbon displaying semiconducting properties, the common characteristics is that the electronic structure is based on π-conjugated double bonds between carbon atoms. The delocalization of the electrons in the π-molecular orbitals is the key feature, that allows injection delocalization and charge transport.

Beside the strong intramolecular forces in the molecular skeleton, the solid (crystal or thin film) is held together by weaker van der Waals forces [4].

Because of these weak interactions, it is to be expected that the properties of the individual molecules are mostly retained. Indeed, many studies show how it is possible to tune solid state properties adjusting the molecular structure by means of chemical tailoring. At the same time the ”supramolecular level” should not be disregarded. In this case the molecular order [5] in the solid state packing and the polymorphism [6] play a crucial role in determining properties such as optical emission and charge transport.

π-conjugated materials can be divided into two main classes according to their molecular weight (MW). Low MW organic semiconductors are usually named small molecules, whereas π-conjugated polymers have MW reaching many thousands of g/mol.

1.1.1 Small molecules

An organic small molecule is a molecule based on carbon which presents low MW, low spatial extent and generally short conjugation length. Typically, interactions between different small molecules are dominated by van der Waals forces.

A plethora of organic species belong to this class: polycondensate aromatic hydrocarbons as pentacene (Fig. 3a) and perylene (Fig. 3b), organo-metallic complexes such as metalphtalocyanines and oxy-quinoline (Fig. 3c) fullerens and dendrimers. However, the largest part of small molecules is represented by oligomers (from the Greek: *oligos,* “a

few", and *meros*, "part"). An oligomer consists of a finite number of monomer unit. Some examples of oligomers are: oligo-phenylenes or oligo-thiopenes (Fig. 3d).

Generally, molecular materials are processed by vacuum sublimation and solution-based processing techniques can rarely be employed. Films grown on dielectric substrates are mainly poly-crystalline, and their growth (and consequently the morphology of the film) can be partially controlled acting on the vacuum sublimation parameters and selecting the nature of the substrate. Using small molecules, the analysis of the early growth stages of the active layer via atomic force microscopy (AFM) is also possible.

Concerning the transport properties, there is a large number of hole transport (*p-type*, e.g. α sexy-thiophene, named α-6T) and electron transport (*n-type*, e.g. perylene derivative, named PTCDI-$C_{13}H_{27}$) semiconductor small molecules (see Chapter 3). In the last years, ambipolar small molecules (e.g. DHCO4T, Fig. 3e) have also been synthesized; these molecules are able to transport both electrons and holes.

To date, small molecules present the best carrier field-effect mobility values in OFETs based on rubrene (Fig. 3f) single crystals[7].

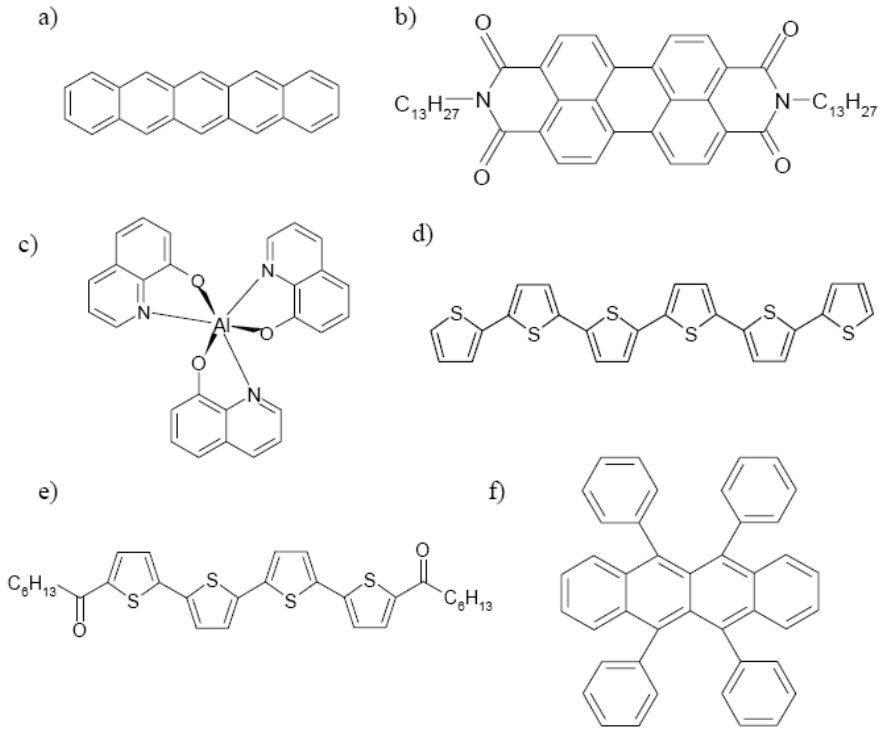

Figure 3. Chemical structure of some widely studied small molecule organic semiconductors. a) Pentacene; b) N,N - ditrydecylperylene - 3,4,9,10 - tetracarboxylic diimmide (PTCDI-C13H27); c) Allumin oxyquinolina (Alq3); d) α sexy-thiophene (α-6T); e) α,ω-dihexylcarbonylquaterthiophene (DHCO4T); f) Rubrene.

1.1.2 Polymers

A polymer (from Greek: *polu*, "many"; and *meros*, "part") consists of the repetition of structural units, typically large mass molecules called *monomers* (from Greek *mono* "one" and *meros* "part") forming a long molecular chain along which π-electrons are delocalized. Chemical chains can take up a range of different conformations by rotating, twisting or distorting its backbone bonds. In addition, it may contain chain interruptions, chemical and structural defects which contribute to break the conjugation. So the π-electrons delocalization becomes shorter and with distributed lengths. Indeed, the fundamental studies of Bässler and co-workers have shown that conjugated polymers must be considered rather as a linear arrays of conjugated segments [8].

In amorphous polymers (the great majority), the case is further complicated as each conjugation section of the chain is randomly oriented with respect to the others. In this situation there is a range of conjugation lengths, with the obvious consequence that energy levels are spread out over a wider interval.

The most studied organic semiconductor polymers belong principally to three families: poly (phenylenevinylene), e.g. MEH-PPV (Fig. 4a); poly-thiopene, e.g. P3HT (Fig. 4c); and poly-fluorenes, e.g. F8T2 (Fig. 4d).

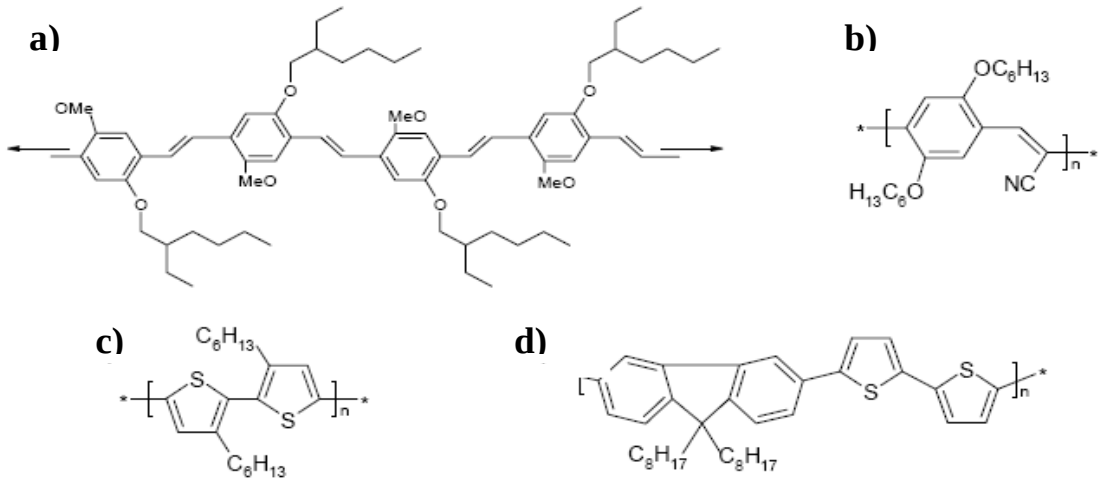

Figure 4. Chemical structure of some widely studied polymer organic semiconductors. a) Long chain of Poly[2-methoxy-5-(2-ethylhexyloxy)-1,4-phenylene-vinylene] (MEH-PPV); b) Poly[2,5,2',5'-tetrahexyloxy-7,8'-dicyano-di-*p*-phenylenevinylene] (CN-PPV); c) Poly[3-hexylthiophene] (P3HT); d) Poly[9,9'-dioctyl-fluorene*co*-bithiophene] (F8T2).

Processability of polymers is usually restricted to wet techniques; this can be an advantage, because of the inherently low cost and large area coverage of such techniques, but also a disadvantage, as the structural and morphological control of usually amorphous thin films is limited. As a consequence, charge mobility in polymeric thin films is typically lower with respect to that of small molecule films.

Theoretically, there is no particular reason for the majority of polymers not to be ambipolar [9]; however they are found to be mainly p-type, and only a few are n-type (e.g. CN-PPV Figure 20b).

1.2 Linear optical properties in molecular materials

The linear optical properties of organic semiconductors are mainly determined by their fundamental photoexcitations. It is straightforward that in solids with proper long-range translational order, the quantum of excitation can move on different molecular units leading to a quasi-particle called ”exciton”. A very simple but clear definition of the exciton can be found in the book of Dexter and Knox [10]: “It is a quantum of electronic excitation travelling in a periodic structure, whose motion is characterized by a wave vector”.

Many theoretical and experimental works have underlined that in van der Waals solids, due to the weak intermolecular interactions, the fundamental excitations are Frenkel excitons [11]. These are characterized by a very small radius of the electron hole pair (< 5 Å) due to a strong binding energy

between them (~1 eV). Thus, the electron-hole pair is situated on only one molecular site, except in the case of charge transfer state (see below).

The opposite case is represented by Wannier-Mott excitons, typical of covalent solids (inorganic semiconductors), where electron and holes are delocalized on many molecular or atomic sites of the solid. The Wannier-Mott exciton radius has values in the range 40-100 Å.

According to the electronic structure of the molecule and to the molecular packing in the solid, excitons can have different properties. A first very simple classification involves, as

for molecular excitation, the electron hole total spin moment that divides excitons in triplet and singlet.

Other types of excitons have been found in organic π-conjugated materials: charge transfer excitons, excimers and surface excitons. In the following we will give an overview of the characteristics that distinguish them.

In charge transfer exciton (CTE) electron and hole are more delocalized, usually spreading on the nearest neighbor molecules. They remind the Wannier-Mott excitons in inorganic semiconductor and are of primary importance in the photoconduction processes (i.e. exciton dissociation and electron-hole separation). CTE have a weak oscillator strength and are usually detected with electroabsorption spectroscopy or non-linear spectroscopy such as photoinduced absorption spectroscopy [12]. Since CTE are delocalized states their transition energy can be tuned with the intermolecular distance as demonstrated in reference [13].

Excimers (**Ex**cited-Di**mers**) are formed by an excited pairs of molecules. They consist of an excited state which form a complex between two molecules.

This complex is unstable (dissociative) when the molecules are in their ground states [4]. As a consequence, the ground state potential energy surface is lacking of any minima and has higher energy with respect to that of the isolated molecule ground state. Thus, the excimer photoluminescence (PL) is characterized by a broad (unbound ground state) red-shifted band and a longer PL decay with respect to the isolated molecule. Molecules that show typical excimer emission are perylene and pyrene, in which the pair-like solid state packing is highly favorable for excimer formation.

Surface Excitons are quite rare states and can be observed only in molecular crystals at very low temperature (below 10 K). The appearance of these states is related to the abrupt change in the molecular environment for molecules at the crystal surface with respect to that in the bulk. This influences strongly the PL features, according to the unit cell geometry and the exposed surface. Detection of surface excitons can be performed with reflectance or PL spectroscopy [14]. Surface excitons have narrow transition bands (for anthracene FWHM 2.2 meV), absence of vibronic progression and null Stokes shift. They have been observed in highly pure anthracene and tetracene crystals.

1.2.1 Physical dimers

The physical dimer consists of two identical molecules that are close to each other, without any chemical bond between them. The physical-dimer Hamiltonian operator can be written as the sum of energy operators of the isolated molecules H_1 and H_2 and a term V_{12} representing the intermolecular interaction energy, thus

$$H = H_1 + H_2 + V_{12}$$

Suppressing the vibrational and spin parts of the overall wavefunction, the ground-state dimer can be approximated as

$$\Psi = \varphi_1 \varphi_2$$

where φ_1 and φ_2 are the ground-state wavefunctions of isolated molecules. In this description *configuration interaction* mainly due to van der Waals energy contribution to the stability of the dimer is neglected.

Within this approximation the ground-state energy of the physical dimer is

$$E = E_1 + E_2 + W$$

$$W = \left\langle \varphi_1 \varphi_2 \middle| V_{12} \middle| \varphi_1 \varphi_2 \right\rangle$$

where E_1 and E_2 are the energies corresponding to the monomer states φ_1 and φ_2 respectively. The last term W denotes the coulombic binding energy for the pair. The integration is over all electronic coordinates for both the molecules.

Considering now the low-lying excited state of the dimer, only the case of the nondegenerate monomer excited case will be treated.

The dimer excited wave function can be described as

$$\Psi_{EX} = c_1 \varphi_1^* \varphi_2 + c_2 \varphi_1 \varphi_2^*$$

in which φ_1^* and φ_2^* are the wave functions of the equivalent excited electronic states of molecules 1 and 2.

In the case the molecules are identical:

$$|c_1| = |c_2| = 1/\sqrt{2}$$

in order to satisfy normalization conditions.

In quantum mechanical terms, the electronic excitation (*exciton*) oscillates coherently between the two molecules instead of being localized on one molecule with equal probability of finding the excitation on either molecules.

The corresponding energy eigenvalues are:

$$E_{\pm}^{*} = E_1^{*} + E_2 + W^{'} \pm J$$

$$W^{'} = \left\langle \varphi_1^{*}\varphi_2 \middle| V_{12} \middle| \varphi_1^{*}\varphi_2 \right\rangle$$

$$J = \left\langle \varphi_1^{*}\varphi_2 \middle| V_{12} \middle| \varphi_1\varphi_2^{*} \right\rangle$$

where W' represents the coulumbic energy of the interaction of the charge distribution of the excited state of molecule 1 with the ground-state of the molecule 2 (or the reverse). J is the resonance interaction energy between the excited states of the two molecules.

The scheme in Fig. 4 shows the dimer energy levels. In the figure the single arrow lines indicates optical transitions to the excited states. The corresponding absorption spectrum will have two distinct bands. Their separation in energy can provide a direct measurement of the splitting 2 × J between the two energy states.

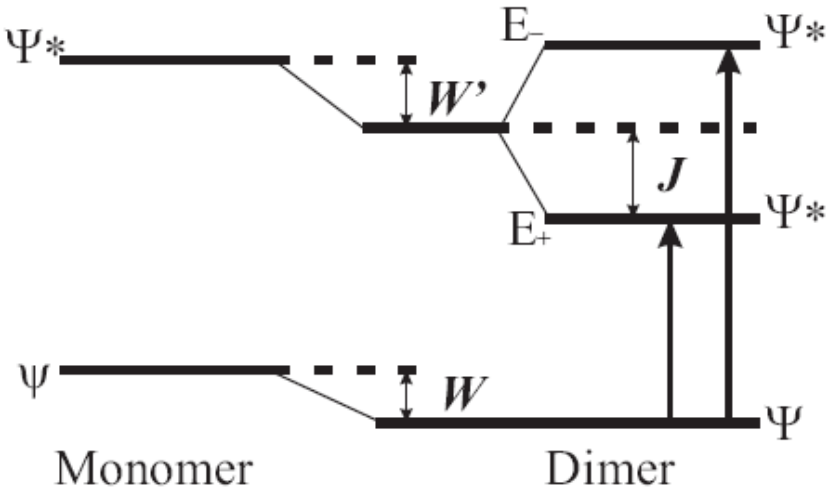

Figure 4. Energy level scheme for a physical dimer. On the left, energy levels for the ground and first excited state of the monomer. The right part shows the splitting of the first excited state of the dimer with the different contributions (see text for details). The splitting correspond to 2 × J. Single arrow lines indicate optical transitions.

The intensity of the absorption bands depends on the magnitudes of W and W' and on the orientation of the monomer dipole moments (as illustrated in Fig. 5). In the two extreme cases of collinear or cofacial dipole moments one of the two transitions has no oscillator strength (zero intensity) and is undetectable in the absorption spectrum. For collinear (head-to-tail) orientation the lowest energy level corresponds to the in-phase

coupling of transition dipole moments. In this case a red-shifted (with respect to monomer) absorption band is observed. For cofacial orientation the in

phase coupling corresponds to the higher energy level and the absorption is blue-shifted.
In the case of oblique dipoles both energy levels are detectable in absorption and their polarization (dipole sums in the figure) are perpendicular to each other.
In emission, the radiative relaxation to the ground state (luminescence) takes place always from the lowest level. It is interesting to note the case of cofacial dipoles where the null oscillator strength of the lowest state precludes to observe luminescence from this state.

From this simple analysis the concept of exciton as an electronically excited, mobile, neutral, nonconducting state of an insulating solid emerges.

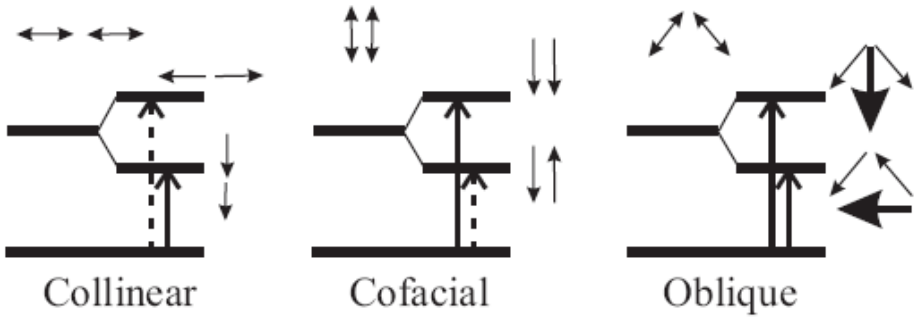

Figure 5. Absorption transitions for physical dimers with different orientations of the molecular transition dipoles (double arrow lines). Collinear, Cofacial and Oblique. Single arrow lines represent how transition dipoles sum in the corresponding energy level. Absorption transition are illustrated as dotted/continuous lines in the case of null/nonnull oscillator strength.

1.2.2 Excitons in molecular crystals

The natural extension of a physical dimer is a molecular crystal, in which a unit cell with Z molecules is repeated in the three dimensions to generate the solid. In the following we will refer to the mathematical treatment of Craig and Wamsley [11] for the case of a crystal with M molecules, h unit cells and $Z = M/h$ traslationally equivalent molecules. The basis functions for the exciton states can be written as

$$\phi_{ip}^{r} = \varphi_{11} \cdots \varphi_{ip}^{r} \cdots \varphi_{hZ}$$

where φ_{ip}^{r} denotes the excited state wavefunction (wf) of the *i*-th molecule in the *r*-th excited state while all the other wfs represent molecules in the ground state. p refers to the class of traslationally equivalent molecules.

These functions are used to construct the exciton wfs. Crystal symmetry helps to classify exciton wfs since they must transform as irreducible representation of the translational group. They can be constructed from linear combinations of functions φ_{ip}^{r} taking into account the periodic boundery conditions. Indeed the basis functions are multiplied by the phase factor $e^{\mathbf{ikr}}$ where **k** is the wave vector that also label irreducible representations of the translation group.

Thus exciton wfs are:

$$\Phi_i^r\left(\bar{k}\right) = Z^{-1/2}\sum_p \exp\left(i\bar{\bar{k}}\bar{\bar{r}}\right)\varphi_{ip}^r$$

In order to obtain the energy eingenvalues a secular determinant must be solved

$$\left|\left\langle \Phi_i^r \middle| V \middle| \Phi_j^r \right\rangle - \left[\left\langle \Phi_G \middle| V \middle| \Phi_G \right\rangle + \Delta E\right]\delta_{ij}\right| = 0$$

in which V is the electrostatic interaction operator and Φ_G is the ground-state crystal eigenstate.

This determinant has zero elements when wfs span different wave vectors **k**. As a consequence the determinant is reduced in block form, each with dimensions $Z \times Z$.

When introducing the pertinent wfs the determinant is reduced in the following diagonal and off-diagonal elements

$$D^r + J_{ii}^r - \Delta E \qquad \textit{Diagonal elements}$$

$$J_{ij}^r \qquad \textit{Off-diagonal elements}$$

which can be analytically determined

$$D^r = \sum_n^{n\neq m}\left[\left(\varphi_m^r\varphi_m \middle| V_{mn} \middle| \varphi_m^r\varphi_n\right) - \left(\varphi_m\varphi_n \middle| V_{mn} \middle| \varphi_m\varphi_n\right)\right]$$

$$J_{ii}^r = \sum_q^{q\neq p}\left(\varphi_{ip}^r\varphi_{iq} \middle| V_{ip,iq} \middle| \varphi_{ip}\varphi_{iq}^r\right)$$

$$J_{ij}^r = \sum_q\left(\varphi_{ip}^r\varphi_{jp} \middle| V_{ip,jq} \middle| \varphi_{ip}\varphi_{jp}^r\right)$$

D_r is the difference in electrostatic energies in the ground and excited states (W' in the case of the dimer). J_{ii}^r is the sum of resonant coupling energies between translationally equivalent molecules, whereas J_{ij}^r refers to inequivalent ones.

In Fig. 6 the effect of diagonal and off-diagonal elements on the molecular levels of a crystal where the unit cell is composed of two traslationally inequivalent molecules is reported.

From the figure it is easy to understand that diagonal interaction elements J_{ii}^r form the exciton band, whereas the off-diagonal interactions J_{ij}^r are responsible for the excited state splitting (Davydov splitting). Thus the Davydov splitting is due to translationally inequivalent molecules in the unit cell whereas the mean energy displacement downwards depends on interactions between equivalent molecules.

The width of each Davydov band depends on both types of intermolecular interactions.

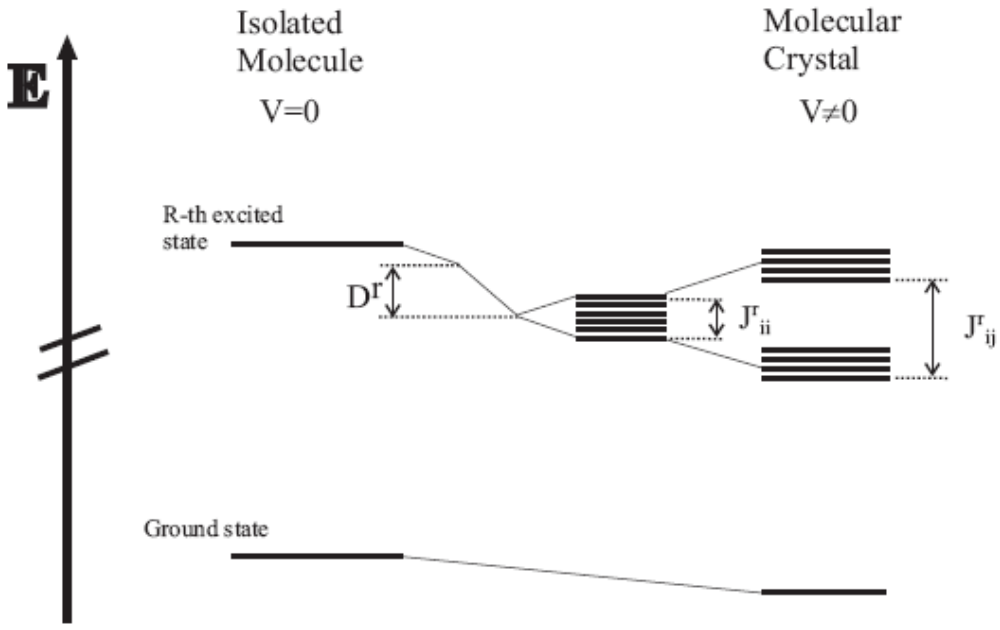

Figure 6. Energy level diagram for an isolated molecule and the corresponding molecular crystal with two molecules per unit cell. The variation in energy of the ground and *r*-th excited state are displayed with the contribution of diagonal and off-diagonal elements.

1.2.3 Excitons in thin films

As discussed, the excitonic energy levels of a molecular solid are strongly influenced by the molecular arrangement. In thin films, according to the preparation procedure, it is possible to obtain different degrees of molecular order. As a consequence the film morphology has a direct impact on the optical properties of the film [15, 16].
The substrate on which the film is prepared has a role in the molecular ordering. Epitaxial growth or quasi-epitaxy has been demonstrated by using single crystal substrates [16]. In particular, in the case of quaterthiophene on a KAP (potassium acid phosphate) substrate the high level of order leads to collective phenomena such as superradiance [15]. In the case of amorphous substrates it has been observed that molecules in direct contact with the surface can have aggregation forms very different form those of the single crystal [17].
As a general rule if the film has a crystalline morphology, the exciton levels and the optical properties will be very similar to those of the corresponding single crystal. In the case of amorphous films, intermolecular interactions are relaxed or even absent and the absorption or PL spectra will resemble those of the isolated molecule [18].
Between these two extreme there are a plenty of cases in which the film morphology tunes the optical properties. One of the most common situation is the concomitant presence of ordered crystallites and disordered or amorphous regions. In this case excitons that are generated in the crystalline domains diffuse -if they do not decay- with a thermally activated hopping process till they find a low energy level. Then excitons are trapped if the thermal energy is not sufficient for detrapping. These trapping sites can be created by a more disordered molecular aggregation with respect to that of the crystal.

1.2.4 Exciton generation, diffusion, energy transfer and relaxation

In the previous sections we have shown how the isolated molecule energy levels split to form the exciton band and the Davydov components in a molecular solid. Here we describe how an exciton can be created and discuss the processes it may undergo after, such as diffusion and relaxation.

EXCITON GENERATION

An exciton can be generated exciting the crystal or the thin film with an electromagnetic wave. This light must have a frequency resonant with the energy gap and the right polarization with respect to the transition dipole moments. Moreover, in order to have light absorption and exciton creation optical selection rules must be satisfied.

In particular, the photon momentum **q** must be equal to the **k** wave vector of the electronic level. Since in the UV/VIS region **q** ~ 0, only **k** = 0 states are probed. If the crystal has an inversion center then states are classified as gerade (*g*) and ungerade (*u*) and only $u \leftarrow g$ transition are allowed. Two photon absorption (i.e. absorption of light through a mid gap virtual state), being a second order process, is capable to perform $g \leftarrow g$ transitions [19].

Either Davydov components of a particular singlet component can be produced, but the lowest-lying singlet exciton represents the surviving state after about a picosecond. Thus, while a triplet exciton can be generated directly, the absorption coefficient for this transition can be quite small; for example in anthracene the singlet-singlet transition rate is 10^8 higher than the singlet-triplet one.

An electrical way to generate excitons is by charge carrier recombination. This process involves: the injection of holes and electrons in the material by means of electrodes, their diffusion in the presence of an electric field, charge recombination and exciton formation. In this case both triplet and singlet exciton are created with a ratio 3/1, respectively. Light emission of electrically generated exciton is called electroluminescence (EL) and in organic semiconductors was first observed by Pope [20]. Electroluminescence is at the basis of the operation of optoelectronic devices such as organic light-emitting diodes (OLEDs) [16] and organic light-emitting field-effect transistors (OLETs) [21] (see § 1.4.3).

EXCITON MIGRATION

As pointed out in the definition of exciton, this quasiparticle is characterized by a wave-like motion. This aspect is relevant not only from the fundamental viewpoint of the energy transport but also because of its importance in opto-electronic device realization.

The absorption of a photon by the organic solid creates a Frenkel state with **k** wave vector near to zero. Immediately after exciton creation, the phases of the wfs of all excited molecules have a unique defined relationship to each other. If the phases are maintained during the excitation migration, the exciton moves as a wave and is said to be coherent. However, because of the interactions with lattice modes (phonons) and imperfections (physical and chemical) in the crystal, transitions are induced among the various state

accessible to the exciton and the coherence may be lost. For time greater that the *coherence time* (time for which the exciton remains coeherent) the eciton is viewed as a localized excitation undergoing a random hoppihg-like motion.

Typical values of the exciton diffusion coefficients for single crystals are $10^{-3} \div 10^{-5}$ cm^2 sec^{-1}.

During the hopping movement, excitons can experience sites with an energy lower than the exciton band edge. In this case, if the thermal energy is not sufficient to promote the hopping, the exciton is trapped. Then it can relax with emission of radiation or with a non radiative pathway.

An analysis of the exciton absorption line width can provide a measure of the degree of the exciton coherence if the magnitude of the homogeneous line width can be estimated. Homogeneous line broadening is caused by local site energy fluctuation from site to site due to thermal effects and natural isotopic impurities thus reflecting the motion of the individual (as opposed to ensamble) molecular excitation. So in the case of highly delocalized exciton and weak exciton-phonon coupling Lorentzian optical absorption line shape is expected. The presence of Gaussian line shapes is interpreted as from the statistical nature of phonon effects on the local site energy of the electronic excited state, i.e. inhomogeneous line broadening. This line shape is indicative of localized, incoherent exciton motion corresponding to strong exciton-phonon coupling.

A detailed review of migration processes in organic semiconductor can be found in reference [4].

EXCITON ENERGY TRANSFER

The term *energy transfer* is used to describe a process that involves one donor molecule and one acceptor molecule, whereas *energy migration* refers to the process of movement of the exciton. Usually migration involves a series of transfers if no intervening trap halts the process [22].

The process of photon reabsorption, sometimes called *cascade* or *trivial energy transfer*, is important at long distances typically more than 100 Å from the site of the of excitation. In this process fluorescence is emitted from a donor and reabsorb by the acceptor. Reabsorb fluorescence can play a significant role in increasing photoconductivity produced by highly absorbed light because the fluorescent light can detrap carriers far removed from the illuminated surface which ordinarily could not be detrapped either thermally or by exciton interactions.

The second mechanism of transfer, known as resonant or Förster transfer, depend upon the overlap between the absorption spectrum of the acceptor (A) and the fluorescence spectrum of the donor (D). In Fig. 7 we report the energy level diagram of a donor-acceptor system in which a Förster energy transfer can occur.

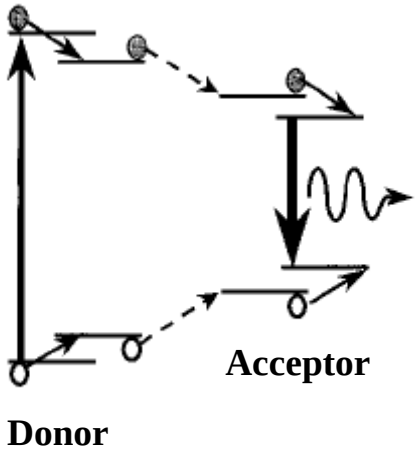

Figure 7. Energy level diagram of donor-acceptor system illustrating the excitation of acceptor molecules by means of nonradiative Förster energy transfer from donor molecules (dashed arrows) and the Franck–Condon shift (solid arrows).

This transfer occurs without the appearance of a photon, and is primarily a result of a dipole-dipole interactions between the donor and the acceptor. The rate of energy transfer depends upon the extend of overlap of the emission spectrum of the donor with the absorption spectrum of the acceptor, the relative orientation of the donor and the acceptor transition dipole moments, and the distance molecules. It is this latter dependence upon distance which has resulted in a widespread use of the energy transfer to measure distances between donors and acceptors.

The rate of energy transfer from a specific donor to a specific acceptor is given by

$$k_T = \frac{1}{\tau_D}\left(\frac{R_0}{r}\right)^6$$

where τ_D is the lifetime of the donor in absence of acceptor, r is the distance between the donor and the acceptor and R_0 is a characteristics distance called the Förster radius at which the efficiency of the transfer is 50%.

A detailed analysis of Förster energy transfer process in organic blends is given in Chapter 4.

EXCITON RELAXATION

There are many pathways that an exciton can undergo in order to relax to the fundamental ground state. The investigation of the energetics and the dynamics involved in these processes is the fundamental question of solid state photophysics. We will discuss in detail all the typical processes of relaxation pathways for an exciton which are reported in Fig. 8.

Initially, light with a resonant frequency is absorbed and an exciton is created in the upper or lower Davydov component (upward arrow) according to frequency and polarization. Few hundred of femtoseconds later the exciton can either relax to the lowest Davydov component (curved arrow) or it can hop to the nearest sites (thick bend arrow) and eventually dissociate to the nearest or next-nearest molecular neighbours to form a charge transfer state. All these early stage processes are non radiative and are usually probed with ultrafast pump and probe spectroscopy [12].

It is important to point out here that, due to the Kasha rule, radiative relaxation always takes place from the lowest state of the exciton band since the *internal conversion* from higher singlet excited states to the lowest takes place in less than 10^{-11} s. As a consequence, we expect light emission from the lowest excitonic level and eventually from ”relaxed states” that lie just below the exciton band. In Fig. 8 it is shown that is possible to observe fluorescence (downward arrow) from the above mentioned singlet states and eventually phosphorescence (oblique arrow) from triplet exciton states.

The fluorescence process occurs spontaneously.

The radiationless transition from an excited singlet state to a triplet state can be induced by internal perturbations (spin-orbit coupling, substituents containing nuclei with high atomic number) as well as by external perturbations (paramagnetic collision partners, like O_2 molecules in the solution, or solvent molecules containing nuclei of high atomic number). These radiationless transitions are termed *intersystem crossing*. The transition from the first triplet state to the singlet ground state has a much longer lifetime (ranging from milliseconds to several seconds) with respect to fluorescence process since it is a forbidden transition.

All the transitions illustrated in Fig. 8 are characterized by a rate constant k that is the sum of at least two components $k = k_r + k_{nr}$, that take into account both radiative and non-radiative deactivation processes. In the case of fluorescence the measured lifetime is the reciprocal of k.

In order to obtain k_r a measure of the fluorescence quantum yield Φ_F has to be carried out, given the following relation

$$k_r = \Phi_F k$$

The fluorescence quantum yield is a number ranging between 0 and 1 and indicating how many photons are emitted in the fluorescence process per photon absorbed.

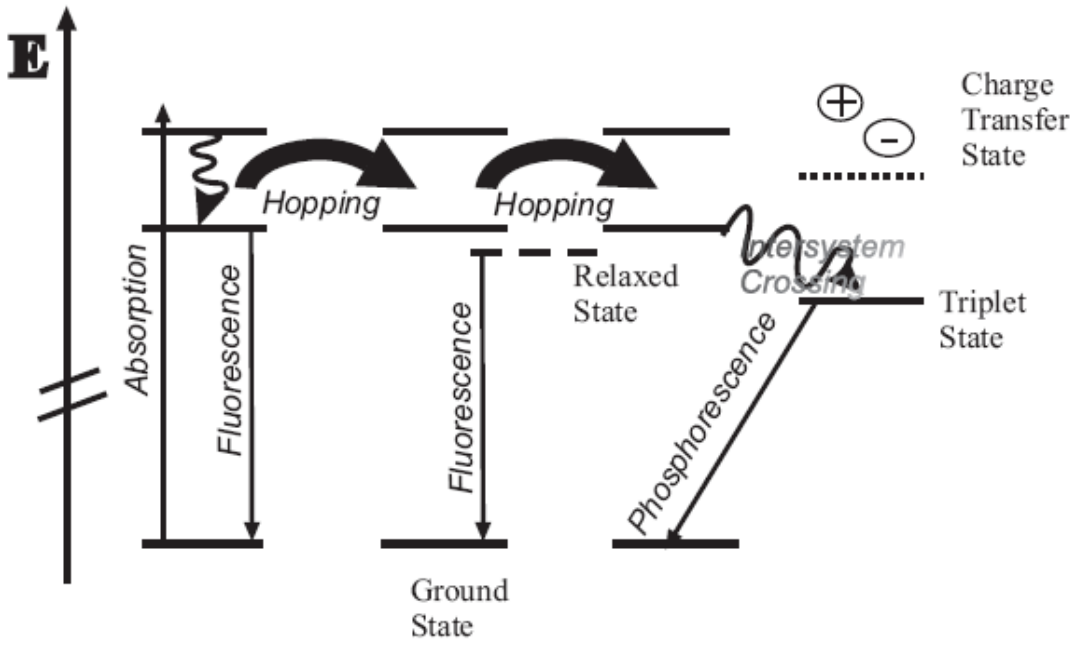

Figure 8. Energy diagram for a molecular solid with two Davydov components, a charge transfer state and a relaxed state. Upward arrow shows the absorption of a photon with an energy matching the higher Davydov band. Thick bend arrows show the exciton hopping between adjacent molecular sites. Wavy downward arrows show nonradiative processes (such as *internal conversion* and *intersystem crossing*) while straight downward arrows represent radiative processes.

1.3 Lasing properties

The demonstration of the first laser, made with ruby in 1960 [23], has led to a revolution in science and technology. Since then the progress of the laser has happened very rapidly, and nowadays lasers are used almost in every field of our life. They are used in a remarkable range of applications ranging from medicine to telecommunications. We now find them throughout everyday life in CD/DVD players, printers, and supermarket scanners.

Materials developments have played a crucial role in the development of new lasers. Organic semiconductors are attractive candidates as laser materials since they can combine novel optoelectronic properties with simple fabrication and the tunability of the chemical structure to give desired features.

After the first inorganic laser realization organic materials started gathering interest played in the development of lasers. The broad spectra of organic molecules was exploited in dye lasers to give laser sources whose wavelength could be tuned and capable of short-pulse generation.

Optically-pumped dye lasers generally operated using dye solutions. Solid-state lasers using organic materials were demonstrated using dye-doped polymers in 1967 [24] and doped single crystals in 1972 [25]. Since the growth of high-quality single crystals is demanding, the much newer generation of easily processed organic semiconductors that opened up to organic semiconductor lasers obtained by conjugated polymer in solution in 1992 [26] and in solid-state [27].

The rapid recent effort in developing organic semiconductor lasers (OSLs) builds on the realization of organic light-emitting diodes, which are now commercially available in displays and TV. It opens up the prospect of compact, low-cost visible lasers suitable for applications from point of care diagnostics to sensing.

We have to notice that electrically-pumped organic lasers are been claimed several times in the last decades, but subsequently discredited [28] and withdrawn [29].

The three main issues to be considered relating to the feasibility of electrically pumped OSLs based on organic light-emitting diodes are the current densities required, the additional losses due to the contacts presence, and the additional losses due to the injected charges and triplet formation.

A typical inorganic semiconductor diode laser operates at a current density as high as 1000 A cm^{-2}. In contrast a typical OLED in a display is operated at around 0.01 A/cm^2. It is not possible to pass 1000 A/cm^2 DC current density through OLEDs because they would overheat and destroy.

All three issues relate to the low charge carrier mobility achievable in organic semiconductor in OLED vertical configuration.

The rapid development of ambipolar organic field-effect transistors (OFET) [30] with increasing light emission properties spreads new possibilities in OSL realization. The intrinsic differences in OFET and OLED architecture (see § 1.4.3) can allow in the field-effect transistor case to avoid the typical drawbacks in OSL realization we have outlined above. In particular, the expected current density in typical devices is much higher (1-10 A/cm^2) and the exciton-polarons quenching and electrode absorption are drastically reduced (see Chapter 5).

1.3.1 Basic principles in of lasing action

In a laser, three fundamental processes are taking place when an electromagnetic wave interacts with a material, absorption, spontaneous emission and stimulated emission.

A more detailed introduction to lasers can be found elsewhere [31]. We will first deal with the spontaneous emission process.

Let us consider that in a material two energy states $|1\rangle$ and $|2\rangle$ are present (Fig. 9). For simplicity hereafter those states are labelled as 1 and 2 levels respectively.

For simplicity we will assume that 1 level is the ground state of the material and that the molecule is initially in its ground level so that the molecule will remain in this level unless some external stimulus is applied to it. If we now assume that a photon with frequency v is incident on the material, there will be a finite probability that the molecule will be raised to 1 level. The energy difference required to undergo such a transition (E_2 - E_1) is obtained from the energy of the incident photon. According to Planck, the energy of this photon will be $hv = E_2 - E_1$, where h is Planck's constant.

The rate of *absorption* will be given by the following equation with B_{12} being a constant factor called the Einstein coefficient for induced absorption, $\rho(v)$ is the spectral energy density and N_1 is the population of the ground state.

$$\frac{dN_1}{dt} = -B_{12}\rho(\nu)N_1$$

If one atom (or molecule for the dye case) is initially in level 2, it will tend to decay to level 1. When this transition takes place, an energy (E_2 - E_1) will be emitted by the molecule. When this energy is liberated as a photon, this process is called *spontaneous emission*. Spontaneous emission is therefore characterized by the emission of a photon of energy $h\nu = E_2 - E_1$ when the atom decays from level 2 to level 1. This radiative emission is one of the two possible ways in which the atom can decay. The decay can also happen in a non radiative way, such as by transfering kinetic energy to the surrounding molecules (see § 1.2.3). This process is completely independent of the presence of an incident field.
The rate of decay of the molecules due to the spontaneous emission is given by equation

$$\frac{dN_2}{dt} = -A_{21}N_2$$

in which A_{12} is the Einstein coefficient for the spontaneous emission and N_2 is the population of level 2.
One final process that has to be taken into account, is the possibility of a radiation field incident on the material, with a frequency that matches that of the spontaneously emitted radiation, and the molecules of the material already excited to level 2. In this case there is a finite probability that this wave will force the molecule to undergo the transition from level 2 to level 1. In this case the energy difference $h\nu = E_2 - E_1$ is delivered in the form of another photon with the same energy as the incident one.

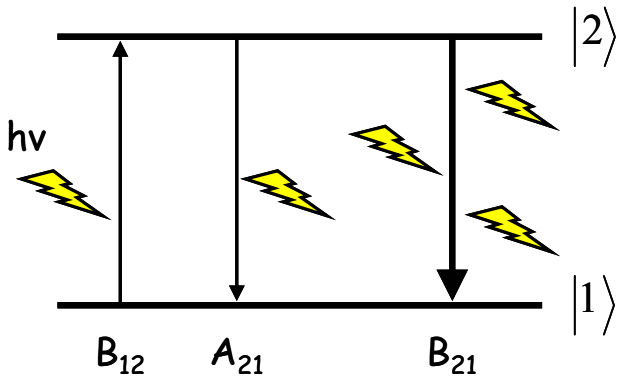

Figure 9. From left to right: absorption, spontaneous emission and stimulated emission in a two-level system

This phenomenom is called *stimulated emission*. The rate of stimulated emission can be expressed in a similar fashion to induced absorption as:

$$\frac{dN_2}{dt} = -B_{21}\rho(\nu)N_2$$

However there is a fundamental distinction between the spontaneous and stimulated emission processes. In the case of spontaneous emission the molecule emits radiation with no definite phase relation with that emitted by another atom. Furthermore, the wave can be emitted in any direction. In the case of stimulated emission, since the process is forced by the incident radiation, the emission of any molecule adds in phase to that of the incoming wave. This wave also determines the direction of the emitted wave. Stimulated emission amplifies the incident radiation as the energy difference between the two energy levels is delivered in the form of a photon that adds to the incident one. The three processes above mentioned, absorption, spontaneous emission and stimulated emission are shown in Fig. 9.

To find out the relationship between the Einstein coefficients, we are going to see how the 2 level system interacts with a stationary thermal radiation field at temperature T. According to Planck's distribution, the spectral energy density $\rho(\nu)$ will be:

$$\rho(\nu) = \frac{8\pi h\nu^3}{c^3}\frac{1}{\exp\left(\frac{h\nu}{kT}\right)-1}$$

where h and k are the Planck's and Boltzmann's constants and c the speed of light.
Since the radiation is stationary, the absorption rate must be the same as the emission rate, and this means:

$$N_1 B_{12}\rho(\nu) = N_2 A_{21} + N_2 B_{21}\rho(\nu)$$

Since we are in thermal equilibrium, the population of both states is described by the Boltzmann distribution. This leads to the notion that the probability of absorption and of induced emission is the same ($B_{12} = B_{21}$) and to the fallowing relation between spontaneous emission and absorption/stimulated emission

$$A_{21} = \frac{8\pi h\nu^3}{c^3}B_{21}$$

After having developed the physics underneath the basic processes of light-matter interaction for a two-level system, now it would be very interesting to describe behaviour the excited level population in two extreme cases: (i) when there is no incident field and (ii) when a strong field is applied.

The rate equation for the two-level system are [32]:

$$\frac{dN_1}{dt} = A_{21}N_2 + \sigma\phi\left(N_2 - N_1\right)$$

$$\frac{dN_2}{dt} = -A_{21}N_2 - \sigma\phi\left(N_2 - N_1\right)$$

The first term on the right part of this equations represents the spontaneous decay from the higher level (independent of incident radiation), the second term, is dependent on the incident radiation and represents the stimulated absorption and emission between the two energy states. ϕ represents the photon flux of the incident field, and σ represents the cross-section for stimulated absorption and emission. It can be shown that $\sigma\phi$ is proportional to $B_{21}\,\rho(\nu)$. Since there are only two levels in this model $\left(dN_1/dt\right)+\left(dN_2/dt\right)=0$. So, N is the total population $N_1 + N_2$ it can be shown that [32]:

$$\frac{dN_2}{dt} = -\left(A_{21} + \sigma\phi\right)N_2 + \sigma\phi N$$

The solution of this differential equation in the absence of any incoming field is the exponential decay of the spontaneous emission.

But in the case of a strong incoming pumping field (condition very similar to what happens in a laser) we find that

$$N_2(t) = \left(N_2(0) - \frac{N}{2}\right)\exp\left(-2\sigma\phi t\right) \approx \frac{N}{2}$$

In this case of very strong pumping the population is equally divided between energy levels 1 and 2. This is a very important point, since in order to achieve lasing, there needs to be what is called *population inversion*, that is, more population in the excited level than in the ground level. This last result comes to show that it is physically impossible to achieve a laser in a system with only two energy levels, at least three are necessary (e.g., in the case of a laser dye, the energy levels are 4).

Let us assume that we have a two level system with N_1 and N_2 populations in each of its levels. If a plane wave with intensity corresponding to the photon flux ϕ travels along the z direction in the material, the elemental change of this flux due to both stimulated emission and stimulated absorption will be

$$d\phi = \sigma\phi\left(N_2 - N_1\right)dz$$

This equation shows that the material can be as an amplifier if $N_2 > N_1$, or it can be as an absorber if $N_2 < N_1$. In thermal equilibrium, according to the Boltzmann statistics, $N_2 < N_1$

and the material will always act as an absorber. In order for a material to act as an amplifier, it is necessary to reach a population inversion state (i.e. $N_2 > N_1$). A material having a population inversion is called an *active material*.

A part from an active material, some kind of *positive feedback* is needed in order to fabricate a laser One of the most simple ways to achieve feedback, is by placing the active region in between two highly reflective mirrors. One of the mirrors is made partially transparent, so that an output can be extracted.

It is important to realize that for a laser to operate, a certain *threshold condition* must be fulfilled. For the oscillation to start, the gain of the active material must compensate the losses in the laser. According to the previous equation, the gain per pass in the active material (i.e. the ratio between the output and the input flux) is

$$g = \exp\left[\sigma\left(N_2 - N_1\right)l\right]$$

where l is the length of the active material.

If the only losses present in the cavity are due to the transmission of the mirrors, the threshold will be reached when

$$R_1 R_2 \exp\left[2\sigma\left(N_2 - N_1\right)l\right] = 1$$

where R_1 and R_2 are the reflectivities of the mirrors.

This equation shows that the threshold is overcome when the population inversion is higher than a critical value known as *critical inversion*

$$\left(N_2 - N_1\right)_c = -\frac{\ln(R_1 R_2)}{2\sigma l}$$

Once the critical inversion is reached, oscillation will build up from the spontaneous emission. The photons that are spontaneously emitted along the cavity axis, will initiate the amplification process. This is the basis of a laser oscillator.

The first step is to achieve population inversion, so we have to find out a system with more than two energy states. A four-level system is shown in Fig 10a. Light excites a molecule from the ground state to an excited state (transition 1 in the figure), and then it rapidly relaxes to another energy level (transition 2). The lasing transition (3) occurs down to a fourth level, which is above the ground state. There is then a rapid return to the ground state via transition 4. The advantage of a four-level system, such as this, is that there can be a population inversion between levels c and d, even when most molecules are in the ground state, so lasing can be obtained for a very low rate of excitation, that is, the threshold for lasing is low.

The energy levels in a typical organic semiconductor (such as organic dye) are shown in Fig. 10b. The figure shows the ground state and first excited singlet state. Each of these electronic energy levels is subdivided into vibronic sublevels. The spacing of these sublevels is approximately 0.2 eV, so at room temperature, there is little thermal excitation from the lowest level. Light can excite the molecule from its ground state to an excited vibrational level of the singlet manifold (corresponding
to transition 1 in Fig. 10a). This will be followed by rapid vibrational cooling to the bottom of the singlet manifold (transition 2). Lasing can then take place by transition 3 to a vibrationally excited level of the ground state manifold, followed by vibrational relaxation (transition 4). Hence the energy levels of organic semiconductors enable them to behave as four-level lasers, with associated low thresholds. It also explains why the emission occurs at longer wavelength than the absorption (a typical strategy for separating absorption from emission in solid-state so reducing the threshold is detailed in Chapter 4).

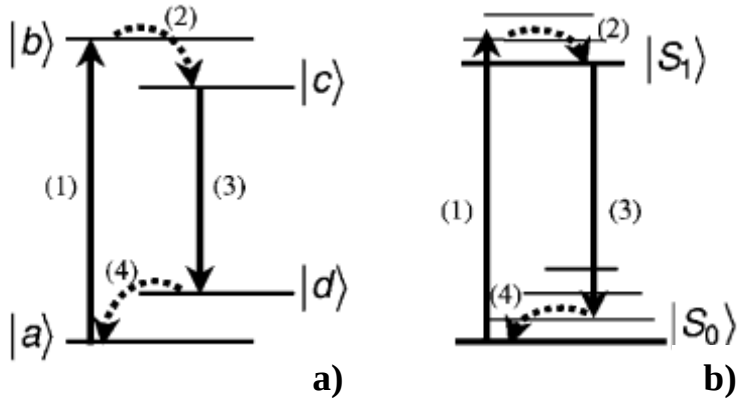

Figure 10. Energy level diagrams for optical gain media: (a) energy levels and transitions of a generic four-level laser materials transitions 1 and 3 are optical absorption and emission, and transitions 2 and 4 are thermal relaxations; (b) energy levels of the lowest two singlet states in an organic semiconductor, including the corresponding optical and thermal transitions to those in (a)

1.3.2 Amplified Spontaneous Emission (ASE)

In this section we will give a short description of the basic features of Amplified Spontaneous Emission (ASE).

In 1996 initial reports [33] demonstrated the dramatic change of luminescence behaviour of conjugated organic solid-state materials when excited at high-density conditions. In contrast to the characteristically broad PL spectrum ranging over about 100 nm, the increase of excitation density results in a spectral confinement of light emission (typically $\Delta\lambda \sim 7$ nm). In the first phase of investigations the underlying mechanism of this effect was not quite clear, so initially the effect was pragmatically named line narrowing.

With the results of more extended investigations (particularly with those making use of a line-focus geometry for excitation) there is now a widespread agreement that the emerging picture of the spectral line-narrowing effects is that of ASE.

However, at the early stage interpretations other than ASE were also considered because of the very details found in the particular investigations. The directions of explanation included superfluorescence (SF) [33] and high-density interaction leading to exciton condensation [34].

SF and ASE are closely related processes representing the transient and the steady state form of phase-coherent light amplification [35].

SF, as well as superradiance (SR), are cooperative spontaneous emission processes (while ASE is a collective process) constituting pulses characterized by time duration and delay proportional to the reciprocal of N (with N being the number of radiative species), and the peak intensity proportional to N^2 [36]. Following primary definitions the term SF further specifies the situation in which the medium is non-resonantly pumped. In this way the excited states are initially uncorrelated and no residual polarization is left after excitation. The SF process is initiated by ordinary spontaneous emission that induces phase correlation between the ensemble of emitters (self-phase locking) and the system evolves toward a state of correlated emission.

One of the limiting conditions for the SF regime is given by the relation $l/c < T_c < T_1, T_2$ (l being the active volume length, c the speed of light, T_c the self-induced correlation time of SF, T_1 spontaneous decay time and T_2 dephasing time).

The more the left-hand side of the relation is violated the more stimulated effects become prominent, thus resulting in a gradual transition from SF to ASE [37]. In the limit $L/c >> T > T2$ the SF is totally suppressed and luminescence is due to single pass amplification of spontaneous emission. In the case of an ASE process, coherent light amplification is provided by the single pass amplification of photons gaining intensity by going through the active volume of the inverted medium.

Generally, the following physical evidences stand for an ASE process to take place: (i) the line narrowing depends on film thickness and size of excitation area; (ii) a high degree of polarization and directivity of emission; (iii) a threshold-like behaviour rather than a gradual increase of light output; (iv) a gain line width saturation at high excitation conditions.

However, SF can only build up for very short pulse excitation since too long excitation pulses smear out the phase correlation. So considering SF in conjugated polymers the excitation pulse duration has to be compared with a rather short dephasing time that is in the region of $T_2 \approx 100$ fs.

In ASE, the spontaneously emitted photons that travel along the active region (the one in which, through optical pumping, population inversion has been achieved) of a high gain medium, can stimulate the emission of more photons, and thus lead to a very substantial increase at the end of the medium. Let us consider an amplifying medium with a gain coefficient *g*, and a field propagating in it. The change of intensity per unit length will be

$$\frac{dI}{dz} = g(\lambda) + (A_{21} N_2 h\nu)\left(\frac{\Omega}{4\pi}\right)$$

The second term on the right side is the contribution of the spontaneous emission to the gain in the *z* direction. Since the spontaneous emission is emitted isotropically, we only take into account the few photons that are emitted in the direction where the amplification is taking place. (That is the reason for the factor $\Omega/4\pi$, Ω is the solid angle subtended by the ASE, and 4π represents in steradians all the possible directions). The solution of this equation is:

$$I(z) = \left(\frac{A_{21} h\upsilon \Omega N_2}{4\pi g(\lambda)}\right)\left(e^{g(\lambda)z} - 1\right)$$

ASE is very dependent on the length of the amplifying medium. Since the gain depends on the wavelength, the wavelengths around the position of the peak gain will experience much larger amplifications than those experienced by other wavelengths. It is for this reason, that ASE results in a very sharp narrowing of the emission spectrum, that will occur around the wavelengths where the gain is maximum. ASE full widths at half maximum (FWHM) are typically below 10 nm and can easily be confused with a lasing line.

Spontaneous Emission (SE) processes, either ASE or lasing requires sufficiently high excited state densities in order to provide the collective interaction of emitters by the radiation field.

Excitation densities typically range from $n = 10^{16}$ cm^{-3} up to 10^{20} cm^{-3} when the cross-section for SE processes is studied in pump–probe or in line-narrowing experiments (see § 2.4). The upper limit is usually given by the photo-thermal damage threshold of the organic materials.

Quite generally, the transition from spontaneous emission to SE processes in organic thin films is roughly about an excited state threshold density of $n = 10^{18}$ cm^{-3}, and in the laser devices this threshold is lowered by orders of magnitude due to the optical feedback structure. Nevertheless, high-density effects have also to be taken into account for organic laser devices, since operation for high laser output once again requires high excitation density conditions. Therefore, it is important to know about the physical interaction processes that come into play at elevated photoexcitation.

In the onset regime of SE processes which is at excitation density of $n > 10^{18}$ cm^{-3}, bimolecular recombination processes also become significant [38].

These possible recombination paths include enhanced non-radiative relaxation of exciton–exciton annihilation [38] and formation of non-emissive interchain species [39].

Furthermore, in the high-density regime, there is the possibility of exciton association [40] resulting in the formation of biexcitons, a phenomenon which is well known in inorganic semiconductors.

1.4 Electrical properties

All the organic compounds designed as *semiconductors* are those made of sp^2 hybridized carbon atoms, also called *conjugated*. As we report in section 1.1, under such circumstances, each carbon is linked to its neighbours by three σ bonds resulting from the hybridazation of 2s, $2p_x$, and $2p_y$ orbitals while the remaining $2p_z$ orbital forms a π bond which presents a significantly less overlap with respect to σ bonds. For this reason, the energy distance between the bonding and the antibonding molecular orbitals is somewhat reduced thus allowing visible light absorption by the material and semiconductor behaviour at nonzero temperature.

In the case of a ideal long chain of carbon atoms, the π bonds delocalize over the whole chain and form a one-dimensional electron system. The resulting one-dimensional band has substantial band width and the chain can be viewed as a one-dimensional semiconductor with a filled valence band originating from the HOMO (*highest occupied molecular orbital*) and an empty conduction band coming from LUMO (*lowest unoccupied molecular orbital*). In this scenario it is quite understandable why charges can be injected and reside in conjugated molecular system.

However, the limiting step for charge transport in a solid is not within the molecular unity but it involves charge transfer between molecules (or molecular chain). Because orbital overlap between molecules is low the phenomenon of charge transport in conjugated solids is not unambiguously rationalized.

1.4.1 Charge transport in organic materials

BAND TRANSPORT

Band transport refers to the mechanism occurring in crystalline inorganic solids like metals and semiconductors. Band theory can be found in many textbooks and will not be detailed here [41]. Briefly, when a very large number of interacting atoms are brought together, energy bands in solids form since their energy levels become so closely spaced that they become indistinct.

The likelihood of any particular band to be filled is given by the Fermi-Dirac statistics:

$$f(E) = \frac{1}{1 + \exp\left(\frac{E - E_F}{kT}\right)}$$

so that at zero temperature bands are filled up to the so-called Fermi energy E_F.

On this basis, solids can be divided into insulators, in which the highest occupied band (*valence band*) is completely filled and the lowest unoccupied band (*conduction band*) is completely empty, and metals in which the conduction band is partly filled. Semiconductors are a particular case of insulators in which the energy gap between the top of the valence band and the bottom of the conduction band is small enough that, at nonzero temperature, the smoothing out of the Fermi-Dirac distribution causes an appreciable number of states at the top of the valence band to be empty and an equivalent number of states at the bottom of the conduction band to be filled.

The simplest model of charge transport in delocalized band is the Drude model which assumes that the carriers are free to move under the influence of an applied electric field but subject to collisional damping forces. Note that scattering centers are phonons (lattice vibration) or impurities.

According to this model, mobility can be defined as

$$\mu = \frac{q\lambda}{m^* \upsilon_{ph}}$$

in which q is the elemental charge, m^* is the charge effective mass, υ_{th} is the electron thermal velocity and λ is the electron mean free path.

The temperature dependence of the mobility vary according to the nature of the scattering centers (acoustical or optical phonons, charged impurities…). However, in all cases, it is found that the dependence follows the general law

$$\mu(T) \propto T^{-n}$$

with n positive in most practical cases so that the mobility increases when the temperature decreases.

Evidence of *band transport* is often claimed to be brought when such temperature dependence of mobility is observed. However, even in highly pure crystalline molecular solid, this argument is denied by the fact that for temperature higher than 100 K the calculated value of mean free path λ is smaller than the distance between molecules in the crystal which is not physically consistent with diffusion limited transport [42].

POLARON HOPPING

The main reason why the model band is unable to describe completely for charge transport in organic semiconductors is that it fails to account for *polarization* in this materials. Polarization in organic solids has been analyzed in detail by Silinsh and Cápek [42]. A charge carrier residing on a molecular site tends to polarize its neighbouring region. As the barely- formed polarization cloud moves with then charge, the travelling entity is no longer a *naked* charge but a *dressed* charge. This quasi-particle is called *polaron*.

In conjugated solids the main polarization effect is that on the charge density formed by π-electrons. In order to estimate the stability of the polaron, two typical times are defined: (i) the residence time τ_{res} which corresponds to the average time a charge resides on a molecule and (ii) the electronic polarization time τ_{el} which is the time that the polarization cloud need to form around the charge.

By implementing the Heisenberg's uncertainty principle, an estimation of the order of magnitude for both time can be obtained. For the residence time, the pertinent energy is the width of the allowed band which is typically 0.1 eV in an organic semiconductor and 10 eV in an inorganic semiconductor, thus giving a residence time of 10^{-14} s and 10^{-16} s respectively. For the electronic polarization time, the corresponding energy is that of an electron transition, i.e. the energy gap (~ 1 eV), so that the time is of the order of 10^{-15} in both cases.

So in organic semiconductor, charges do not move so fast to prevent the polarization cloud to have time to form in the molecular site and charge transport is allowed by movements made by polarons along the conjugation, and by the jump of the charge carriers from one molecule to a neighbour, or from a polymer chain to a near chain (Fig. 11).

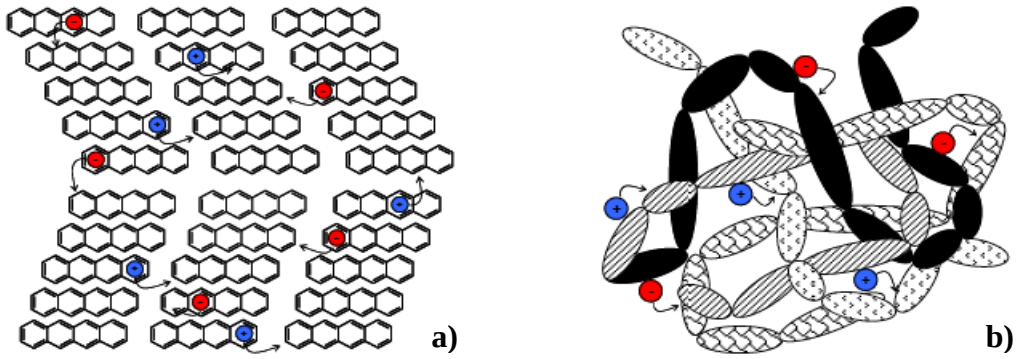

Figure 11. Scheme of electrons and holes hopping conduction. Holes are represented by blue circles and electrons by red circles. (a) Small molecules case (e.g. tetracene, that is an ambipolar materials): intramolecular and intermolecular hopping in a crystalline structure. (b) Polymers case: intra-chain and interchain hopping in an ideal ambipolar polymer.

Now we briefly introduce the Marcus model as an approach for describing charge transport in polarizable media [43].

In the case of a localized state without interactions between nearest-neighbour, the total energy of the excess carrier (or of the polaron) residing in a molecular site at the configurational coordinate Q

$$E(Q) = E_0 - AQ + BQ^2$$

where $A>0$ is the local electron-phonon coupling constant, BQ^2 represents the elastic energy produced by the lattice distortion, and E_0 is the carrier energy in absence of phonons.

The linear phonon-electron interaction lowers the carrier energy by $E_b = A^2/4B$ (*zero-order polaron binding energy*) by altering the local configuration of the lattice, so that the minimum energy is achieved. This corresponds to a change in equilibrium position from $Q = 0$ to $Q_0 = A/2B$ (Fig. 12). The electron and its associated local distortion as a whole are called *localized polaron*.

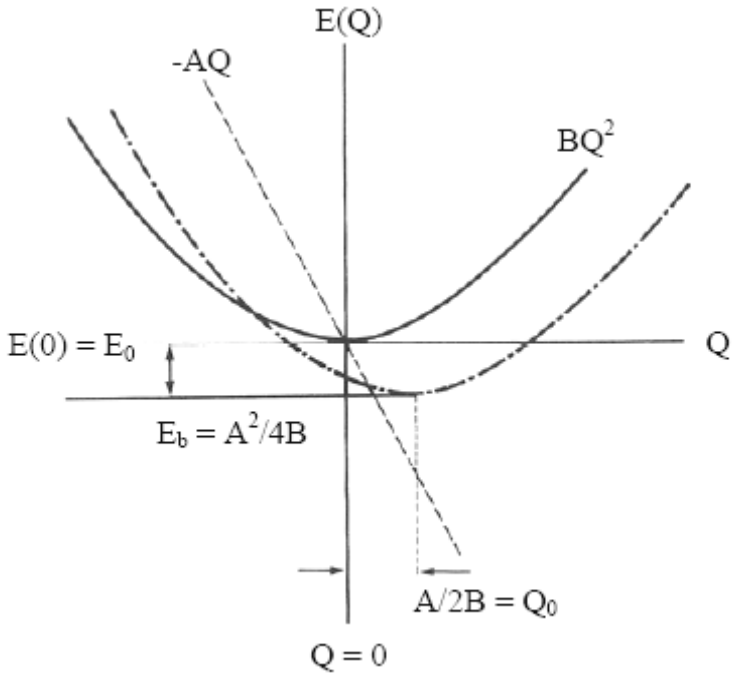

Figure 12. The total energy of a polaron *E(Q)* in a solid as a function of the configurational coordinate *Q*.

Transfer between different molecular sites occurs when the configuration of lattice atoms offers the same energy on both site. The linear phonon coupling does not alter the phonon frequencies [44], so B is unchanged and the condition of equivalent electron energy for

two different sites is $Q_1 = Q_2$. The activation energy needed to distort both molecules in order to obtain this configuration is:

$$W_a = B(Q_0 - Q)^2 + BQ^2$$

which is minimized for $Q = A/4B$.

The polaron transfer in this configuration is allowed by the medium thermal fluctuations.

So far the discussion was limited to the case of a localized small polaron. If there is an interaction energy (J) between neighbouring molecules, the energy degeneracy at X (as shown in the previous case) is lifted, giving rise to new states (X_1 and X_2, Fig. 13). The activation energy for transfer is lowered from X to X_1 and the new potential energy barrier for the charge motion is $W_a^{'}$.

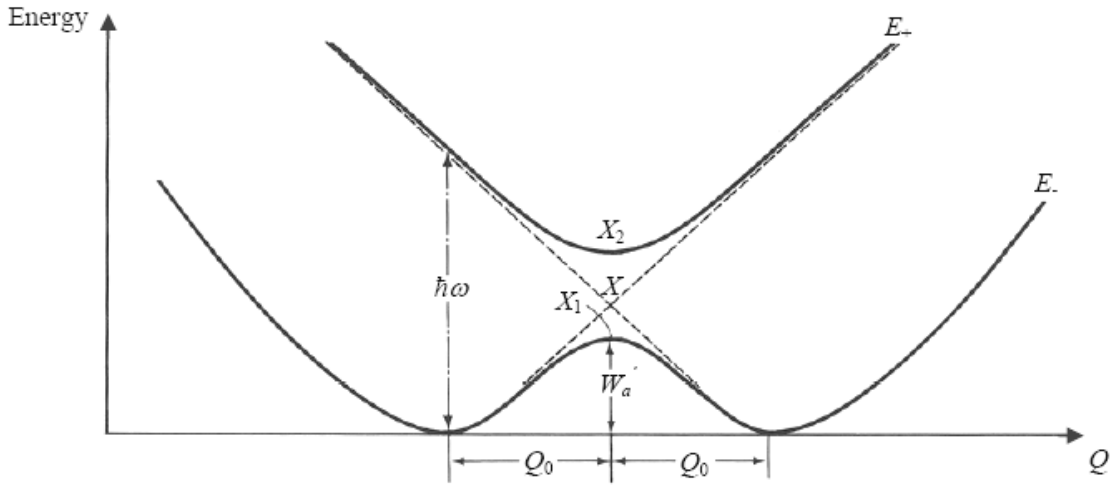

Figure 13. The activation energy ($W_a^{'}$) of a small polaron in two-site system as a function of the configurational coordinate Q.

If the magnitude of J is so large that the transition between E_- and E_+ is improbable, the carrier moves *adiabatically* [45]. Otherwise, if J is small enough to allow the transition, the transfer is called *non-adiabatic* [46].

A generalization of the Marcus theory establishes an important criterion for distinguishing activationless (band-like) and localized transport; namely, the former occurs when $J > \hbar\omega$ while the latter dominates when $J < \hbar\omega$.

The temperature dependence of mobility is also different in each one of the two cases. At low temperatures J is the dominant factor, and the motion is band-like, with the polarons moving with different effective mass [46] in either cases.

As T increases, the polaron bandwidth narrows. Eventually, at a temperature T_c lifetime broadening caused by other scattering processes, e.g., defects and electron-phonon interactions, is comparable to or larger than the polaron carrier bandwidth. In this limit, inelastic scattering dominates with the corresponding absorption and emission of phonons.

The problem with the hopping transport is that dozens of different model have been proposed, based on different physical principles and approximations.

In most cases temperature functional dependence of charge carrier mobility is expressed as

$$\mu \propto \mu_0 \exp\left[-\left(\frac{T_0}{T}\right)^{1/\alpha}\right]$$

in which α is an integer ranging from 1 and 4 according to the dimensionality of the system, T_0 is inversely proportional to the density of states at the Fermi level and μ_0 is a mobility pre-factor.

In real organic transistors, charge transport is most of the limited by localized states induced by defects and undesirable impurities. Clear evidence for such a process is given by the fact that the performance of the devices is strongly sample dependent. *Multiple trapping and thermal release* (MTR) model can take into account for such a trend.

In particular, MTR model [47] applies to well-ordered materials such as vapour-deposited small molecules like pentacene or oligothiophenes (see Chapter 3) in which thermally activated mobility is often observed. The basic assumption of the model is a distribution of localized energy levels located in the vicinity of the transport band edge. During the transit in the delocalized band, the charge carriers interact with the localized levels through rapping and thermal release.

The model rests on the fallowing assumptions: (i) carriers that arrive at a trap are instantaneously captured with a probability close to one, and (ii) the release of trapped carriers is controlled by a thermally activated process. The resulting effective mobility μ_{eff} is related to the mobility in the transport band μ_0 by the relation

$$\mu_{eff} = \mu_0 \alpha \exp\left[-\left(\frac{E_c - E_t}{kT}\right)\right]$$

in which E_c is the energy corresponding to the transport band edge, E_t is the energy of a single-trap level and α is the ratio of the trap density of state to the effective density of states (DOS) at the transport band edge.

An important outcome of the MTR model is that in the case of an energy distributed DOS, mobility is gate-voltage dependent [48]. It is worth noting that in transistors made with single crystal, the mobility is found to be very seldom gate dependent, which indirectly confirms that the gate voltage dependence originates from localized levels associated with chemical and physical defects.

1.4.2 Charge injection in organic materials

The organic semiconductor/metal contact interface is usually treated as a Mott-Schottky barrier, where the barrier height is given by the difference between the metal work function (WF_m) and the semiconductor Highest Occupied Molecular Orbital (HOMO) for hole injection; or between WF_m and Lowest Unoccupied Molecular Orbital (LUMO) for the electron injection. The barrier is formed after the contact between the metal and the semiconductor, and physically consists of a region of uncompensated charge. This *space charge* causes a voltage drop at the interface. From the energetic point of view, there is a bending of the energetic levels of the semiconducting material at the interface, as metal creates a gap with respect to its work function. When the WF_m and the electronic level of the semiconductor are energetically closer, a good ohmic contact is achieved. In the case of non-ohmic contacts, a high potential barrier is formed, thus leading to poorly efficient charge injection.

In the simplest analytical treatment of the semiconductor/metal interface we suppose that vacuum levels of both the metal and the organic semiconductor are in registry. This is the basic assumption in Mott-Schottky theory (Fig. 14a). Indeed, when the metal and the organic semiconductor come in intimate contact, the organic material is in the potential rise of the tail of the metal electron distribution. Thus, both the vacuum levels get aligned in a very narrow interfacial gap

As it can be seen from Fig. .14 a, the metal and the organic semiconductor interface is not at the equilibrium because WF_m is larger than the work function of the work function of the organic material (ϕ) so some electrons can move through the interface from the

organic to the metal leaving the organic semiconductor locally positive in the proximity of the interface.

This charge redistribution obstructs further electrons movements until the Fermi levels of the metal and the organic semiconductor are aligned.

As a result, a diffusion layer (W) with band bending is formed to align the Fermi energies of the two solids, hence building up the organic layer potential (V_{bi}, in Fig. 14b).

Equations for the hole and electron injection are easily express from the physical properties of the system as:

$$\Phi_B^p = I - WF_m$$

and

$$\Phi_B^n = WF_m - A = E_{gap} - \Phi_B^p$$

that are the classic Schottky-Mott equations for simple contacts. I and A are the organic semiconductor ionization energy and electron affinity.

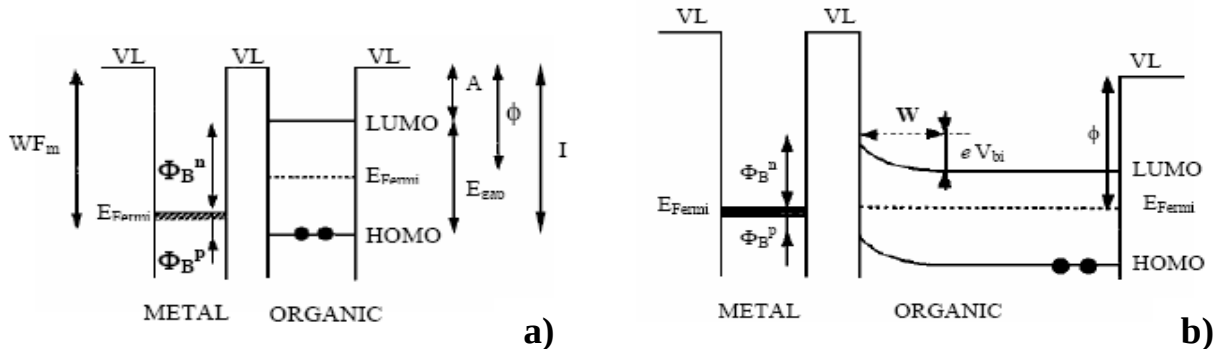

Figure 14 a) Schematic representation of an ideal organic semiconductor/metal interface with WF_m metal working function, A organic semiconductor electron affinity, I ionization energy, E_{gap} energy band gap. Φ_B^p and Φ_B^n are the energy injection barrier for holes and electrons respectively and ϕ the work function of the organic material. b) Energy level band bending at the organic semiconductor/metal interface. A diffusion layer of thickness W compares.

In real cases, however, many organic semiconductor/metal interfaces do not follow the Mott-Schottky model and the electronic structure is significantly more complicated with respect to what depicted in Fig 14. Often, an interface dipole (Δ) is present so shifting upward the vacuum level of the semiconductor with respect to the metal. Interface dipoles have several possible origins, including charge transfer between the semiconductor molecules and the metal, reduction of the metal work function due to adsorption of the organic layer and population of metal-induced mid-gap (new energy levels) at the

interface. Sometimes, simple chemical notions (e.g., high or low electron affinities) can be used to predict the sign of the dipole (i.e., whether it points to the metal or to the semiconductor), but it is a difficult computational problem to predict its magnitude. The magnitude of the potential change due to the dipole presence must be included in the calculation of the valence band offset

$$\Phi_B^p = I - WF_m \pm \Delta$$

in which the sign in front of Δ is chosen to reflect the direction of the interfacial dipole.

1.4.3 Electronic and opto-electronic devices

1.4.3.1 Organic Light-Emitting Diode (OLED)

An organic light-emitting diode (OLED) is a solid-state device whose emissive electroluminescent layer comprises a film of organic material sandwiched between two electrodes. OLEDs can be based on thin films of organic small molecules or polymers that generate light when a voltage bias is applied between electrodes. Usually the two electrode materials are selected to favour hole (anode) and electron (cathode) injection. Generally the anode is made of ITO (Indium-Tin-Oxide, transparent material with high work function, ideal for hole injection) and the cathode of Al (low work function material, ideal for electron injection).

The first demonstration of the OLED dates back to the 1960s when electrically driven light emission from non-crystalline organic materials was first observed [49]. After that, several studies were carried out by academic groups and companies (Kodak, Pioneer, Motorola, NEC, etc…) both for fundamental physics comprehension and application purposes.

The study of the OLEDs was so impressive and massive because they are, combined with transistors, the main component for flat panel displays. Nowadays electronic products containing displays are becoming more and more portable. Therefore, they need some peculiarities like lightweightness, flexibility, brightness, etc… These, with many others, are the strong points of the OLEDs. In fact they are thinner, lighter and more flexible with respect to their inorganic counterpart. Moreover, OLEDs can be as bright as LEDs and they consume much less power. Due to the organic processabilty, they are easier to produce and can be made to larger area. Finally OLEDs have large fields of view, about

170 degrees, a significantly advantage over, for example, liquid crystal displays. Obviously, these devices present also some disadvantages: they have typically shorter lifetime (in particular life time of the blue emitter is critical, about 1.000 hours), they are not very stable and can easily be contaminated by water or oxygen.

Most of organic materials (also the most highly emitting) show either p-type (hole) or n-type (electron) charge transport characteristics [50, 51]. For this reason different organic materials are combined in a multi-layer architecture to improve the performances. It can thus be employed a material for hole transport, another one for electron transport and a third one for light emission (Fig. 15).

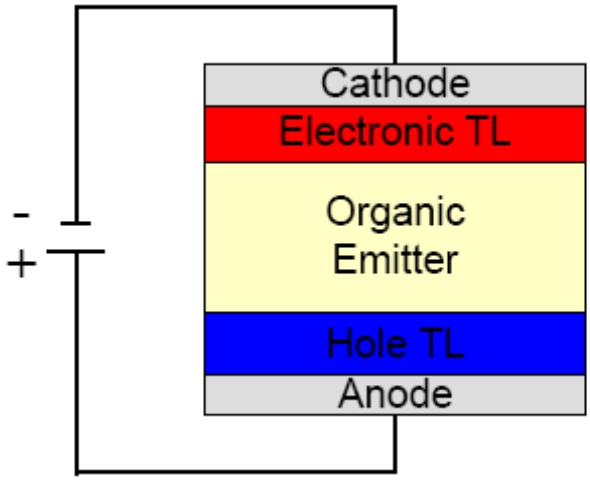

Figure 15. Scheme of a classic 3-layer OLED architecture.

To understand the basic working principles of an OLED we can use the example of a basic three-layer device reported in Fig. 15. When a positive electrical potential is applied to the anode, the injection of holes occurs from this electrode into the hole transport layer (HTL), while the injection of electrons occurs from the cathode to the electron transport layer (ETL). The injected carriers move through the organic materials toward the oppositely charged electrode.

The OLED works if the energy gap and the energetic positions of the HOMO and LUMO levels of the materials are positioned as in the scheme of Fig. 16. The hole injection from the HTL layer to the organic emitter is supported, ensuring hole blocking at the ETL one.

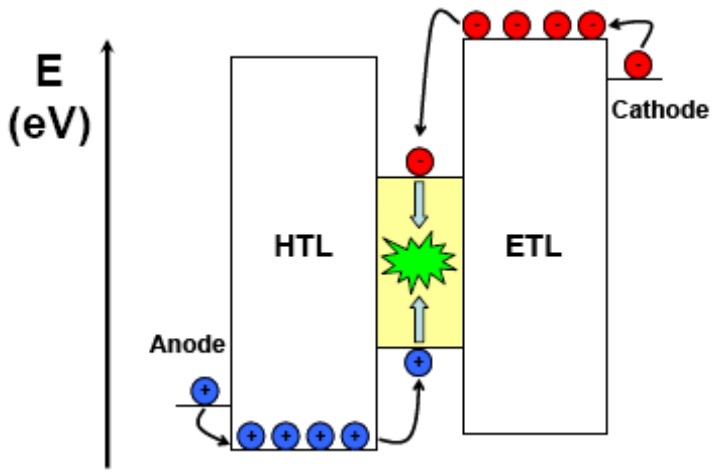

Figure 16. Scheme of energy levels for a three layers OLED. On the left the hole injection occurs in the hole transport layer (HTL). On the right the electron injection takes place in the electron transport layer (ETL).The radiative recombination occurs in the organic emitter (pale yellow).

Similarly, electron injection from the ETL to the organic emitter and the electrons blocking at the HTL is ensured. In these way we increase the probability of exciton formation and radiative recombination in the emitting layer.

1.4.3.2 Organic Field-Effect Transistor (OFET)

A transistor is a semiconductor device commonly used as an amplifier or an electrically controlled switch. The first field-effect transistor (FET) was inorganic and was invented in 1947 by John Bardeen, William Shockley and Walter Brittain (Nobel prize, 1956).

Since their discovery, transistors have dominated the mainstream microelectronics industry; in fact, they are the fundamental building blocks for basic analytical circuits.

An Organic Field-Effect Transistor (OFET) is a transistor based on organic semiconductors.

The interest in using organic semiconductors as the active layers in FETs stemmed from the demonstration of field-effect conduction in small organic molecules[52] and conjugated polymers [53]. In 1986 the first OFET was reported by A. Tsumara [54]. From that moment a huge improvement in materials performances and development of new fabrication techniques took place.

OFETs are technologically attractive because all their layers can be deposited at low temperature and with low cost, in a large area and on a flexible substrate [55]. OFETs have also already been demonstrated in flexible electronic applications such as active matrix electronic paper displays, sensors, and low-cost radiofrequency identification cards (RFIDs). In order to render these devices more suitable for various applications an important step is to increase the charge carriers mobility. Indeed, the performances of OFETs are still lower with respect to those of the amorphous silicon devices.

Since conjugated organic solid are more similar to insulators than semiconductors, charge transport in these materials is much less efficient than in conventional semiconductors. Clearly, the problem is more crucial in transistors where charges have to travel along much longer paths than in diodes. At the current state of the art, mobility in organic thin-film transistor ranges between 0.01 and 10 cm^2/Vs, which is still much lower than what found in inorganic semiconductors (mobility is around 10^3 cm^2/Vs in crystalline silicon), but substantially higher than the typical values obtained in organic light-emitting diodes or photovoltaic cells.

In particular, hole mobility on the order of 1 cm^2/Vs and 0.1 cm^2 /Vs was reached using respectively small molecules [56] and conjugated polymers [57] as organic semiconductor materials.

The highest mobility and most intrinsic charge transport properties in organic semiconductors are observed in single crystals, in particular, hole mobility of up to 20 cm^2/Vs is observed in rubrene [58].

High mobility in OFET is the result of large research efforts at improving structural order in the organic semiconductor film. However, the physical origin of high mobility in organic solid is still an unresolved theoretical question. In addition to high mobility values, the major objectives are:

stability under ambient conditions and under bias stress, device to device fabrication reproducibility as well as easy processing, e.g., from solution, which would make organic semiconductors a viable alternative to amorphous silicon.

OFETs WORKING PRINCIPLES

A field-effect transistor is composed by a semiconducting material working as a *channel* in which current flows. At one extremity of the channel there is an electrode called *source* and at the opposite side there is a second electrode called *drain*. The physical dimension of the channel are fixed but the potion of the active material actually used for the conduction

can be varied by applying a voltage to a third electrode called *gate*. The FET conductivity depends on the portion of the channel open to the current. Little changes in the gate voltage can involve great changes in the current flowing from the source to the drain, thus amplifying the signal. If the channel is composed by an organic material, we have an *organic field-effect transistor* (OFET). The channel is in contact with a dielectric layer working as a capacitor, and allows current modulation through the gate voltage

The main constituting elements of an OFET are: three contacts (source, drain and gate), an active semiconducting material and a dielectric layer. These key elements can be differently combined to obtain different device structures. The most common configurations are: *bottom gate - bottom contact* (in which the drain and source electrodes are positioned directly on the dielectric film), *bottom gate - top contact* (in which the source and drain electrodes are grown on the organic semiconductor) and *top gate - bottom contact* (in which the dielectric film is deposited on the organic semiconductor and the gate contact is placed on top of it).

Since throughout this thesis we deal only with *bottom gate-top contact* configuration (Fig. 17), we use this simple configuration to explain briefly how a classic OFET works.

The physical dimension of the channel is fixed and it is described by the channel length (L) and the channel width (W). We refer to the voltage applied between drain and source as V_{ds}, while the voltage applied to the gate is labelled as V_g. By convention, the source is generally considered grounded and the voltage is applied to the drain contact. The current flowing through the channel is called I_{ds} and it is a strong function of V_g.

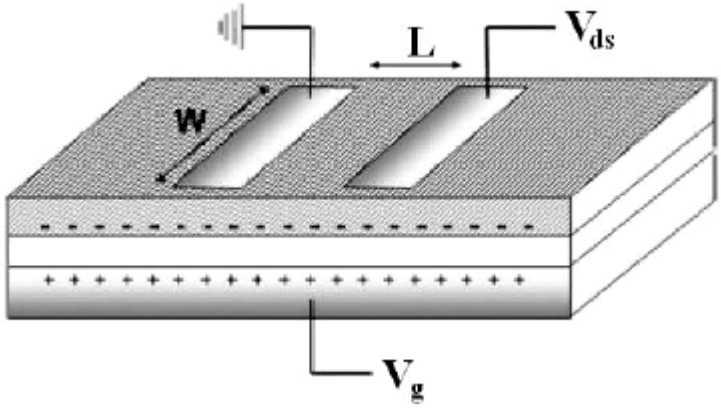

Figure 17. Classic BG-TC geometry with physical channel dimensions labelled: W as channel width, L as channel length.

The dielectric is sandwiched between the gate and the organic semiconductor, and they work as two plates of a plane capacitor. Thus, when a V_g is applied, charges of different sign are accumulated at gate/dielectric and dielectric/organic semiconductor interfaces (as in a classic capacitor, in Fig. 17 a positive gate voltage applied as an example). Much of this accumulated charge in the active material is mobile and moves in response to the applied V_{ds}. When no V_g is applied there are ideally no free charge carriers, and the device is *off*. Otherwise, with applied V_g the device is *on*. This gate-induced charge carrier creation is called *field-effect*, and it is the key-idea of the working principle of FETs [59].

An n-channel OFET (i.e., electrons are transported through the channel) can be used as an example to understand the basic device operational regimes due to the gate voltage dependence of the distribution of "free" charges in the active material [60]. If we assume ohmic contacts and no trap presence (*ideal case*), when a Vg > 0 is applied free electrons start accumulating at organic semiconductor/dielectric interface. Without any voltage difference between drain and source (V_{ds} = 0), this negative charge density is uniform along all the active material, thus having a uniform *conduction channel*. If a positive V_{ds} is applied, the induced charge superficial density in a certain position *x* of the semiconductor is described by:

$$q_{ind} = n(x)et = C_i\left[V_g - V(x)\right]$$

where *t* is the thickness of the charge layer in the channel, *n(x)* is the number density of charges in the channel, *e* is the electron charge and C_i is the insulator capacitance per area unit.

However, real devices are far from being ideal and not all induced charges are mobile; a large number of deep charge traps are present in the film (deep enough to effectively immobilize electrons trapped in them). Deep traps have to be filled before the additionally induced charge can move. Thus, a minimum gate voltage has to be applied to obtain free electron density in the channel, the *threshold voltage*, V_t. Obviously, in n-channel OFETs Vt is higher than zero (for a p-channel OFETs, V_t is lower than zero since the charges flowing are positive). If we include the threshold voltage in the previous equation:

$$q_{ind} = n(x)et = C_i\left[V_g - V_t - V(x)\right]$$

As V_t is not ideally a function of *x*, with V_{ds} = 0 and $V_g > V_t$ a homogeneous charge density is present in the channel. When a small source-drain voltage is applied ($V_{ds} << V_g - V_t$) a *linear gradient* of charge density is formed. The voltage drop between organic

semiconductor and gate is larger at the source, where V(x) = 0 (grounded), than at the drain, where V(x) = V_{ds}. This is the *linear regime* in which the current flowing through the channel is directly proportional to V_{ds} (Fig. 18a).

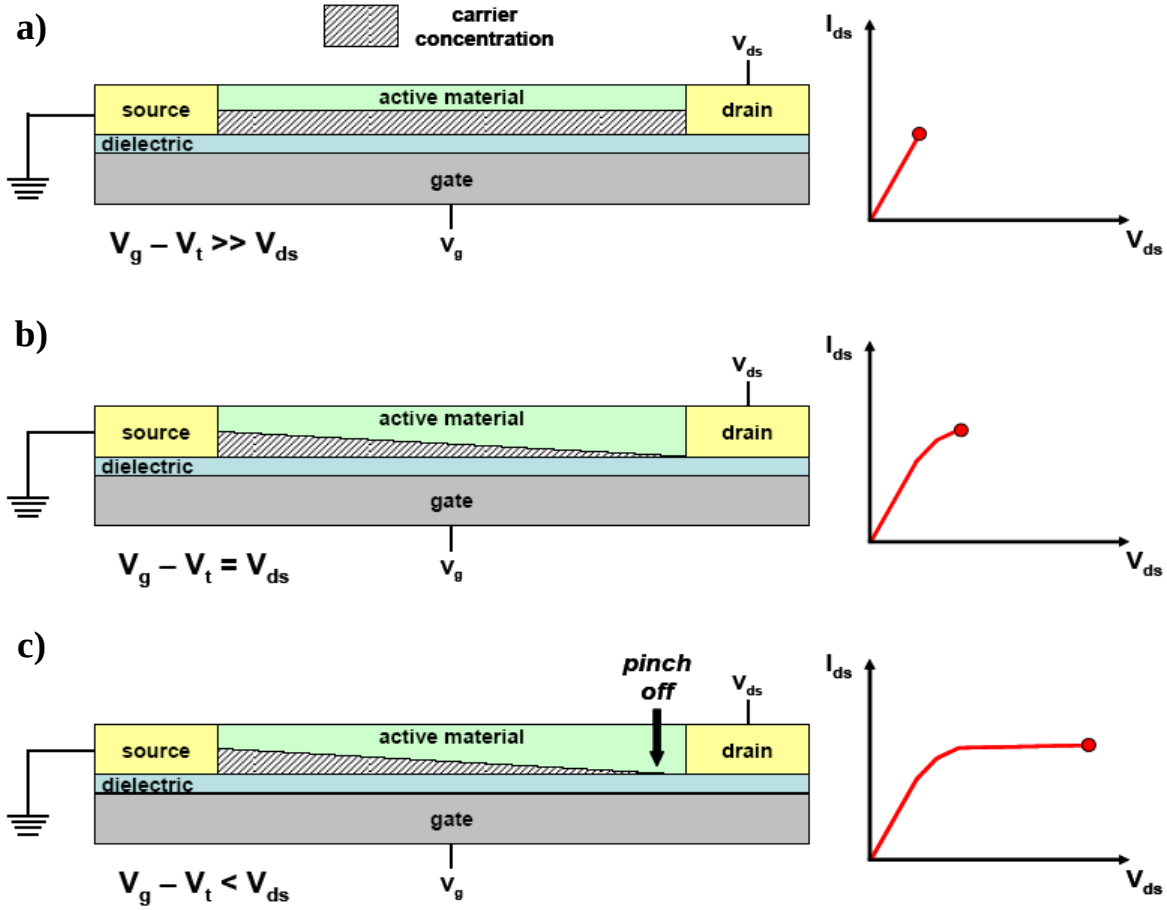

Figure 18. Schematic structure of an OFET.
a) Carrier concentration profile in the linear regime;
b) Carrier concentration profile when the pinch off occurs near the drain electrode ($V_g - V_t = V_d$);
c) Carrier concentration profile in the saturation regime.

When the source-drain voltage is further increased, we reach a point where a potential difference between the gate and the part of the channel near the drain no longer exists, the channel is *pinched off*. This means that a charge carrier depletion region is formed next to the drain, because the difference between the local potential V(x) and V_g is lower than the threshold voltage.

A space-charged-limited saturation current can flow across this narrow depletion zone. Carriers are swept from the pinch point to the drain by a comparatively high electric field in the depletion region (Fig.18b).

A further increase in V_{ds} pushes the pinch-off point further away from the drain (Fig. 18c). However the length of the channel (L) shortens only slightly, as it is infinitely larger than the width of the depletion region, and the integrated resistance of the channel from the source to the pinch point remains more or less the same. For these reasons once pinch off condition is met, current saturates at I_{ds}^{sat}. From a mathematical point of view, pinch off is reached when $V_{ds} = V_g - V_t$.

The current-voltage characteristics in the different operating regimes of an OFET can be described analytically, in a simplistic way assuming that (1) the transverse electric field induced by the gate voltage is largely higher than the longitudinal field induced by the gate bias (*gradual channel approximation*) and (2) the mobility is constant all over the channel.

Assumption (1) is justified by the geometry of the device since the distance from source to drain is often much larger than the thickness of the insulator. Assumption (2) is almost always fulfilled in inorganic semiconductors. However, this is far from true in organic solids as we pointed out in § 1.4.1.

In short, I-V characteristics can be drawn by either varying the drain voltage at a constant gate voltage (*output characteristics*) or changing the gate voltage at a fixed drain voltage (*transfer characteristics*). *Locus characteristics* are obtained by varying simultaneously drain voltage and gate voltage and keeping them at the same value so that the pinch-off condition is always reached in the reached the drain electrode.

In the output characteristics, the curves are divided into a linear regime at low V_{ds} that turns into the saturation regime when $V_{ds} > V_g$.

The current I_{ds} in both regimes is given by the equations

$$I_{ds}^{lin} = \frac{W}{L} C_i \mu \left[\left(V_g - V_t \right) V_{ds} - \frac{V_{ds}^2}{2} \right] \quad \textit{Linear Regime}$$

$$I_{ds}^{sat} = \frac{W}{2L} C_i \mu \left(V_g - V_t \right)^2 \quad \textit{Saturation Regime}$$

in which μ is the charge carrier mobility.

A widely used method for parameter extraction from the characteristics curve consist of plotting the square root of the saturation current as a function of gate voltage. As it is clear

from the saturation-regime curve, the square root of the saturation regime is supposed to give a straight line whose slope is an estimation of the mobility while its extrapolation to the *x* axis corresponds to the threshold voltage.

Mobility value can be calculated also in the linear regime but often is different from the one calculated in the saturation regime (usually it is higher). This happens because the conduction channel resistance in saturation is higher than in the linear case, hence contact resistance is less critical than in the linear region. However, the two mobility values must be equal in devices with good injection contacts.

Since the mobility is gate-bias dependent, an exact estimation of the saturation current would require integrating the mobility all along the channel, which does not appear feasible given that the gate-bias dependence of the mobility for a device is not known beforehead.

GATE DIELECTRICS

The crucial process of charge accumulation and transport in OFET takes place at and very close to the interface between the gate dielectric and the semiconductor. Thus, the properties of this interface and the dielectric have a huge influence on device characteristics. Device parameters such as mobility, threshold voltage, subthreshold swing, etc. depend not only on the nature of the semiconductor but also on the chemical structure and dielectric properties of the insulator.

The requirements for gate dielectrics in OFET are rigorous. They should show high dielectric breakdown strength, contain only minimal concentrations of impurities, that could act as traps, easily processable and be environmentally stable. Apart from their breakdown strength, gate dielectrics are mainly characterized by their dielectric constant ε (also named κ), which determines the capacitance $C_i = \varepsilon\varepsilon_0 / d$ of a dielectric layer of thickness d (ε_0 is the permittivity in vacuum) and thus the amount of induced charges per applied V_g.

Hence, in order to achieve a certain amount of charges in the transistor channel, one can either reduce the dielectric thickness or use a dielectric with a higher ε. Since the ready availability of doped silicon wafers with high quality, smooth, thermal silicon dioxide that can also be used as substrates and give reproducible results for many semiconductors, typically organic semiconductors are grown on SiO_2 ($\varepsilon = 3.9$) for testing purpose.

Many groups investigated the influence of surface treatments of SiO_2 (e.g., with hexamethyldisilazane (HMDS) or self-assembled monolayers of different silanes) on the performance of organic transistors, looking at the change of morphology of semiconductor film, number of trap states, and dipoles at the surface [61].

Other metal oxides with higher ε such as, e.g., Al_2O_3 ($\varepsilon = 10$) [62] and Ta_2O_5 ($\varepsilon = 10$) [63] have also been investigated as possible gate dielectrics for organic transistors. Nevertheless, for the application of organic semiconductors in flexible electronics, SiO_2 and other oxides are not ideal dielectrics. In order to use them on flexible substrates, they usually need to be sputtered or anodized, which leads to inferior device performance.

Another option are insulating polymers that can be processed from solution, that do not require high temperature processing, and whose characteristics can be tuned over a wide range by changing their chemical structure. Polymer gate dielectrics have been used in top as well as bottom gate transistors, and their impact on morphology and mobility was investigated [64]. They are easily applied in top gate transistors, where they are spun on top of the semiconductor from solvents orthogonal to the semiconductor and do not influence the interface morphology or damage the semiconductor [65].

CHARGE INJECTION AT METAL-ORGANIC INTERFACES

Despite the that significant potential barriers (> 0.3 eV) exist at metalorganic semiconductor interfaces, it is possible to obtain *ohmic* source and drain contacts in OFETs. A likely explanation for such a behaviour is that the charge injection mechanism is probably not simple thermionic emission in which carriers must overcome the full potential barrier.

Instead, at intense interfacial electric field, filed emission (tunnelling) through the barrier can become possible thus lowering effectively the potential barrier. Another possible injection mechanism involves defect-assisted transport in which carriers by-pass the barrier by hopping through midgap states. In Fig. 19 we report simple comparison of these different charge injection mechanisms.

Measurements on the source contact resistance as a function of temperature reveal that the injection process is indeed thermally activated (which is consistent with thermionic emission), but the activation energies are generally much smaller than the estimated energy potential barriers determined by photoemission spectroscopy. In some cases, the activation energy associated with the source contact resistance is very similar to the activation energy associated with the carrier field-effect mobility, thus suggesting that transport of charge in

the semiconductor near the contact (*depletion region*) is the limiting bottleneck not the actual metal-to-semiconductor emission process.

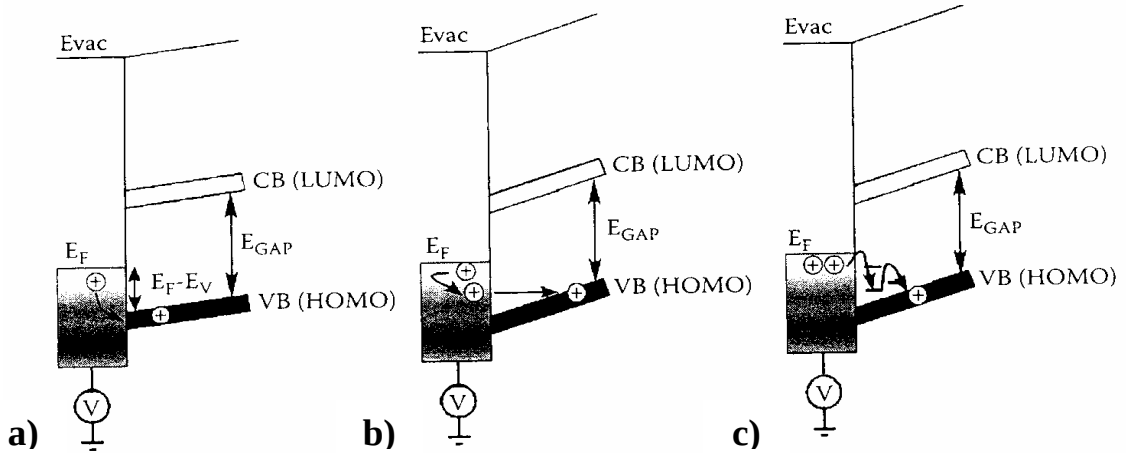

Figure 19. Comparison of different charge injection mechanisms at a biased metal-semiconductor contact: (a) thermionic emission, (b) field emission (tunnelling), (c) defect assisted injection.

Moreover the source and drain contact resistances are strongly gate voltage dependent; specifically, they decrease with increasing gate voltage. The variation of the contact resistance with gate voltage is essentially identical for both the source and the drain, and it is also similar to the variation of the channel resistance. The close tracking of the gate voltage dependence on the source, drain and channel resistances also indicates that resistance depends on the film transport properties and morphology near the contact.

1.4.3.3 Organic Light-Emitting Field-Effect Transistor (OLET)

While the development of ambipolar (both hole- and electron-transporting) OFETs is still in the early stages, it is certainly an exciting subject within the OFET community. These devices offer not only new possibilities for complementary logic circuit design, but also the potential to control electron-hole recombination within the semiconductor channel to afford light emission. Light-emitting organic field-effect transistors (OLETs) are particularly intriguing because they posses charge carriers densities that are order of magnitude higher than those found in OLEDs [30].

Even if different device architectures can be engineered for obtaining balanced ambipolarity and maximizing light emission (see Chapter 5), in Fig. 20 we report the scheme of single-layer and single-material BG-TC LET for showing LET main working principles and components.

Indeed, a LET is a three-terminal device that couples the electrical characteristics of a FET to the controlled radiative recombination of the electrons and holes injected in the channel via the drain and source contacts. Excitons are thus created by the recombination of in-plane moving electron- and hole-currents, which are controlled by the gate electrode. Electroluminescence intensity is tuned by both the drain and gate voltage. The gate electrode allows higher control on charge injection, electron and hole-currents balance and light-generation processes with respect to the standard sandwich configuration of an LED. Crucial aspects of the device's characteristics concern (i) metal electrodes that should guarantee efficient electron and hole injection; (ii) active materials that should sustain ambipolar field-effect transport and efficient electroluminescence emission; (iii) dieletric surfaces that should be trap-free to favour effective mobility of both electrons and holes at the dielectric/active material interface.

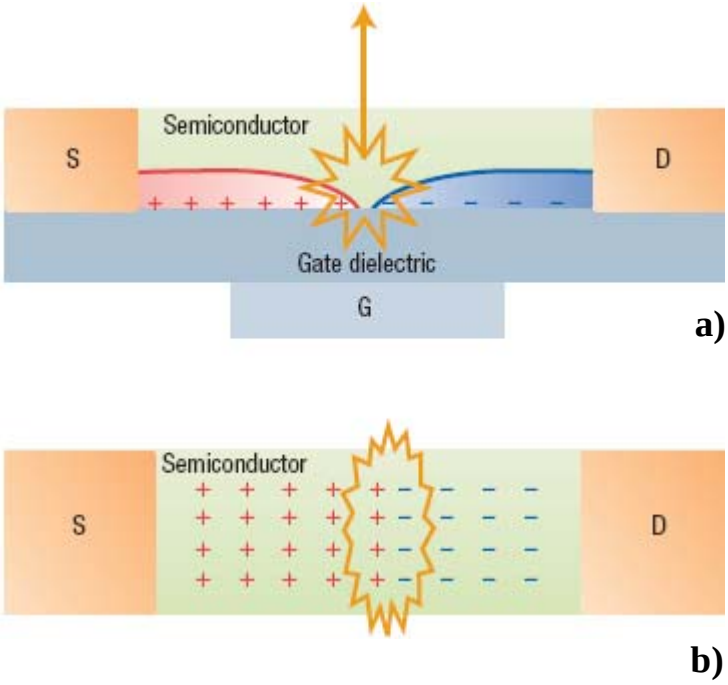

Figure 20. Scheme of a light-emitting field-effect transistor. (a) Side view. (b) Top view. In a simple model, the device can be modelled as a sort of a two-dimensional forward-biased pn junction. Electrons and holes are injected from the drain (D) and source (S) contacts and recombine within the channel position controlled by the gate (G).

When an ambipolar FET is biased with the gate voltage in between the source and the drain voltage, an electron accumulation layer should form near one electrode coexisting with a hole accumulation layer near the other electrode. This regime can be difficult to reach even if electron and hole accumulation layers can be induced separately at high positive and negative gate voltages, respectively, because the coexistence of both carriers requires the threshold voltage difference for electron and hole accumulation to be sufficiently small. In the truly ambipolar regime, electrons and holes are expected to recombine where the two accumulation layers meet, leading to light emission from a well-defined zone.

Based on energy band line-up considerations with the organic semiconductor HOMO and LUMO, depositing two different contact materials at either end of the transistor channel may facilitate more efficient hole and electron injection respectively. However, at the state of the art it is still unclear whether separately engineering distinct contacts for hole/electron injection in ambipolar OFET will prevail over opting for symmetric contacts.

Also in unipolar FET light-emission can occur [66], but radiative recombination is always confined to a spatial region near the drain metal electrode where the complementary charge carriers are injected.. Thus, in this thesis we will deal only with ambipolar OLET in which a gate-controlled location of the light emission is possible.

References

[1] A. Sacco, *Fondamenti di chimica* (Casa editrice Ambrosiana, 2a Edizione, 1996)**.**

[2] C. Cohen-Tannoudji, B. Diu, and F. Laloe, *Quantum Mechanics: Volume I* (volume 2nd ed. John Wiley and Sons, 1992).

[3] I. H. Campbell and D. L. Smith, *Physics of Organic Electronic Devices* (Solid State Physics **55,** Academic Press, 2001).

[4] M. Pope and C. E. Swenberg, *Electronic processes in Organic Crystals* (Oxford: Clarendon Press, 1982).

[5] C. D. Dimitrakopoulos, A. R. Brown, and A. Pomp, *J. Appl. Phys.*, **1996**, 80, 2501.

[6] B. Servet, G. Horowitz, S. Ries, O. Lagorsse, P. Alnot, A. Yassar, F. Deloffre, P. Srivastava, R. Hajlaoui, P. Lang, and F. Garnier, *Chemical Materials*, **1994**, 6, 1809.

[7] V. Podzorov, E. Menare, A. Borissov, V. Kiryukhin, J.A. Rogers, M.E. Gershenson, *Phys. Rev. Lett.*, **2004**, 93, 086602.

[8] R. Kersting, U. Lemmer, R. F. Mahrt, K. Leo, H. Kurz, H. B¨assler, and O. Göbel, *Phys. Rev. Lett*., **1993**, 70, 3820.

[9] N. Karl, *Synth. Met.*, **2003**, 649, 133.

[10] D. L. Dexter and R. S. Knox, *Excitons* (New York: Wiley interscience, 1965).

[11] D. P. Craig and S. H. Walmsley, *Excitons in molecular crystals: Theory and Applications* (Amsterdam: W. A. Benjamin, Inc., 1968).

[12] G. Lanzani, S. V. Frolov, P. A. Lane, Z. V. Vardeny, M. Nisoli, and S. De Silvestri, *Phys. Rev. Lett.*, **1997**, 79, 3066.

[13] M. A. Loi, C. Martin, H. R. Chandrasekhar, M. Chandrasekhar, W. Graupner, F. Garnier, A. Mura, and G. Bongiovanni, *Phys. Rev. B*, **2002**, 66, 113102.

[14] J. M. Turlet, P. Kottis, and M. R. Philpott, *Adv. Chem. Phys.*, **1983**, 54, 303.

[15] F. Meinardi, M. Cerminara, A. Sassella, A. Borghesi, P. Spearman, G. Bongiovanni, A. Mura, and R. Tubino, *Phys. Rev. Lett.*, **2002**, 89,157403.

[16] S. R. Forrest, *Chem. Rev.*, **1997**, 97,1793.

[17] E. D. Como, M. A. Loi, M. Murgia, R. Zamboni, and M. Muccini, *J. Am. Chem. Soc.*, **2006**, 128, 4277.

[18] E. Lunedei, PhD thesis, Univ. Stuttgart, 2003.

[19] N. Periasamy, D. Danieli, G. Ruani, R. Zamboni, and C. Taliani, *Phys. Rev. Lett*., **1992**, 68, 919.

[20] M. Pope, H. Kallmann, and P. Magnante, *J. Chem. Phys.*, **1963**, 38, 2042.

[21] C. Rost, S. Karg, W. Riess, M. A. Loi, M. Murgia, and M. Muccini, *Appl. Phys. Lett.*, **2004**, 85, 1613.

[22] R. Lakowicz, *Principles of Fluorescence Spectrocopy* (New York, Plenum Press, 1983).

[23] T. H. Maiman, *Nature* **1960**, 187, 493.

[24] B. H. Soffer, B. B. McFarland, *Appl. Phys. Lett.* **1967**, 10, 266.

[25] N. Karl, *Phys. Status Solidi A*, **1972**, 13, 651.

[26] D. Moses, *Appl. Phys. Lett.* **1992**, 60, 3215.

[27] N. Tessler, G. J Denton, R. H. Friend, *Nature* **1996**, 382, 695.

[28] L. El-Nadi, L. Al-Houty, M. M Omar, M. Ragab, *Chem. Phys. Lett.* **1998**, 286, 9.

[29] J. H. Schon, C. Kloc, A. Dodabalapur, B. Batlogg, *Science* **2002**, 298, 961.

[30] J. Zaumseil, R. H. Friend and H. Sirringhaus, *Nature Materials*, **2006**, 5, 69.

[31] O. Svelto and D.C. Hanna, *Principles of lasers*, *volume 3rd* (New York, Plenum Press, 1989).

[32] P.W.Milonni and J.H.Eberly, *Lasers* (Wiley, 1988).

[33] S. V. Frolov, W. Gellermann, Z. V. Vardeny, M. Ozaki, K. Yoshino, *Synth. Met.* **1997**, 84**,** 471.

[34] G. H. Gelinck, J. M. Warma, M. Remmers, D. Neher, *Chem. Phys. Lett.* **1997**, 265**,** 320.

[35] R. Bonifacio, L. A. Lugiato, *Phys. Rev. A*, **1975**, 11**,** 1507.

[36] R. Bonifacio *Dissipative systems in quantum optics Topics in Current Physics*, vol. 27 (ed) 1982.

[37] M. A. Bouchiat, J. Guena, Ph. Jacquier, M. Lintz, L. Pottier *J. Physique* II, **1992**, 2, 727.

[38] G. J. Denton, N. Tessler, N. T. Harrison, R. H. Friend, *Phys. Rev. Lett.*, **1997**, 78, 733.

[39] M. Yan, L. J. Rothberg, E. W. Kwock, T. M. Miller, *Phys. Rev. Lett.*, **1995**, 75**,** 1992.

[40] H. Hanamura, H. Haug *Phys. Rep.*, **1977**, 33, 209.

[41] N. W. Ashcroft and N. D. Mermin, *Solid State Physics* (New York, Holt, 1976).

[42] E. A. Silinsh and V. Cápek, *Organic molecular crystals: Interaction, localization and transport properties* (New York, AIP press, 1994).

[43] Z. Bao and J. Locklin, *Organic field-effect transistors* (Boca Raton, CRC Press, 2007).

[44] A. A. Maraudin, E. W. Montrol, G. H. Weiss, *Theory of Lattice Dynamics in the Harmonic Approximation*, 2nd edition, Solid state Physics Suppl. 3 (New York, Academic Press).

[45] I.G. Austin, N.F. Mott, *Adv. Phys.*, **1969**,18, 41.

[46] T. Holstein, *Ann. Phys.*, **1959**, 8, 343.

[47] P. G. Bomber and W. E. Spear, *Phys. Rev. Lett.*, **1970**, 25, 509.

[48] A. Miller and E. Abrahams, *Phys. Rev.*, **1960**, 120, 745.

[49] P. R. Emtage, J. J. O'Dwyer, *Phys. Rev. Lett.*, **1966**, 16, 356.

[50] E. M. Conwell, M. W. Wu, *Appl. Phys. Lett.*, **1997**, 70, 1867.

[51] V. I. Arkhipov, E. V. Emelianova, Y. H. Tak, H. Bassler, *J. Appl. Phys.*, **1998**, 84, 848.

[52] G. H. Heilmeier, L. A. Zanoni, *J. Phys. Chem. Solids*, **1964**, 25, 603.

[53] G. H. Heilmeier, L. A. Zanoni, *J. Phys. Chem. Solids*, **1964**, 25, 603.

[54] A. Tsumara, H. Koezuka, T. Ando, *Appl. Phys. Lett.*, **1986**, 49, 1210.

[55] S. R. Forrest, *Nature*, **2004**, 428, 911.

[56] M. M. Payne, S. R. Parkin, J. E. Anthony, C. C. Kuo, T. N. Jackson, *J. Am. Chem. Soc.*, **2005**,
127, 4986.

[57] H. Sirringhaus, P. J. Brown, R. H. Friend, M. M. Nielsen, K. Bechgaard, B. M. W. Langeveld-Voss, A. J. H. Spiering, R. A. J. Janssen, E. W. Meijer, P. Herwig, D. M. de Leeuw, *Nature*, **1999,** 401, 685.

[58] E. Menard, V. Podzorov, S.H. Hur, A. Gaur, M.E. Gershenson, J.A. Rogers, *Adv. Mater.*, **2004**, 16, 2097.

[59] C. R. Newman, C. D. Frisbie, D. A. da Silva Filho, J. L. Bredas, P. C. Ewbank, K. R. Mann, *Chem. Mater.*, **2004**, 16, 4436.

[60] J. Zamuseil, H. Sirringhaus, *Chem. Rev.*, **2007**, 107, 1296.

[61] F. Dinelli, J. F. Moulin, M. A. Loi, E. Da Como, M. Massi, M. Murgia, M. Muccini, F.Biscarini, J. Wie, P. Kingshott, *J. Phys. Chem. B*, **2006**, 110, 258.

[62] J. Lee, J. H. Kim, S. Im, *Appl. Phys. Lett.*, **2003**, 83, 2689.

[63] L. A.Majewski, M. Grell, S. D. Ogier,; J. Veres, *Org. Electron.*, **2003**, 4, 27.

[64] X. Z. Peng, G. Horowitz, D. Fichou, F. Garnier, *Appl. Phys. Lett.*, **1990**, 57, 2013.

[65] H. Sirringhaus, T. Kawase, R. H. Friend, T. Shimoda, M. Inbasekaran, W. Wu, E. P. Woo, *Science* **2000**, 290, 2123.

[66] A. Hepp, H. Heil, W. Weise, M. Ahles, R. Schmechel, H. von Seggern, *Phys. Rev. Lett*., **2003**, 91**,** 157406.

Chapter 2

Experimental setups

2.1 Confocal Laser Scanning Microscope (CLSM)

Optical microscopy has been used in a variety of scientific disciplines in order to obtain magnified images of specimen like living cells, biological tissue, metal surfaces, stones and crystals.

By this technique using properly designed optical systems, it is possible to obtain magnified optical images of objects with size in the micron and submicron scale. There is a fundamental limit to the spatial resolution attainable with optical microscopy. This limit is imposed by the wavelength of light (λ) that in the visible spectrum range spans from 400 to 750 nm. Thus the in-plane resolution *r*, according to the Rayleigh formula is:

$$r = 1.22 \frac{\lambda}{2NA}$$

where NA is the objective *numerical aperture* defined as:

$$NA = n \sin \alpha$$

where *n* is the refractive index of the medium between the objective and the sample and α is half of the collecting angle of the objective.

The need of studying new systems with smaller structural details such as micro- and nano-structured materials and the effort to understand properties of materials at the molecular level, have triggered the development of new experimental techniques, providing higher spatial resolution such as Scanning Near-field Optical Microscopy (SNOM) [1] and confocal microscopy [2].

Conventional optical microscopy uses extended light sources to illuminate all the sample field of view at the same time in order to create a magnified image, viewed by eyes or by an extended detector. In confocal microscopy light from a point source probes a very small region and a point detector ensures that only light from the very same small area is

detected. For this purpose a point detector must be located in a plane conjugated (*confocality*) with the point source. Figure 1 shows a simplified scheme of the working principle of a confocal microscope. The spatial filter (pinhole) ensures that the detector is practically point-like.

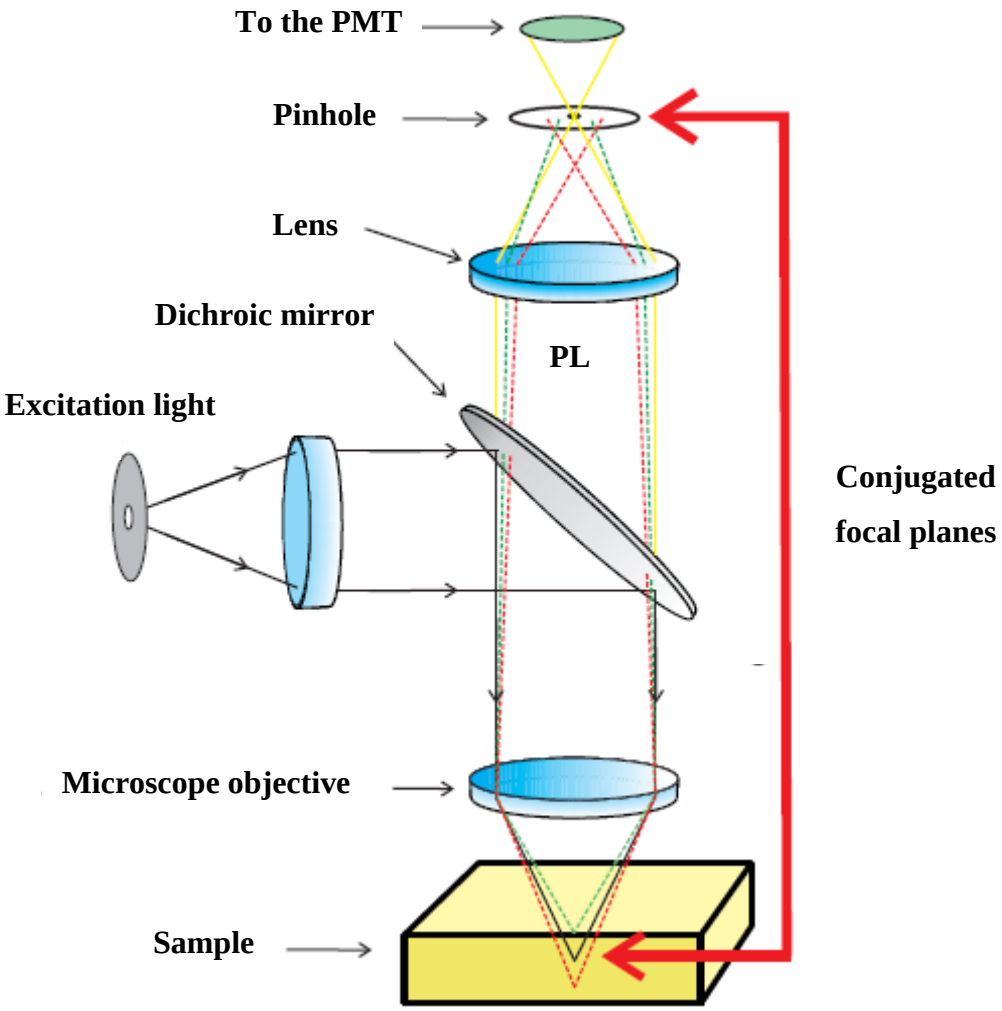

Figure 1. Schematic diagram illustrating the operation principle of a confocal microscope. The excitation light is reflected by a dichroic mirror and focused by the objective, the sample PL (colored lines) is recollected by the objective and focused on the pinhole that prevents the out of focus PL rays (dotted lines) to reach the detector.

In the figure only the PL (colored lines) from the focal plane of the sample is focused on the detector (a photomultiplier tube, PMT). Thus confocal microscopy is able to reject features that are out of focus. Confocal microscopy presents two main advantages with respect to conventional microscopy: (i) optical sectioning and 3-D reconstruction of translucent specimens and (ii) in-plane spatial resolution increased by a factor 1.4 [2].

Spatial resolution is one of the most desired features of every microscope. The resolution can be measured or calculated considering the FWHM of the image of a sub-resolved point object which is usually called point-spread-function (PSF). In Tab. 1 the spatial in-plane (*x*-*y*) and axial (*z*) resolution for different optical microscopy techniques are listed. Note that resolution is expressed as a function of the wavelength of light, considering an objective with NA = 1.4 (which is the typical value for oil-immersion objective) for far-field techniques such as optical and confocal microscopy, and the SNOM near-filed technique. In the confocal case, a pinhole of null size is considered (an exhaustive investigation of the effect of the pinhole size on the confocal microscope in-plane resolution can be found in reference [2]).

The resolution values reported in the table refer to the case in which light of the wavelength λ is used both to illuminate the sample and to reconstruct the optical image.

	Optical microscope	**Confocal microscope**	**SNOM**
***x-y* resolution**	0.436λ	0.31λ	~0.05λ (*)
***z* resolution**	2λ	0.46λ	(**)

Table 1. In-plane (*x*-*y*) and axial (*z*) resolution for conventional optical microscopy, confocal microscopy and SNOM. (*) strongly dependent on shape of the fiber tip. (**) detection is limited to the near-field in proximity of the sample surface and optical sectioning is not possible.

Two different wavelength are involved in the process of image formation: λ_1, for exciting the sample and λ_2, the PL wavelength. In order to take this into account, values reported in Tab. 1 in confocal microscopy are linearly dependent on a factor β that is defined as $\beta = \lambda_2/\lambda_1$.

Even if it is practically impossible to work with $\beta = 1$, this value represents the ideal limit once the exciting wavelength λ_1 is fixed.

Since in confocal microscopy only a diffraction limited point is imaged, the sample or the exciting light must be scanned in order to obtain an image of the desired field of view. It has been demonstrated that *sample* scanning confocal microscopy has a better resolution than *laser* scanning [3]. However, the latter allows to obtain fast imaging without sample degradation and has found a wider diffusion in commercial instruments. The scan of the exciting laser beam can be accomplished with scanning galvanometric mirrors. In Fig. 2 a schematic drawing of a typical scanning head for confocal microscopy

is shown. The exciting laser beam is illustrated as a continuous line and is scanned by two galvanometric mirrors. The PL beam is represented by the dotted line. The confocal PL image of the studied sample is reconstructed by the microscope
software, collecting the PL point by point. It is worthwhile noting that the optical path of the exciting laser and the PL are the same until they reach the dichroic mirror: the incoming laser beam is reflected by the mirror while the PL beam passes through it.

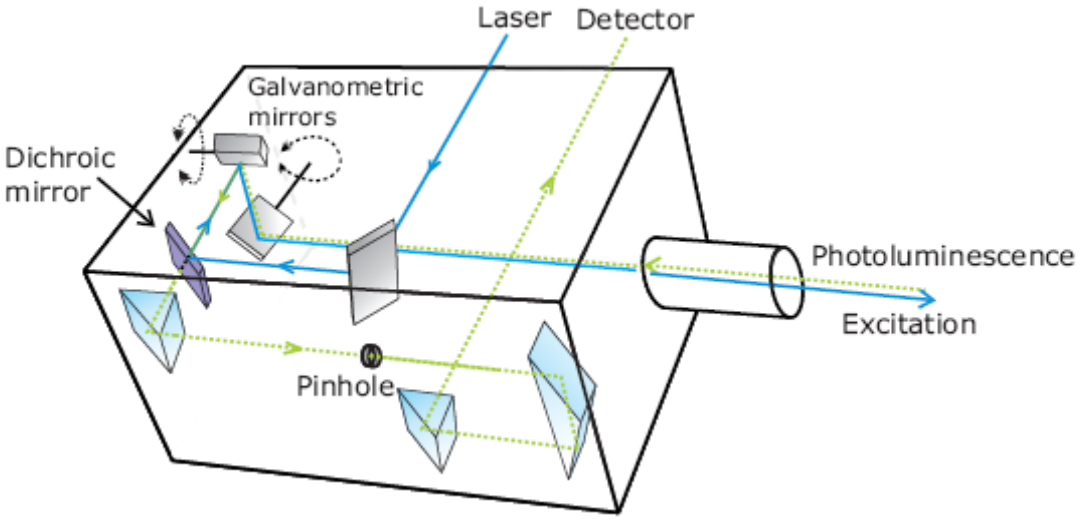

Figure 2. Schematic drawing of a laser scanning head. Excitation laser beam (continuous line) is reflected by the dichroic mirror and is scanned on the sample surface by galvanometric mirrors. PL is collected through the same optical path passing through the dichroic mirror, the pinhole and finally reaches the detector.

The confocal laser scanning microscope used in this Ph.D. work consists of an inverted microscope (Nikon Eclipse TE-2000-E) equipped with a confocal scanning head similar to one reported in Fig. 2. The microscope has a series of Nikon infinity-corrected objectives with different characteristics. Those more extensively used to perform images of the samples studied are reported in Tab.2 with the respective magnification, aberration correction and NA.

	Objectives			
Magnification	20X	60X	60X	100X
Characteristic	Plan Fluor	Plan Fluor	Plan Apo	S-Fluor
Numerical Aperture	0.5	0.7	1.4	1.3

Table 2. Technical characteristics of objectives used in this thesis.

To reach a NA of 1.3 or larger special immersion fluid must be placed between the sample coverslip and the collecting lens of the objective. In particular, oil with refractive index of 1.52 is used. As pointed out previously and from the Rayleigh equation a higher NA value corresponds to a higher spatial resolution.

Three continuous wave (cw) lasers (laser diode 408 nm, Ar^+ 488 nm and He/Ne 543 nm) that are coupled either independently or contemporarily to the scanning head of the confocal microscope by a multimode optical fiber are used as sources for exciting simultaneously the different chromophores and electronic states.

The laser beam is then reflected by the dichroic mirror and by two galvanometric mirrors that scan the focused laser spot on the sample. PL is collected through the same focusing objective, it passes the dichroic mirror and is focused on the pinhole. The galvanometric mirrors provide precision scanning of the laser beam on the sample surface, while the axial tomography is obtained by scanning the sample through the focal plane with minimum step of 50 nm. The *xyz* spatial control of laser excitation allows the imaging of the sample by sequential detection of the photoluminescence intensity. In order to develop the scanning confocal microscope as a spectroscopic tool, several dichroic mirrors (Fig. 2) with complementary spectral properties that allow PL spectra measurements in the entire visible range are custom designed to be inserted in the scanning head.

PL signal is then coupled by an optical fiber to the potomultiplier tubes (PMT) that are used as detectors. The galvanometric mirrors and the three channel PMT are computer-controlled in order to obtain PL images in three different spectral ranges independently or simultaneously. The spectral ranges of the three PMT channels are located at 450±25 nm, 515±15 nm for the blue and green channels respectively and at wavelengths higher than 600 nm for the red channel. The independent detection channels provide information on the spatial location of chromophores or electronic states emitting at different wavelengths.

The microscope software allows also to excite selectively sample portions and zoom down the scanned area to a resolution limited point, according to the exciting wavelength and objective NA.

2.2 Atomic Force Microscopy (AFM)

Atomic force microscopy (AFM) belongs to the family of the Scanning Probe Microscopy (SPM) techniques. SPM are based on 3-D scanning of a sample surface, through a probe which locally interacts with the surface. The probe is placed near the surface ($d < 100$ nm). An electronic system measures the surface-probe interaction at every (x,y) point in the sample. The probe is moved on top of the sample by a piezoelectric actuator, in order to cover a path called *raster*. The interaction strength (whatever it is, depending on the SPM techniques) depends on the sample-probe distance. By mapping the strength in the (x,y) points, we could obtain an *image* of the sample surface. AFM was invented by G. Binning, C. Gerber and C. Quate [3]. It overcomes the limits of other SPM (like Scanning Tunneling Microscopy, STM) because it permits the analysis of all type of samples (insulator, semiconductor, etc…). Furthermore, it allows processing in air, vacuum or liquid environment.

The main components of an AFM are (Fig. 3):

- the probe which can interact with the surface (Fig. 4). The different interactions (magnetic, electric, etc…) settled between the surface and the probe are strictly dependent on the nature of the probe itself;
- the piezoelectric transducer (also called *scanner*) which permits probe or sample movements. Movements are possible in all the three spatial directions with an accuracy in the order of 10^{-12} m. Vertical movements are guided by a feedback system which keeps the surface-probe interaction fixed. These movements are recorded and used to determine the topological profile of the surface;
- an electronic system used to measure and to amplify the probe-surface interaction;
- a mechanical system, to damp the external vibrations;
- the above mentioned feedback system for keeping the signal with the physical information at a set value (*setpoint*);
- a control system for the acquisition and visualization of the data.

In the AFM technique, the probe is a very sharp pyramidal or conical tip fabricated on the edge of a lever called *cantilever*. When the tip and the surface interact, a force modifies the cantilever's mechanical balance. These change is detected by a laser beam focused on the back of the cantilever (Fig. 3). The laser beam, after a convenient optical path, reaches a

sensor (*beam and bounce*). During the surface scanning, the sensor (usually a photo-diode) reveals the different laser beam positions that, after a suitable amplification, are used to reproduce the surface topography.

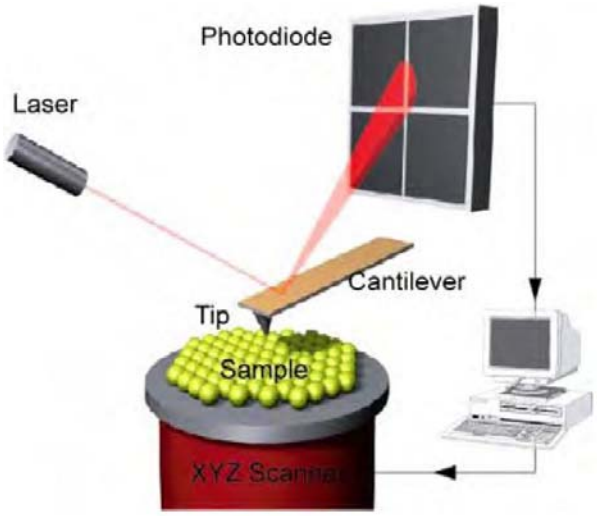

Figure 3. Scheme of the working principle of the beam-and-bounce. The scanner moves the sample thereby changing the tip/surface interaction and the optical path of the laser beam.

The probe is the fundamental part of the instrument since it sets the minimal spatial resolution of the AFM. Ideally, it is conceived to be sensitive to a single chemical-physical interaction with the surface. But in practice this in not possible, so fabrication is important to minimize parasite interactions.

There are rectangular or triangular shape levers with conic or pyramidal tip. Classic conic tips present these features: length around 100-130 μm, 35 μm wideness, 2 μm thickness, tip radius of curvature of 10 nm and an elastic constant less than 10 N/m.

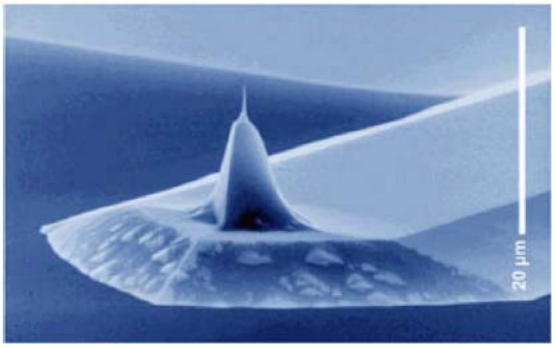

Figure 4. Scanning electron micrograph of a micromachined silicon cantilever with an integrated tip pointing in the [001] crystal direction (Wolter *et al.*, 1991).

2.2.1 AFM operating modalities

Several forces typically contribute to the deflection of an AFM cantilever. The force most commonly associated with atomic force microscopy is an interatomic force called the van der Waals force. The dependence of the van der Waals force upon the distance between the tip and the sample is shown in Fig. 5.

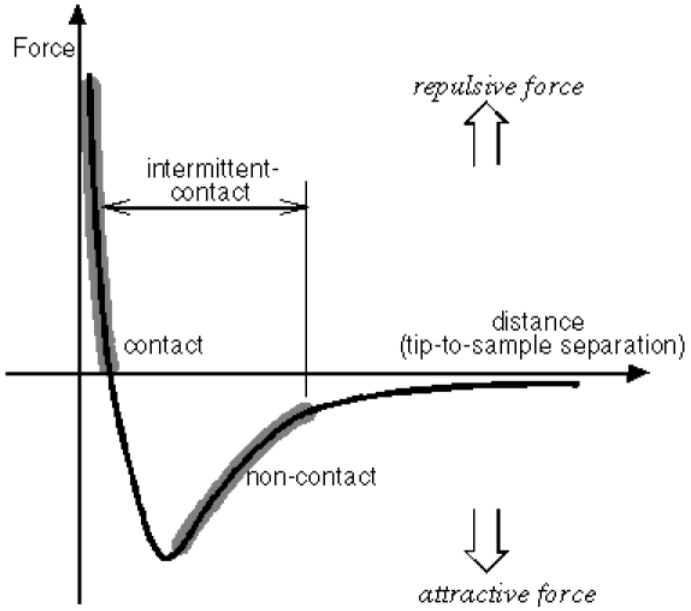

Figure 5. Interatomic force versus tip-sample distance.

Two distance regimes are labelled on Fig. 5: (i) the *contact regime*; and (ii) the *non-contact* regime. In the contact regime, the cantilever is held less than a few angstroms from the sample surface, and the interatomic force between the cantilever and the sample is repulsive. In the non-contact regime, the cantilever is held on the order of tens to hundreds of angstroms from the sample surface, and the interatomic force between the cantilever and sample is attractive (largely a result of the long-range van der Waals interactions).

CONTACT MODE

Contact mode AFM operates by scanning a tip attached to the end of a cantilever across the sample surface while monitoring the change in cantilever deflection with a split photodiode detector. The tip contacts the surface through the adsorbed fluid layer on the sample surface and a feedback loop maintains a constant deflection between the cantilever and the sample by vertically

moving the scanner at each *(x,y)* data point to maintain a *setpoint* deflection.
By maintaining a constant cantilever deflection, the elastic force between the tip and the sample remains constant. Force constants usually range from 0.01 to 1.0 N/m, resulting in forces ranging from nN to μN in an ambient atmosphere.
The distance the scanner moves vertically at each *(x,y)* data point is stored by the computer to form the topographic image of the sample surface.

NON-CONTACT MODE

In *non-contact mode* the cantilever oscillates freely at a frequency which is slightly above the cantilever's resonance frequency, typically with an amplitude of a few nanometers (<10nm) in order to obtain an AC signal from the cantilever.
The tip does not touch the sample surface, but oscillates above the adsorbed fluid layer on the surface during scanning. Thus, the cantilever's resonant frequency is decreased by the van der Waals forces, which extend from 1 to 10 nm above the adsorbed fluid layer, and by other *long range forces* which extend above the surface. The decrease in resonant frequency causes the amplitude of oscillation to decrease.
The feedback loop maintains a constant oscillation amplitude or frequency by vertically moving the
scanner at each *(x,y)* data point until a *setpoint* amplitude or frequency is reached. The distance the scanner moves vertically at each *(x,y)* data point is stored by the computer to form the topographic image of the sample surface. This mode operation is less detrimental for the sample but has a worse lateral resolution.

TAPPING MODE

A third operation mode has been developed, between the contact and non contact modes: the *semi-contact* or *Tapping Mode* (Fig. 6).
In *Tapping Mode* AFM the cantilever is oscillated at or near its resonance frequency with an amplitude ranging typically from 20 to 100 nm. During the scan the tip lightly "taps" on the sample surface contacting the surface at the bottom of its swing.
The feedback loop keeps constant the oscillation amplitude by maintaining a constant root-mean-mean value of the oscillation signal acquired by the split photodiode detector (*setpoint*).
Then the vertical position of the scanner at each *(x,y)* data point is stored by the computer to form the topographic image of the sample surface. Clearly in this scanning modality a

constant tip-sample interaction is maintained during imaging since a constant oscillation amplitude is maintained.

Operation can take place both in ambient and liquid environments. When imaging in air, the typical amplitude of the oscillation allows the tip to contact the surface through the adsorbed fluid layer without getting stuck.

The advantages of this procedure are low sample damaging and good lateral resolution. The semi-contact mode is usually employed for soft and biological materials.

Figure 6. Scheme of the AFM working modalities. In *contact mode* the topography is obtained by the cantilever bending; in *no- contact mode* and *semi-contact* (or *tapping*) *mode* the signal comes from the variation of frequency, magnitude and phase of the cantilever oscillation.

2.3 Picosencond time-resolved PL spectroscopy

As excitation source for performing time-resolved PL spectroscopy we implement a mode-locked Ti:sapphire laser pumped by a doubled Nd:YVO_4 (532 nm). The mode locking technique consists of an in phase locking of laser modes inside the cavity. A rigorous mathematical treatment of the mode locking process can be found in reference [5]. When the laser is mode locked it delivers a train of pulses with a time duration and a repetition rate that depends on the cavity geometry and on the number of locked modes. The laser in our laboratory is capable to emit pulses with a FWHM of ~ 100 fs at a repetition rate of 80 MHz. One of the main features of this laser is the large gain bandwidth of the active material that is responsible of the tenability of the emission wavelength between 750 and 950 nm.

The second harmonic of the Ti:sapphire laser is used to extend the excitation wavelength in the range 350–500 nm and is generated by coupling the Ti:sapphire laser beam into a β–barium borate (BBO) nonlinear crystal [5]. The Ti:sapphire fundamental laser emission provides excitation energy that can be used for two-photon excitation (TPE) in organics, while the doubled frequency laser beam is used for single photon excitation since it matches the optical gap of many organic semiconductors.

In order to perform conventional time-resolved PL measurements on chromophores dispersed in solutions or on thin-films without correlating the PL signal with film morphology features, a lens system on the optical bench is implemented for focalising the exciting beam on the sample holder (quartz cuvette, vacuum chamber or cryostat) and collecting the PL towards the detector system (*vide infra*).

A direct correlation of the spectroscopic properties of materials and devices with morphological features can be achieved at the nanoscale -thus providing fundamental understanding of nanostructured materials and device- by combing the confocal laser scanning microscope with the femtosecond mode-locked laser and the appropriate detector system.

The pulse temporal broadening in media with high refractive index due to the *group velocity* dispersion precludes the possibility to couple the Ti:sapphire laser to the confocal microscope through an optical fiber. For this reason an external optical setup has been designed for coupling and obtaining good imaging performances. The laser beam pulse

duration is estimated to be of the order of few hundred femtoseconds at the microscope focal plane.

In Fig. 7 a scheme of the set-up for spatially and time-resolved spectroscopy is reported. Pulse excitation switch from the range 750-950 nm to the range 350-500 nm is achieved by insertion/removal of M1 and M2 mirrors.

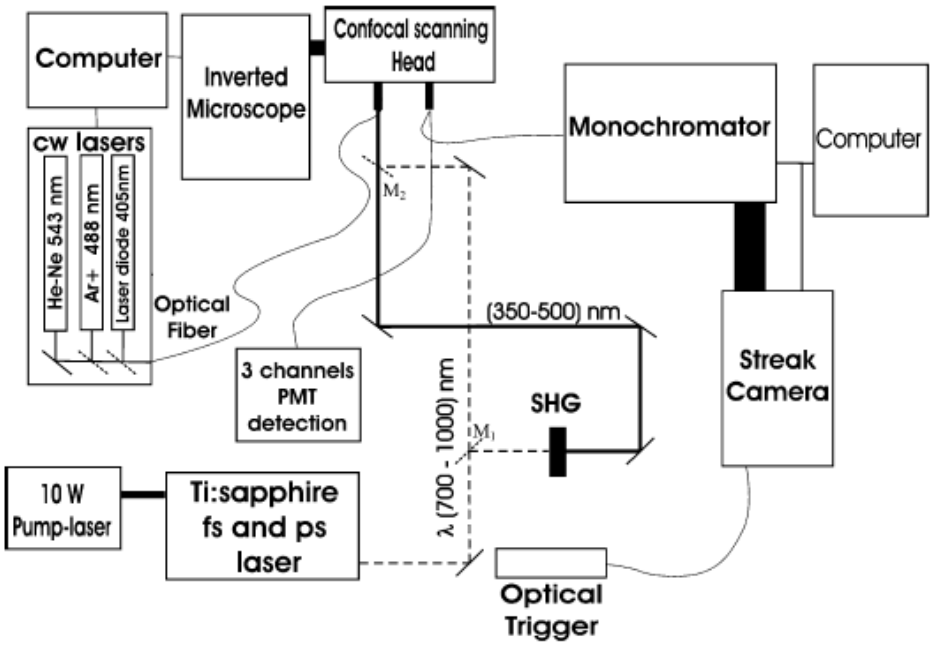

Figure 7. Schematic of the nanoscale femtosecond facility for material science and nanotechnology. The system has femtosecond, picosecond and continuous laser excitation sources coupled to a confocal laser scanning microscope and to a detection set up for integrated and time-resolved photoluminescence measurements. 3D imaging of samples is performed by mapping of one- or two photon excited photoluminescence with controlled laser scanning. Samples can be excited simultaneously by three independent laser lines and photoluminescence imaging at three selected wavelength ranges can be acquired simultaneously. Pulsed excitation switch from the range 700 -1000 nm to the range 350–500 nm is achieved by insertion/removal of M1 and M2 mirrors.

A Hamamatsu Streak Camera system with a temporal resolution of ~ 2 ps coupled to a monochromator is used to spectrally resolve photoluminescence and to measure its time evolution.

A Streak camera is an optoelectronic device used to observe light emission phenomena occurring on the sub-nanosecond time scale. Together with the time-correlated photon counting (TCSPC) is one of the most widely used technique to record PL time decays.

Streak cameras are constituted by three building blocks: photocathode, streak tube and an image recording device, such as a charge-coupled device (CCD).

A scheme of the device with the main parts is illustrated in Fig. 8. The operating principle can be explained considering a light pulse with a certain time profile *f(t)*. When the light impinges the photocathode a proportional amount of electrons is emitted and is accelerated across the streak tube. In the streak tube two parallel deflection plates are settled, across which an electric field **E** is applied. In synchrony with the arrival of electrons a rising sawteeth voltage ramp is applied to the plates. Electrons that first enter the tube are deflected very little, since the value of the electric field **E** is low. Electrons which enter later are further deflected, because of the increased field. In this way the original light pulse *f(t)* is swept in space into *f(y)*, so that a *streak* in the direction *y* that is parallel to the applied electric field. At the tube end a phosphor screen converts electrons back to photons that are recorded as an image by a CCD. The resulting data are obtained as an image in which the *y* axis represents time and *x* the wavelength if a spectrograph is coupled in front of the photocathode at the entrance slit.

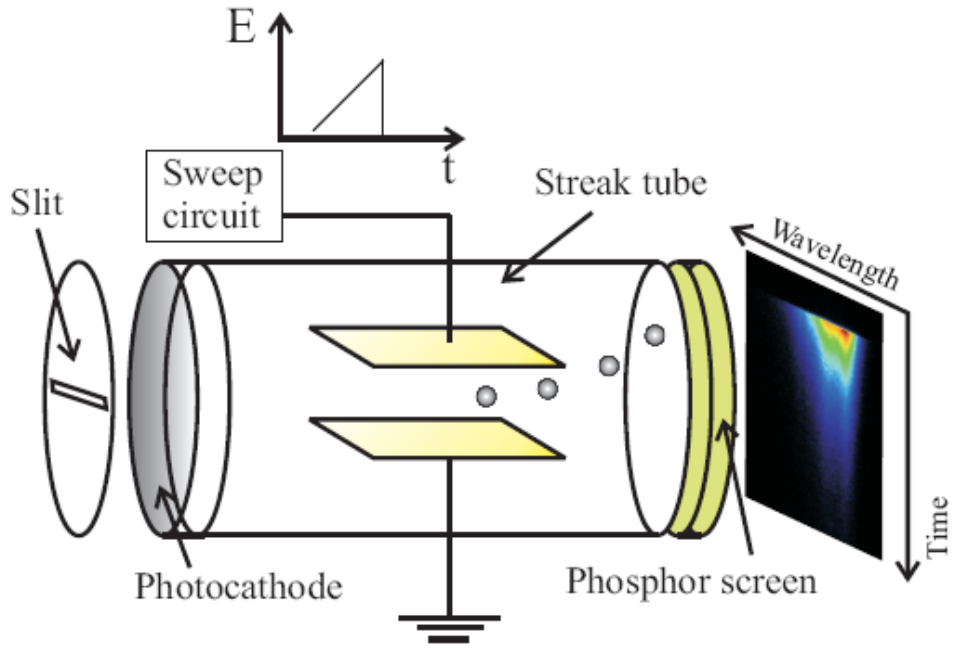

Figure 8. Scheme of the streak camera. The slit selects the photons that impinge on the photocathode. The photocathode converts photons into electrons. Inside the streak tube two plates are used to deflect electrons according to the voltage ramp applied by the sweep circuit. The phosphor screen converts electron into photons. Photons are recorded with the CCD (not shown) located at the end of the phosphor screen

In the right part of Fig. 8, a typical streak camera image with the PL intensity reported in false colour it is shown. In our setup a spectrograph with three different gratings (50 g/mm, 100 g/mm and 1200 g/mm) is used to disperse the wavelength along the *x* axis before entering the horizontal slit. The spectral resolution calculated at 500 nm for the three different gratings is: 17 meV, 10 meV and 0.8 meV respectively.

In the Streak camera the arrival of light pulses and the sweep of the electric field must be synchronized with a trigger. The optical trigger used for this purpose is shown in Fig. 7 and consists of a fast PIN diode that drives the sweep circuit according to the Ti:sapphire repetition rate (~80 MHz).

The temporal resolution of the streak camera employed in the setup of Fig. 7 is 1.9 ps. However, this is the so called one-shot resolution since actual time resolution during signal integration is larger. In particular, the unremovable time jittering of the streak camera during integration is responsible for a time resolution of 4 ps. Exhaustive reviews on streak cameras can be found in references [6, 7].

2.4 ASE, loss and gain measurements

The Amplified Spontaneous Emission (ASE) properties of small molecules thin-films are measured by a frequency tripled 355 nm line of a 10 Hz, 25 pulse duration, Q-switched Quantel Nd:YAG laser. The output intensity of the laser is controlled by inserting a calibrated neutral density filters onto the laser beam path. An adjustable slit and cylindrical lens are used to shape the laser beam into a narrow rectangular stripe with a width of approximately 1 mm and a length of 4 mm. The films are pumped at normal incidence with the long axis of the pump beam perpendicular to the edge of the sample.

When the excitation intensity is sufficiently high, the spontaneously emitted photons that are waveguided along the stripe region are amplified via stimulated emission. This results in most of the light being emitted along the direction of the stripe. It has to be noticed that the difference in refractive indexes between the Spectrosil® fused silica substrate (~1.47) on which the organic thin-film is deposited and the organic thin-film itself (~1.7) guarantees an efficient waveguiding.

Light at the peak of the gain spectrum of the material will be amplified more than other light wavelenghts, leading to a spectrally narrowed emission (typically a few nanometers full width at half-maximum) above a particular pumping intensity.

The output signal is efficiently focused on a fiber-coupled Hamamatsu CCD spectrometer by a lens system aligned along the stripe direction (Fig. 9).

The pumped energy from the laser are measured using a calibrated laser power and energy meter (Scientech). Measurements are performed at 20 K since the sample are mounted into a Helium close-circuit Leybold cryostat.

Two physical observables can be extracted from the ASE peak profile: the enhancing output intensity of the peak (expressed in arbitrary unity) and the decreasing peak full width at half maximum (FWHM). Typically the ASE threshold value is extracted from the curves displaying peak intensity and peak FWHM in function of the energy of the laser beam pulse.

Since ASE strictly has no defined threshold, throughout this thesis it is decided, for the purposes of comparison, to define that ASE starts to occur when the FWHM of the emission is halved. This reduction in FWHM is accompanied by an abrupt increase in the output intensity growing in a superlinear fashion.

It is fundamental in ASE threshold measurement curve to convert the [μJ/pulse] *x* axis unity, which expresses the energy of the impinging laser pulse, into [kW/cm^2] that is related to laser beam power per surface unity so that ASE threshold values obtained from different experimental setups may be directly and reliably compared. For the laser characteristics and stripe shape we mentioned above, in all our measurements 1 μJ/pulse corresponds to 1 kW/cm^2.

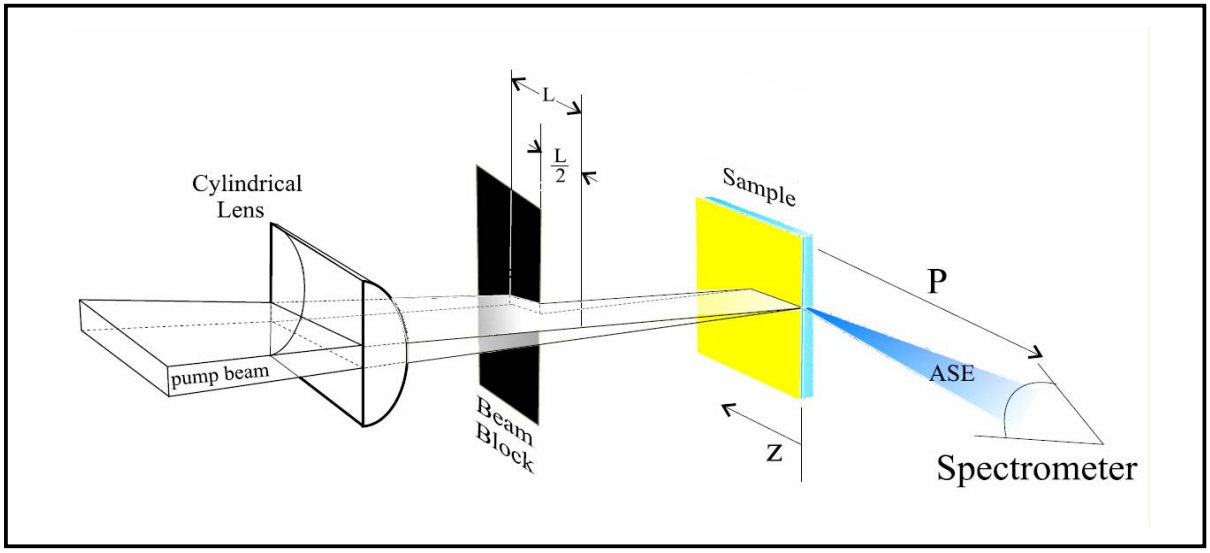

Figure 9. Scheme of the optical setup for performing Amplified Spontaneous Emission (ASE) measurements.

To investigate the net gain of the organic thin-film, the *variable stripe length* (VSL) method can be used. It has been widely used for both organic and inorganic materials prepared in slab geometry [8, 9]. This technique involves pumping the sample with a stripe of variable length and monitoring the edge output as a function of stripe length. The distance from the edge of the pumped area to the detector remains fixed

The net gain $g(\lambda)$ is then determined by fitting the output intensity versus stripe length variation with respect to the expected *small-signal regime* dependence. Indeed the following equation refers to the regime where saturation of the material gain with increasing field intensity does not play an important role in the output intensity (the so called *small-signal regime*):

$$I_{OUT}(\lambda) = \frac{A(\lambda) I_0}{g(\lambda)} (e^{g(\lambda) l} - 1)$$

Here, I_{OUT} is the ASE intensity and l is the length of the stripe, whilst $A(\lambda)$ is a constant related to the emission cross section, I_0 is the pumping intensity. So by monitoring the line-narrowing emission as a function of the stripe length one may calculate the net gain g(λ).

The corresponding waveguide losses are measures via the *stripe displacement method* (SDM).

In this method the length of the stripe is kept constant and the stripe is gradually moved away from the edge of the sample, so that the ASE signal has to travel across an increasing length of *unpumped* sample before reaching the edge and being focused in the CCD fiber. The possible reduction of signal collected by the fiber due to the spreading of the light is completely eliminated since we use a lens system for collecting and focusing the emission from the sample edge to the CCD fiber.

The emission from the end of the stripe was assumed to is constant, since in every measurement the pump energy and the pumped area are invariant. The signal reduction of the emission from the sample edge with increasing stripe displacement can then be assigned to absorption and scattering losses that occur within the *unpumped* region. The output ASE signal should then depend on the distance from the end of the sample edge as follows:

$$I_{OUT}(\lambda) = I_0 e^{-\alpha(\lambda)x}$$

Where x is the length of the *unpumped* region between the edge of the sample and the end of the stripe and $\alpha(\lambda)$ is the waveguide loss coefficient (modelled as an effective absorption).

2.5 *Low current opto-electronic measurements*

Three types of electrical measurement are mainly performed to test OFETs: the I-V or *output* curves, which are obtained keeping V_{gs} fixed and sweeping the V_{ds}; the *transfer* curves, which are obtained keeping V_{ds} fixed and sweeping V_{gs}; the *locus* curves, which are plots obtained by collecting Ids current during the V_{ds} and V_{gs} sweeping, which are kept at the same value.

Moreover in all these measurements a suitable detector is implemented for collecting photons that may be emitted by the working devices.

All the measurements are performed typically in controlled atmosphere, i.e. vacuum or glove-box nitrogen atmosphere, since air moisture and oxygen have a very dendrimental effect on devices opto-electronic characteristics due to the interaction with the active organic material.

The overall accuracy of the measurement system is one of the most important parameters to be considered in any low signal analysis. For any given test configuration, a number of variables can affect the measurement accuracy.

Some of the ways noise or errors can effect low signal measurements are:

- From the signal source
- From the measuring instrument itself
- From external disturbances, such as variable electrostatic and /or electromagnetic fields
- From connections between the device under test (DUT) and the measuring instrument

Other factors may also seriously compromise the measurement accuracy such as: noise, instrument accuracy, configuration of the probe system, leakage currents, stray capacitance, shielding and guarding methods, cable quality, and connector quality.

The key task for making accurate low signal measurements is to identify, and then eliminate, the potential error sources.

The following example are few of the most common sources of parasitic signals.

TRIBOELECTRIC EFFECT

Friction, caused by vibration or cable bending between coaxial cable insulators and conductors, generates a static charge that results in stray triboelectric currents (Fig. 10 a).

PIEZOELECTRIC EFFECT

Many types of insulator materials have either piezoelectric characteristics or they can store charges. In either cases, mechanical deformation or stress cause the insulator to generate small error currents.

ELECTROSTATIC COUPLING

Electrostatic coupling can happen when a wire with an applied voltage or a charged object is brought close to the device that has to be measured. A stray current can be coupled into the device by varying the voltage or by moving or vibrating the charged object, as shown in Fig. 10 b.

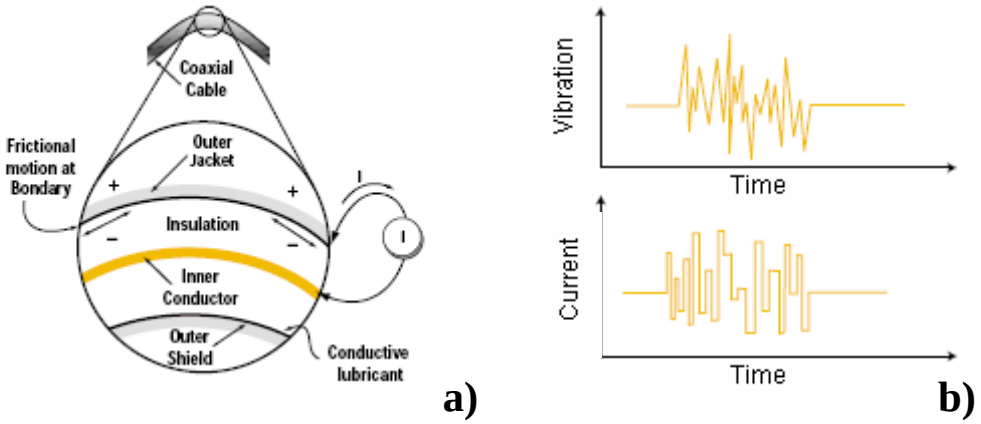

Figure 10. a) Schematic representation of triboelectric currents. b) Currents generated by vibrations.

ELECTROCHEMICAL EFFECT

Contamination on the device or on the probe arms and tips, such as finger oil and solder flux combined with humidity, causes an electrochemical reaction that can result in spurious currents ranging up to pA.

DIELECTRIC ABSORPTION

Dielectric absorption in insulating materials can occur when a voltage across that insulator causes the polarization within the insulator with a net separation of charge density with opposite signs. When the voltage is removed, the separated charges relax and generate a decaying current as shown in Fig. 11 a.

GROUND LOOPS

When the source and measuring instruments are both connected to a common ground bus, ground loops can generate effective noise signal and spurious voltages, as shown in Fig. 11 b.

Connecting all equipment to a single point ground source can eliminate this error source.

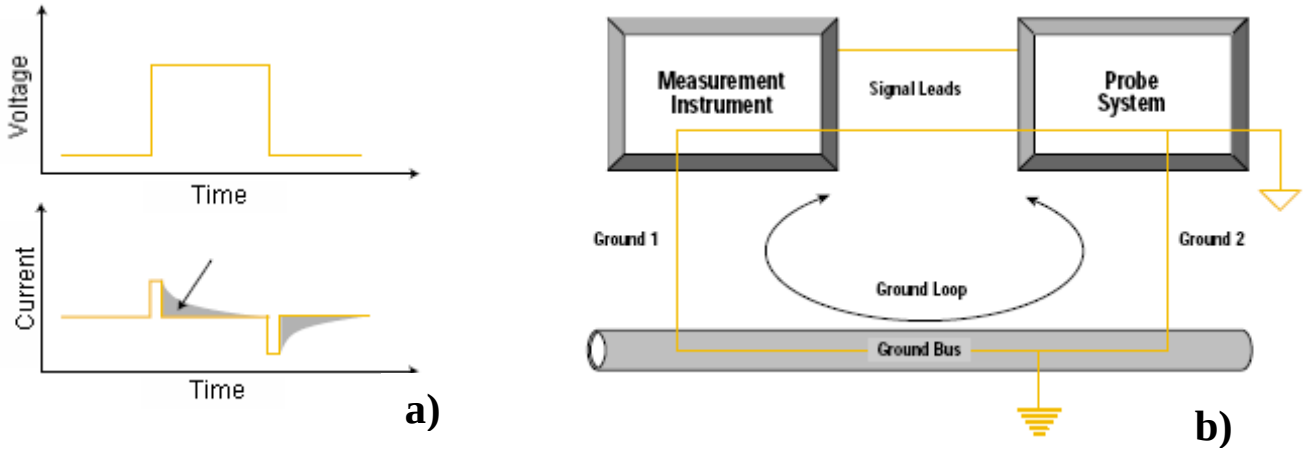

Figure 11. a) Decaying parasitic currents due to dielectric absorption. b) Ground loops between a probe station and a measurement instrument eliminated by a common ground.

The system's noise floor defines the lowest signal level measurement possible. Both the measurement instrument and the device probing system noise floor define the overall measurement system noise floor. The instrument accuracy and resolution together with total system noise floor define the quality of device measurements.

There are many instruments available for low signal DC measurements. The more self-contained an instrument is, the better the overall noise characteristics are. With the coming of instruments that combine current and voltage sourcing with current and voltage measuring capabilities, a high degree of versatility can be achieved from a single instrument.

The major benefit of this Source-Monitor/Measure (SMUs) is versatility and low signal measurement capabilities. In particular all the electrical measurements on OFET are carried out by a Agilent B1500A Semiconductor Device Analyser, which is a modular instrument that supports both I-V and C-V measurements and also fast high-voltage pulsing. It presents extremely low-current, low-voltage, and integrated capacitance measurement capabilities with a measurement resolution of 0.1 fA / 0.5 μV in I-V measurements.

In order to prevent the environmental signal noise to be introduced in the collected low-current signals, we connect the Semiconductor Device Analyser with the probing system with *triaxial* cables in all the measurements.

Indeed, all electrically floating or unconnected conductors are noise collectors. Therefore, all conductive items must be tied to either a defined voltage, or a guard connection (common or ground) which is a conducting cable shield driven by a low impedance voltage source. Triaxial cables are very effective in protecting a voltage signal from unwanted influences. Typically, the outer shield is connected to the chassis or ground, the inner shield is connected to the guard and the signal is collected by the core wire. Since the guard surrounding the core wire and the core wire itself are at the same potential all the possible leakage currents are avoided and the current signal is completely screened from the outer environment. The guard technique reduces not only the leakage currents, but also the response time because cable charging is induced by low impedance source. So the polarization due to the signal current passing through is very little since the residual cable capacitance left.

All the parasitic sources in low-current measurements we dealt with are carefully taken into account in the two setups for opto-electronic OFET measurements we implemented throughout the Ph.D. thesis work.

2.5.1 Opto-electronic Probe Station

For performing opto-electronic device characterization immediately after fabrication without any interaction of devices with atmosphere, we set-up a Süss PM5 Analytical Probe System (Fig. 12 a) in the N_2-atmosphere glove-box system which is coupled to the growth vacuum chamber.

In a probe station by micrometric positioning of tungsten tips on the device pads we are able to apply voltage to device and collect low-current signal (noise level tens of pA) that can be correlated to the device electroluminescence because of the presence of photodiodes in the proximity of the device active area.

The probe platen has enough area and heavy mass to provide extreme rigidity and accessibility to the probeheads. Platen can travel vertically along Z axis for 40 mm with a 0.2 mm contact/separation stroke.

The chuck is mounted on a rigid X/Y table with ergonomic coaxial controls. The chuck position can be finely tuned in the Z direction. A pull-out stage moving along the Y axis permits quick and safe device loading as well as superior positional repeatability for packaged devices and substrates.

For locating accurately the tungsten tips on the three device electrodes manual probeheads are magnetically blocked onto the base plate. The probehead arms are connected to *triaxial* wires.

The probehead incorporates an independent X, Y and Z stage system with a maximum mechanical cross-talk deviation of 3 microns. Each stage incorporates hardened steel rails and ball bearings assembled to strict specifications. Each axis has 8 mm of travel with the choice of either 50 or 100 tpi (threads per inch) resolution.

The *triaxial-chuck* connection (Fig. 12 b) is created to minimize the chuck leakage current. It is guarded and completely separated from the base machine by a Teflon insulation. The guard has an insulation resistance value of 1.0 TΩ. The chuck guard must be connected to the instrument's guard connection to guarantee accurate and ultra low-current measurements.

A 70X-magnification optical microscope is mounted vertically on the chuck plate to allow precise positioning of the probing tungsten tips.

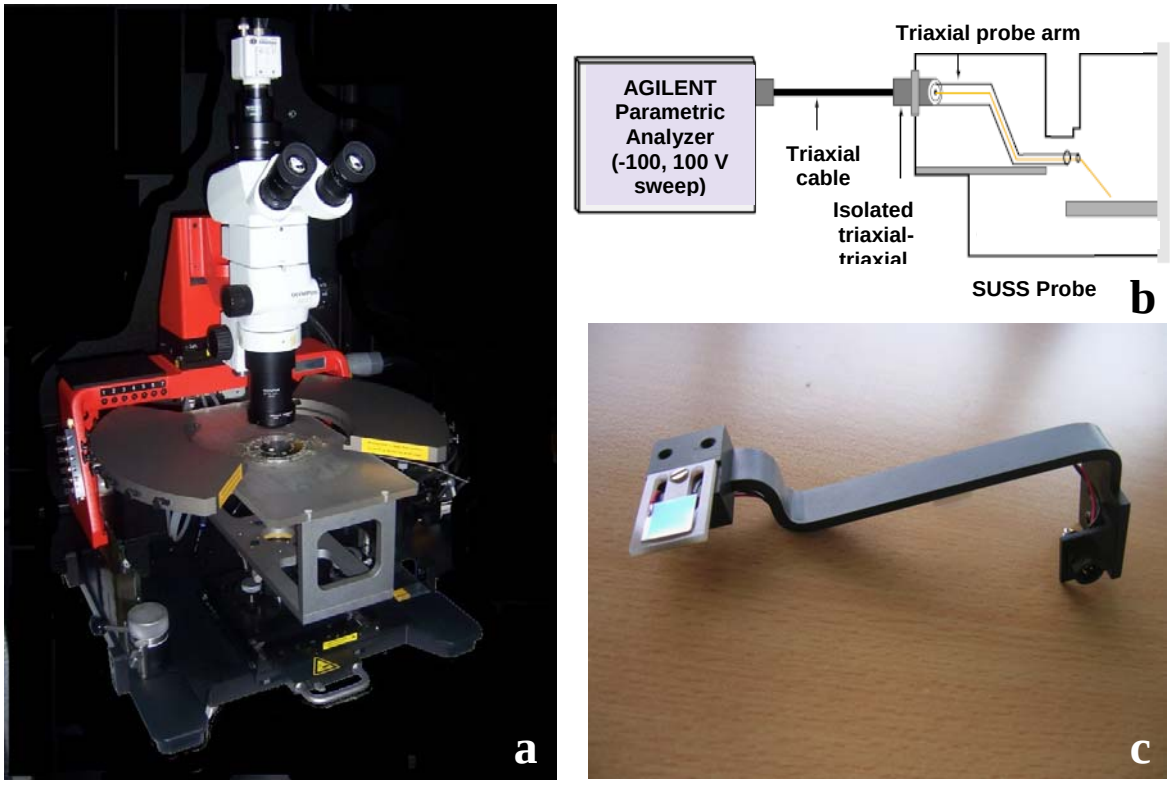

Figure 12. a) Süss PM5 Analytical Probe System. b) Scheme of the *triaxial* cable connection between the Semiconductor Device Analyser and the Analytical Probe System. c) Hamamatsu photodiode used for electroluminescence measurements.

In order to collect the electroluminescence two Hamamatsu photodiode (S1337) are mounted on two are arms (Fig. 12 c) that can be positioned over and underneath the device substrate by two probeheads with micrometric X,Y, Z stages. Thus, in the case of all-transparent devices it is possible to collect photons emitted upward and downward through the transparent substrate are easily collected. The photodiode effective area is 100 mm^2 and photosensitivity at 633 nm (He-Cd laser) is 0.6 A/W.

2.5.2 Opto-electronic Integrating Sphere

For performing device electrical characterization in a 10^{-6} mbar vacuum atmosphere an integrating sphere is used (Fig. 13 a). Moreover this set-up allows to perform PL and EL quantum yields.

The setup consists in a Labsphere-manufactured 12 in-diameter integrating sphere made of a material reflecting 99.8 % in the spectral range 300-900 nm. Thus, the internal surface of the integrating sphere can be considered a Lambertian surface which distributes homogeneously within the sphere volume the total amount of light that hits the surface

itself. Therefore, the flux received at an aperture of the sphere is proportional to the total light emitted from the sample, irrespective of its distribution. Thus, knowing all the geometrical parameters of the sphere it is possible to obtain a quantitative measurement of the EL quantum yield just by having a calibrated detector and supposing the emitting sample as a point-like source.

A vacuum chamber is built to contain the sphere with optical quartz windows corresponding to the horizontal and the meridial apertures. Both the apertures allow us to check if the light emitted by the devices may be visible by naked eye.

The vacuum chamber has a removable top cover for inspection and cleaning of the internal part and of the sphere. The top cover is designed to fit a sample holder endowed with suitable electrical feedthroughs which permit to carry out electrical measurements in vacuum (Fig. 13 b). The sample holder enters the sphere placing the sample at the center of the sphere. The sample is located in a teflon clamp which present a central hole (Fig. 13 c), thus minimizing any perturbation on the distribution of the emitted light induced by the sample holder.

The electrical cables for applying tensions and collecting currents are fixed in the teflon clamp. Thin copper threads welded by tin on the incoming signal cables are electrically connected to the device-under-test pad by silver paste. Device pad are properly engineered to facilitate this operation.

At the meridial aperture of the vacuum chamber a photomultipliar for the detection of integrated signal is screwed. The photomultiplier is a preamplified head-on R347 photomultiplier tube (PMT) from Hamamatsu, whose sensitive part is set 5 mm apart from the internal surface of the sphere. The radiant cathode and anode sensitivity at 420 nm is 64 mA/W and 3.4×10^4 A/W respectively.

Although the head-on configuration of the PMT helps to overcome the dependence of the measured signal from the spatial distribution of the light intensity on the sensible area of the PMT, a spectral diffuser between the surface of the sphere and the PMT is set.

A mechanical and turbo pump system is connected to the vacuum chamber and to the sphere through an aperture located near the sample holder. A vacuum of 10^{-6} mbar is guaranteed by mechanically pressed O-rings at each quartz window, at the interface between the cryostat and the cover of the chamber, as well as between the cover of the chamber and the chamber itself.

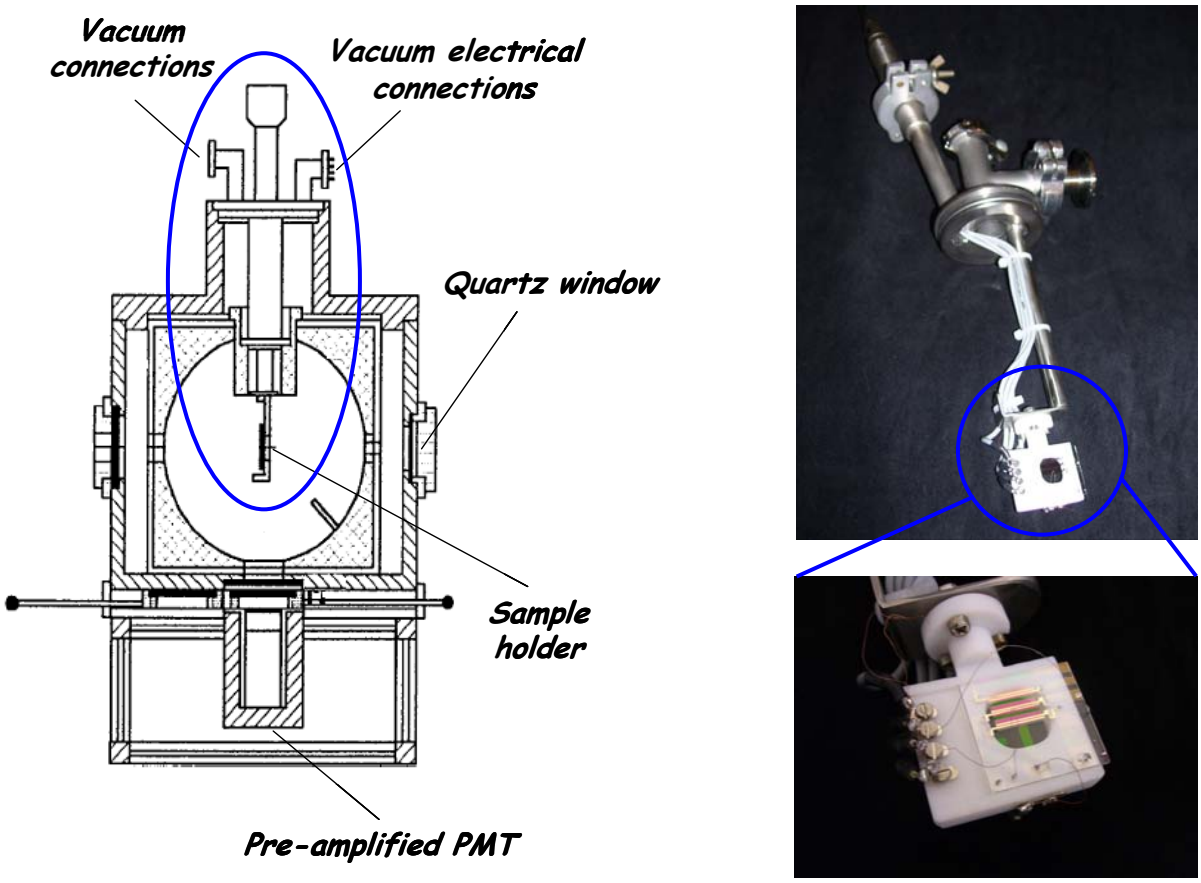

Figure 13. a) Sketch of the integrating sphere set-up. b) Sample holder implemented during the opto-electronic measurements. c) Particular of the sample holder with the teflon on which a three-device substrate is located.

References

[1] D.W. Pohl,W. Denk, andM. Lanz, *Appl. Phys. Lett.*, **1984**, 44, 651.

[2] T. Wilson, *Confocal Microscopy* (London: Academic Press, 1990).

[3] J. B. Pawley, *Handbook of biological Confocal Microscopy* (New York and London: Plenum Press, 1990).

[4] G. Binning, C.F. Quate, C. Gerber, *Phys. Rev. Lett.*, **1986**, 56, 930.

[5] W. Demtröder, *Laser Spectroscopy: Basic Concepts and Instrumentation* (3rd Ed. Berlin: Springer-Verlag, 2003).

[6] J. R. Lakowicz, *Topics in Fluorescence Spectroscopy*, *Volume 1: Techniques* (New York: Plenum Press, 1991).

[7] A. J. Campillo and S. L. Shapiro, *IEEE J. Quant. Elec.*, **1983**,19, 585.

[8] K.L. Shaklee and R.F. Leheny, *Applied Physics Letters,* **1971**, 18, 475.

[9] M.D.McGehee, R.Gupta, S.Veenstra, E.K.Miller, M.A.Diaz-Garcia, and A.J.Heeger, *Physical Review B*, **1998**, 58(11), 7035.

Chapter 3

π-conjugated oligothiophenes

3.1 Linear oligothiophenes

The recent and spectacular development of conjugated oligothiophenes is essentially related to their use as active materials for electronic device applications [1]. In 1974 an initial article by H. Kuhn et al. [2] described photocurrent measurements on Langmuir-Blodgett films of α-quinquethiophene (α-5T). In the mid-1980's, conjugated all-α-linked oligothiophenes (α-nT, where n is the number of thiophene rings in the oligomeric sequence, see Fig. 1) were used as model compounds and starting monomers for the preparation of electrically conducting polythiophenes [3].

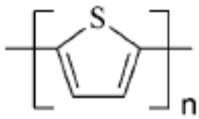

Figure 1. Chemical structure of α–linked oligothiophenes.

Both in bulk and in thin-films the majority of unsubstituted conjugated organic thiophene oligomers (such as oligomers with four [4], five [4], six [5], and eight [7] thiophene rings) crystallize into the monoclinic system with a $P2_1$ space group ($P2_{1/a}$, $P2_{1/b}$, $P2_{1/c}$ according to the oligomer chain length) which is called herringbone structure (in Fig. 2 we report one of two polymorphs of α–6T as example). Moreover they form polycrystalline films in which the molecule long axis is orientated perpendicularly to the substrate.

In this packing motif, molecules minimize π–orbital repulsion by adopting an edge-to-face arrangement forming a two-dimensional layer [7]. The angle between molecular planes of side-by-side molecules is 40-60° and the distance between the sulphur atoms is around 3.6-3.9 Å [8]. This particular molecular arrangement is probably responsible for the reduction of the transport properties in the direction normal to the long molecular axis.

It has been theorized that forcing the oligomers to adopt a face-to-face arrangement (π stack) would increase the π-orbital overlap and thus enhance the charge mobility by

maximizing electronic coupling between adjacent molecules [9]. Several oligomers that have been shown to adopt a cofacial packing arrangement include fused-ring oligomers [10], oligomers containing bulky substituents [11] and oligomers incorporating both electron-rich and electron-deficient aryl rings [12]. The electric performances of the devices obtained from these oligomers are quite promising as compared with analogues that adopt a herringbone structure, but further investigations are needed to demonstrate conclusively that face-to-face π-stacking results in higher charge mobility.

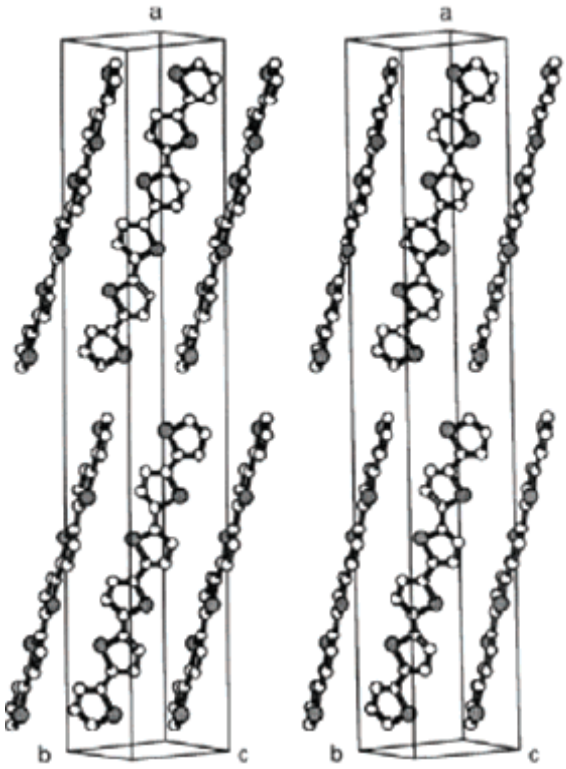

Figure 2. Crystal structure of α-6T deposited from the vapor phase, displaying a typical herringbone packing motif [13].

This great interest in the study of the charge transport properties of semiconducting α-nT thin-films is due to the very promising implementation of linear oligothiophenes molecules as active materials in Organic Thin-film Transistor (OFET). In particular, it has been demonstrated that α–6T-based OFETs show an improved carrier mobility when long range molecular ordering is achieved [14]. The highest mobilities ($\mu \sim 0.04$ cm^2 V^{-1} s^{-1}) are obtained in devices using highly oriented thin-films and are close to that measured on

α–6T single crystals (μ ~ 0.16 cm^2 V^{-1} s^{-1}) [15]. This shows that charge transport between source and drain of a OTFT occurs essentially through molecular channels of α-6T molecules oriented perpendicular to the substrate and having the herringbone arrangement found in the single crystal.

The highest reported mobility value for α-8T is 0.33 cm^2 V^{-1} s^{-1} and was obtained when the substrate was heated to 120 °C during deposition [6]. This mobility value is an order of magnitude higher than previously reported for α-8T [4], and is attributed to the formation of elongated, terraced grains.

The majority of the investigations on the transport properties of oligothiophene films do not show any effects that could be related to band-like descriptions of the excitonic or the charge carriers up to now. The strong thermal activation behaviour and the influence of the structure and the morphology of the polycrystalline oligothiophene films on transport processes establish a picture of the noncoherent hopping transport where different trapping levels dominate the motion of the charges [16]. In contrast to that, it was reported on the temperature dependence of field effect mobilities, which were attributed to a coherent carrier motion at very low temperature (T < 50 K) [17].

The optical properties of the α–nT films reflect very well the orientational aspects. Oelkrug's group determined the dichroic behaviour [67] of the optical transitions within vapour-deposited films. Being a representative member of the linear unsubstituted oligotiophenes family we report the typical polarized absorption spectra of thin-film of 6T on quartz are displayed in Fig. 3.

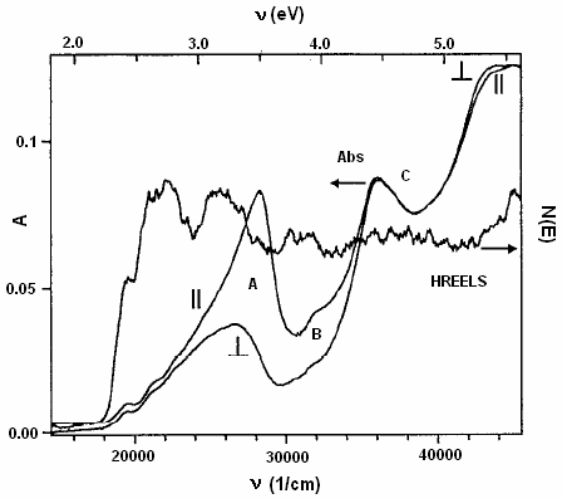

Figure 3. Polarized absorption spectra of a 2.5 nm thick α–6Tfilm on fused silica. The spectra are taken under angle of 50° with respect to the surface normal orthogonal and parallel polarization.

For thin-films, the bands are labelled A, B and C can be well distinguished as it is also reported for the oligothiophenes in solutions. By using *s*- (orthogonal) and *p*- (parallel) polarized light it becomes apparent that the bands labelled A and B are polarized perpendicular, whereas band C is polarized parallel to the surface. Despite of the dichroism the overall shape of the lowest energy bands changes drastically from solution to thin-films. However, even if the most intense feature in oriented films is peaked around 28000 cm^{-1} the onset of the absorption band is located around 18500 cm^{-1}. If the sample thickness increases, the degree of orientational order decreases and the shape of the optical spectra change drastically for the lowest transition between 18000 and 30000 cm^{-1}. In contrast to the low resolution found for the absorption spectra within most of the literature, Fichou et al. [18] succeeded in a much better resolution of the vibronic structure for thin α–nT films. From the spectra it became quite clear that the electronic origin of the optical transition for 6T films must be located lower than 18500 cm^{-1}. The spectra features for different oligomers (n = 4-6) were found to be very similar as expected from the matrix-isolation [19], although the vibronic fine structures could not be fully assigned at that time [18].

In addition to the α-6T absorption, PL spectra were also analysed to disentangle the nature of the lowest excited state [20]. By going from solution to thin films PL quantum yield decreases by three order of magnitude [21] and apparently broad emission lines dominate the spectra: even at very low temperatures the resolution of the optical spectra is rather poor (several 100 cm^{-1}) and spectroscopic details are smeared out. In most cases a considerably red-shift between the absorption and PL onsets together with multiple PL-components could found within the spectra. The main radiative decay channels are attributed to deep trap levels and aggregates which are strongly dependent on films preparation conditions and thickness so that not only thin-film morphology features change (from 2D to 3D) but also the phophysical properties.

As an explicative example, in Fig. 4 we report on the low temperature PL spectra of T6 thin films grown on mica substrate with an increasing thickness [22]. In this case, after a nominal thickness of 20 nm, the excitonic emission is buried under the defect emission. Excitonic emission (see zero delay time spectrum) can be detected only in the first 50 ps [23], before the exciton migration to these low energy states is completed.

A variety of experiments highlighted that, unless the thin-films quality could have been increased, it would not have been possible to reveal a detailed description of the spectroscopic features of oligothiophesnes in solid state. In order to satisfy this requirements, two different approaches towards the realization of highly-ordered

oligothiophenes systems had been undertaken, i.e. the growth of single crystals by Garnier's group [24] and the thin-film growth by epitaxial preparation which was established by Umbach's group [25]. Since both these approaches go beyond the growth by high vacuum sublimation on amorphous substrates we performed for all the thin-films experimental data we present in this chapter, we just refer to the literature for a complete spectroscopic analysis of highly-ordered linear oligothiophenes systems.

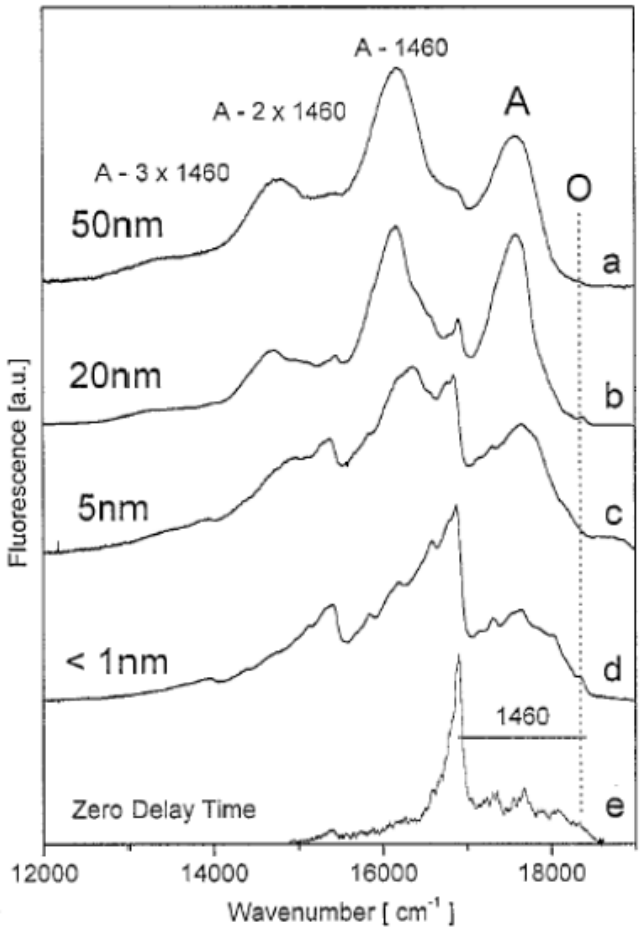

Figure 4. Low temperature PL spectra of α-6T thin films on mica. The film nominal thickness is reported on the left of each spectrum. Bottom spectrum is the PL at zero delay time after excitation. (from reference [22])

Hereafter we report on a p-transport and a n-transport linear oligothiophene derivatives that not only show state-of-the-art electrical characteristics thin-film transistors realization, but are also implemented as constitutive layers in the tri-layer heterojunction OFET we present in Chapter 5.

3.1.1 High mobility hole-transport molecule: α,ω-dihexylquaterthiophene (DH4T)

Many synthetic methods have been developed to functionalize either the α- or β-positions of the thiophene ring, in order to increase the solubility or to influence the solid-state ordering of oligothiophenes [1]. Functionalization at the α-positions of the oligomer typically does not affect the planarity of the conjugated backbone but does little to help solubility unless branched substituents are used. End-substitution with alkyl chains has been found to be particularly useful, because it gives the molecules liquid-crystalline-like properties, which dramatically increases the ordering and enhances the charge mobility of the resulting evaporated films [7]. Functionalization of the β-positions in thiophene oligomers can significantly increase the solubility of the oligomers but tends to warp the conjugated plane and in most cases leads to low-mobility materials.

Halik and co-workers have also demonstrated the sensitivity of alkyl-substituted oligothiophenes to device configuration [26]. Charge mobility in bottom contact devices was found to be independent of the oligomer length and independent of the alkyl chain length. However, in top contact devices oligomers containing short alkyl end groups (less than six carbons) were found to have an order of magnitude higher mobility. The authors attribute this phenomenon to an intrinsic barrier to charge injection from top contact devices when large insulating alkyl chain groups are present.

Among all the alkylend-substituted short oligothiophenes, we focus our attention on the study of α,ω-dihexylquaterthiophene [DH4T] (see Fig. 5) since this molecule can organize in thermally grown polycrystalline thin-films presenting very high mobility and highly ordered structures.

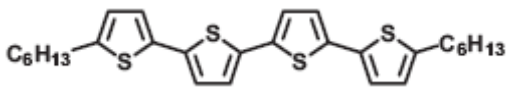

Figure 5. Chemical structure of α,ω-dihexylquaterthiophene (DH4T) molecule

Transmission electron microscopy (TEM) [27] of the films on carbon grids reveals a very smooth and flat morphology of lamellar single crystals. At high deposition temperatures (e.g., 100 °C) the flat crystals extend over many tens of micrometers without exhibiting

substantial multilayering. Their only distinguishing feature is the existence of transverse cracks. Because this feature is not seen for DH4T films deposited at lower temperatures, they are most likely the result of contraction during cooling.

Since this molecule presents fluorescence properties all these morphological features can be clearly revealed by CLSM investigation on DH4T thin-film, as we report in Fig. 6

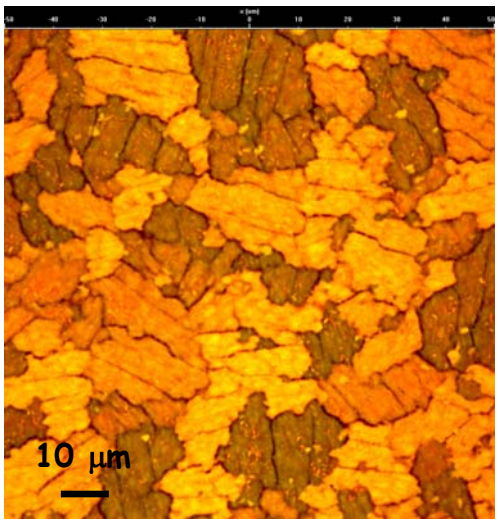

Figure 6. Confocal image of a 45 nm-thick film of DH4T grown on Si/SiO_2 substrate (oil 60× objective).

X-ray diffraction (XRD) [27] of the films grown on Si/SiO_2 shows a series of sharp peaks, all corresponding to successive orders of the molecular repeat at 28.5 Å. With increasing substrate temperature, the sharpness of the peaks increases, as it is expected, and the spacing between molecules shrinks. The 28.5 Å molecular repeat is consistent with molecules being essentially normal to the substrate and with their hexyl chains directed toward the sulfur side of the 5 and 5''' positions of the quaterthiophene core. The spectrum at 180°C is completely amorphous in agreement with a liquid phase.

From Differential Scanning Calorimetry (DSC) measurements [28] it is inferred that at 84°C DH4T goes through an endothermic phase transition from a 3D crystalline phase to a liquid crystal smettic phase. This observation together with XRD data corroborates a structural model in which the alkyl chains rotate from an extended chains trans conformation to a skew/gauche conformation by passing through the phase transition temperature, whereas the thienylene sequence responsible for the charge trasnsport remain faced at the typical van der Waals distances.

The electrical properties of this alkylated quaterthiophene can be expected to be largely dominated by such long-range 2D organization. Indeed, top contact/bottom gate linear transistors fabricated from DH4T deposited at 0.1 Å/s deposition rate on Si/SiO_2 substrate held at 90°C and with a hexamethyldisilazane (HMDS) treatment on top of SiO_2 gate dielectric surface show remarkable amplification characteristics (Fig. 7) with very well-defined linear and saturation regime. The calculated hole mobility value is around 0.01 cm^2/Vs.

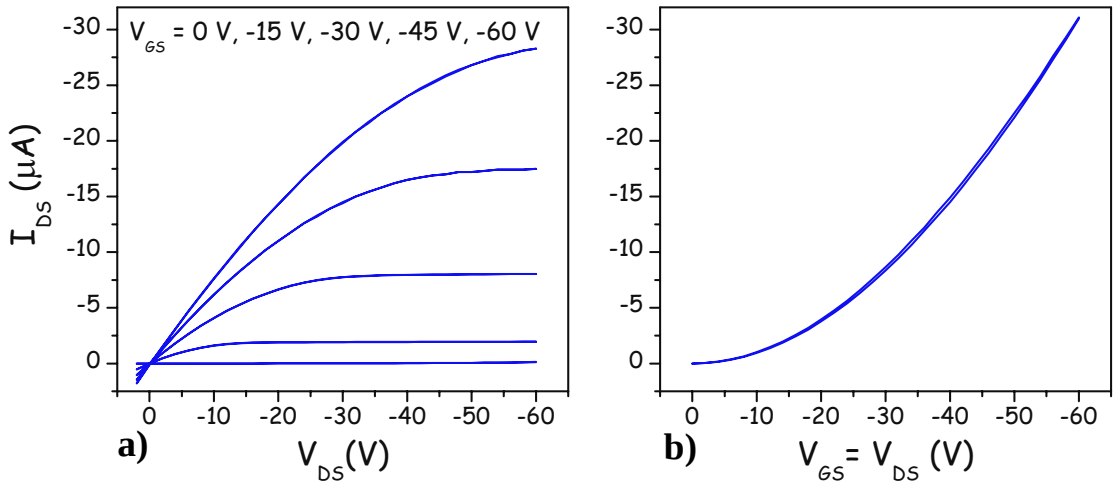

Figure 7. a) Output characteristics with increasing applied gate voltage and b) locus characteristics of DH4T-based TFT fabricated by treating the SiO_2 gate dielectric surface with hexamethyldisilazane (HMDS). Top contacts are 50nm-thick gold thin-films.

It is worthy noting that the very high mobility value together and the low voltage threshold (around 5 V) are attributed to the surface treatment we implemented.

As many surface treatments on SiO_2 surface do, HMDS treatment involves the creation of a self-assembled monolayer bonding directly on the –OH groups present on SiO_2 surface, which are commonly indicated as sources for the charge-carriers trapping. [29].

Moreover the HMDS treatment makes the surface completely hydrophobic (contact angle around 95°) so reducing the interaction strength between the surface itself and the almost apolar DH4T incoming molecules. In this way the molecule-molecule interaction is the driving force that allows a layer by layer thin-film growth and DH4T molecules in the thin-film are able to rearrange according to the single-crystal herringbone structural motif since the substrate temperature is higher than the temperature of the phase transition between crystal and smettic phases.

Concerning the morphology of the DH4T-dielectric layer interface where charge transport occurs, we have investigated the early stages of DH4T growth by AFM. The images in Fig. 8 reveal an initial layer-by-layer growth mechanism with a high density of nucleation centres. The height distribution of the DH4T islands is peaked around a characteristic value of 5 nm. This bi-dimensional growth affords good film connectivity, essential for a good charge transport since the first layer covers almost completely the channel area before the second layer starts growing.

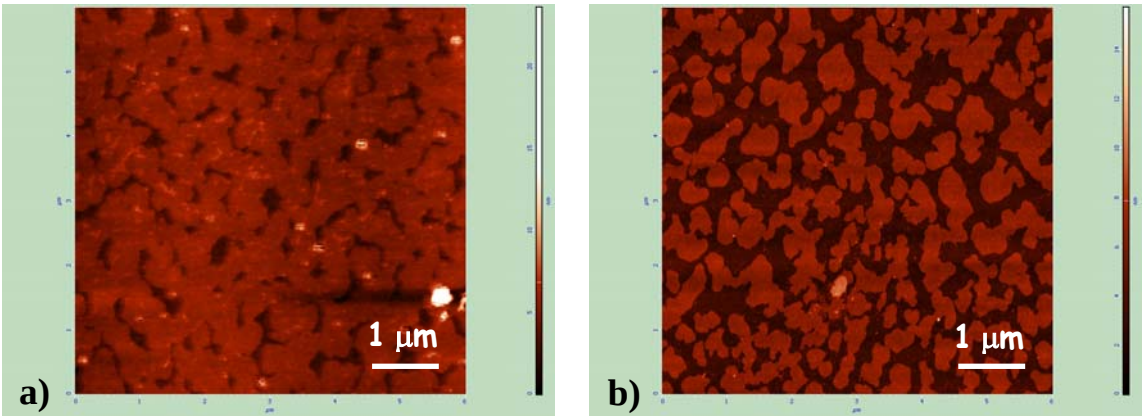

Figure 8. Topological AFM images of the TFT channel area: a) after the first layer is almost complete and b) during the second layer growth. The probing mode is semi-contact.

Concluding, OFET mobility of DH4T thin-films deposit at 90°C is higher than it has ever been observed in a thiophene *hexamer*, as high as it has ever been observed in any *polycrystalline* organic semiconductor, and it is over an order of magnitude higher than the highest reported mobility of the parent α-4T. As for pentacene-based devices, the high field-effect mobility is correlated with the single-crystal nature of the organic semiconductor film.

It is remarkable that among all the organic compounds screened so far for field-effect activity, especially p-channel activity, only pentacene and DH4T have been shown to form large-area single-crystal films [27].

3.1.2 High mobility electron-transport molecule: α,ω-diperfluoro quaterthiophene (DHF4T)

When incorporating organic semiconductors into field-effect transistor configurations to evaluate their charge transport characteristics in combination with a particular gate dielectric such as SiO_2, many of these materials exhibit hole accumulation behaviour for negative applied gate voltages. However, when the gate voltage polarity is reversed to positive values, the formation of an electron accumulation layer is much less commonly observed. For many organic semiconductor-based FETs, only p-channel operation seems possible.

Demanze and co-workers were among the first to demonstrate that functionalization of these oligomers with electronwithdrawing groups can change them from p-type to n-type materials [30]. Electron injection was found to occur in a series of cyano-functionalized oligothiophenes with three to six thiophene rings [31]. However, no semiconducting behavior was seen in OTFT devices, because these cyano-substituted oligomers orient parallel to the substrate instead of perpendicular, resulting in poor charge transport in the direction measured in field-effect transistors.

Facchetti and co-workers were the first to demonstrate that n-type behavior could be obtained in oligothiophenes through functionalization with perfluoroalkyl chains [32]. A series of oligomers was synthesized containing two to six thiophene rings functionalized in the α- or *β*-positions with perfluorohexyl chains [33, 34]. The introduction of perfluoroalkyl chains on the oligomer cores was found to increase the ionization potential and electron affinity but minimally affected the ground- and excited-state energies of the molecules. Organic thin-film transistor devices measured under nitrogen atmosphere only displayed semiconducting behavior with positive gate voltages, indicating that these materials are exclusively electron conductors.

The complementary semiconductor behaviour of fluoroalkyl- (n-type) and alkyl- (p-type) α-nTs is firstly due to the electron-withdrawing capacity of fluoroalkyl end-capping groups. Indeed, the thiophene ring is electron-rich and all the known thiophene unsubstituted oligomers and polymers are hole-transport as thin-film. These systems are intrinsically p-type, and σ–electron donating alkyl substitution has the effect of enhancing this property. So, for all thiophene oligomers, fluoroalkyl substituents impart sufficient

electron-withdrawing capacity lo lower the HOMO/LUMO core energy allowing electron injection to exceed hole injection [34].

Among fluoroalkyl thiophene oligomers, we focused our investigation on realization of devices based on α,ω-diperfluoroquaterthiophene (DHF4T) whose chemical structure is reported in Fig. 9.

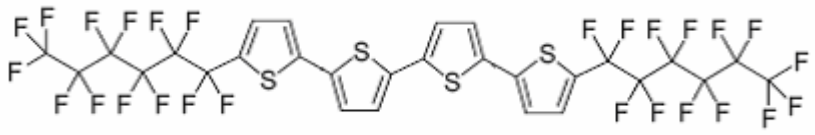

Figure 9. Chemical structure of α,ω-diperfluoroquaterthiophene (DHF4T)

The molecular packing of DFH4T shares the familiar herringbone motif found in all members of the oligothiophenes series, with an angle of 50°. between mean planes of adjacent molecules (Fig. 10). Typical herringbone angles for oligothiophene α-nTs (with n = 4-6, 8) range between 55 and 70°.

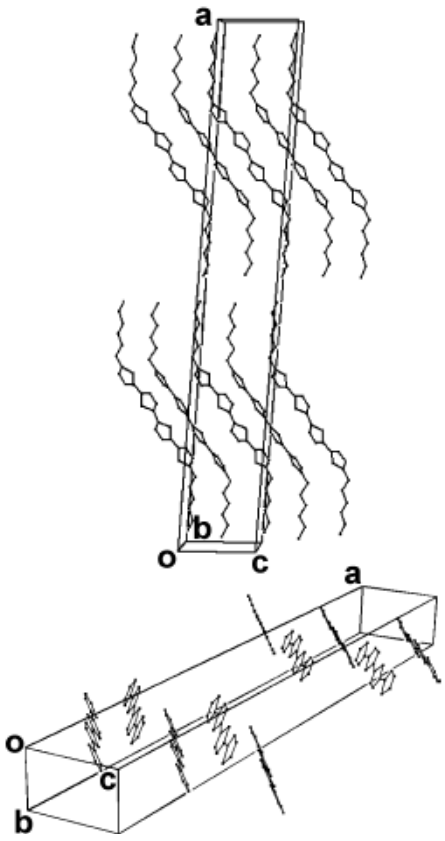

Figure 10. Crystal packing of DHF4T. Fluorine atoms (up) and fluorocarbon chains (bottom) are removed for clarity.

As we underlined previously, the origin of this angle, which is also typically found in many aromatic hydrocarbons crystal structures (i.e. p-oligophenylenes and acenes), is principally due to intermolecular π–electron repulsion. [33].

When it is implemented as active material in OFET realization, DHF4T when grown on SiO_2 surface shows morphological features quite different with respect its alkyl-substituted counterpart.

Holding the substrate at room temperature DHF4T molecules on a PMMA-treated SiO_2 surface tend to form 2D islands with ragged grain boundaries which then coalesce completely in the first monolayer (Fig. 11a). As the thickness of the film is increased, columnar 3D growth takes place with very high oblate protrusions (Fig. 11b).

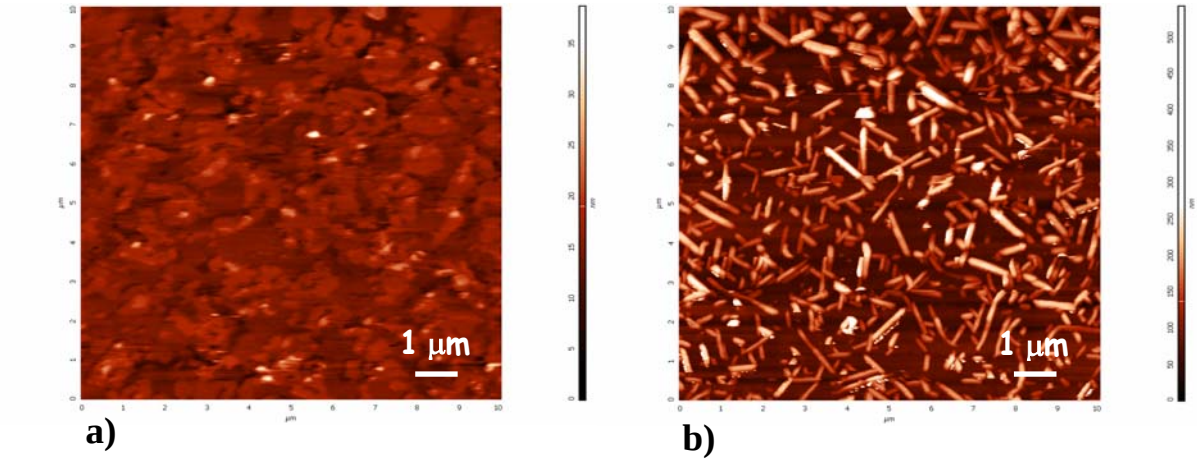

Figure 11. a) Contact-mode topological AFM image of DHF4T first monolayer and b)semi-contact topological AFM image of DHF4T 15 nm-thick film grown on 150 nm-thick PMMA film deposited on SiO_2 surface.

Nonetheless, electrical performances of DHF4T-based thin-film transistors are very interesting since the field-effect current is very high, the electron mobility is around 0.1 cm^2/Vs and the hysteresis in the electrical characteristics is almost negligible (Fig. 11).

Indeed, as it is well known [35], the field-effect charge carrier transport is spatially restricted to the first nanometers from the dielectric/organic semiconductor interface so that only a good in-plane connectivity in the first monolayer is sufficient for guaranteeing charge carrier transport.

The quite high voltage threshold (~ 55 V) shown by these device electrical characteristics can be correlated to the possible inefficient electron injection from gold source electrode due to the lack of smoothness and sharpness of metal/organic semiconductor interface. Holding the substrate temperature at 70°C during the film deposition can enhance the

metal/organic semiconductor interface quality since at this temperature DHF4T film offers the best compromise between large grain sizes and space-filling grain connectivity with highly interconnected thin crystallites aligned parallel to the substrate [34].

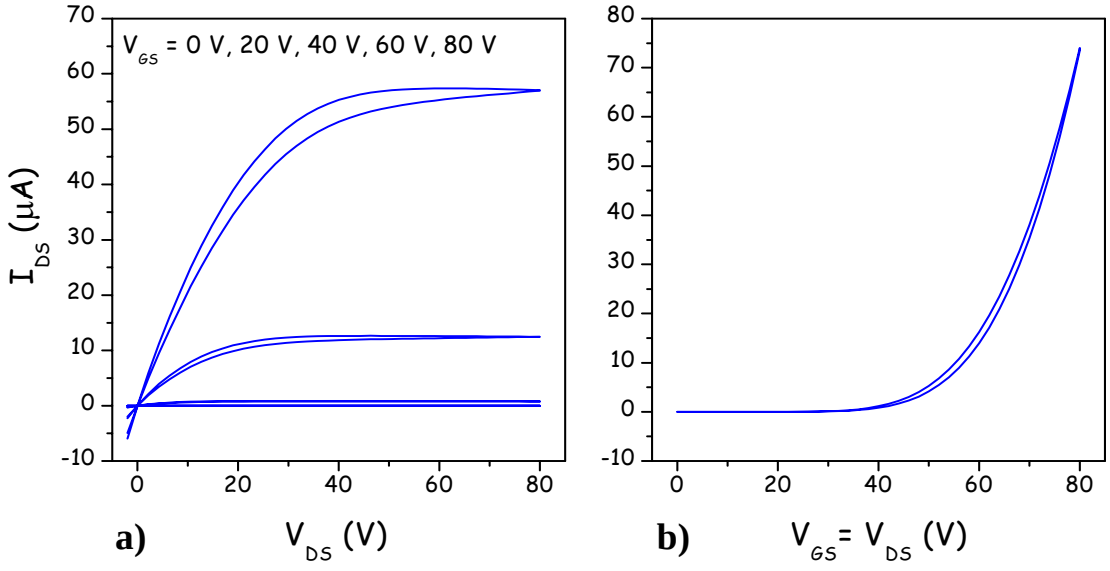

Figure 12. a) Output characteristics with increasing applied gate voltage and b) locus characteristics of linear DHF4T-based thin-film transistor fabricated by spin-coating a 150 nm-thick PMMA film on the SiO_2 gate dielectric surface. Top contacts are 50nm-thick gold thin-films.

3.2 Spider-like oligothiophenes

As we highlighted in the previous paragraph, OFETs based on polycrystalline films of linear oligothiophenes or pentacene prepared by thermal evaporation have reached hole mobility values exceeding that of amorphous silicon, with values larger than 1.0 $cm^2 V^{-1}s^{-1}$ [26]. Moreover high hole mobility values (up to 0.10 $cm^2 V^{-1} s^{-1}$) have also been observed for solution-processed thin films of poly(3-hexylthiophene) (P3HT) [36]. Despite their different chemical structures, these materials have in common the unidimensionality of their elemental structural unit which results in anisotropic charge transport and optical properties. An important consequence of this anisotropy is that the realization of efficient electronic or photonic devices requires a precise control of the material organization. In addition to the tight molecular packing and strong intermolecular interactions needed to reach a high charge-carrier mobility, proper control of the orientation of the conjugated chains on the substrate is imperative to obtain optimal charge transport in the desired direction. The considerably larger charge-carrier mobility obtained on single crystals of, for example, pentacene or rubrene compared to the values measured on polycrystalline thin films of the same materials clearly demonstrate the validity of this approach [37].

The development of organic semiconductors with higher dimensionality and isotropic charge transport and optical properties could represent an exciting alternative strategy for avoiding all the device fabrication issues related to the specific control of molecular interactions and orientation. In fact, such materials would allow the realization of all kinds of electronic or photonic device without any constraint in terms of molecular orientation. Provided they can combine adequate processability and reasonable charge-carrier mobility, 3D organic semiconductors could considerably simplify the fabrication of organic devices by simple printing techniques and represent versatile active materials for the realization of different types of devices [38].

Among all the 3D π-conjugated molecules, many synthetic efforts have been spent on the realization of multi-thiophene molecules presenting different overall number of thiophene units, substituents, inter-ring connectivity, molecular symmetry and shape. Swivel-cruciform [39], star- [40] and X-shaped [41], and dendrimeric oligothiophenes [42] have been prepared in the last few years and, in some cases, preliminary practical applications of these compounds as sensitive materials for OLED, OLET and photovoltaic devices have been described [42].

Apart the aesthetic appeal exerted by these large and constitutionally ordered molecules, it is worthwhile wondering if there is a remarkable correlation between the increasing dimensions of the multi-thiophene molecules and their molecular basic properties, especially with respect the much simpler unsubstituted α-oligothiophenes.

This is, however, a difficult task, since only selected parameters are reported in literature for the different classes of compounds, which makes impossible a complete and reliable comparison between all of them. The situation is further complicated by the fact that the same parameter is often evaluated not only under different experimental conditions (solvent, concentration, reference electrode), but also the method of recording the data is not standardized.

Sannicolò et al. [43] tried to rationalize this huge amount of information by collecting from the literature the optical band-gaps calculated from the absorption spectrum maximum wavelengths and calculated from the absorption spectrum onset wavelengths for linear α–nT and for some classes of branched oligothiophenes. Then the energy gap values are displayed as a function of the reciprocal of the overall number of thiophene units of the molecule and of the number of thiophene units in the longest α-conjugated chain present in the molecule.

The trend that can be extrapolated is that even big dendritic molecules having many α-conjugated branches with different lengths display an optical gap close to that exhibited by the unsubstituted α-oligothiophene α-nT with *n* corresponding to the longest α-conjugated branch of the dendrimer. Large multi-thiophene molecules display, however, energy gaps generally higher than expected due to some distortion from coplanarity of the main α-conjugated chain which is produced by branching.

It is understandable, however, that electronic spectra of very large molecular assemblies would be better described by the absorption spectrum onset wavelengths, since absorption curves undergo massive broadening as the molecules become larger and larger. Plotting the energy gap values calculated from absorption spectrum onset wavelengths against the reciprocal of thiophene units in the longest α-conjugated chain present in the molecule the energy gap values substantially flatten when five α-conjugated thiophene units are present independently on the whole number of thiophene units constituting the molecule and on inter-rings connectivity.

From these observations we can conclude that the synthetic engagement required to prepare molecules constituted by a very large number of thiophene rings is not always

accompanied by the acquisition of extraordinary conjugation properties, even though other very interesting physical features are acquired, like high chemical stability and solubility in non-polar organic solvents.

In this context Sannicolò et al. [43] considered an alternative, very simple design of all-thiophene assemblies, which is a compromise between size and properties, named "spider-like" oligo-thiophenes. In the rest of the chapter they are labelled as TX_n, where T means thiophene, X denotes the total number of thiophene units constituting the molecule and subscript n the longest chain displaying exclusively α junctions.

The spider-like oligothiophenes are characterized by the "spider body" in which the α conjugation of the molecule is increased with increasing thiophene units, and by the "spider legs", namely 5-(2,2'-bithiophen)yl pendants for $T9_5$, $T14_6$, $T19_7$ and 2-thiophenyl pendants for $T5_3$, $T8_3$, $T11_5$, $T17_7$. All the compounds present unique α-conjugated main chain with increasing thiophene units up to 7 being the pendants thiophene rings and α-bithiophene moieties. All the molecular structures of TX_n is reported in Fig. 13.

Spider-like oligothiophenes appear easily accessible through a single reaction (a Stille coupling reaction), mostly involving commercially available, inexpensive starting materials. Thus, the synthetic burden is much lower than that generally required to prepare any of the oligothiophenes reported in literature. The electrochemical oxidative multiplication of these substrates can generate very large all-thiophene branched macromolecules. Simple dimerization produces compounds with a number of thiophene units much larger than the critical value at which the electronic conjugation properties tend to flatten.

Good regioselectivity can be expected in the electrochemical oxidative coupling, since, out of the many α positions of the terminal thiophene units, the two end α positions belonging to the main conjugated system should be preferred.

Moreover the high symmetry of these molecules (C_{2v} or C_{2h}) makes the α positions of all the systems homotopic, thus a very high constitutional order can be expected in the electrooxidative coupling process.

Considering all-thiophene pendant substitutes in thiophene β positions of the longest α-conjugated chain we can draw some considerations on how the TX_n structural characteristics of macromolecules are also responsible for functional properties displayed.

Firstly, this branching pattern allows the maximum structural flexibility, thus minimizing steric hindrance and enabling in principle the synthesis of much larger systems.

Secondly, and more importantly, the β branching positions disrupt the local π-electron excitation conjugation between adjacent all-thiophene moieties [44]. As a result, the individual α-conjugated chains are electronically decoupled from the resonative conjugation of the longest linear α-conjugated chain. This decoupling allows different chains to act as sites of a localized excitation, with a well-defined vibrationless electronic excitation energy. Due to the well-prescribed symmetry and the identical chain length of all the legs in this class of dendrimers, it seems likely that these molecules do not act as energy funnels. An exciton which may initially be localized on a particular thiophenic chain will not experience an energy gradient, and thus any movement to adjacent chains occurs via random hopping transfer events [45]. As we shall see only a spectroscopic investigation can reveal the correlation between structural arrangement and photophysical emission properties in this class of macromolecules.

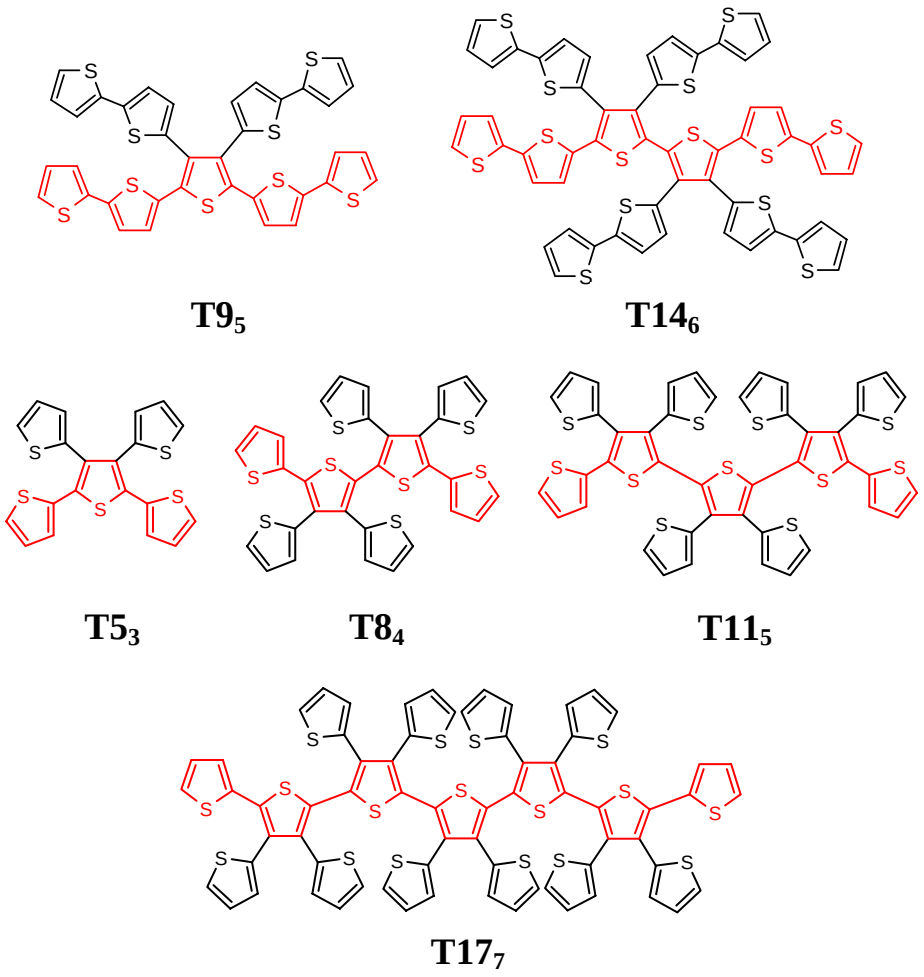

Figure 13. Molecular structures of TX_n spider-like oligothiophenes.

3.2.1 Spider-like oligothiophenes (TX_n) *dissolved in dilute in solution: structural, electronic and optical properties*

THEORETICAL ANALYSIS

To gain insight into the structural, electronic and optical properties of the investigated oligomers, Dr. Filippo De Angelis performed at the CNR in Perugia Density Functional Theory (DFT) and Time Dependent DFT (TDDFT) calculations on $T5_3$, $T8_4$, $T9_5$, $T11_5$, $T14_6$ [43] in order to investigate the effect of increased conjugation and branching. Hereafter we report briefly on optimized geometry structures and molecular electronic orbitals of spider-like oligothiophenes since these information are essential for a deep comprehension of the photophysical properties of TX_n molecules dissolved in solution.

The optimized geometry of $T9_5$ is reported in Fig. 14a along with selected geometrical parameters (Å). A schematic representation of the frontier molecular orbitals together with selected isodensity plots of such orbitals are reported in Fig. 15a.

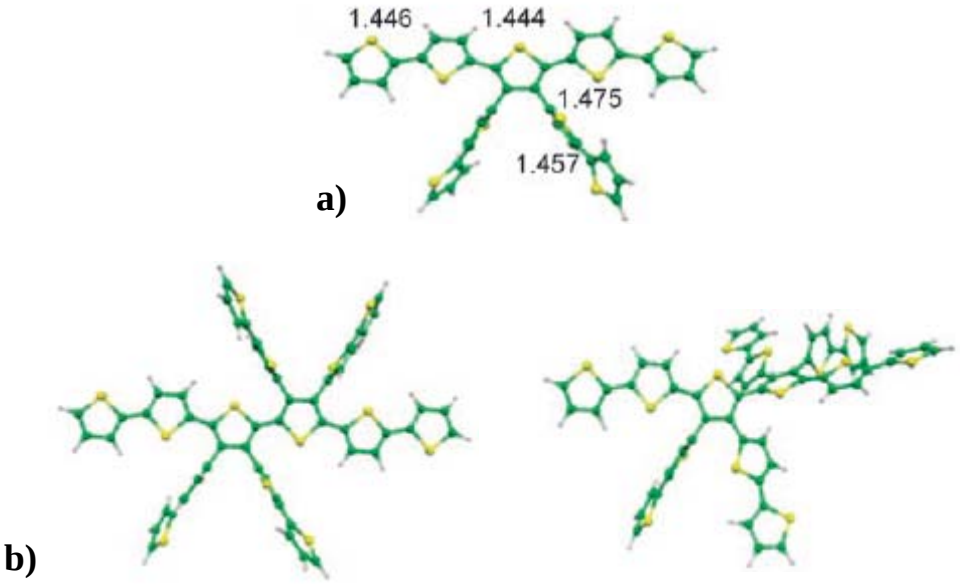

Figure 14 a) Optimized geometrical structure of $T9_5$ with bond lengths indicated in Å. b) Optimized planar and twisted structures of $T14_6$.

The optimized $T9_5$ structure shows an almost planar arrangement of the α-pentathiophene chain, with two "spider legs" lying orthogonal to the "body". The increased conjugation and charge delocalization across the α framework is reflected by the slightly shorter C-C distances interconnecting different thiophene units with respect to the sequences including α-β connections (1.446 vs. 1.451-1475 Å).

For $T14_6$, two almost isoenergetic conformers are calculated, corresponding to a planar and to a twisted configuration with respect to the central C-C bond (Fig. 14b). The twisted conformer, characterized by a twisting dihedral angle of 107.7 º, is the more stable structure, being 0.5 kcal/mol lower than the planar conformer (twisting dihedral angle of 176.6 º). The small energy difference between the two conformers suggests that a high degree of conformational fluxionality effectively exists.

Inspection of the calculated electronic structure of $T9_5$ (Fig. 15a) shows that the HOMO, found at -4.84 eV, is a combination of thiophene π bonding orbitals extending across the whole α-conjugated body. At lower energy (-5.52/-5.55 eV), the HOMO-1/HOMO-2 are a degenerate couple of π bonding orbitals confined within the two spider legs, while the HOMO-3 (-5.61 eV), almost degenerate with the HOMO-1/HOMO-2 couple, again extends on the α framework only. The HOMO and HOMO-1/HOMO-2 have therefore a similar character, although a different localization; the HOMO destabilization of ca. 0.7 eV compared to the HOMO-1/HOMO-2 couple is possibly due to the increased electrostatic repulsion arising from the proximity of five sulphur lone pairs in the former.

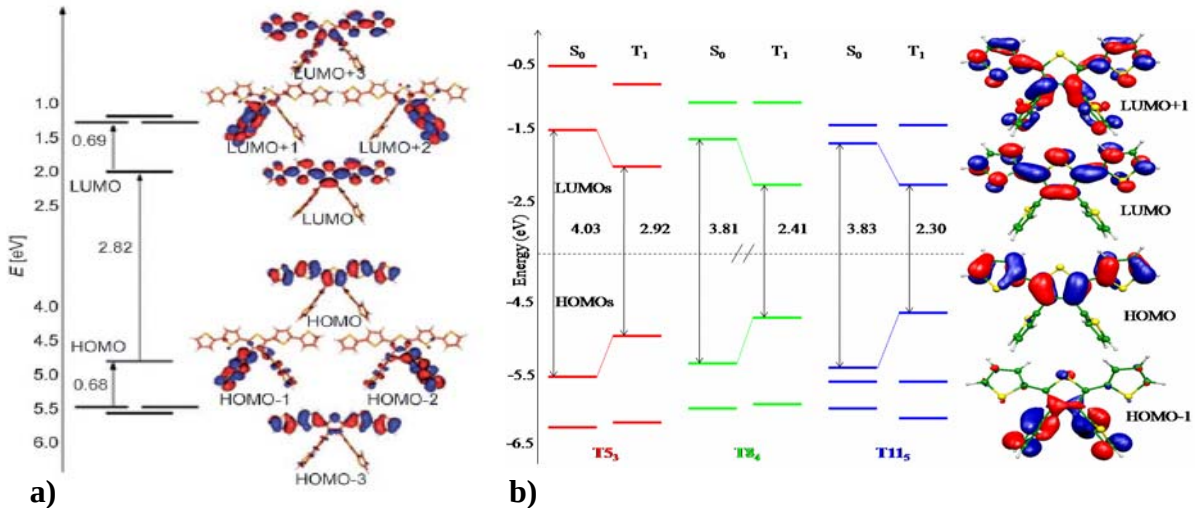

Figure 15. Schematic representation of the frontier molecular orbitals of a) $T9_5$, along with isodensity plots of selected orbitals and b) $T5_3$, $T8_4$, $T11_5$ along with $T5_3$ isodensity plots of selected orbitals.

The LUMO, calculated at -2.02 eV, is a combination of π* orbitals delocalized over the α framework, followed at higher energy (-1.33/-1.32 eV) by a degenerate couple of π* orbitals belonging to the β branches. Almost degenerate with the LUMO+1/LUMO+2 couple, the LUMO+3 is, instead, localized on the α framework. Interestingly, the HOMO/HOMO−1 and the LUMO/LUMO+1 splitting are comparable (ca. 0.7 eV).

The more stable $T14_6$ twisted conformer present an electronic structure similar to the $T9_5$ one, with an isolated HOMO lying at -4.92 eV and a LUMO at -1.95 eV. Notably, the planar $T14_6$ conformer shows a more positive HOMO energy than its twisted counterpart (-4.74 vs. -4.92 eV), while the LUMO energy is less sensitive to the twisting angle (-1.95 vs. -2.08 eV)

Also $T5_3$, $T8_4$ and $T11_5$ spider-like oligothiophenes are investigated by DFT and TDDFT.

The ground and lowest triplet excited state geometries were optimized without any symmetry constraints. While TDDFT calculations at the ground state geometry correspond to the absorption spectrum, the lowest triplet excited state geometries are taken here as an approximation to the lowest singlet excited state, so that to the emitting state.

The optimized geometry of the singlet ground state (S_0) and lowest triplet excited state (T_1) for the three species are reported in Fig. 16. All the optimized ground state structures show a considerable twisting of the thiophenes rings.

The optimized geometrical conformation of the ground state for $T8_4$ is in good agreement with the X-ray structure with the two central thiophene rings considerably twisted (SCCS dihedral angle of 58º). Increasing the number of thiophene units this behaviour is particularly evident: in the sterically crowded $T11_5$ structure the two thiophenes adjacent to the central ring are bound at SCCS dihedral angles close to 60º.

Considering the excited state structures, a general trend which can be outlined is the planarization of the thiophenes compared to the ground state with increasing the length of the α-conjugated backbone. As an example, in $T5_3$ the SCCS dihedral angle between the central ring and α-bound thiophenes increases from about 151° to 173º while in $T8_4$ this parameter reduces from 58 to 23º. A rationale for this behaviour can be found by inspecting the frontier molecular orbitals of the investigated species.

As in the case of $T9_5$, the $T5_3$ HOMO is a π orbital delocalized across the α-fused thiophenes system, while a series of orbitals at lower energies are localized on the β-linked rings (Fig. 15b). The LUMO is the π* counterpart of the HOMO, being therefore

delocalized across the fused thiophenes, while the LUMO+1 is delocalized throughout the entire molecular system. The HOMO-LUMO gap decreases from 4.03 to 3.81 eV in going from $T5_3$ to $T8_4$, while negligible differences are calculated between $T8_4$ and $T11_5$.

Most notably, dramatic energy differences in the HOMO and LUMO are calculated in going from the S_0 to the T_1 optimized geometries since the other frontier orbitals are much less sensitive to the geometrical changes. These orbital energy differences are clearly related to the planarization of the structures calculated in T_1 compared to S_0. The extent of LUMO stabilization is somehow a measure of the effective conjugation in these systems, which seems therefore to saturate in $T11_5$.

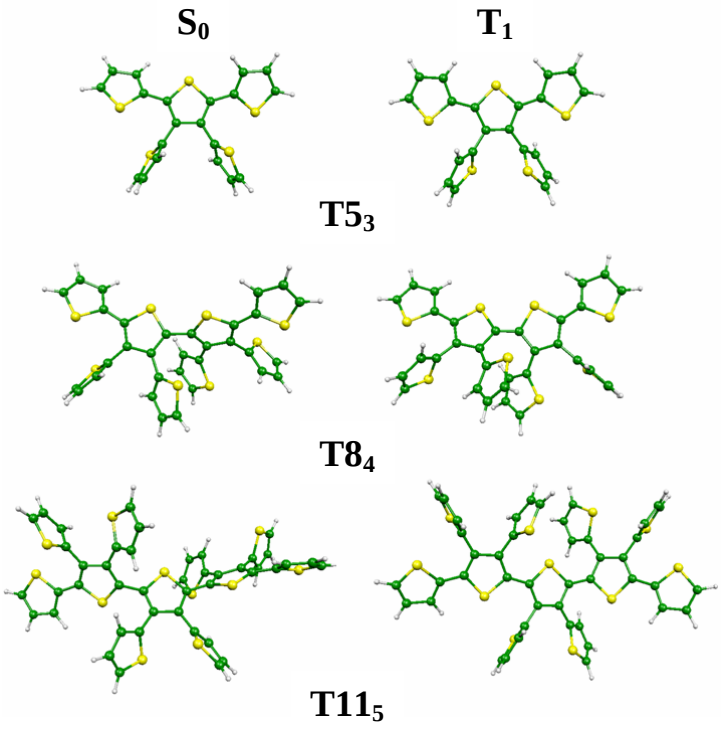

Figure 16. Optimized geometrical structures of the ground state (S_0) and of the lowest excited triplet state (T_1) of $T5_3$, $T8_4$ and $T11_5$. Frontier molecular orbitals for the ground state at the S_0 and T_1 optimized structures of $T5_3$, $T8_4$ and $T11_5$.

STEADY-STATE SPECTROSCOPIC PROPERTIES

For highlighting how the geometrical arrangement of the spider-like thiophenes influences their photophysical properties, we performed a detailed spectroscopic investigation on TX_n molecules dissolved in dilute solutions. Just for convenience, we

describe first the optical properties of $T9_5$ and $T14_6$ and then those of $T5_3$, $T8_4$, $T11_5$ and $T17_7$.

The spectra of $T9_5$ and $T14_6$ (and also those of $T19_7$ not reported here) display multiple absorption peaks at similar energetic positions, but with different relative intensities (Fig. 17). Differently from $T14_6$, $T9_5$ shows a well defined vibronic structure (i.e., 307, 345 and 419 nm). In particular, the absorption peak positions are in agreement with the observations on which the structural design of spider-like oligothiophenes was based. Firstly $T9_5$ and $T14_6$ show a π-conjugation efficiency equivalent to or even slightly higher than linear oligothiophenes having the same number of α-linked thiophene units (i.e., α-5T and α-6T). Secondly the energy gap values flatten when five α-conjugated thiophene units are present, independently on the whole number of thiophene units constituting the molecule. Indeed, $T9_5$ and $T14_6$ display nearly identical energy gap values, independently on the length of the main α-conjugated sequence (n_α = 5, 6) and on the overall number of thiophene units constituting the molecule (n = 9, 14). This can be explained by considering that an increased number of α–α linkages is associated to some distortion from coplanarity, as suggested by the theoretical calculations performed on $T14_6$.

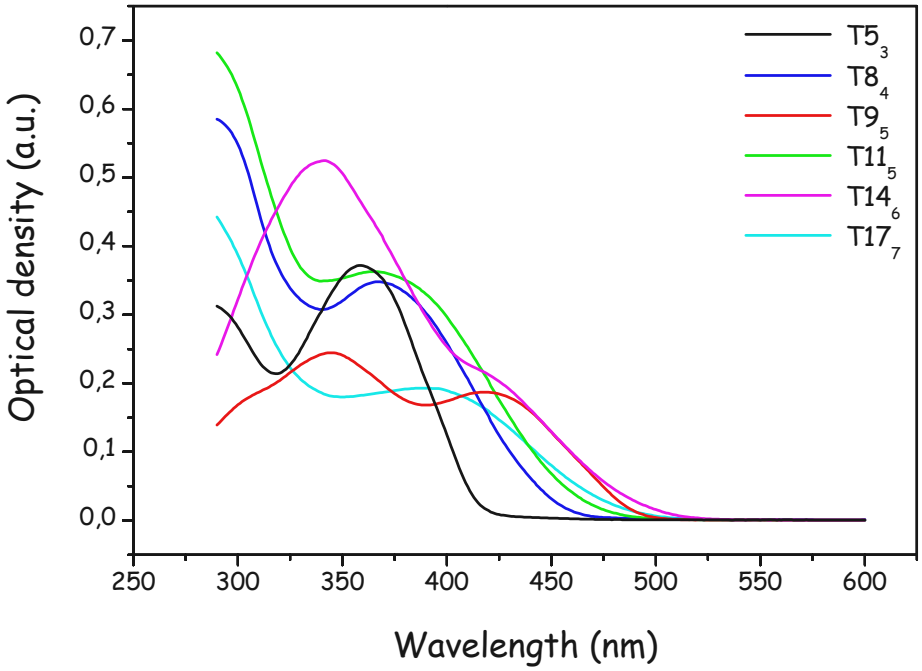

Figure 17. Absorption spectra of TX_n in 10^{-5} M CH_2Cl_2 solutions.

On the other hand, the band occurring at about 345 nm could be assigned to absorptions involving the spider legs, as suggested by the extinction coefficient values e (24500 for $T9_5$, 52 500 for $T14_6$ and 68 700 for T197) which are linearly dependent on the number of bithienyl pendants present in the molecule (2 and 4). The extinction coefficient is known to be dependent upon the number of the thiophene units also in linear α-oligothiohenes (12500 for α-2T, 26 600 for α-4T and 59 700 for α-8T) [46].

Given that the $T9_5$ HOMO and the LUMO are largely delocalized on the main α-conjugated sequence, the lowest energy transition is readily assigned to a π–π* excitation within the body framework. The band experimentally found at 345 nm appears to be related to two transitions of different character, calculated at 364 and 322 nm, involving both the body and legs framework. The band experimentally found at 307 nm is finally calculated to be due to two almost overlapping transitions calculated at 309 and 308 nm; the most intense transition at 308 nm takes place within the legs framework. It is interesting to note that in α-2T the main transition happens at 306 nm. The calculated vertical transitions are in fair agreement with the experiments: in particular, the involvement in the lowest absorption band of the α-conjugated backbone is consistent with the experimental observation that this band is less affected by increasing the number of spider legs than the higher energy second feature. On the other hand, the fact that the second absorption peak takes place within the spider legs is consistent with the experimental increased intensity of this feature with increasing the number of legs.

The TDDFT calculations performed on the two $T14_6$ conformers reveal a pattern of vertical excitations similar to that calculated for $T9_5$. In particular, the calculated lowest excited state corresponds to an intense HOMO–LUMO transition in both cases, but while for the $T14_6$ twisted conformer this transition is calculated at 2.55 eV (similar to the lowest transition in $T9_5$), for the planar conformer a red-shift of the lowest excitation energies is calculated, which brings its value to 2.39 eV. This result is consistent with the increased conjugation of the planar conformer. While both the calculated values are red-shifted compared with the experiment, the fact that for the most stable twisted conformation we calculate a lowest transition at essentially the same energy as that of $T9_5$, suggests that the twisted conformer dominates the absorption spectrum.

$T5_3$, $T8_4$, $T11_5$ and $T17_7$ absorption spectra are unstructured, broad and display absorption maximum peak positions redshifting with increasing the number of thiophenes moieties (358, 368, 371 and 392 nm respectively). Differently from $T9_5$ and $T14_6$, molar

extinction coefficients only slightly increase with molecules dimension, even decreasing in the case of $T17_7$.

The structural arrangement of these molecules display that all the β positions of the thiophene units in the longest α-conjugated chain are saturated. As the optimized geometries of the singlet ground state show, the β position substitutions allow for distortions from a planar configuration due to orientational flexibility. As we already mentioned this nonplanarity enables the synthesis of much larger systems, by overcoming steric hindrance but it decouples electronically the resonative conjugation among different branches, introducing a kind of local disorder which localizes the π-electron excitations of the thiophenes rings [47].

It is well known that any delocalization of the electronic excitation over a larger molecular domain should reduce its energy [47]. The slight reduction in energy can mean only the absence of delocalization, i.e., the presence of localization. So it is interesting to note that the maximum absorption peak of α-3T is located almost in the same position of $T5_3$ (356 nm and 358 nm respectively) highlighting that the absorbing moiety in the branched molecule is the longest α-conjugated chain. Nevertheless, the absorption peaks for $T8_4$, $T11_5$ and $T17_7$ do not correspond to those of the α-oligothiophenes 4T, 5T and 7T since the increasing non-planarity of the molecule with the increasing size allows the delocalization of the excitation over highly torsional conjugated branches. Also the enhancement of the peaks full width at half maximum (FWHM) with the molecular size (from 66 to 106 nm) corroborates this hypothesis: a distribution of conjugation chain lengths in the molecules account for broad absorption spectra.

Furthermore, such localized excitations should be created independently via photon absorption, resulting in a molar absorbance that would increase monotonically with size. Differently from $T9_5$ and $T14_5$, the molar absorbance is almost invariant from $T5_3$ to $T11_5$ and even diminishes for $T17_7$. This behaviour reveals that the periphery thiophenes unities decorating in β positions the core α-α conjugated chain weakly participate to the absorption process. So the oscillator strength of the transition is mainly correlated to the transition dipole moment of the longest conjugated chain which decreases as the molecule becomes less planar when the molecular size increases.

It is worthwhile noting that even if $T9_5$ and $T14_6$ can be considered as $T5_3$ and $T8_4$ to which a thiophene unit is added in α position to all the periphery thiophenes, they present absorption features completely different. Not taking into account the steric hindrance and

non-planar arrangement of the specific molecules, with the increasing molecular size the $T9_5$ and $T14_6$ show pinned absorption peaks and increasing molar absorbance while the $T5_3$ and $T8_4$ absorption peaks redshift and the molar absorbance is almost invariant. These observations reveal that for $T5_3$ and $T8_4$ (as well as $T11_5$ and $T17_7$) the electronic excitation is mainly delocalised over increasingly larger molecular domains, while for $T9_5$ and $T14_6$ the excitation is localised in specific branches of the molecules.

In dendrimer structures [45] the localization of the excitation is the necessary condition for an efficient energy transfer or hopping form the periphery (shorter conjugated branches) to the core (longer conjugated branches) of the molecule so that dendrimers can act as an efficient light-harvesting material by funnelling photons spread in a broad energy range to the energy trap at the locus.

Nonetheless, we have to pay attention to the fact that the spider-like oligotiophenes cannot defined directly as dendrimers since their structures cannot be described by Caylay tree-like topology [48]. So an exhaustive description of TX_n molecules has to take account both of localization and delocalization of the excitation modulated by the steric congestion and intermolecular interactions.

The optical emission properties can be described within this complex frame. In Fig. 18, we report the PL spectra of TX_n molecules dissolved in 10^{-5} M CH_2Cl_2 solution. All TX_n are excited around their absorption maxima (for $T9_5$ and $T14_6$ the highest energy peaks).

All the PL spectra are broad, featureless and each curve can be well interpolated by three Lorentzians. The fact that PL spectrum of α-3T is structured (almost two vibronic peaks present) and redshifted with respect $T5_3$ one, indicates that even for the simplest molecule of the series the emitting state is only partly related to the longest α-conjugated branch and that the torsional motions of the thiophenes moieties broaden the emission spectrum.

As theoretical analysis on the optimized geometries of the emitting state has highlighted, the energetically stable configurations $T8_4$, $T9_5$ and $T11_5$ present the longest α-conjugated chain planar: this structural rearrangement would induce a stabilization in emission energy due to a more delocalized electronic excitation. Indeed, the emission peaks generally redshift with increasing the length of the α-conjugated chain.

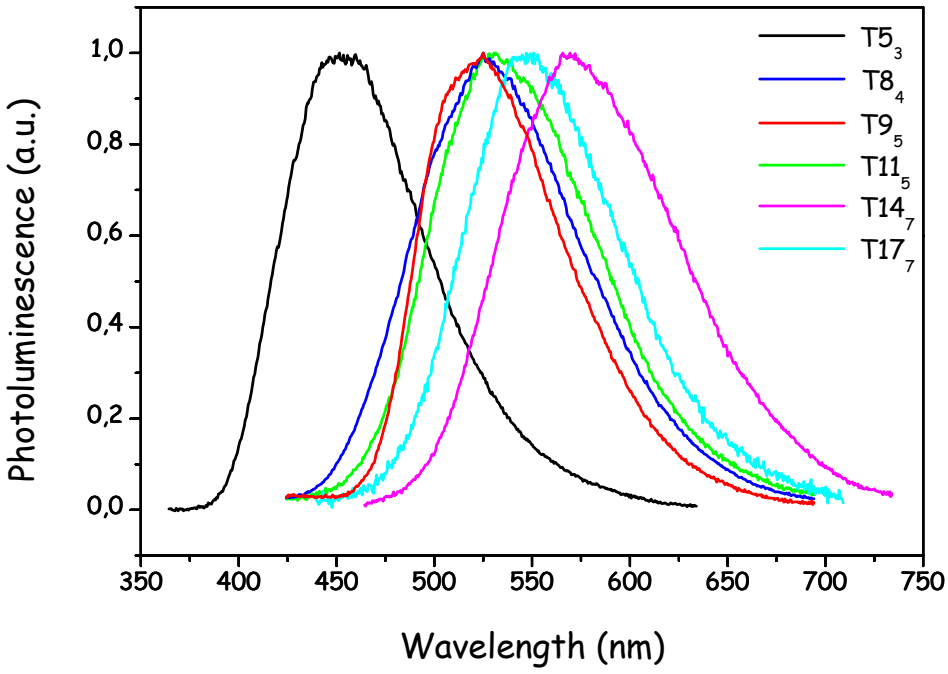

Figure 18. Normalized photoluminescence spectra of TX_n in 10^{-5} M CH_2Cl_2 solutions.

Also $T14_6$ can be inserted within this trend, even if its energetically stable conformer is twisted. In fact it is the planar conformer that presents a non-negligible red-shift of the lowest excitation energy compared with $T9_5$ (~ 0.15 eV), that nicely compares with value experimentally observed in emission.

Anyway $T9_5$ and in particular $T17_7$ are exceptions since their maximum emission wavelengths are blueshifted with respect those of $T8_4$ and $T14_6$. We can advocate that in those molecules the emission properties result from two opposite contributions: the increased α-conjugation that relaxes energetically the molecule and the high steric hindrance that enhances the structural rigidity.

Also FWHM values corroborate this hypothesis since $T9_5$ and $T17_7$ present the lowest ones apart from $T5_3$. Since at room temperature FWHM can be taken as a rough measurement of inhomogeneous broadening of the emitting state, intramolecular static disorder seems to be lowered in these molecules due to structural rigidity.

EXCITON DYNAMICS

Considering PL time-resolved measurements reported in Fig. 19, the molecules from $T5_3$ to 14_6 present time decay profiles around emission maximum that can be well fitted with a mono-exponential curves. Instead $T17_7$ temporal decay is well-fitted by a bi-

exponential curve with an initial time constant of around 136 ps merging into a tail of 256 ps, being the amplitude of the slower component the larger one (A~0.6).

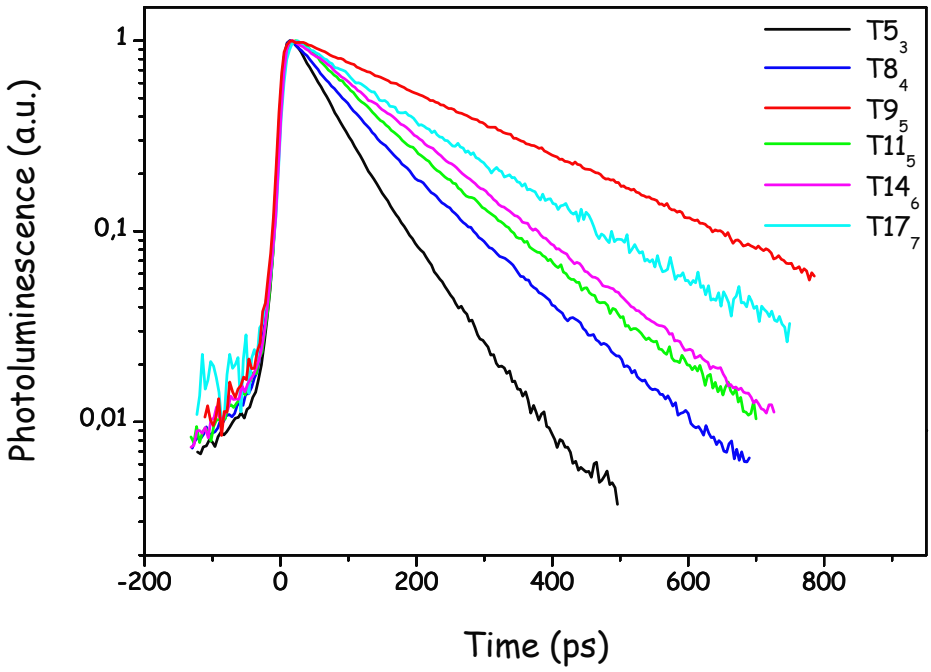

Figure 19. Photoluminescence time decay of TX_n in 10^{-5} M CH_2Cl_2 solutions at the emission maxima. The intensity is normalized at T = 0.

For $T5_3$, $T8_4$ and $T11_5$ single-lifetime constants (Tab. 1) generally increase with the length of the core α-α conjugated chain as it is expected when the planar configurations are more stable energetically. Generally speaking delocalisation of the excitation could contribute to a significant hindrance to photoisomerization (conformation) process thus leading to elongation of the fluorescence decay time [49]. Nevertheless, as it can be inferred from Tab. 1, the fast relaxation of the excited states of all the spider-like oligothiophenes can be referred to the large number of non-radiative pathways activated by the complex architecture of these macromolecules.

$T5_3$	**$T8_4$**	**$T9_5$**	**$T11_5$**	**$T14_6$**	**$T17_7$**
73 ps	110 ps	269 ps	130 ps	154 ps	136 ps 256 ps

Table 1. Lifetime constants of **TX_n** in 10^{-5} M CH_2Cl_2 solutions.

Apart from increasing the number of light-adsorbing moieties, increasing dendrimers molecular size can also increase the number non-radiative processes that may intervene to dissipate the excitation energy. Thus, PL intensity and lifetimes are reduced with increasing molecular size.

In $T14_6$ the increase of the branching in β positions clearly enhances molar absorbance by means of excitation localization but also diminishes PL lifetimes with respect to $T9_5$. In order to gain a deep insight into $T14_6$ exciton dynamics the temporal PL red-shift is monitered by comparing the emission collected within the first 15 ps after excitation with the almost steady-state PL spectrum (Fig. 20a). As time after excitation increases emission spectrum FWHM increases from 108 to 110 nm and maximum emission wavelength red-shifts of around 9 nm.

Time decay profiles are always well-fitted by mono-exponential curves regardless of the wavelength emission and lifetime constants slightly decrease with emission energy. Moreover the PL spectrum collected 15 ps after excitation can be well fitted by a single lorenztian curve.

The observation at longer wavelengths of very rapid fluorescence risetime and the high degree of conformational fluxionality of $T14_6$ can indicate that conformational excited states variation is at the origin of the macromolecule dynamics. Unfortunately risetime constant is comparable to time resolution of our experimental set up so that we cannot investigate any further the intramolecular energy-relaxation processes.

Thus, the time-dependent spectral shift seen in Fig. 20 implies either that there are small variations in the radiative lifetimes of the ensemble of disordered oligomer molecules dispersed in solution or that there is a intramolecular relaxation of the excited molecules that takes place at the time scale of the PL decay [50].

Since broad, unstructured and red-shifted emission spectrum could possibly be due to the formation of excimers in solution [51], we performed PL measurements on $T14_6$ solution at 10^{-6} M concentration. The presence of excimers can be ruled out because PL spectrum presents the same structureless emission, peak position, FWHM and single lifetime constant of solutions with 10^{-5} M concentration.

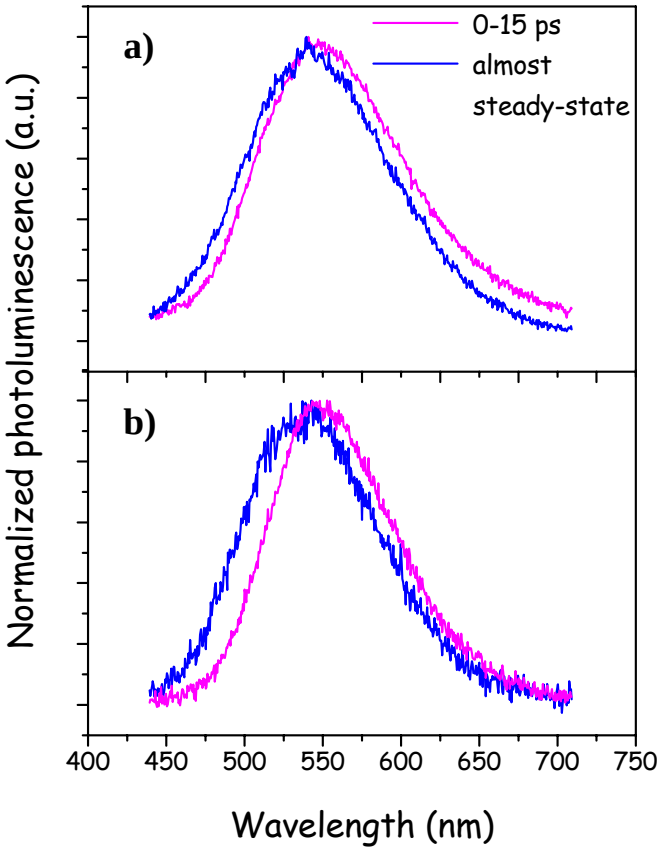

Figure 20. Photoluminescence spectra for $T14_6$ (a) and $T17_7$ (b) within 15 ps-integration time after excitation and at almost steady-state condition.

In Fig. 20b we report the temporal dynamics of $T17_7$ comparing time-resolved PL spectrum collected 15 ps after excitation with an almost steady-state spectrum. As it can be seen, PL emission spectrum red-shifts of about 11 nm with a reduction of FWHM of about 8 nm.

Differently from the other spider-like oligothiophenes, $T17_7$ temporal decay can be well-fitted by a bi-exponential curve revealing that apart from a vibrational relaxation a more complex process is taking place. We find out that in the high-energy portion of the decay spectrum the lifetime constants values (146 ps and 27 ps) are smaller than the ones reported for the emission maximum decay. Moreover the low-energy decay profile can be described by a mono-exponential radiative de-excitation presenting a 200 ps lifetime constant (magenta decay curve in Fig. 21) together with initial rise (~ 7 ps) in intensity at early times reaching a maximum value, whereupon the signal starts its natural decay (blue decay curve in Fig. 21).

We propose that a Coulombic process of excitation energy transfer from longer to shorter conjugated chains takes place within the complex architecture of the molecule after excitation. In particular Coulumbic theory in its simplest form such as Förster theory (see § 1.2.4) can describe $T17_7$ radiative relaxation since the high-energy decay can be well-fitted by Förster decay function.

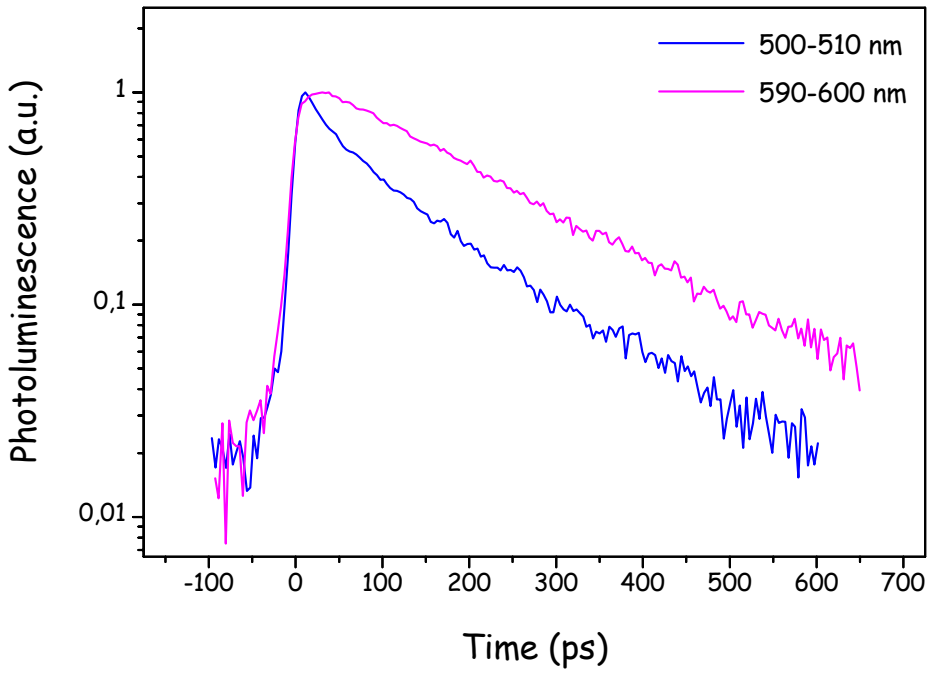

Figure 21. PL time decay of $T17_7$ in 10^{-5} M CH_2Cl_2 solutions in the emission spectral ranges 500-510 nm (*donor* rise curve) and 590-600 nm (*acceptor* decay curve). PL intensity is normalized at T= 0.

Clearly in spider-like oligothiophenes we cannot identify simply the donor as the periphery moieties and the acceptor as the core locus as reported in many dendrimeric systems [45] because TX_n are all-thiophene molecules and the energy hierarchy is related only to the lengths of α-α conjugation chains.

Nevertheless we suppose that the energy migration happens by an excitonic-type coherent transport mechanism and not by energy incoherent hopping through thiophene branches since we observe a time-dependent reduction of the spectrum FWHM.

Depolarization fluorescence measurements could give a complete and clear insight into fast kinetics related to the energy-redistribution (migration) process around the branching centers, which results from strong intramolecular interactions.

3.2.2 Photophysical and morphological investigations on 5-(2,2'-bithiophen)yl thiophene ($T9_5$) *and 5-(2,2'-bithiophen)yl 2,2'-bithiophene* ($T14_6$) *thin films*

In the previous paragraph we investigated the spectroscopic features of spider-like oligothiophenes dispersed in dilute solutions. However, many applications such as light emitting diodes and photovoltaic cells require thin-films of the active materials to be prepared. Thus, to better understand the potential use of the spider-like oligothiophenes in opto-electronic devices realization, it is fundamental to understand their excited-state properties in solid.

In solid-state dendrimers show fascinating structure and unique properties such as their globular shape, highly controlled size, radially controlled chemical composition, multivalent periphery, and variable inner volume [52]. Self-assembly of dendrimers with or without guest molecules at the ensemble [53] as well as the single molecule level [54] is of special interest because this creates a wide collection of novel structures and surfaces with higher complexity and promising properties.

The self-assembly of dendrimers into mono- or multilayers on a solid substrate through electrostatic

Interactions [55], polydentate interactions [56], or covalent bonding [57] has been investigated. The self-assembled dendrimer mono- or multilayers were found to exhibit unique properties and potential applications such as their use as nanoreservoirs [58], as molecular gate membranes [59] and as effective resists for high-resolution lithography [57].

Hereafter we report on the spectroscopic measurements and the morphological study with confocal laser scanning microscopy (CLSM) and atomic force microscopy (AFM) which we performed on $T9_5$ and $T14_6$ systems in different solid-state aggregation forms such as molecular thin-film, polymer film and powder.

Molecular thin-films are obtained by wet deposition processes from 1 g/l dichloromethane solutions. $T14_6$ thin-films are spin-coated on a quartz substrate for 45 s at 1000 rpm, while $T9_5$ thin-films are obtained by drop-casting since the low wettability of the spin-coated film on the quartz substrate. After deposition the samples are heated at 60°C for one hour for evaporating completely the solvent. Molecular thin-films are micrometer-thick and show morphological inhomogenities that can be observed by eyes.

Polymer films are deposited on an ITO substrate by repeating voltammetry cycles around the first oxidation peak of the molecules dispersed in a 2.3×10^{-3} M dichloromethane solution with TBAP 0.1 M as supporting electrode. Indeed $[T9_5]_m$ and $[T14_6]_m$ polymer films show good mechanical properties and are very stable even in the neutral state and after one-month exposure to air. The former is deposited with higher efficiency, resulting in a thicker film.

STEADY-STATE SPECTROSCOPIC PROPERTIES

In Fig. 22 TX_n absorption spectra in thin films are reported together with those in dilute dichloromethane solution for comparison. The absorption spectra of the both $T9_5$ and $T14_6$ thin films are found to be quite similar in shape to those in solution since the main spectral features observed in solution are also observed in thin films. Indeed, while $T9_5$ absorption spectra seem to be more structured in solid-state, $T14_6$ vibronic progression is overwhelmed at the low energy by light scattering that broadens the entire spectrum possibly due to surface inhomogenities and film roughness.

Both the molecular film absorption spectra present a 20 nm red-shift which is attributed, in part, to the increased polarizability of the surrounding medium in thin film [51] and more likely to the fact that the emitting chromophores adopt a broader distribution of conformations in solid state [60].

The UV/Vis absorption spectra of $[T9_5]_m$ and $[T14_6]_m$ films shift to significantly longer wavelengths with respect to the corresponding TX_n molecular film, thus confirming that coupling has indeed occurred resulting in a more extended π–conjugated system. This conjugation improvement is significantly higher than the expected one considering linear oligomers in solution; this points to a solid-state effect, possibly connected with π-stack interactions between adjacent molecules at short interchain distances in the conducting film [61]. As it can be seen from the spectra $[T9_5]_m$ presents the onset of the optical absorption at the longest wavelength, so that it has the more extended conjugation. Investigation on the regiocemistry of the electrochemical oxidative coupling [43] reveals that $[T9_5]_m$ has the highest α–α constitutional order and then a higher conjugation degree.

Moreover we observe that the absorption maxima of both the polymers are higher than that of polyalkylthiophenes (434 nm) [62], suggesting that a dendritic hyperbranched polythiophenes formation is favoured over a disordered 3D growth.

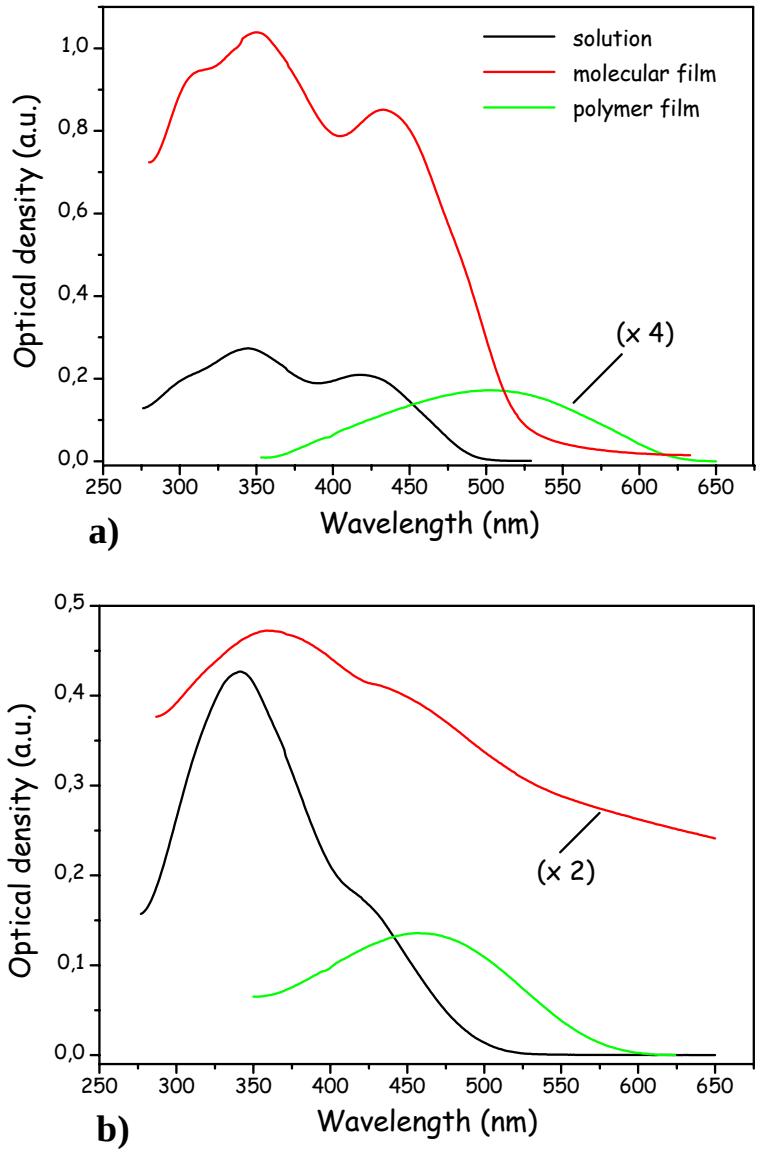

Figure 22. Absorption spectra of $T9_5$ (a) and $T14_6$ (b) dispersed in 10^{-5} M CH_2Cl_2 solutions, deposited as films by spin-coating from solution and electrodeposited as polymers on ITO.

Steady-state PL measurements (Fig. 23) show that there are no significant differences in the emission properties between dendrimers in solution and in thin films. Indeed, exciting at 385 nm the spectra are broad, almost unstructured and featureless. The remarkable spectroscopic features that vary extensively according to the aggregation state of the materials is the maximum peak position and FWHM values.

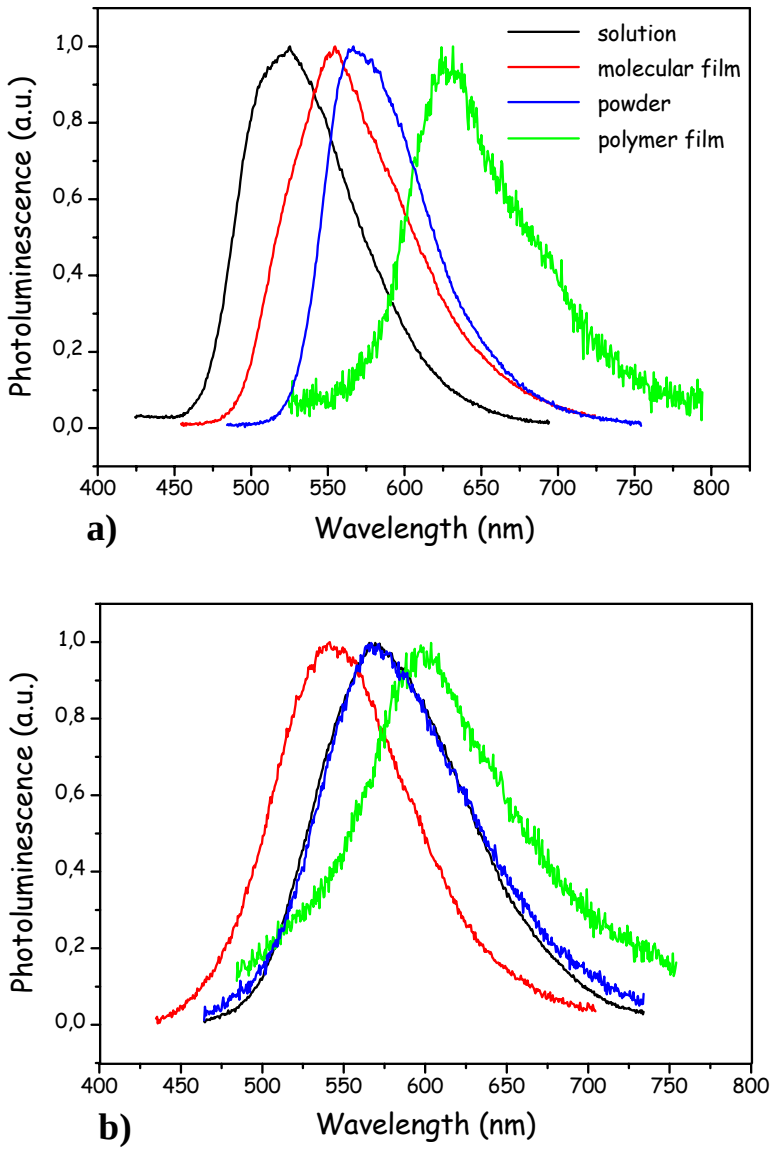

Fig. 23 Normalized PL spectra of $T9_5$ (a) and $T14_6$ (b) dispersed in 10^{-5} M CH_2Cl_2 solutions, deposited as films by spin-coating from solution, electrodeposited as polymers on ITO and in powders.

Typically a comparison with the PL properties of linear conjugated polymers is often used for getting insights in dendrimers conformational properties. PL spectra of conjugated polymer thin films often show a relatively sharp component that is reminiscent of conjugated polymer spectra in solution, as well as a broad red-shifted component due to aggregate species. The relative fraction of solution-like and aggregate species depends, in part, on the 3D conformation of the conjugated polymer. However the specific $T9_5$ and $T14_6$ spectroscopic properties in solid-state allow us to describe better conjugated spider-like oligothiophenes as discotic 2D conjugated macromolecules.

In particular we suppose that the planar 5-thiophene-member π-conjugated chain in $T9_5$ (see previous paragraph) facilitates the intermolecular electronic interaction by forming a tight-packing geometry of interchain π stacked aggregates. Indeed the PL spectrum in solid state is redshifted of about 30 nm and broadened of about 5 nm with respect to the one in solution as it is expected. Moreover, as it is reported in Tab. 2, PLQY five-times reduction from solution to thin-film can also be attributed to molecular interaction since the disc-like structure of $T9_5$ molecules can promote close and parallel stacking in solid state.

It is likely that a slight redistribution of the weight of the vibronic peak intensity is present in the thin-film PL spectrum, which can be considered a clear signature of interaction between nearest neighbours molecules in solid-state. For example, it can be expected that the excitons produced by direct photoexcitation in molecular aggregate are likely to migrate readily to the lower energy trapping sites [51]. However, only low temperature PL measurements can clearly reveal the vibronic progression and estimate the residual inhomogeneous broadening due to the distribution of local environments that results from the macromolecules packing in the thin-film.

Nonetheless we note that in solid-state the slight increase of the FWHM, which is a rough measurement of inhomogeneous broadening of the emitting state, and the relatively high PLQY with respect to typical values reported for linear thiophene-derivative molecules in thin-films (less than 1%) can highlight that the molecular aggregates extend to few molecular units and that the exciton dynamics is mainly intramolecular.

	Solution	**Film**
$T9_5$	10 %	2 %
$T14_6$	4 %	1.5 %

Table 2. Photoluminescence quantum yields of $T9_5$ and $T14_6$ in 10^{-5} M CH_2Cl_2 solutions and deposited as films from solution.

PL powder spectrum is again structureless, but less broad and more redshifted with respect to solution and molecular film PL spectra. Although the polarizability of the surrounding medium around the emitting moieties slightly changes according to the aggregation state, the spectroscopic features of the emission of $T9_5$ in powders can point out that also in drop-cast films higher intermolecular interaction and long-range π–π stack order can be obtained if the deposition conditions are properly optimized.

Differently from $T9_5$ molecular film, $T14_6$ molecular film spectrum displays a blueshift of about 26 nm with respect to the solution spectrum together with a reduction in FWHM of about 8 nm. In both solution and molecular film the PL spectra are broad and completely structureless.

At first by referring to the conformation structure of the two molecules we can say that the globular shape of the larger $T14_6$ may hinder the formation of aggregates compared to the case of the more rigid structure of $T9_5$, in which the planar α-conjugated chain can more tightly pack leading to stronger intermolecular interactions. Moreover from the theoretical calculations we reported in the previous paragraph, more stable structure of $T14_6$ is a twisted conformer in which the α-conjugation is severely reduced and the steric hindrance enhanced. Differently from solution, in solid state the bulky twisted conformer of molecules cannot easily energetically relax into the planar configuration so causing the intense blue-shift in emission with respect to the solution one. So the FWHM reduction can be explained as a lack of rotational rearrangement for the molecules in the solid state aggregates.

The PL spectrum profile is invariant from solution to thin-film so indicating that the emission is due to a distribution of almost independent different emitting states. The fact that powder and solution $T14_6$ PL spectra are almost identical points out that energy relaxation due to the extend π delocalization induced by a more planar structure is possible also in solid state aggregates. Clearly molecular film and powder emission properties can be compared since the polarizability of the two media can be considered almost identical.

In solution the polar solvent used (CH_2Cl_2) strongly stabilizes the excited state which has a dipole moment larger than the ground state one therefore lowering its energy and red shifting the emission peak. But the conformer flexibility of $T14_6$ molecular structure in solution causes a severe reduction of PLQY with respect to $T9_5$ since the enhanced internal conversion processes typically associated to extended macromolecules.

In solid state, instead, emission efficiency of the two materials is identical so indicating that the presence of significant non-radiative relaxation pathways such as energy migration to quenching sites within the film, and energy transfer to aggregate states that are only weakly emissive.

It is plausible that in $T9_5$ thin-film the tight packing leads to a strong intermolecular interaction between the exposed core states, i.e. the longest conjugation chains, while in $T14_6$ thin-film the steric effects on one side reduce the conjugation length and attenuate the

π delocalization and on the other side induce a physical separation among the emitting moieties due to the increased branching. It would be interesting to perform a spectroscopic study on a hyper-branched compound such as $T17_7$ in solid state for verifying this hypothesis.

Considering the polymer PL spectra, the maximum emission wavelengths of $[T9_5]_m$ and $[T14_6]_m$ are located at about 630 and 610 nm, respectively, suggesting a more extended α- conjugation in $[T9_5]_m$ with respect to $[T14_6]_m$. In particular, in $[T9_5]_m$ PL profile an enhancement of the longer-wavelength component is clearly visible with respect to the molecular thin-film one. This spectroscopic feature can indicate that in polymer more efficient exciton migration and trapping processes are present due to the complex spatial arrangement of the conjugated chains.

$[T14_6]_m$ emission profile is as broad as the powder one with a red-shift in the PL maximum wavelength of about 20 nm. It is likely that the planarization of the conjugated backbone induced by the polymerization leads to the increase of the conjugation length and thus to a lower bandgap, but the larger branched structure introduces a local environmental disorder that prevents the reduction of the FWHM.

EXCITON DYNAMICS

Time-resolved PL measurements provide information regarding the excited state dynamics in spider-like oligothiophenes thin films. In Fig. 24 we report the fluorescence decay of $T9_5$ and $T14_6$ in dilute solution, as molecular films, as powders and as electro-deposited polymers. The decay signal is collected at the emission maxima.

In the previous paragraph we have shown that PL decay of $T9_5$ and $T14_6$ dissolved in dichloromethane are adequately fitted by a single exponential function whose lifetime constants are quite short (Tab. 3). The extracted natural radiative lifetimes indicate that in each case, the radiative transitions are fully allowed, consistent with the large molar decadic extinction coefficients. In particular $T14_6$ in solution presents higher absorbance and longer natural radiative lifetime but lower PLQY with respect to $T9_5$ highlighting that many intramolecular non-radiative channels such as ultrafast spectral diffusion are activated. For example the internal conversion tendency can be reduced slightly enhancing the rigidity of the molecule by means of chemical substitution of bulky side chains.

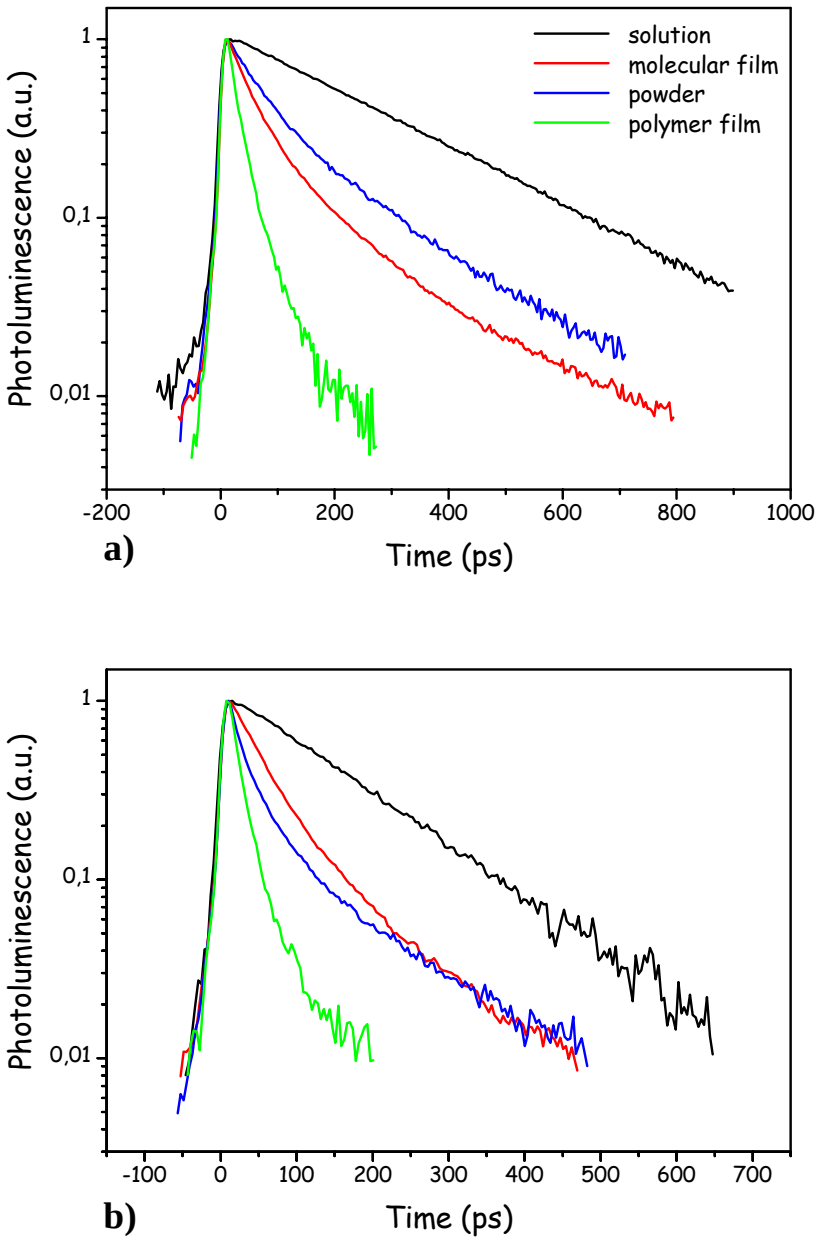

Figure 24. PL time decay of $T9_5$ (a) and $T14_6$ (b) dispersed in 10^{-5} M CH_2Cl_2 solutions, deposited as films by drop-cast ($T9_5$) and spin-coating ($T14_6$) electrodeposited as polymers on ITO and in powders. The signal is collected at the emission maxima and is normalized at T = 0.

	Solution	Film	Powder	Polymer
$T9_5$	269 ps	38 ps, 152 ps	46 ps, 178 ps	14 ps, 52 ps
$T14_6$	154 ps	40 ps, 126 ps	18 ps, 89 ps	13 ps, 60 ps

Table 3. Lifetime constants of $T9_5$ and $T14_6$ in 10^{-5} M CH_2Cl_2 solutions, deposited as films by drop-cast ($T9_5$) and spin-coating ($T14_6$) from solution, electrodeposited as polymers on ITO and in powders.

In solid state, PL dynamics are highly non-exponential. Decay fitting based on a sum of two exponential functions can well reproduce the decay profiles, whose lifetime constants values are reported in Tab. 3. Curve fitting based on a sum of exponentially decaying components may not accurately describe the complex excited state dynamics of the molecular and polymer thin films [63], nevertheless they are useful in providing a measure of the PL decay rate. A major fraction of the $T9_5$ and $T14_6$ molecular thin film PL decay (almost 80%) occurs at the same rate which is significantly faster than the decay rate in solution. The fast relaxation may reflect a distribution of different emitting states, excitation hopping between macromolecules (similar to the hopping of excitons in linear conjugated polymer thin films) [63], as well as migration to quenching sites. There is also a longer residual component in the tail part of the emission which relaxes radiatively in the same timescale solution of the solution decays. This longer-time component likely reflects the relaxation from weakly emissive aggregate states which we exclude to be due to excimer formation. Indeed, the ground-state absorption is clearly responsible for the broad-band emission and the lifetime constant of the this component is shorter than the non-aggregated emission band of the molecules in dichloromethane solutions.

In polymers emission dynamics the longer-time component disappears since the PL decay is dominated by a very fast quenching (about 50 ps) due to the many non-radiative channels activated at room temperature in agreement with the almost negligible PLQY.

A further insight in the processes that dominate the exciton dynamics in molecular films can be inferred by comparing an almost steady state emission spectrum with the emission spectrum collected in a 4 ps-wide temporal window after the pump excitation (Fig. 25).

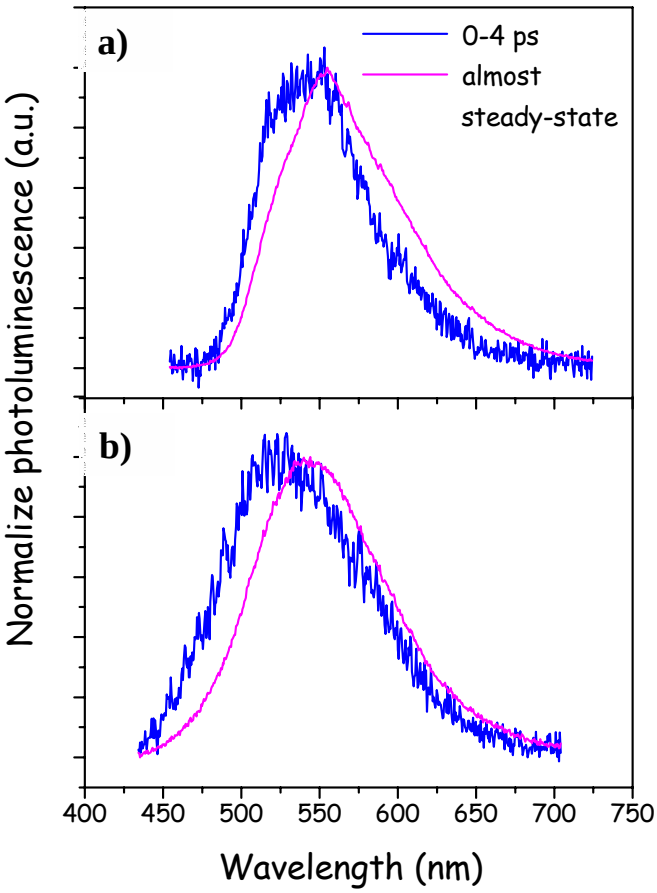

Figure 25. PL spectral red-shift for $T9_5$ (a) and $T14_6$ (b) deposited as films by drop-cast ($T9_5$) and spin-coating ($T14_6$) in the first 4 ps after excitation and in almost steady-state.

In both the molecular films, the non-exponential decay correspond to a time-dependent spectral red-shift of the emission spectrum (15 nm for $T9_5$ and 20 nm $T14_6$ thin-film). Time-evolution of $T9_5$ emission profile highlights that FWHM increases and the high-energy shoulder of the early-time spectrum is almost suppressed in favor of low-energy tail of the steady-state spectrum. Moreover the early-time spectrum resembles the solution steady-state one. It is likely that excitons after being formed in small domain of weakly interacting molecules migrate towards lower-energy domain of the aggregate where the π delocalization is higher since the stronger molecule interaction. The time elapse between the early-time and the almost steady state spectra is long enough for guaranteeing a significant contribution to the decay, even if we are not able to define which specific process (hopping, energy transfer…) is responsible for the migration.

$T14_6$ dynamics seems to evolve differently. As time after excitation increases PL spectrum FWHM diminishes from 102 nm to 97 nm while the emission profile is well-fitted by a

Guassian curve at the early times and by a Lorentzian curve in the almost steady-state case. It is plausible that for $T14_6$ molecular film the major non-radiative quenching mechanism is the migration to extrinsic, impurity-related or traps-related centers [64]. Given the high site-specific disorder in the thin-film, excitons are strongly localized due the exciton coupling with the local surrounding, hopping from site to site through incoherent exciton migration.

When the hopping time is shorter that the time constants of the local potential fluctuations, the exciton line shape becomes more Lorentzian in character and narrower with homogeneous processes dominating [51].

THIN-FILM MORPHOLOGICAL INVESTIGATION

Nanoscopic order in π-conjugated systems has become more and more important, because it determines the performance of the materials when used as components in optoelectronic devices. In particular, due to their highly branched architecture dendrimers [65] when assembling among themselves or with other guest molecules create a wide collection of novel structures and surfaces with new and promising properties. Potentially, a variety of supramolecular structures can be built by changing the nature and concentration of surface groups, functional fragments, and polymer backbone architecture.

Dendrimers or dendritic polymers can also self-assemble into three-dimensional structures. Percec and co-workers [66] have reported the self-assembly of monodendritic building blocks in bulk into spherical, cylindrical, and more complex supramolecular and supramacromolecular dendrimers. Stupp et al. [67] reported that dendron rodcoil molecules self-assembled into well-defined nano-ribbons with uniform width and thickness. Masuhara et al. [68] also demonstrated that wire-type dendrimers could self-assemble into doughnut-like structures.

So, the morphological study on $T9_5$ and $T14_6$ arrangement in thin-films is fundamental not only for deciding the possible application of spider-like oligothiophenes as active materials in opto-electronic devices but also for understanding how much the self-assembly of these macromolecules on solid substrate is related to strong π–π interactions.

Their film morphology is probed by confocal laser scanning microscopy (CLSM) exciting the sample at 488 nm (Fig. 26) and by atomic force microscopy (AFM) in tapping mode (Fig. 27). Both the films exhibit a quite good film-forming ability, but the increased

branched structure of $T14_6$ molecule plausibly reduces the wettability of the film on quartz substrate.

Indeed, observing confocal images (Fig. 26) $T9_5$ and $T14_6$ present completely different film morphology that can be only partly related to the different film deposition techniques implemented.

$T9_5$ molecular film adheres completely to the substrate showing a texture of micrometric wide islands merging together at the boundaries. It is likely that after nucleation processes has started in few positions on the substrate the islands growth takes place isotropically on the plane resulting in an entangled fibril morphology. At higher resolution, it is evident the tree-like branches structure that expands from the island center to the periphery with the longest branches merging in three-fold knots.

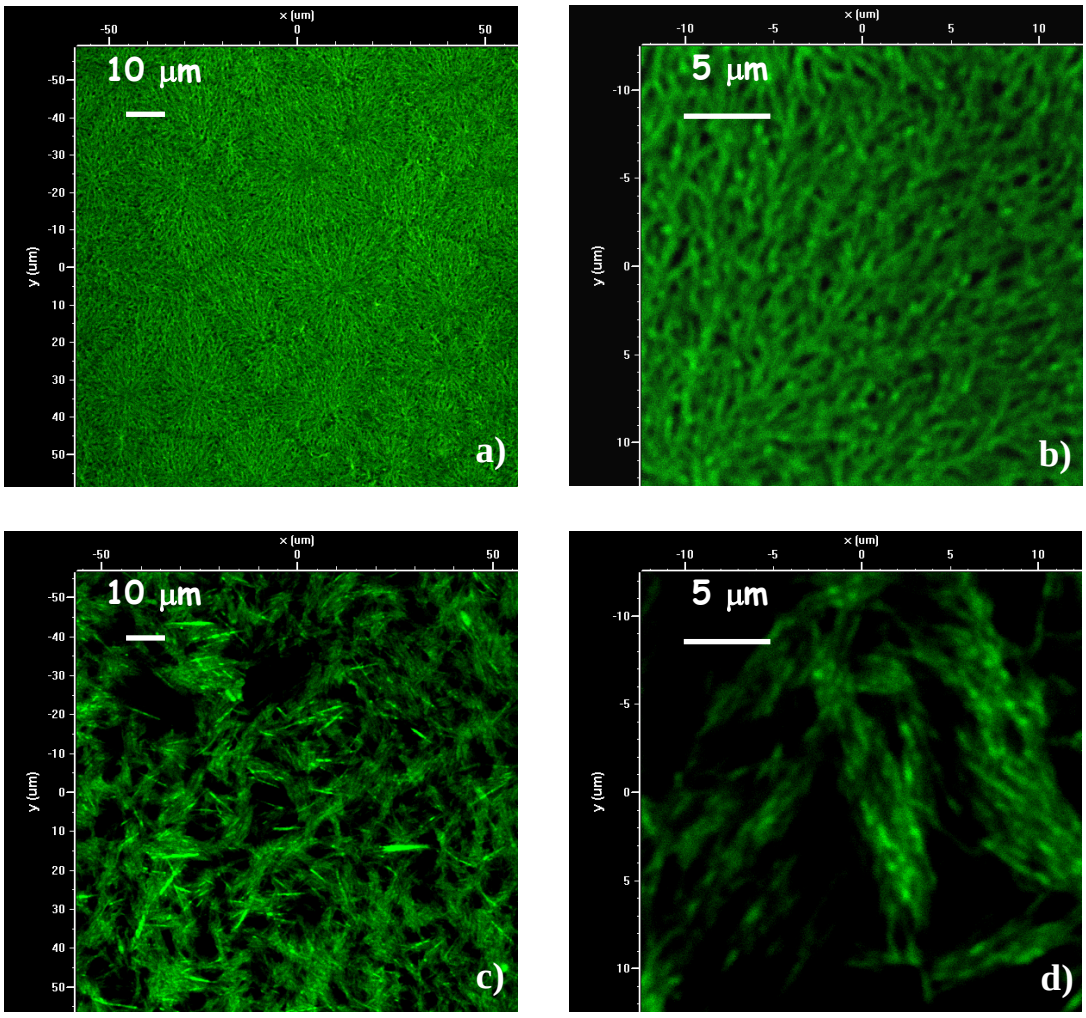

Figure 26. Confocal images of $T9_5$ (a, b) and $T14_6$ (c, d) molecular thin-films. The objective is 60x oil, the excitation source is 488 nm Ar^+ and only PMT green channel is open.

As it is known, the interplay between the conjugated molecules, the solvent, and the substrate surface is very important during self-assembly processes [68]. $T9_5$ molecular assembly likely results from the interplay between two molecular structural features: the long planar α-conjugated chain which is expected to promote π–π stacking, thus enabling efficient intermolecular electronic coupling, and the large molecular surface due to the (2,2'-bithiophen)yl legs in β positions that enhance the 3D branching of the structure.

Also the polar interaction between the molecular electric dipole and the quartz substrate may be another factor facilitating the macromolecules spontaneous assembly onto the entire substrate.

$T14_6$ molecular film presents a much more unstructured morphology with molecular aggregates formed by a random distribution of micrometric-long wires hardly sticking on the substrates. At higher resolution we recognize that globular repeating motif constitute the wire and rod structures, as it can be expected from slightly polar bulky macromolecules poorly interacting with the substrate.

Given the nanometric size and the globular shape of the aggregates it is likely that the few molecules in the aggregates assume a steric hindered and twisted conformation as we deduced from the thin-film PL spectra analysis. In general the morphological data clearly show no long-range structure for $T14_6$ but rather untextured aggregates, probably as a consequence of the absence of specific intermolecular interactions.

This hypothesis is further corroborated by the AFM analysis (Fig. 27) since the images show the presence of an almost monodispersed distribution of independent nanometric globular structures in the proximity of the larger wires, which are likely poorly emitting in fluorescence confocal images.

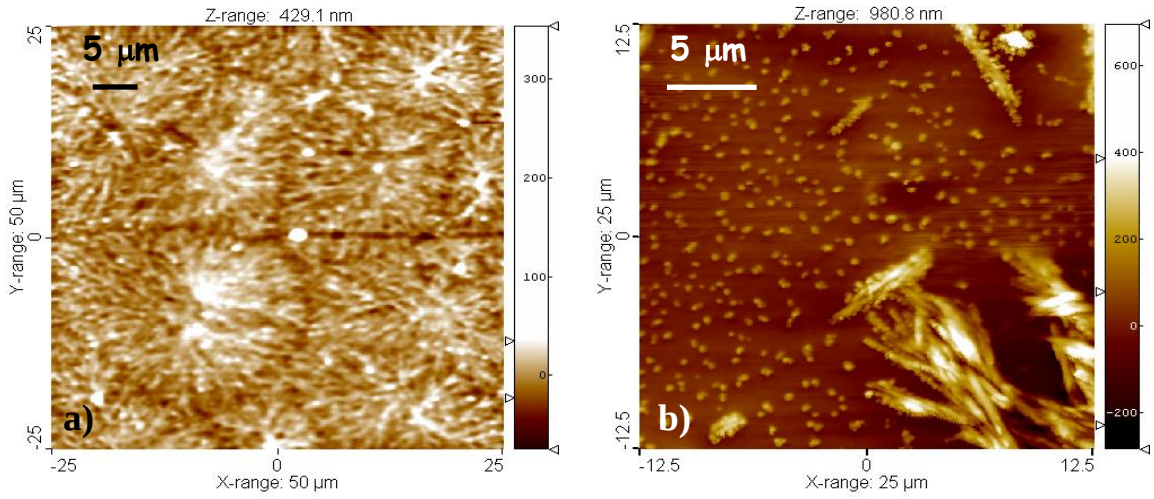

Figure 27. Tapping mode AFM images of $T9_5$ (a) and $T14_6$ (b) molecular thin-films.

We cannot exclude that locally more ordered domains are formed during film deposition since the brightest wires seem to be quite sensitive to the light polarization. In order to discern the degree of order in molecular packing of the different aggregates a localized photoluminescence study is necessary.

Also morphology of the polymeric films is briefly investigated. Unfortunately the very low PLQY of $[T9_5]_m$ and $[T14_6]_m$ films prevents us from collecting clear confocal images. Nonetheless, as it can be seen in Fig. 28a and 28b, $[T9_5]_m$ morphology is much less homogeneous with respect to $[T14_6]_m$ one, with brighter fibril-like agglomerates on top of a smoother surface.

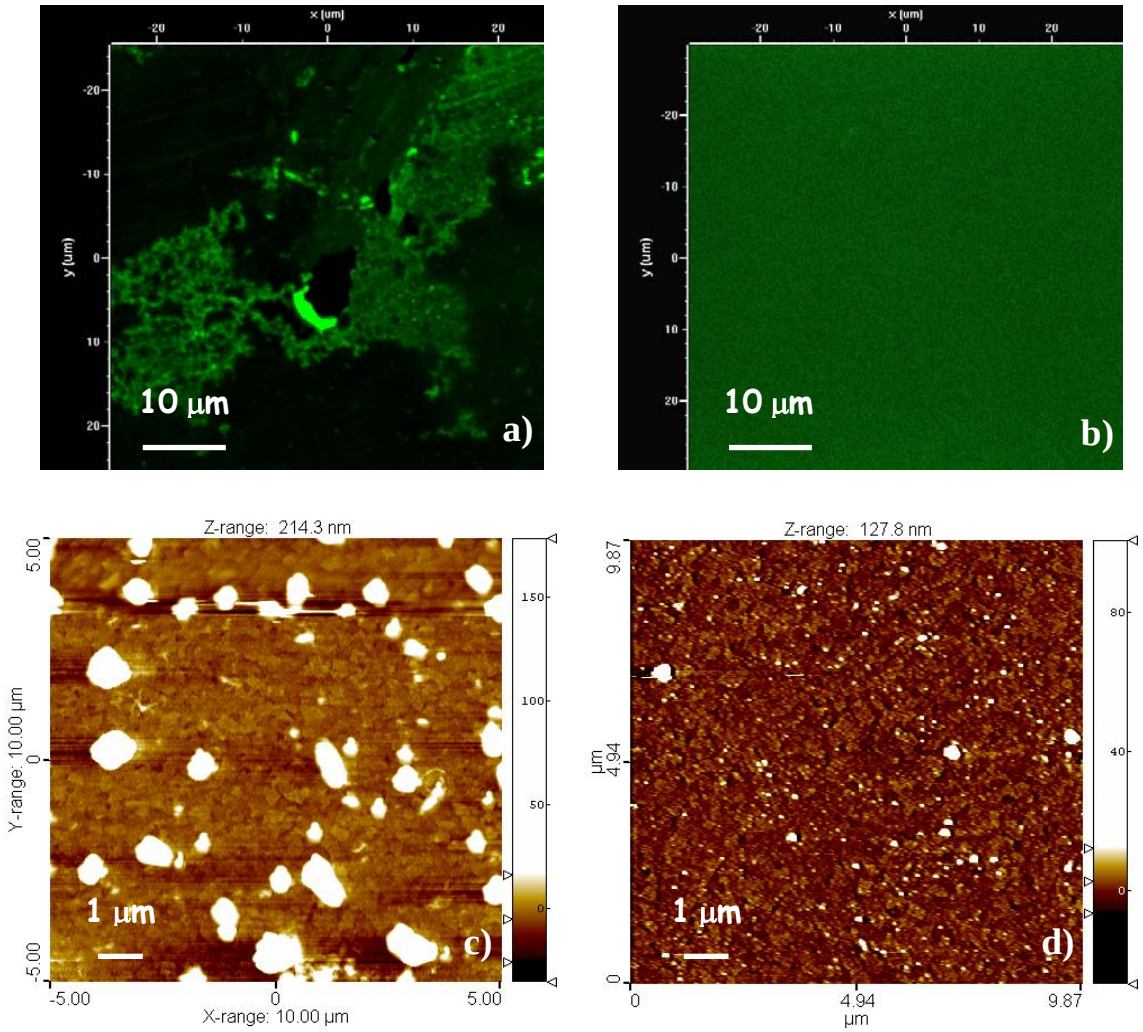

Figure 28. Confocal image (a) and AFM image (c) of polymer $[T9_5]_m$ on ITO. Confocal image (b) and AFM image (d) of polymer $[T14_6]_m$ on ITO. Confocal images are performed with 60x oil objective, 488 nm Ar^+ excitation source and PMT green channel open. AFM images are performed in contact mode.

AFM analysis in contact mode (Fig. 28c and 28d) highlights that even far from those agglomerates the protrusions present onto $[T9_5]_m$ film surface are higher in density and larger in dimensions (peak height can reach even 60 nm) with respect to the other polymer.

With increasing the AFM images contrast we can observe that in both the film the smooth surface underneath the protrusions is composed by a texture of globular and nanometric-wide grains. In the $[T14_6]_m$ case the analysis of the mosaic-like morphology reveals that the grains are well-interconnected with smaller dimensions and a root-mean-square roughness around 3-4 nm.

3.2.3 OFET devices based on 2,3,4,5-tetra(2-tienyl)thiophene ($T5_3$) *thin-films*

When compared to their linear analogues, conjugated dendrimers have a number of potential advantages in terms of applications in optoelectronics. Their shape persistency allows them to maintain structure in a solution-processable form, which can therefore minimize the π-stacking, and increase quantum efficiency. In addition, an internal local electric field may be created during the charge transfer to the core of the dendrimer, which can capture opposite charges. This strategy has been adopted for designing novel materials for OLED applications [69]. However, the study of dendrimer aggregation behaviour in the solid state, or in ultra-thin films, seems to be more intriguing because of their monodisperse and periodic structures. Some of these dendrimers form supramolecular structure. For example, the phenylene dendrimers can self-assemble into nanowires and other supramolecular structures as a result of π-π stacking interactions [70].

In OFET realization dendrimeric-like molecules are used as active material mainly because they are easily solution-processible, i.e star-shaped [71] and swivel cruciform oligo-thiophenes [72] which show promising mobility values.

In principle dendrimers supramolecular architecture can play a relevant role in enhancing light emission properties in small molecule-based OFET since the degree of intermolecular π-stacking overlap between the conjugated branches is a crucial parameter that at the same time determines the charge-transport and light emission properties of the device. Indeed, using 3D macromolecules as active materials in OFET we aim to obtain a balance between the long-range highly ordered structure required in field-effect transport and the suitable electronic structure that can guarantee high PLQY.

The implementation of spider-like oligothiophenes in OFET structure is to be considered in this scenario. Moreover, since spider-like oligothiophenes are molecules constituted only by thiophenes units, we expect that TX_n opto-electronic characteristics can provide some information also on the charge transport processes taking place in their analogue linear oligothiophenes.

Among all the members of the spider-like oligothiophenes, $T5_3$ is chosen to carry out a preliminary study on FET realization because $T5_3$ molecules can be deposited by thermal sublimation and can form crystal powder as X-ray diffraction analysis shows (Fig. 29).

As a first step we investigate the self-organization of $T5_3$ on different types of substrates: graphite, SiO_2, quartz and mica. The samples were prepared by thermal sublimation in vacuum of 10 nm-thick thin-films on substrate held at room temperature with a 0.12 Å/s sublimation rate.

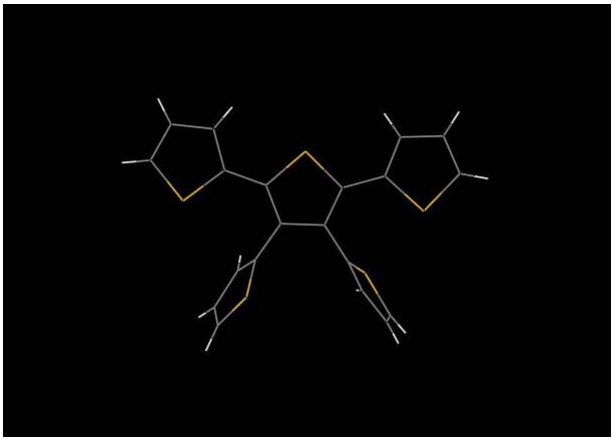

Figure 29. Projection of the preferred conformation of $T5_3$ obtained from X-ray diffraction analysis of crystal powders.

Linear oligothiophene derivatives are well known to form supramolecular structures on solid substrates. Depending on the energy difference between the molecule-substrate and the molecule-molecule, either 2D crystals or nanoribbon structures can be formed [1] For example strong π-π interactions between each α-6T unit governed the supramolecular assembly on graphite or silicon substrate and formed ribbonlike structures [73]. When the molecule-substrate interaction is strong, a sensibly packed 2D crystal structure can be observed, as shown by Bäuerle et al. [46] where the strong hydrophobic interaction between the graphite and the long alkyl chain greatly facilitated the 2D packing of the oligothiophenes. Thiophene dendrimers have also been shown to aggregate into nanowires on graphite surfaces [74].

When $T5_3$ molecules are deposited on the graphite substrate they tend to self-assemble into V-shaped wires structures (Fig. 30a). The size of the wires seems to be quite uniform on the graphite surface and the length of the wire arms is about hundred of nanometers. It is interesting to note that the wire arms tend to be aligned along three directions at an angle of 120° to each other. This arrangement is reminiscent of the three-fold symmetry of the graphite surface, indicating that interactions with the substrate are fundamental in the molecules packing in the solid.

Indeed $T5_3$ can be considered a slightly polar molecule since, as it can be inferred from the energy-minimized arrangement of the molecule reported in the previous paragraph, its ground-state electric moment dipole is non-negligible and preferentially directed along the longest conjugated chain. So the intense π–π interaction between the spider-like oligothiophenes units induce them to aggregate in columnar structures on the graphite hydrophobic surface. From AFM topographic preliminary investigation we can guess that V-shaped wires are mainly formed by 2D plates (lamellae) parallel to the surface.

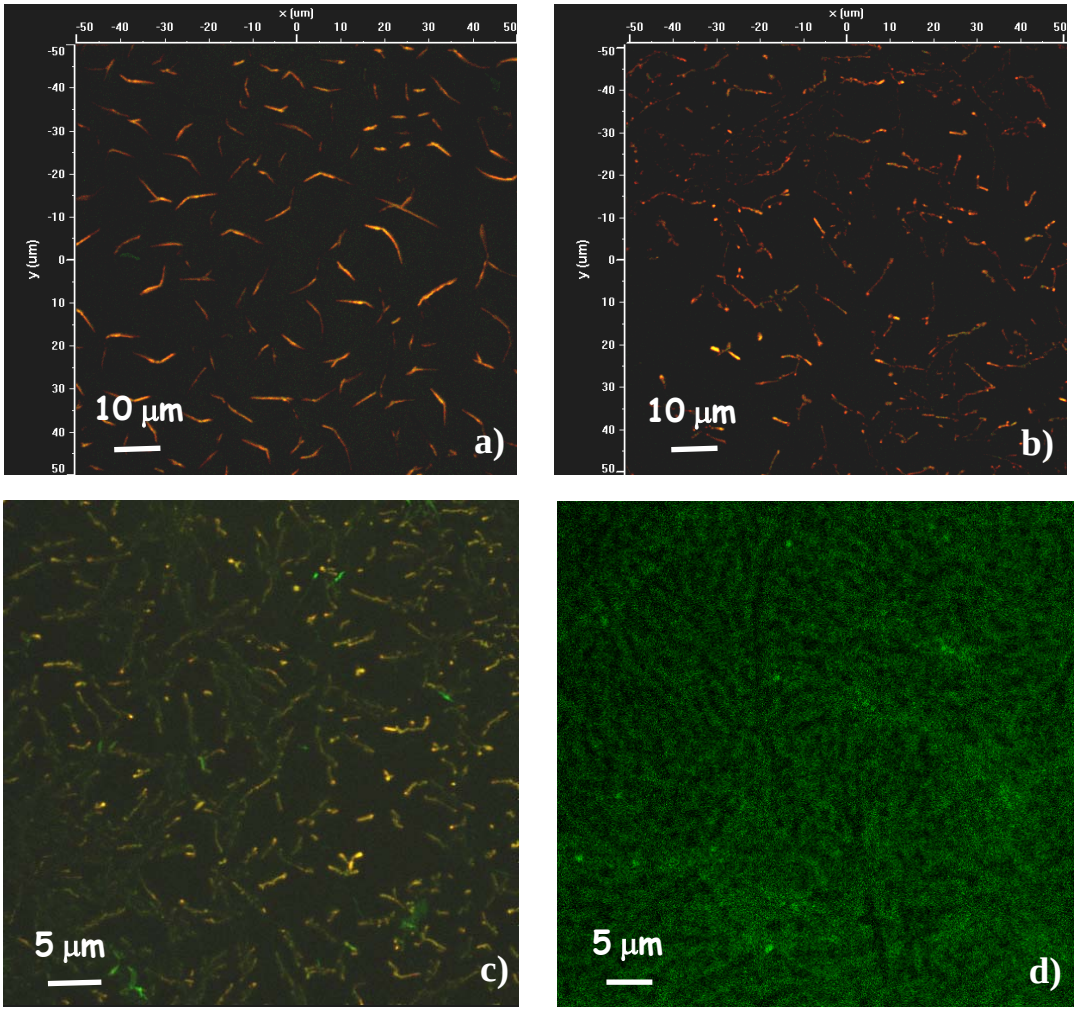

Figure 30. Confocal images of 10 nm-thick $T5_3$ thin-film evaporated on graphite (a), SiO_2 (b), quartz (c) and mica (d). Confocal images are performed with 60x oil objective, 488 nm Ar^+ excitation source and PMT green channel open.

When increasing the hydrophilicity of the surface from SiO_2 to quartz and mica, the strength of the interaction between molecules and substrate increases as the larger and

larger wettability of the aggregates on the surfaces indicates (Fig. 30). Being the amount of material deposited constant, the morphological investigation indicates that the nucleation process becomes favourite as the polarity of the surface increases. So firstly $T5_3$ molecules form globular objects which then tend to coalesce into micrometric-long fibers. In particular, the high degree of coverage on the mica surface (Fig. 30c) is mainly due to the high affinity of molecules towards this surface. Moreover the lack of steric hindrance and rigidity in $T5_3$ structure helps in achieving a complete contact of thiophene groups with the surface.

Indeed this morphological investigation reveals that $T5_3$ spider-like oligothiophene can be considered a trade off between a linear oligothiophene and a discotic molecule since the π–π interaction among molecules is still strong enough for assuring long-range π electrons overlap in solid state aggregates but also the high degree of conformational freedom of the molecules play a fundamental role in controlling the aggregate formation on substrates presenting different superficial energy.

Discotic molecules or, more generally, planar 2D conjugated systems have recently been implemented in the fabrication of devices in which the direction of charge-transport is particularly critical [75]. Indeed 1D conjugated systems, such as linear oligothiophenes, implemented as active material in OFET can reach very high charge-carrier mobility only when the molecular packing inside crystalline domains is favourable to in-plane charge-carrier transport.

So molecular systems presenting isotropic optical and charge-transport properties due to π–delocalization in different directions require less substrate surface-functionalization treatments and less strict growth conditions.

In order to verify the potential charge-carrier transport properties of spider-like oligothiophenes molecules we carried out a preliminary study on the realization of OFET devices having $T5_3$ as active material.

We deposited in high-vacuum a 45 nm-thick film of $T5_3$ with a 0.12 Å/s rate on a Si/SiO_2 substrate kept at room temperature. Intentionally SiO_2 surface is not functionalized, but simply cleaned according to the standard wet procedure. Gate electrode is obtained by doping negatively Si substrate and 50 nm-thick gold films deposited on $T5_3$ layer work as source and drain electrodes in a linear transistor configuration.

Interestingly $T5_3$ devices show a promising ambipolar field-effect transport behaviour with well-balanced hole and electron currents ($\mu_n \sim 1.4 \times 10^{-2}$ cm^2/Vs and $\mu_p \sim 4 \times 10^{-3}$ cm^2/Vs).

Moreover the threshold voltages for both the polarization reveal to be very small ($V_{th}^{n} \sim 8$ V and $V_{th}^{p} \sim -2$ V) as it can be inferred from the p-polarized transfer curve we report in Fig. 31.

Since the analysis of the data reported in literature leads to the conclusion that oligothiophenes should have at least four conjugated rings in order to have significant mobility in FET devices [71], the high mobility values obtained from $T5_3$-device indicate that the longest π-conjugated chain extends over the three thiophene rings displaying exclusively α–conjugation, as it is expected from a 2D π-delocalized system. Moreover the high aggregation tendency of $T5_3$ molecules can guarantee sufficient intermolecular π–π stacking interactions for good in-plane charge-carrier transport.

Nevertheless the results we report are preliminary since some devices present instability in working conditions even if all the measurements are performed in vacuum. Probably the scarse affinity between the non-treated SiO_2 and $T5_3$ molecules that we observed in the morphological study can prevent a complete coverage of the channel length.

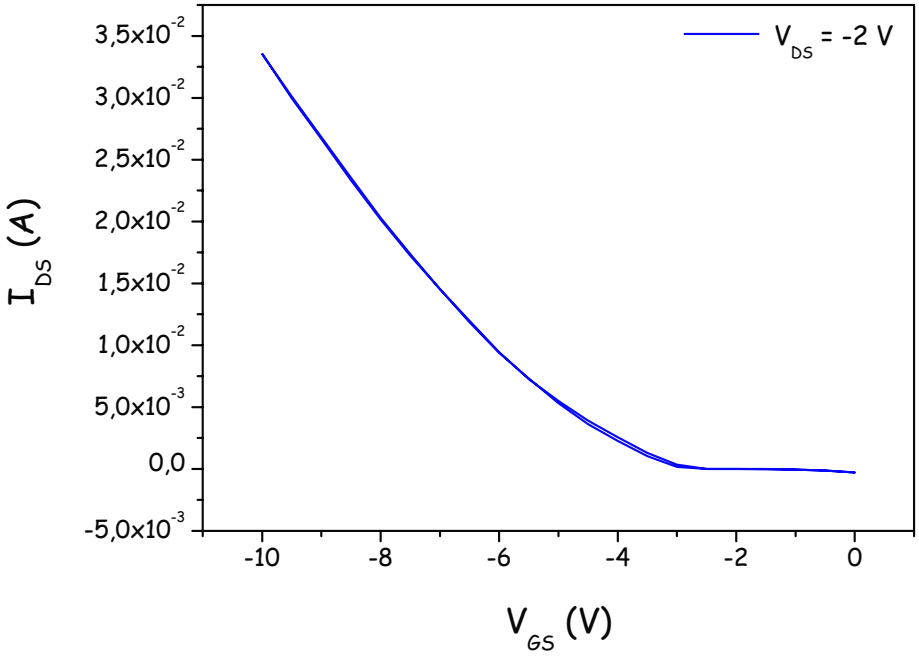

Figure 31. p-polarized transfer characteristics curve of a linear transistor with 45 nm-thick thin-film of $T5_3$ as active layer. The channel length is 600 μm. Gate contact is doped Si. Dielectric is 300 nm-thick bare SiO_2. Top contacts are 50 nm-thick gold films.

Indeed, AFM topography analysis (Fig. 32)performed on the active region of the transistor we fabricated shows that $T5_3$ molecules tend to aggregate in globular grains even if the amount of deposited material is increased. Nucleation processes on SiO_2 surface are favored over the concomitant coalesce of the grains, so preventing the percolation paths to be long enough for the charges to reach the electrodes. Moreover from the topography profile a root-mean-square roughness value of about 50 nm can be extracted.

In order to achieve a more homogenous and continuous film one should fabricate devices either decreasing the deposition rate or keeping the substrate temperature in the proximity of $T5_3$ crystallization temperature (about 120 °C) to assure the molecules sufficient time and energy to rearrange themselves in larger crystalline domains. Another possibility is chemically functionalize the SiO_2 surface in order to slightly improve the hydrophilic affinity between the substrate and the

impinging $T5_3$ molecules.

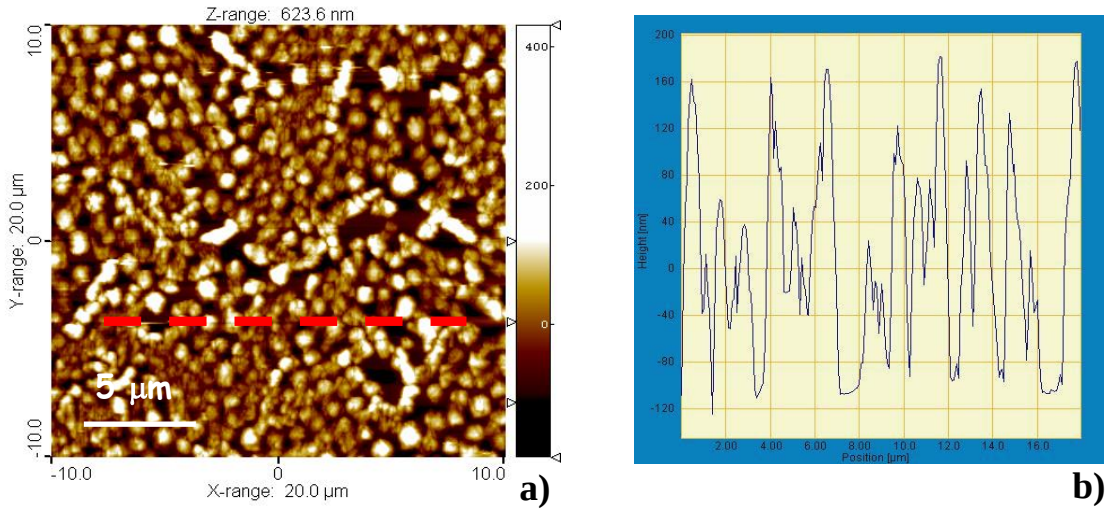

Figure 32. AFM topography image (a) and roughness profile (b)of 45 nm-thick thin-film $T5_3$ used as active material in a linear transistor.

3.3 Conclusions

The great deal of work carried out in recent years on thiophene-based functional materials indicates great potential for successful developments in many directions. Clearly much systematic effort is required in order to better understand properties such as charge transport and light emission and their relationship to molecular structure, molecular ordering and morphology.

The chemical robustness of thiophe-based compounds and the easy tenability of their properties via minor structural modifications have allowed the realization of a great amount of chemical structures. The rapidity of recent developments in the preparation of stable n-type materials, the realization of new, air-stable ambipolar compounds presenting also high photoluminescent properties will soon follow.

By now, end-substituted α-oligothiophenes seem to be the suitable materials that can provide good charge transport properties in field-effect devices together with the possibility of controlling their supramolecular organization in thin-film.

Clearly, as in the case of DH4T and DHF4T α-oligothiophenes we have presented in this chapter, the substituted groups play a fundamental role in determining not only if the α-oligothiophene molecule shows p- or n-type transport properties in solid-state, but also all the chemical-physical interactions between the active material and all the surfaces in contact with it (such as those of the dielectric and metal electrodes).

So we tried to optimize 2D long-range crystalline-like organization and the interfaces morphology in single-layer devices based on DH4T and DHF4T thin-films in order to obtain higher electrical performances. Since the field-effect conduction occurs in a narrow region of the active material at the interface with the dielectric layer, the properties of this interface have a huge influence on the device characteristics.

Moreover controlling the growth process in single-material devices is the first step for achieving complex vertical multi-layer structures (see Chapter 5) in which different organic layers have to interact through different interfaces without degrading their pristine functional properties.

In the second part of the chapter a new class of branched all-thiophene molecules, namely spider-like oligothiophenes, is presented.

Branched macromolecules, known as dendrimers, present many advantages with respect linear oligomers. They are able to form π-π stacking structures necessary for an efficient intermolecular charge hopping also in thin-films obtained by deposition from solution.
In addition, dendritic architecture provides a number of other attractive properties, including the ability to control independently the processing from the optoelectronic properties and the possibility to control the intermolecular interactions (and thus the device performances) by the dendrimer generation. Moreover when assembling among themselves or with other guest molecules dendrimers create a wide collection of novel structures and surfaces with new and promising properties.

After performing a detailed photoluminescence spectroscopy study on all TX_n molecules dispersed in dilute solution, we instigated how the molecular spectroscopic features are modulated by the solid-state aggregation in thin-films.
Spider-like oligothiophenes spectroscopic properties in solid state are determined by the balance between two molecular structural features: the long planar α-conjugated chain which is expected to promote π–π stacking (thus enabling efficient intermolecular electronic coupling) and the large molecular surface due to the pendant legs in β positions that enhance the 3D branching of the structure. So increasing the length and the number of β-substituted α-conjugated branches, different exciton intermolecular migration processes (hopping, energy transfer…) can take place in solid-state aggregates. In particular, the largest spider-like oligothiophene is likely to present intramolecular energy transfer also in solution.
Moreover molecular steric hindrance and different energetically-stable conformer configurations are responsible for the variation on the molecular aggregate morphological features when depositing as thin-film the members of this class of oligothiophenes.

In particular, $T14_6$ can be considered a good candidate for organic solar cell realization since its high molar decadic extinction coefficient and its high tendency to release electrons. When absorbing light, this molecule presents excitation localization which is the necessary condition for an efficient energy transfer or hopping form the periphery (shorter conjugated branches) to the core (longer conjugated branches) of the molecule.
Due to the discotic or 2D planar configuration of few members spider-like oligothiophenes, TX_n can be also be implemented as active material in OFET device realization.

So using branched oligothiophenes as active materials in OFET we aim to obtain a balance between the long-range highly ordered structure required in field-effect transport and the suitable electronic structure that can guarantee high PLQY.

However, $T5_3$ vacuum-sublimed single-layer devices shows very promising ambipolar charge transport properties even without having optimised the dielectric-active material interface, but no light emission is detected.

References

[1] Handbook of Oligo- and Polythiophenes, ed. D. Fichou, (WILEYVCH, Weinheim, 1999).

[2] U. Schoeler, K. H. Tews and H. Kuhn, J. Chem. Phys., **1974**, 61, 5009.

[3] M. Akimoto, Y. Furukawa, H. Takeuchi, I. Harada, Y. Soma, M. Soma, *Synth. Met.*, **1986**, 15, 353.

[4] R. Hajlaoui, G. Horowitz,; F. Garnier, A. Arce-Brouchet, L. Laigre, A. El, Kassmi, F. Demanze, F. Kouki, *Adv. Mater.* **1997**, 9, 389.

[5] A. Dodabalapur, L. Torsi, H. E. Katz, *Science* **1995**, 268, 270.

[6] M. E. Hajlaoui, F. Garnier, L. Hassine, F. Kouki, H. Bouchriha, *Synth. Met.* **2002**, 129, 215.

[7] D. Fichou, *J. Mater. Chem.* **2000**, 10, 571.

[8] A. Gavezzotti and G. Filippini, *Synth. Met.*, **1991**, 40, 257.

[9] G. Horowitz, R. Hajlaoui, R. Bourguiga, M. Haijlaoui, *Synth. Met.*, **1999**, 101, 401.

[10] X. C. Li, H. Sirringhaus, F. Garnier, A. B. Holmes, S. C. Moratti, N. Feeder, W. Clegg, S. J. Teat, R. H. Friend, *J. Am. Chem. Soc.* **1998**, 120, 2206.

[11] J. E. Anthony, J. S Brooks, D. L. Eaton, S. R. Parkin, *J. Am. Chem. Soc.* **2001**, 123, 9482.

[12] M. H. Yoon, A. Facchetti, C. E. Stern, T. J. Marks, *J. Am. Chem. Soc.* **2006**, 128, 5792.

[13] G. Horowitz, B. Bachet, A. Yassar, P. Lang, F. Demanze, J. L. Fave, F. Garnier, *Chem. Mater.* **1995**, 7, 1337

[14] F. Garnier, G. Horowitz, D. Fichou, A. Yassar, *Supramol. Sci.*, **1997**, 4, 155.

[15] G. Horowitz, R. Hajlaoui, F. Kouki, *Eur. Phys. J: Appl. Phys.*, **1998**, 1, 361.

[16] C. Väterlein, B. Ziegler, W. Gebauer, *et al.*, *J. Appl. Phys.*, **1996**, 76, 133.

[17] M. Wu and E. M. Conwell, *Chem. Phys. Lett.*, **1997**, 266, 363.

[18] D. Fichou, G. Horowitz, B. Xu, F. Garnier, *Synth. Met.*, **1992**, 48, 167.

[19] D. Birnbaum, D. Fichou, B. E: Kohler, *J. Chem. Phys.*, **1992**, 76, 165.

[20] R. N. Marks, E. Lunedei, M. Muccini *et al.*, *Chem. Phys.*, **1997**, 227, 49.

[21] D. Oelkrug, H. J. Egelhaaf, D. R. Worral, F. Wilkinson, *J. Fluorecsence*, **1995**, 5, 165.

[22] E. Lunedei, P. Moretti, M. Murgia, M. Muccini, F. Biscarini, and C. Taliani, *Synth. Met.*, **1999**, 101, 592.

[23] R. N. Marks, R. H. Michel, W. Gebauer, R. Zamboni, C. Taliani, R. F. Mahrt, and M. Hopmeier,, J. Phys. Chem. B, **1998**, 102, 7563.

[24] G. Horowitz, B. Bachet, A. Yassar, P. Lang, F. Demanze, J. L. Fave, F. Granier, *Chem. Mater.*, **1995**, 7, 1337.

[25] W. Gebauer, M. Bässler, A. Soukopp, *et al.*, *Synth. Met.*, **1996**, 83, 227.

[26] M. Halik, H. Klauk, U. Zschieschang, G. Schmid, S. Ponomarenko, S. Kirchmeyer, W. Weber, *Adv. Mater.* **2003**, 15, 917.

[27] H. E. Katz, A. J. Lovinger, J. G. Laquindanum, *Chem. Mater.*, **1998**, 10, 457.

[28] F. Garnier, R. Hajlaoui, A. El Kassmi, G. Horowitz, L. Laigre, W. Porzio, M. Armanini, F. Provatoli, *Chem. Mater.*, **1998**, 10, 3334.

[29] J. Puigdolers, C. Voz, A. Orpella, R. Quidant, I. Matrin, M. Vetter, R. Alcubilla, *Organic Electronics*, **2004**, 5, 67.

[30] F. Demanze, A. Yassar,; D. Fichou, *Synth. Met.* **1999**, 101, 620.

[31] P. Hapiot,; F. Demanze,; A. Yassar,; F. Garnier, *J. Phys. Chem.* **1996**, 100, 8397.

[32] A. Facchetti, Y. Deng, A. Wang, Y. Koide, H.Sirringhaus, T. J. Marks, R. H. Friend, *Angew. Chem.* **2000**, 39, 4547.

[33] A. Facchetti, M. Mushrush, M. H. Yoon, G. R. Hutchison, M. A. Ratner, T. J. Marks, *J. Am. Chem. Soc.*, **2004**, 126, 13859.

[34] A. Facchetti,; M. Mushrush,; H. E. Katz,; T. J. Marks, *Adv. Mater.*, **2003**, 15, 33.

[35] F Dinelli,.; M. Murgia,; P. Levy,; M. Cavallini,; F. Biscarini,; D. de Leeuw, *Phys. Rev. Lett.* **2004**, 92, 6802.

[36] H. Sirringhaus, P. J. Brown, R. H. Friend, M. M. Nielsen, K. Bechgaard, B. M. W. Langeveld-Voss, A. J. H. Spiering, R. A. J. Janssen, E. W. Meijer, P. Hervig, D. M. de Leeuw, *Nature* **1999**, 401, 685.

[37] C. D. Dimitrakopolous, P. Malenfant, *Adv. Mater.* **2002**, 14, 99.

[38] J. Roncali, P. Leriche, A. Cravino, *Adv. Mater.*, **2007**, 19, 2045.

[39] A. Bilge, A. Zen, M. Forster, H. Li, F. Galbrecht, B. S. Nehls, T. Farrell, D. Neher, U. Scherf, *J. Mater. Chem.*, **2006**, 16, 3177.

[40] Y. Nicolas, P. Blanchard, E. Levillain, M. Allain, N. Mercier, J. Roncali, Org. Lett. 2004, 6, 273.

[41] B. X. Sun, Y. Liu, S. Chen, W. Qiu, G. Yu, Y. Ma, T. Qi, H. Zhang, X. Xu, D. Zhu, *Adv. Funct. Mater.* **2006**, 16, 917.

[42] C. Ma, E. Mena-Osteriz, T. Debaerdemaeker, M. M. Wienk, R. A. J. Janssen, P. Bauerle, *Angew. Chem.*, **2007**, 119, 1709.

[43] T. Benincori, M. Capaccio, F. De Angelis, L. Falciola, M. Muccini, P. Mussini, A. Ponti, S. Toffanin, P. Traldi, F. Sannicolò, *Chem. Eur. J.*, 2008, 14, 459.

[44] R. Kopelman, M. Shortreed, Z. -Y. Shi, W. Tan, A Bar-Haim, J. Klafter, *Phys. Rev. Lett.* 1997, 78, 1239.

[45] M. R. Shortreed, S. F. Swallen, Z. -Y. Shi, W. Tan, Z. Xu, C. Devadoss, J. S. Moore, R. Kopelman, *J. Phys. Chem. B*, **1997,** 101*,* 6318.

[46] P. Bäuerle, T. Fischer, B. Bidlingmeier, A. Stabel, J. P. Rabe, *Angew. Chem.*, **1995**, 107, 335.

[47] M. Klessinger, *Excited States and Photochemistry of Organic Molecules* (VCH, New York, 1993).

[48] R. S. Knox, *Primary Processes of Photosynthesis*; (J. Barber, Ed.; Elsevier: Amsterdam, 1977).

[49] O. Varnavski, I. D. W. Samuel, L. –O. Pålsson, R. Beavington, P. L. Burn, T. Goodson III, *J. Chem. Phys.*, **2002**, 116, 8893.

[50] C. M. Heller, I. H. Campbell, B. K. Laurich, D. L. Smith and al., *Phys. Rev. B*, **1996**, 54, 5516.

[51] M. Pope; C. E. Swenberg, *Electronic Processes in Organic Crystals*, (Oxford University Press: Oxford, 1982).

[52] D. A. Tomalia, A. M. Naylor, W. A. III Goddard, , *Angew. Chem., Int. Ed. Engl.* **1990**, 29, 138.

[53] V. V. Tsukruk, *Adv. Mater.* **1998**, 10, 253.

[54] F. Köhn, J. Hofkens, U.-M. Wiesler, M. Cotlet, M.van der Auweraer,; K.Müllen,; F. C. De Schryver, *Chem.-Eur. J.*, **2001**, 7, 4126.

[55] S. Watanabe, S. L. Regen, *J. Am. Chem. Soc.*, **1994**, 116, 8855.

[56] W. M. Lackowshi, J. K. Campbell, G. Edwards, V. Chechik, Crooks, R. M. *Langmuir* **1999**, 15, 7632.

[57] D. C. Tully, K. Wilder, J. M. J Frechet, A. R. Trimble, C. F. Quate, *Adv. Mater.* **1999**, 11, 314.

[58] A. Khopade, F. Caruso, *Nano Lett.* **2002**, 2, 415.

[59] M. Zhao, H. Tokuhisa, R. M. Crooks, *Angew. Chem., Int. Ed. Engl.* **1997**, 36, 2596.

[60] R. Beavington, M. J. Frampton, J. M. Lupton, P. L. Burn, I. D. W. Samuel, *Adv. Funct. Mater.*, **2003**, 13, 211.

[61] M. Muccini, E. Lunedei, C. Taliani, D. Beljonne, J. Cornil, J. L. Brédas, *J. Chem. Phys.*, **1998**, 109, 10513.

[62] J. Pei, J. L. Wang, X. Y. Cao, X. H. Zhou,W. B. Zhang, *J. Am. Chem. Soc.*, **2003**, 125, 9944.

[63] K. Brunner, A. Tortschanoff, Ch. Warmuth, H. Bassler, and H. F. Kaufmann, *J. Phys. Chem. B*, **2000**, 104, 3781.

[64] A. Dogariu, D. Vacar, A. J. Heeger, *Phys. Rev. B*, **1998**, 59, 10218.

[65] V. V. Tsukruk, *Adv. Mater.*, **1998**, 10, 253.

[66] S. D. Hudson, H. T. Jung, V. Percec, W. D. Cho, G. Johansson, G. Ungar,; V. S. K. Balagurusamy, *Science*, **1997**, 278, 449.

[67] Zubarev, E. R.; Pralle, M. U.; Sone, E. D.; Stupp, S. I. *J. Am. Chem. Soc.* **2001**, 123, 4105.

[68] Masuo, S.; Yoshikawa, H.; Asahi, T.; Masuhara, H. *J. Phys. Chem. B* **2001**, 105, 2885.

[69] P. W. Wang,; Y. J. Liu,; C. Devadoss,; P. Bharathi,; J. S. Moore, *Adv. Mater.* **1996**, 8, 237.

[70] D. Liu, H. Zhang, P. C. M. Grim, S. De Feyter, U. -M. Wiesler, A. J Berresheim, K. Mullen, F. C. De Schryver, *Langmuir* **2002**, 18, 2385.

[71] S. A. Ponomarenko, S. Kirchmeyer, A. Elschner, B. –H. Huisman, A. Karbach, D. Drechsler, *Adv. Funct. Mater.*, **2003**, 13, 591.

[72] A. Zen, A. Bilge, F. Galbrecht, R. Alle, K. Meerholz, J. Grenzer, D. Neher, U. Scherf, T. Farrell, *J. Am. Chem. Soc.* **2006**, 128, 3914.

[73] A. P. H. J. Schenning, A. F. M. Kilbinger, F. Biscarini, M. Cavallini, H. J. Cooper, P. J. Derrick, W. J. Feast, R. Lazzaroni, Ph. Leclere, L. A. McDonell, E. W. Meijer, S. C. J. Meskers, *J. Am. Chem. Soc.* **2002**, 124, 1269.

[74] C. Xia, X. Fan, J. Locklin, R. C. Advincula, A. Gies, W. Nonidez *J. Am. Chem. Soc.*, **2004**, 126, 8735.

[75] K. H. Kim, Z. Chi, M. J. Cho, D. H. Choi, H. S. Kang, Mi Y. Cho, J. –S. Joo, *Appl. Phys. Lett.*, **2006**, 89, 202109.

Chapter 4

A new lasing host-guest system with very low ASE threshold

ter(9,9-diarylfluorene) (T3) *: 4-(dicyanomethylene)-2-methyl-6-(p-dimethyl aminostyryl)-4H-pyran* (DCM) *host-guest system*

Since organic light emitting materials are attractive gain media for use in semiconductor lasers, optically pumped laser action has been demonstrated in a broad range of materials in many different configurations with emission wavelengths covering the entire visible spectrum depending on the luminescent materials used. The demonstration of spectrally narrow emission in optically pumped thin organic films even in the presence of injecting metallic contacts is an important step towards the possibility of producing electrically pumped solid-state lasers from conjugated polymers and small molecules [1].

The additional quenching due to the presence of polarons increase the required performances of the lasing active material to be used in an electrically driven device. As a general statement, lowering ASE threshold diminishes the current density required to achieve electrically-pumped lasing emission and reduces the polaron-induced absorption in the "gain" medium [2]. So great efforts are devoted to synthesizing new materials and to engineering new device structures with lower ASE threshold and enhanced net gain coefficient. In this way it would be possible to achieve lasing emission in real devices at an achievable current density even in the presence of residual exciton quenching and photon losses.

To realize organic solid-state lasers one can either utilize diluite solution of dyes embedded in host matrices or alternatively employ films of highly luminescent conjugated polymers. Thin-film vacuum deposition of small organic molecules provides the advantage of a better control on the film morphology and the possible implementation in a

multilayer device structure. Instead conjugated polymers can be easily processable from solutions to realize simplified single-layer structures.

The use of a binary blend in which Förster energy transfer between an absorptive donor and an emissive acceptor takes place allows reducing the optical losses in the thin-film waveguides and decreasing the ASE threshold.

Indeed, the gain profile can be redshifted with respect to the absorption band and the low acceptor concentration (1%-10%) minimizes concentration quenching. Although the benefits of energy transfer have been demonstrated, the way in which the energy transfer affects the ASE is poorly understood [3].

Even if at this stage it is difficult to predict which of these approaches will be the more successful strategy [4], implementing doped matrices in heterojunctions-based organic light emitting transistors (OLETs) seems to be a very promising device architecture for realizing electrical injection laser.

OLETs present fundamental advantages with respect to organic light-emitting diodes (OLED). The exciton quenching at the metal electrodes is reduced by controlling the location of the recombination region inside the device active area using the gate voltage and the exciton-charge quenching is reduced by a better current balance within the device. Moreover inside the OLET active region the current densities achievable are higher (10-10^3 A/cm^2) and the integration of a resonant optical cavity is much easier.

One of the most promising approach for obtaining balanced charge transport and efficient light emission is to realize a heterojunction using different materials each having a specific function (electrons filed-effect transport, holes field-effect transport, light emission). In this perspective a dye-doped matrix is devoted only to charges recombination and light emission since in general it does not present an efficient charge transport.

So we decided to devote our attention to a new host-guest lasing system whose optical properties are modulated by an efficient non-radiative Förster energy transfer. The system is obtained by co-evaporation of a oligodiarylfluorene derivative named T3 as host material and the well-known red fluorescent dye 4-(dicyanomethylene)-2-methyl-6-(p-dimethylaminostyryl)-4H-pyran dye (DCM) as guest material (see Fig.1 for molecular structures).

T3 presents intriguing characteristics, such as high glass transition temperature, ambipolar charge transport in Time of Flight (TOF) measurements and high thin-film PL quantum yield in pure blue [5]. Moreover its ASE threshold and net gain are very competitive with respect to the most efficient polymeric and host-guest systems [6].

The choice of DCM dye as acceptor component in the blend is related to the large overlap between the emission spectrum of T3 thin-film and theabsorption spectrum of the DCM dilute solution (Fig. 1) a necessary prerequisite to achieve efficient Förster non-radiative energy transfer in the host-guest system (see § 1.2.4).

In this chapter we investigate how the guest concentration modifies the energy transfer dynamics and ASE properties of T3:DCM host-guest system. Steady-state and time-resolved photoluminescence spectroscopic study is performed to determine the guest concentration at which the ASE threshold is the lowest. Optical gain of the best performing T3:DCM blend is also measured by femtosecond pump-and-probe experiments.

The ASE characteristics of T3:DCM blend are compared with the case of the reference model system Alq_3:DCM, that has to date the lowest ASE threshold among molecular binary host-guest systems [7]. Since it is known that ASE thresholds and gain values dependent strongly on the experimental conditions used (exciting pulse duration, energy per pulse, illumination area) we performed the measurements on the T3:DCM and Alq_3:DCM systems in exactly the same experimental conditions in order to obtain a reliable direct comparison.

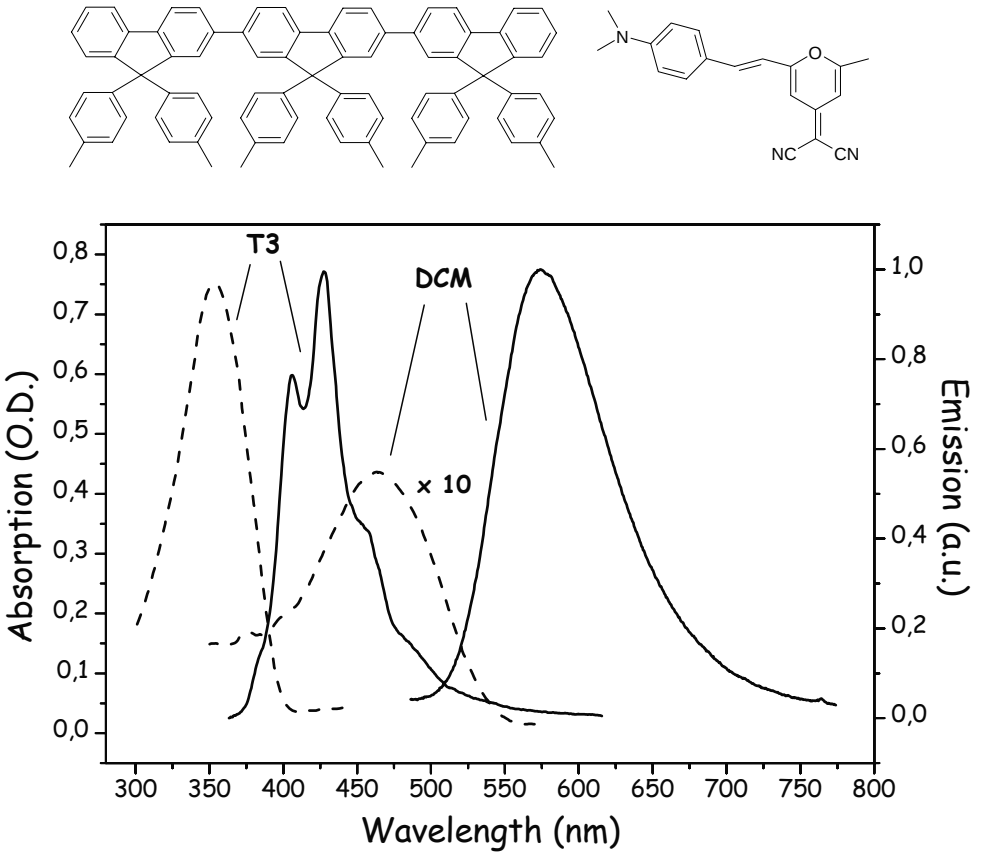

Figure 1. Top: chemical structure of ter(9,9-diarylfluorene) (T3) and 4-(dicyanomethylene)-2-methyl-6-(p-dimethylaminostyryl)-4H-pyran (DCM). Bottom: Absorption spectra (dashed line) and PL spectra (solid line) of a 10^{-5} M solution of DCM molecules dissolved in dichloromethane and of a 100 nm-thick T3 film grown by thermal evaporation.

4.1 Steady-state spectroscopic properties

Förster theory [8] considers the weak coupling between the electronic and vibrational states of donors and acceptors suspended in a liquid solvent or a polymer matrix by dipole-dipole long range interaction. In the system we are considering the T3 thin-film matrix acts both as the donor and the host while the dispersed DCM molecules are the acceptors.

According to this theory the rate of energy transfer from excited donor (D) to unexcited acceptor (A) is given by

$$K_{DA} = \frac{1}{\tau_D}\left(R_0 / R_{DA}\right)^6 \qquad (1)$$

where τ_D is the lifetime of donor in absence of acceptor, R_{DA} is the distance between the donor and the acceptor molecules and R_0 is the Förster radius defined as the distance between donor and acceptor at which energy transfer to the acceptor or decay on the donor occurs with equal probability . R_0 is expressed as

$$R_0^6 = \frac{9000(\ln 10)\langle k^2 \rangle \phi_D}{128\pi^5 n^4 N_A} J \qquad (2)$$

where Φ_D is the donor quantum yield in absence of excitation energy transfer, n is the refractive index of the medium, N_A is the Avogadro's number and k^2 is the molecular orientation factor (for a fixed donor and a random distribution of fixed acceptors $<k^2>$ = 0.476 [9]).

J is the overlap integral between the donor fluorescence and the acceptor absorption expressed in frequency scale as

$$J = \frac{\int_0^\infty F_D(\bar{\nu})\varepsilon_A(\bar{\nu})d\nu/\nu^4}{\int_0^\infty F_D(\bar{\nu})d\bar{\nu}} \qquad (3)$$

where $\varepsilon_A(\nu)$ is the molar decadic extinction coefficient of acceptor at a wavenumber (ν) and $F_D(\nu)$ is the normalized intensity of donor fluorescence at ν.

From the overlap spectra of 10^{-5} M toluene solution of DCM molecules and a neat T3 thin-film we calculated an integral overlap of about 1.2×10^{-13} $M^{-1}cm^2$. Considering the T3 refractive index n=1.75 [5] and the measured T3 thin-film quantum yield of 47%, the estimation of the Förster radius is 36 Å.

In Fig. 2a we report the absorption spectra of DCM:T3 blends obtained by increasing DCM concentration during the coevaporation. The neat T3 thin-film and DCM dilute solution show absorption spectra peaked at ~383 and 463 nm respectively. The blends spectra (which are normalized to T3 peak in Fig. 2a) are simply the linear combinations of the absorption of the pristine materials in the specific molar concentration, except for the slightly blue-shift in the DCM peak probably due to intermolecular interaction in the blend. T3 shows high absorbance at each dopant concentration, while DCM absorbance in the blend increases as expected with its concentration. T3 absorption band is characteristic of the lowest π–π^* transition of the central terfluorene chromophore and DCM absorption band is broad and featureless. From the absorption spectra an estimation of the molar

dopant concentration in the blend film can be achieved. The percentages of doping which identifies the samples refers to the mass deposition flux of DCM with respect to that of T3. By using DCM molar decadic extinction coefficient in dilute solution, it is possible to calculate the guest molar fractions in the solid state samples assuming a homogenous dispersion of non-interacting guest molecules in the host matrix. From the determination of the mean number of guest molecules per volume unit (n_A) we can obtain the nearest-neighbour distance in three-dimensions system by the expression $0.554/n_A^{1/3}$ as derived by Chandrasekhar [10]. It is interesting to note (Tab. 1) that the mean distances (R_{DA}) calculated for all the DCM concentrations are lower than the Förster radius (R_0) obtained from spectroscopic data, thereby highlighting that in each investigated samples the donor decay rate should be lower than the electronic energy transfer rate.

Attention should also be paid to the non negligible integral overlap between the absorption and fluorescence spectra of the donor itself. This can lead to excitation energy transport within the donor, which is also referred to as energy migration.

DEPOSITION RATE	**C_{DCM} [%]**	**R_{DA} [%]**
2 %	14	12.6
5 %	24	10.6
10 %	38	9.1
20 %	43	8.2

Table 1. Estimation of the DCM molar concentration in the blends from the DCM deposition rate value in the film growth. The corresponding calculated donor-acceptor distances (R_{DA}) are reported.

In Fig. 2b the normalized photoluminescence (PL) spectra of the DCM:T3 blends at different concentrations are reported. The direct DCM emission is almost negligible at the excitation wavelength used (325 nm). T3-alone PL shows a vibronically resolved spectrum typical of polyfluorenes with the highest oscillator strength in correspondence of the 0-1 transition at 428 nm [11], while the emission from DCM molecules dispersed in a PMMA matrix is broad (FWHM~91 nm), featureless and peaked around 562 nm.

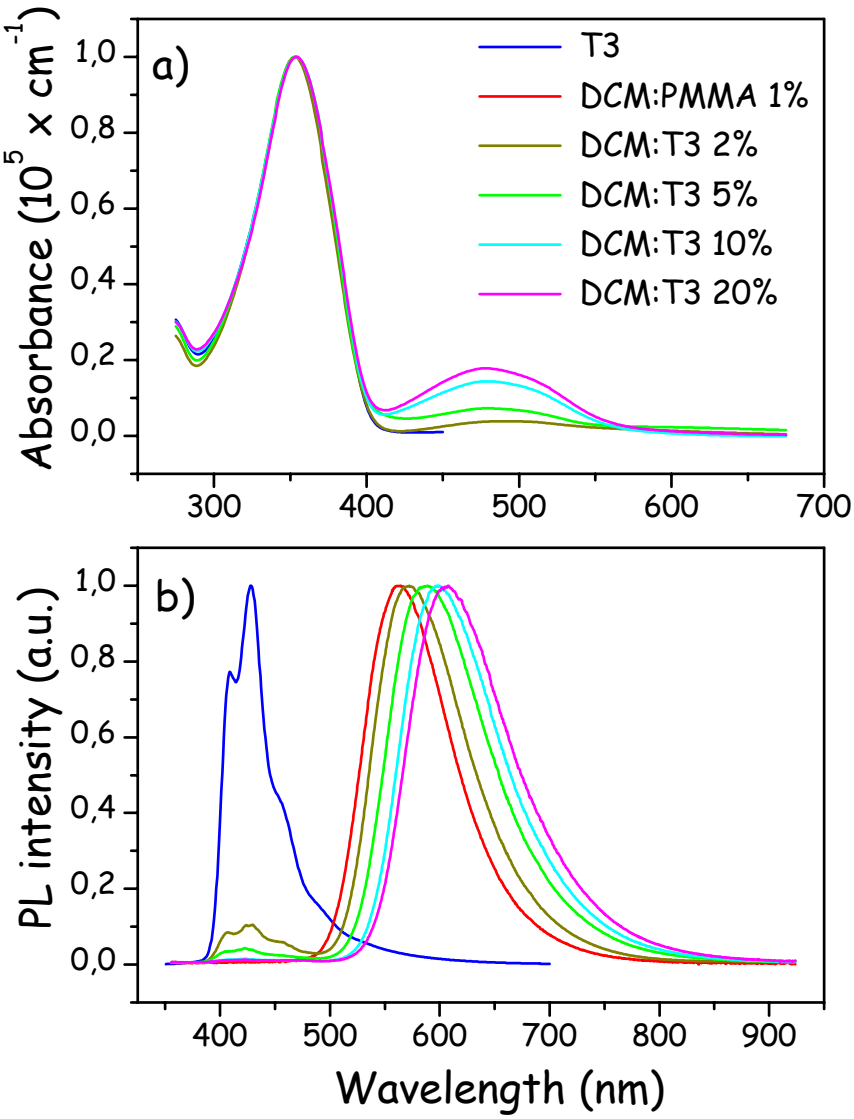

Figure 2. a) Absorption spectra of thin films of different DCM:T3 blends with increasing DCM molar concentration and T3 alone. All the spectra are normalized with respect to T3 alone absorption peak for clarity. b) PL spectra of thin films of different DCM:T3 blends with increasing DCM molar concentration obtained by exciting the donor component. PL spectra of neat T3 thin-film and of DCM solid solution at 1% in weight dispersed in PMMA are reported. PL spectra are normalized with respect their own maxima.

In the spectra of the composite films there is clear evidence of energy transfer from T3 to DCM, since increasing DCM concentration the T3 component gradually disappears (in 10% and 20% samples is completely absent). For the 2% and 5% samples we observe a slight blue-shift in the donor 0-1 PL peak due to DCM molecules reabsorption of the red wavelength portion of the donor fluorescence [12].

As the guest concentration is increased the DCM peak wavelength monotonically red-shifts from 570 nm for the 2% sample to 607 nm for the 20% sample and the peak full width at the half maximum (FWHM) broadens from 98 nm for the 2% sample to 108 nm for the 20% sample. We can infer that DCM molecules dispersed in a solid matrix of T3 undergo an energy shift due to self-polarization for the more dilute samples and to real aggregate formation for the more concentrated ones. As the concentration of highly polar (dipole moment at ground state μ_g=6.1 D [13]) DCM molecules in relatively non-polar T3 is increased, the distance between nearest-neighbour DCM molecules decreases, thereby increasing local electrical field experienced by DCM molecules. In general, polar dopants, such as DCM, tend to arrange locally in oriented domains that minimize the overall energy of the system, causing a spectral red shift with respect to the isolated molecules [14].
We indeed observe that the DCM emission in the 2% blend is red-shifted with respect to the emission of DCM dispersed at 1% in weight in a PMMA matrix.

For better understanding the role of the matrix on DCM emission features, we performed PL measurements exciting only the guest molecules in the blends (Fig. 3). As it can be seen, the DCM peak wavelengths and FWHM are almost the same regardless the fact that the DCM PL emission is collected either after excitation transfer from the host molecules or following direct excitation of the guest molecules.
From steady-state measurements, we can conclude that the time scale of the energy transfer process is much more rapid than the interaction dynamics between guest molecules and their environment. Therefore the inhomogeneous broadening of DCM molecules PL emission with increasing concentration is likely to be due to static disorder associated to acceptors in confined geometry. It seems that after the excitation is transferred, T3 matrix acts just as a host material without altering the emission properties of the acceptor molecules. So it is likely that using this blend as a recombination layer in a device the electroluminescent emission would remain the same regardless the processes that brings DCM molecules in the electronic excited state, i.e. exciton transfer from the donor molecules or direct charge trapping in acceptor molecules.

Also PLQY measurements indicate the interaction between DCM molecules even at relatively low concentration. As it can be seen in Tab. 2, although the PLQY of the DCM molecules dispersed in PMMA matrix is about 70% using a high efficient acceptor material the quantum efficiency of the blend system is not improved with respect to that of the pure T3 host. The 2% sample shows the highest PLQY while in the 10% and 20% samples the emission is severely quenched as expected when physical aggregates are

formed. PLQY measurements exciting exclusively and directly the DCM molecules show a similar trend. However in the latter case the absolute PLQY are much higher pointing out that the energy transfer process affects the overall quantum yield of the blend.

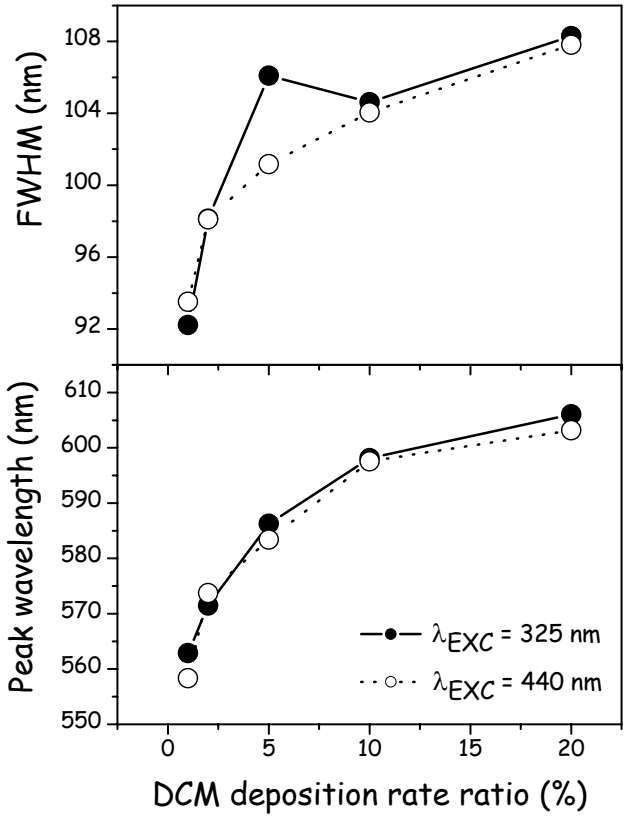

Figure 3. FWHM and emission wavelengths of DCM PL maximum at different excitation wavelengths with increasing DCM concentration. The donor and the acceptor are selectively excited at 325 nm and 440 nm respectively.

	T3	**2%**	**5 %**	**10 %**	**20 %**	**DCM**
PLQY @ 375 nm	0.46	0.25	0.12	0.07	0.06	0.7
PLQY @ 440 nm	-	0.4	0.21	0.1	0.08	0.6

Table 2. PLQY of DCM:T3 blends together with the values obtained from neat T3 thin-film and a solid solution of DCM dispersed in PMMA at 1% in weight. We selectively excite the donor or the acceptor components of the blend by using the 375 nm and the 440 nm wavelengths respectively.

4.2 Time-resolved energy transfer

The transfer of excitation from the excited T3 chromophores to the dye molecules is monitored directly with time resolved PL spectra. In Fig. 4 the 2%, 5% and 20% blend PL transient in three different temporal windows after excitation (0-4 ps, 4-8 ps and 8-12 ps) are reported. At early times only the 2% sample spectrum resembles almost completely the T3-alone one, apart from an instantaneous shift towards lower energy due to direct dyes excitation at this wavelength or to reabsorption effects. At later times we observe an enhancement of DCM emission together with T3 emission quenching which reflects the energy transfer process. The entire dynamical process occurs over a timescale of 30 ps. By increasing DCM concentration, the blend PL spectra shift faster towards lower energy: for the 20% sample the energy transfer is complete within 10 ps.

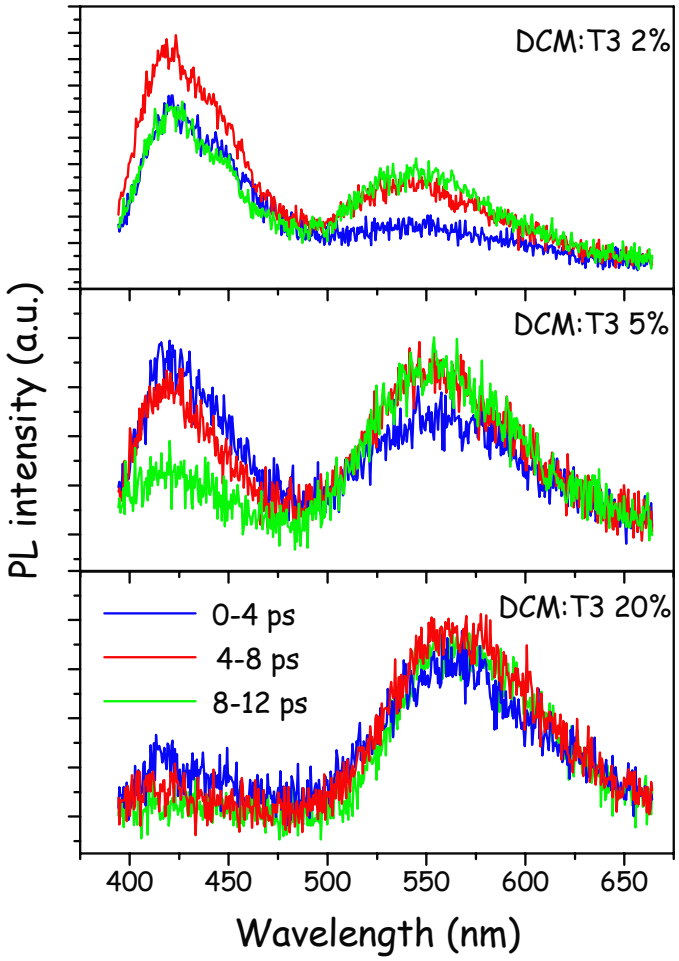

Figure 4. Transient PL spectra at different times for blends with different DCM concentrations.

For a deeper investigation of the energy-transfer time evolution of the blend system, in Fig. 5a we compare the PL decay collected at the T3 emission maximum in all the blend spectra with that of the neat T3 film.

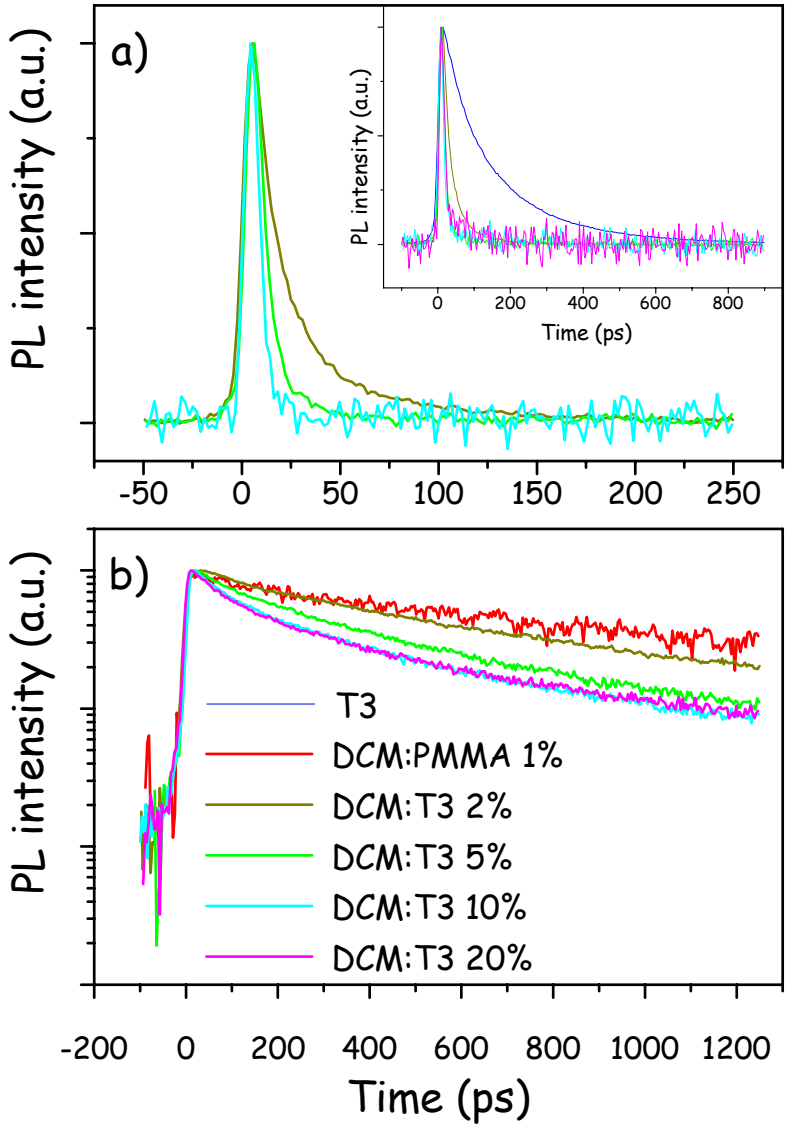

Figure 5. a) DCM:T3 blends PL decay at the T3 0-1 vibronic wavelengths for the 2%, 5% and 10% blends. Neat T3 thin-film and 20% blend PL decay are reported in the inset. The intensity is normalized at T=0. b) DCM:T3 blends PL decay at the DCM maximum emission wavelengths. PL decay of DCM dispersed in PMMA is also reported. The intensity is normalized at T=0

The donor-alone temporal decay is well-fitted by a bi-exponential curve with an initial time constant of around 70 ps merging into a tail of 200 ps, being the amplitude of the fast component the larger one (A~0.53). Since T3 thin-film dynamics is more

appropriately described by a distribution of lifetimes rather than by a single time constant [15], we define as donor lifetime constant the weighted average lifetime values obtained by the bi-exponential decay fitting.

From the time evolution of the neat T3 PL spectrum we can infer that within 10 ps after excitation there is a very fast transient spectral red-shift together with a slower inhomogeneous broadening of the 0-1 emission. It is likely that in competition with the decay to the electronic ground state, a transfer process of electronic excitation within the density of states (DOS) distribution from high-lying to low-lying sites takes place [16]. Since it is energy- and time-dependent, this process is likely to happen through an energy dispersive incoherent hopping transfer mediated by a distance dependent electronic coupling. Even if the inhomogeneous line width (taken as a rough estimation of the DOS) is quite large with respect to the thermal energy of the system at room temperature (~200 cm^{-1}), the relatively short excited state lifetimes prevent the observation of a clear energy-dependent relaxation process [17]. Previous spectroscopic investigations on polyfluorene thin-films showed that the distribution of decay rates could also be attributed to the trapping of excitons by spatially-localized non-radiative traps. In our case we can rule out this possibility since the time decay constants do not depend on the excitation spatial position on the sample [18].

By introducing dopant molecules in the matrix, T3 temporal decay becomes progressively more rapid as the dopant concentration is increased until the temporal resolution limit of the experimental set-up is reached for the 10% and 20% samples.

We will now investigate in deeper details T3 temporal dynamics of the 2% and 5% sample.

In the *2% sample* the donor decay is again satisfactorily fitted a by bi-exponential curve (τ_1~14 ps, τ_2~63 ps) in which the amplitude of the fast component is much larger than the slow one (A_1~0.85, A_2~0.15). The weighted average lifetime is about a factor of three shorter than the value obtained from neat T3 (see Tab. 3).

	Donor spectral range	Acceptor spectral range
T3	70 ps, 200 ps	*
2%	14 ps, 63 ps	92 ps, 695 ps
5%	8 ps	126, 543 ps
10%	resolution limit	74 ps, 490 ps
20%	resolution limit	67 ps, 471 ps
DCM	*	13 ps, 792 ps

Table 3. Lifetimes constants obtained from mono-/bi-exponential interpolations of the decay profiles of the blends, of T3-alone thin-film and of DCM molecules dispersed in PMMA.

The DCM:T3 blend can be described as a three-dimensional system with randomly distributed acceptor molecules in which the overlap integral (3) between the donor emission and the acceptor absorption spectra is not negligible and the donors and acceptors translational diffusion can be neglected. Therefore the donor lifetime decay should be in principle described by the Förster ensemble-averaged nonexponential curve [19]:

$$I(t) = \exp\left[-\left(at + bt^{1/2}\right)\right] \qquad (4)$$

with

$$a = 1/\tau_D \; ; \; b = g\frac{4}{3}\pi^{3/2} n_A R_o^3 \Big/ \tau_D^{1/2} \qquad (5)$$

where τ_D is the fluorescence lifetime of the donor in absence of the acceptors, n_A is the acceptor number density, R_0 the Förster radius and $g = \sqrt{3\langle k^2 \rangle / 2}$ with $\langle k^2 \rangle$ the molecular orientation factor.

Using (4) as interpolating curve we find that the fit quality is not as good as for the bi-exponential one. From the fitting parameters we calculate the donor lifetime τ_D as 70 ps and the acceptor number density n_A as 8.9×10^{18} cm^{-3}.

It is interesting to note that the donor fluorescence lifetime according to Förster fit is similar to the longer lifetime component obtained by fitting the data with two exponentials. Moreover both the Förster lifetime constant and the weighted mean value of

lifetime constants of the bi-exponential decay (22 ps) deviate significantly from the corresponding weighted mean value of the pure T3 (133 ps).

According to (4) the fluorescence is most rapid at the earliest times due to Förster transfer between close-lying donor-acceptor pairs. The decay rate of the host-guest system should asymptotically approach the host decay rate, because the host dynamics is dominated at longer times by excited molecules that lie relatively distant from the acceptor molecules [20]. Taking into account the possible spectral exciton diffusion in the host material we described above, deactivation through diffusion-assisted energy transfer may provide an additional decay pathway that reduces the calculated host lifetime. This scenario is well corroborated by the data we collected. In the first few tens of picoseconds after excitation most of the host photoluminescence is quenched due to the saturation of the guest nearest neighbours sites for energy transfer as the large amplitude of the fast component in the bi-exponential decay highlights. Nevertheless diffusion is expected to reduce the rate of saturation of the nearest neighbours sites since excitons can travel in the host before transferring to the guest [21] as indicated by the reduction of lifetime constant obtained from Förster theory with respect to pure T3. Given that also the 2% sample donor decay is also described by a distribution of lifetimes we can infer that the exactions after being formed in T3 chromophores can diffuse through a distribution of different energy sites due to the inhomogeneous dispersion or to the preferential rearrangement of DCM molecules in the matrix. This hypothesis can be sustained by the fact that the acceptors number density obtained from the *b* parameter in Förster fitting (5) of the PL decay is an order of magnitude smaller than the one calculated from absorption measurements (Tab. 1). Indeed the migration of the excitons in the host matrix would increase the overall energy transfer distance and result in an overestimation of the mean host-guest distance (R_{DA}).

Nevertheless we have to mention that from previous ellipsometry measurements on vacuum-deposited thin-film [5], T3 films exhibit rather significant uniaxial anisotropy with the optical axis along the surface normal. Given that the in-plane extinction coefficients are larger than out-of-plane coefficients, calculating n_A from normal-incidence absorption measurement assuming an isotropic distribution of the host molecules can produce an overestimation of the guest numeric density, and consequently an underestimation of R_{DA}.

In *5% sample* the host temporal dynamics can be well fitted by mono-exponential decay indicating the less dispersive nature of the energy transfer with this specific guest

concentration. It is plausible that the mean donor-acceptor distance does not increase with time since the higher acceptors density guarantees a rapid saturation of all the energy-transfer sites now homogeneously dispersed around the host molecules as the very fast and single lifetime constant indicates (~8 ps).

In Fig. 5b we report the radiative decay profiles collected at the DCM emission maximum for each blend sample pumped at 385 nm. All the blend decay curves are only well-fitted by bi-exponential interpolation curves with the temporal dynamics getting faster as the guest concentration increases. We observe a general PL quenching of the host-guest samples with respect to the solid solution of DCM molecules dispersed in PMMA in which an almost mono-exponential dynamics behaviour is present. Faster PL decay at higher concentrations coupled with a second slower time-constant component suggests that additional nonradiative decay pathways of the DCM excited state now compete with emission from isolated molecules.

In Fig. 6 we compare the transient DCM PL within the first 20 ps with the quasi steady-state PL, for 2% and 20% samples together with the solid solution of DCM molecules dispersed in PMMA. For the latter sample we observe a red-shift of the maximum peak wavelength of about 13 nm without a significative increase of FWHM which can be ascribed to intramolecular energy relaxation. Regarding the 2% sample the wavelength redshift and FWHM variation roughly do not increase in early times with respect to the solution-like sample. We can infer that at low concentration the highly polar DCM molecules firstly start interacting among themselves through a dipolar interaction in the much less polar T3 matrix. In the 20% samples the FWHM and emission wavelengths increase from early times indicating the enhancement with time of the local static disorder around T3 molecules and the formation of weakly emissive DCM aggregates [22, 23]. This scenario is well corroborated by the steady-state measurements we reported above.

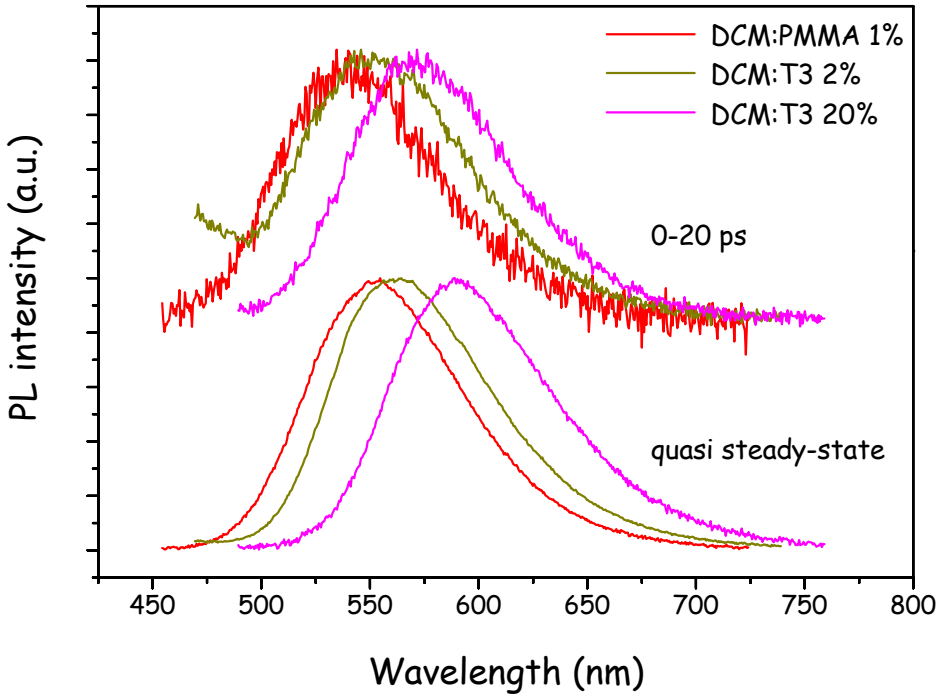

Figure 6. Emission of the DCM component in 2% and 20% blends in the first 20 ps (upper) and in almost steady-state times (lower). Emission from DCM molecules dispersed in PMMA matrix is reported for comparison.

The 10% and 20% samples present identical spectroscopic features, i.e. emission wavelengths, PL quantum yields, lifetime constants. This can highlight that a guest concentration exists, above which the electronic characteristics of the emitting aggregates in T3 matrix reach an equilibrium value.

As it can be inferred from Fig.4 for the 2% and 5% samples the DCM signal shows an initial rise in intensity at early times reaching a maximum value, whereupon the signal starts its natural decay. The initial rise is attributed to the energy transfer process from the T3 host to the DCM guest, resulting in an increasing population of guest molecules in the exited state. After the initial population buildup, the guest molecules undergo natural radiative and nonradiative decay. The amount of time required for buildup of guest molecules in the excited state (referred to as the rise time τ_{rise}) decreases as the guest concentration increases. Fitting the guest transient signal by a negative exponential function in the temporal range before guest PL decay starts [19] it is possible to achieve an estimation of τ_{rise}: around 7 ps and 3 ps for 2% and 5% samples respectively.

We can estimate the energy transfer rate immediately after the host excitation from the guest rise time through the expression: $k_{ET} = \tau_{rise}^{-1} - \tau_{DA}^{-1}$ in which τ_{DA} refers to the donor

single lifetime constant in the blend. The energy transfer rates we calculated for the 2% and 5% blends are 57 GHz and 118 GHz.

Both these values are higher than the ones obtained from the Förster relation $k_{ET} = \tau_{DA}^{-1} - \tau_D^{-1}$ in which donor lifetimes in the blend (τ_{DA}) and alone (τ_D) are taken into account. It is interesting to note that for the 2% blend the energy transfer rate obtained from the guest rise time is much higher than the "steady-state" value, indicating that the energy transfer between the closest-lying donor-acceptor pairs dominates the dynamics at the earliest times following excitation. This is a clear signature of the Föster-like nature of the energy transfer process for the 2% blend.

Complementary information about the energy transfer dynamics between host and guest molecules is obtained from femtosecond time resolved pump and probe spectroscopy, which is able to monitor the optical properties of the sample at a time resolution less than 100 fs. These measurements are performed by Tobias Plötzing at RWTH in Aachen. In pump and probe experiments stimulated emission (and not spontaneous as in PL measurements) is probed so allowing for the direct determination of optical gain within the organic film. In Fig. 7 transmittance variation of the white light probe pulse after passing through the 2% DCM:T3 film is displayed as a function both of detection wavelength and time delay after the optical excitation. Blue coloured regions indicate a decrease of transmittance due to the pump pulse, whereas in red coloured regions the probe pulse is amplified during its propagation through film after the optical excitation of the host molecules. At negative time delays, i.e. when the probe pulse strikes the sample before the pump pulse, no significant change in transmittance is observed. The slight enhancement around the PL emission maximum at 600 nm can be ascribed to the residual spontaneous emission of the excited DCM molecules, which is collected by the detection system. At zero time delay an instantaneous decrease in transmittance occurs for all wavelengths, which subsequently vanishes in the long and short wavelength regions of the graph.

In the centre wavelength region a transient increase to positive transmittance changes with its maximum at ~ 40 ps is present. For a more detailed analysis, temporal cross sections of the probe transmittance variation at the specific wavelengths of 690 nm 600 nm are displayed in Fig. 8. In the long wavelength case (Fig. 8a) the transmittance through the sample abruptly drops when the sample is excited by the pump pulse. Since the pump

energy is predominantly absorbed by the T3 host molecules, the sudden drop in transmittance has to be attributed to an excited-state absorption within the T3 matrix.

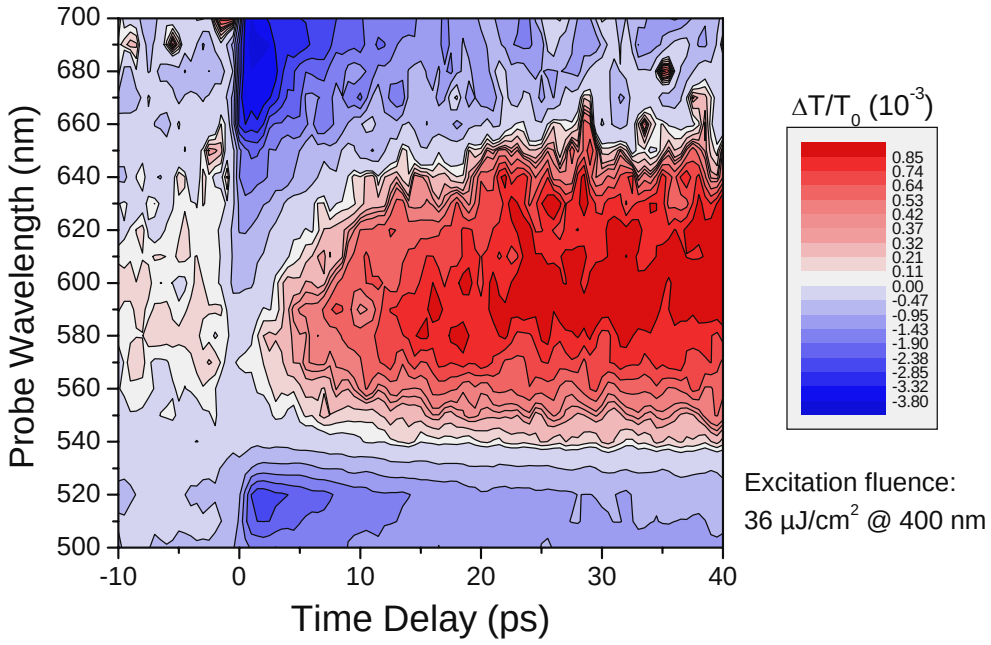

Figure 7. Spectrally and temporally resolved transmittance change of a 130 nm thick DCM:T3(2%) film obtained in a femtosecond pump probe measurement. The sample is excited by a 40 fs laser pulse at 400 nm central wavelength and a fluence of 36 µJ/cm^2. Red coloured regions indicate optical gain, whereas blue regions indicate pump induced additional loss.

At these early time delays the DCM guest molecules are not yet excited. When the energy is subsequently transferred from T3 to DCM molecules, the number of excited T3 molecules decreases and hence the transmittance change recovers to zero exponentially. From a numeric fit, we find a relaxation constant of 9.5 ps. In Fig. 8b the temporal dynamics of the probe transmittance at the maximum PL emission wavelength of DCM is depicted. The short drop in transmission at zero time delay is again attributed to excited-state absorption in T3. Admittedly, at this wavelength the increasing number of excited DCM molecules leads to an amplification of the probe light and quickly the absorption is overcompensated leading to a positive transmission change. An exponential fit to the build-up of gain provides exactly the same time constant of τ_{rise} = 9.5 ps, supporting the above sketched assumptions. Furthermore the time constant τ_{rise} is in good agreement with the value of 7 ps obtained from time-resolved PL measurement.

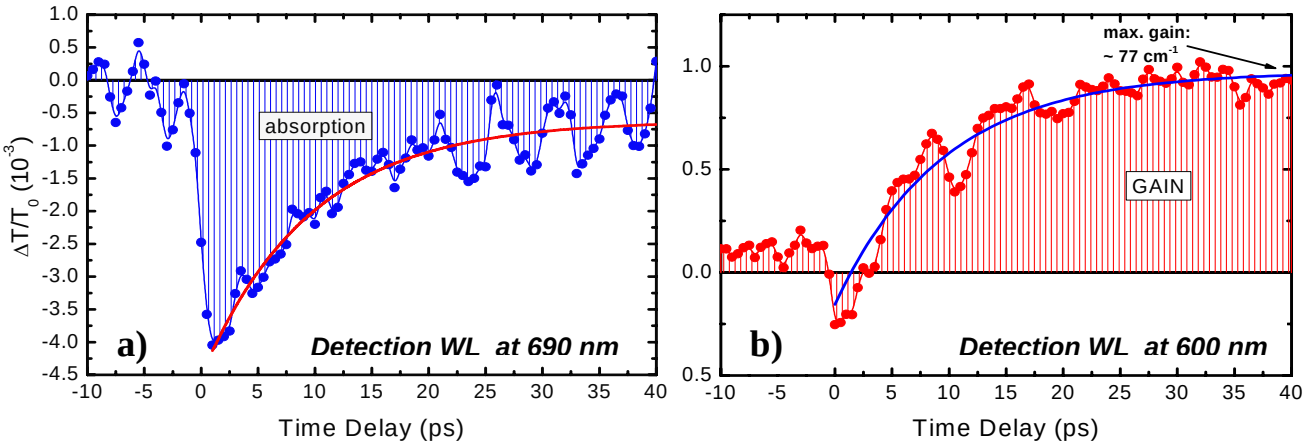

Figure 8. Temporal cross sections of Figure 9. a) Cross section at 690 nm, where a maximum absorption increase is observed (blue circles). b) Cross section at maximum gain wavelength of 600 nm (red circles). From exponential fits to the data for positive time delays (red (a) and blue (b) solid lines) the rise time for energy transfer from T3 host to DCM guest molecules τ_{rise} = 9.5 ps is obtained.

4.3 ASE threshold

Since the feasible application of this new host-guest system is the realization of electrically pumped organic lasers, we need to correlate the energy-transfer dynamics with the mirror-less lasing properties. In Tab. 4 we report the ASE pump intensity thresholds with varying DCM concentrations in the blends together with the T3-alone value. The ASE measurements are carried out as described in Chapter 2 and the ASE threshold is defined as the pump intensity at which the FWHM is reduced to half the FWHM of the PL at low pump intensity.

	T3	2%	5%	10%	20%
ASE THRESHOLD [kW/cm^2]	4.4	0.6	1.1	2.8	3.8

Table 4. values of the amplified spontaneous emission thresholds for the blends and T3-alone thin-films calculated as reported in the text.

The ASE peaks located always in the DCM emission region regardless the dopant concentration reveal that upon T3 molecules excitation the energy transfer towards DCM molecules dominates over the T3 stimulated emission process. Considering the laser exciting pulse (25 ns at FWHM) as steady-state compared with the energy transfer and radiative decay timescale in the system, we can assign the energy transfer rate in the first 20 ps in the 2% sample as an inferior limit for the ASE rate value in the neat T3 thin-film.

Increasing DCM concentration the energy transfer rate seems to increase while ASE threshold does not reduce. It is worthy noting that in ASE spectrum of the 20% sample the DCM ASE peak is much broader and the T3 emission component is clearly visible (but completely absent in the steady-state transmission spectrum) as if T3 and DCM ASE processes were competing (Fig. 9). Moreover the lowest ASE threshold value is found in correspondence of the 2% sample, indicating that the spontaneous emission guided through the exciting stripe is very sensitive to the aggregation state of the emitting molecules.

The overall trend of ASE thresholds at different DCM concentrations can be explained with respect to the spectroscopic parameters we measured. From the acceptor quantum yield (Φ_A) and lifetime constant (τ_A) in the blend it is possible to determine the radiative decay rate ($k_r = \Phi_A / \tau_A$). Here, k_r is related to Einstein's coefficient B (see § 1.3.2) through the relation $B \sim (c^3/8\pi h\nu_0^3)k_r$ where h is the Planck's constant, ν_0 is the frequency of light and c is the velocity of light. Since the ASE threshold is inversely proportional to B coefficient, we would expect a large k_r to result in a low ASE threshold [24]. Indeed the 2% blend presents the higher acceptor radiative decay together with the lowest ASE threshold.

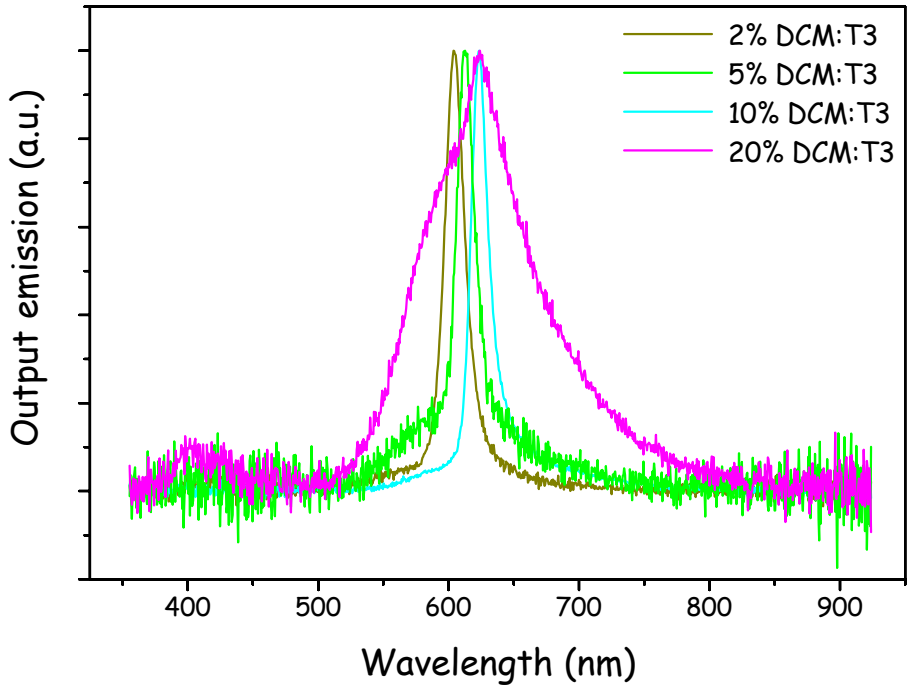

Figure 9. Normalized DCM:T3 blends emission spectra collected from the edge of a 4 mm^2-wide excitation stripe. The pump intensity is higher than the ASE threshold.

This value corresponding to about 0.6 kW/cm^2 is not only 7 times lower than the T3-alone ASE threshold value, but almost an order of magnitude lower than the ASE threshold value we measured under the same experimental conditions for the model system DCM:Alq_3 (Fig. 10). It is important to note that the ASE measurements on the two different host-guest systems are carried out using the same experimental set-up so that the extracted ASE threshold values can be reliably compared. From pump-and-probe

measurements on the 2% sample reported above, it is also possible to extract a maximum gain of 77 cm^{-1} for the investigated pump fluence of 36 $\mu J/cm^2$ (Fig. 10a).

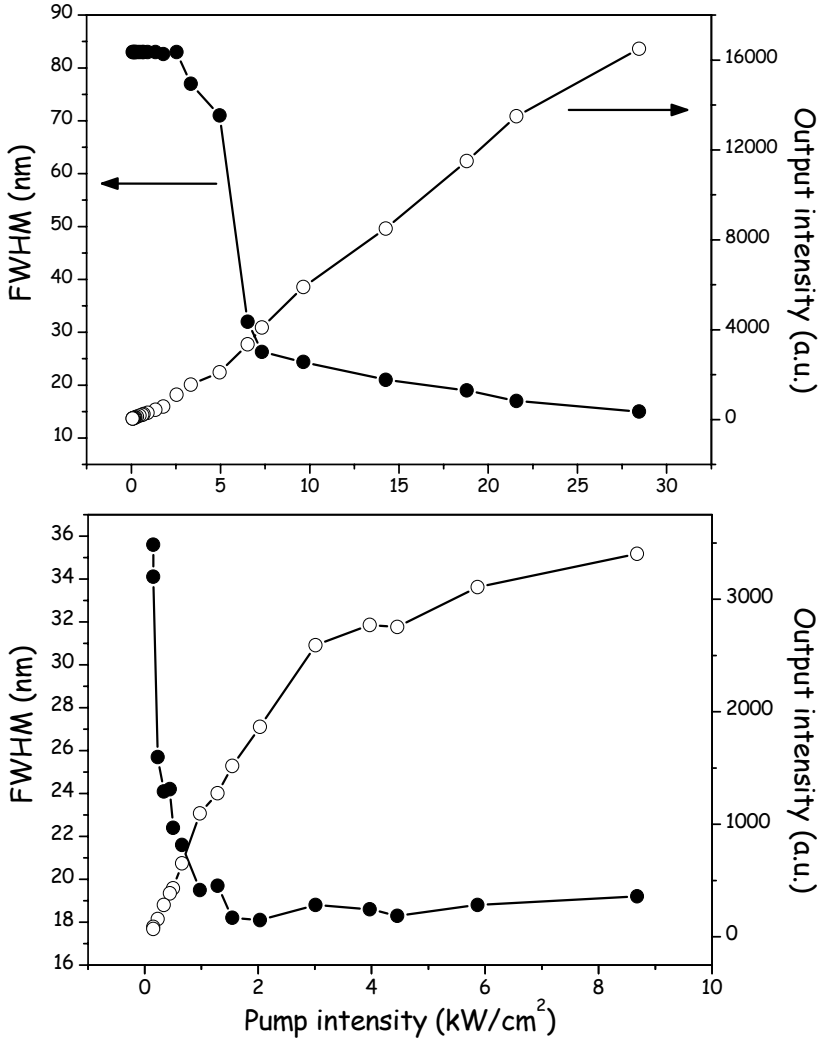

Figure 10. Dependence of the photoluminescence intensity (open circles) and full width at half maximum (solid circles) on the excitation pump intensity for a 300 nm-thick thin film of 2% DCM:Alq_3 blend (upper) and a 150 nm-thick thin-film of 2% DCM:T3 blend (lower).

All the different parameters that can be optimized in a specific ASE threshold measurements (laser pulse duration and repetition rate, stripe dimensions and shape, collecting geometry,…) prevent us from comparing ASE threshold values of materials we used from literature.

Differently from transient absorption measurements, geometrical and physical constrains in the ASE measurements are very close to those of real waveguide lasers. Moreover using

a laser source with a 10 Hz repetition rate, triplets accumulation and undesirable thermal effects are prevented since after excitation the gain medium is given time to recover prior to the arrival of the next excitation pulse [25]. Since we are dealing with host-guest systems, it is important that the laser pulse amplitude is much longer (in the order of ns) than the energy transfer and nonlinear nonradiative processes timescale so that the depletion of the excited DCM molecules can occur via ASE [26].

It can be seen that the ASE peak is located in the low energy region of the PL spectrum because the higher net gain always takes place at the peak far from the absorption edge that would introduce self-absorption [27]. We also note that the ASE peak shift decreases with respect to PL peak with increasing DCM concentration. Since the films present nominally the same thickness (about 150 nm), it is likely that the ASE wavelength position for higher concentration samples could be induced by excited-states absorption (reducing net gain at larger wavelengths) rather than amplification of different modes due to cavity effects.

Consistently photoinduced absorption (PIA) measurements on ms timescale carried out on T3-alone thin-film shows a sharp peak centered at 690 nm with some broaden replica at higher energies (Fig. 11).

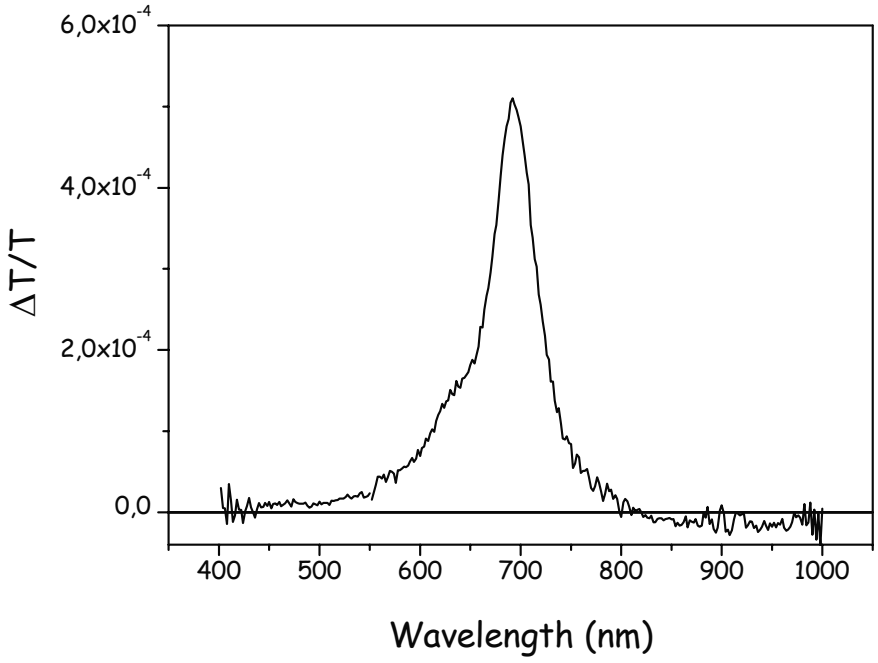

Figure11. Photo-induced absorption spectrum of T3-alone thin-film at 100 K and ω = 80 Hz modulation frequency.

According to J. Cabanillas-Gonzales [28], this peak can be attributed to triplet – triplet absorption from the lowest T_1 state to a generic upper lying T_n state, whose temporal decay can be ascribed to triplet-triplet annihilation through a bimolecular recombination in ms timescale.

4.4 Conclusion

The investigation of the photo-physical properties of the host-guest system T3:DCM highlights that an efficient Förster energy transfer takes place from the T3 matrix to the DCM molecules.

The energy transfer dynamics is deeply affected by the guest concentration as the steady-state and picosecond time-resolved PL spectroscopy probing revealed. Indeed, we find out that the non-radiative energy transfer is Förster-like only for the lowest guest concentration sample. For higher guest concentrations the energy transfer becomes much faster and the overall dynamics is dominated by the guest interaction and aggregation.

As expected the blend system shows lasing properties since DCM spontaneous emission can be amplified in the medium when pumping T3. The mirroless lasing measurements performed on the blends, reveal that the lowest ASE threshold is presented by the blend in which the guest aggregation is almost negligible and the energy transfer is incomplete.

The 2% DCM:T3 ASE threshold value is an order of magnitude lower than that of the 2% DCM:Alq_3 model system measured in the same experimental conditions.

So, DCM:T3 host-guest system is a very attractive candidate as a gain medium for fabrication of organic solid-state lasers since reducing the ASE threshold to ultra-low values is one of the key parameters that allows the reduction of the polaron-exciton interaction in the gain medium of an electrically-pumped devices.

As we will see in the next chapter, implementing doped matrices in heterojunctions-based organic light emitting transistors (OLETs) seem to be a very promising device architecture for realizing electrical injection laser.

OLETs present fundamental advantages with respect to organic light-emitting diodes (OLED). The exciton quenching at the metal electrodes is reduced by controlling the location of the recombination region inside the device active area using the gate voltage and the exciton-charge quenching is reduced by a better current balance within the device. Moreover inside the OLET active region the current densities achievable are higher (10-10^3 A/cm^2) and the integration of a resonant optical cavity is much easier.

References

[1] D. Yokoyama, H. Nakanotani, Y. Setoguchi, M. Moriwake, D. Ohinishi, M.Yahiro, and C. Adachi, *Jpn. J. Appl. Phys.,* **2007**, 46, L826.

[2] H. Yamamoto, H. Kasajima, W. Yokoyama, H. Sasabe, and C. Adachi, *Appl. Phys. Lett.*, **2005**, 86, 83502.

[3] A. K. Sheridan, A. R. Buckley, A. M. Fox, A. Bacher, and D. D. C. Bradley, *J. Appl. Phys.*, **2002**, 92, 6367.

[4] G. Krazelbinder and G. Leising, *Rep. Prog. Phys.* **2000**, 63, 729.

[5] H. W. Lin, C. L. Lin, H. H. Chang, Y. T. Lin, and C. C. Wu, Y. M. Chen, R. T. Chen, Y. Y. Chien, and K. T. Wong, *J. Appl. Phys.*, **2004**, 95, 881.

[6] H. W. Lin, C. L. Lin, C. C. Wu, T. C. Chao, K. T. Wong, *Org. El.*, **2007**, 8, 189.

[7] W. Lu, H. You, J. Fang, and D. Ma, *Appl. Opt.*, **2007**, 46, 2320.

[8] T. Förster, et al., *Modern Quantum Chemistry, Part 2 : Action of Light and Organic Molecules* (Academic, New York, 1982).

[9] I. M. Rozman, *Opt.Spectrosc.*, **1958**, 4, 536.

[10] S. Chandrasekhar, *Rev. Mod. Phys.*, **1943**, 15, 86.

[11] J. Salbeck, N. Yu, J. Bauer, F. Weissörtel, and H. Bestgen, *Synth. Met.*, **1997**, 91, 209.

[12] K. C. Jena, P. B. Bisht, *Chem. Phys.*, **2005**, 314, 179.

[13] G. Kwak, C. Okada, M. Fujiki, H. Takeda, T. Nishida, and T. Shiosaki, *Jpn. J. Appl. Phys.*, **2008**, 3, 1753.

[14] R. Farchioni, G. Grosso, *Organic Electronic Materials* (Sprinter-Verlag Berlin Heidelberg 2001)

[15] B. Mollay, U. Lemmer, R. Kersting, R.F. Mahrt, *Phys. Rev. B*, **1994**, 15, 10769.

[16] S. C. J. Meskers, J. Hübner, M. Oestreich, and H. Bässler, *J. Phys. Chem. B*, **2001**, 105, 9139.

[17] R. Hildner, U. Lemmer, U. Scherf, J. Köhler, *Chem. Phys. Lett.*, **2006**, 429, 103.

[18] B. Haring Bolivar, G. Wegmann, R. Kersting, M. Deussen, U. Lemmer, R. F. Mahrt, H. Bässler, E. O. Göbel, H. Kurz, *Chem. Phys. Lett.*, **1995**, 245, 534.

[19] M. Lee, J. Tang, R. M. Hochstrasser, *Chem. Phys. Lett.*, **2001**, 344, 501.

[20] M. A. Wolak, J. S. Melinger, P. A. Lane, L. C. Palilis, C. A. Landis, J. Delcamp, J. E. Anthony, and Z. H. Kafafi, *J. Phys. B*, **2006**, 110, 7928.

[21] B. P. Lyons, and A. P. Monkman *Phys. Rev. B*, **2005**, 71, 235201.

[22] G. D. Scholes, X. J. Jordanides, and G. R. Fleming, *J. Phys. Chem. B*, **2001**, 105, 1640.

[23] M. Pope, C. E. Swenberg, *Electronic Processes in Organic Crystals* (Oxford University Press, New York, 1982).

[24] T. Aimono, Y. Kawamura, K. Goushi, H. Yamamoto, H. Sasabe, and C. Adachi, *Appl. Phys. Lett.*, **2005**, 86, 71110.

[25] I. D. W. Samuel and G. A. Turnball, *Chem. Rev.*, **2007**, 107, 1272.

[26] C. Kallinger, S. Riechel, O. Holderer, U. Lemmer, and J. Feldmann, S. Berleb, A. G. Mückl, and W. Brütting, *J. Appl. Phys.*, **2002**, 91, 6367.

[27] M. D. McGehee, A. J. Hegeer, *Adv. Mater.*, **2000**, 12, 1655.

[28] J. Cabanillas-Gonzales, C. Sciascia, G. Lanzani, S. Toffanin, R. Capelli, M. C. Ramon, M. Muccini, J. Gierschner, T.Y. Hwu, K.T Wong, *J. Phys. Chem B*, **2008**, 112, 11605.

Chapter 5
Ambipolar light-emitting transistors based on organic heterojunctions with lasing properties

5.1 The organic heterojunction approach

In recent years it has become clear that the chemical structure of the organic semiconductor is not the only factor that determines whether an organic FET exhibits predominantly p-channel or n-channel behaviour. Processing and characterization conditions, device architecture, and choice of electrodes are important as well. It is thus not appropriate to speak of p-type or n-type materials, but one should rather refer to p-channel or n-channel transistors. A key discovery was the identification of the crucial role of the gate dielectric and the identification of electron trapping mechanisms in devices based on SiO_2 gate dielectrics [1]. This subsequently led to the general observation of n-channel and ambipolar characteristics in a broad range of organic semiconductor FETs based on trap-free gate dielectrics [2]. This and other recent experimental and theoretical studies suggest that organic semiconductors are intrinsically ambipolar and thus capable of conducting both electrons and holes in suitable device configurations and under inert testing conditions.

In an ideal ambipolar transistor with just one semiconducting layer, the ambipolar regime is characterized by a hole and an electron accumulation layer next to the respective electrode that meet at some point within the transistor channel. There, oppositely charged carriers recombine. In electroluminescent materials, this leads to light generation within the channel. The length of each channel and thus position of the recombination zone depend on the applied gate and source-drain voltage and mobility ratio. The behaviour of an ambipolar field-effect transistor in the ambipolar regime of a transfer characteristic can

roughly be imagined as that of a saturated hole and electron field-effect transistors in series [3].

One of the reasons in the increasing interest in realizing ambipolar OFETs is that they seem predestined for light emission since they can provide an effective pn-junction within the transistor channel and thus radiative recombination of holes and electrons [4].

Even if the first results were reported unexpectedly for unipolar organic transistors [5] and many examples of that kind have been demonstrated since then [6] most of the scientifically and technologically remarkable properties that make light-emitting transistors desirable are, however, only present in ambipolar organic light-emitting transistors (OLETs). These include control over the position of the emission zone, emission far away from metal electrodes, high current densities, low charge concentration within the emission zone, and perfectly balanced hole and electron currents. These properties could make light-emitting transistors attractive for novel integrated electro-optical switches and, potentially, electrically pumped lasers. They also offer a convenient planar structure with which to investigate recombination physics in organic semiconductors using spatially resolving probes [1].

In particular these aspects are of increasing importance when devices are driven under high-injection conditions for high-brightness emission. It should be noted that the current density in an OLET is expected to be higher (1–10 A/cm^2 assuming a 1-nm-thick accumulation layer) than in OLEDs (10^{-3}–10^{-2} A/cm^2) [7]. However, the extreme spatial localization of charge carriers in an OLET could be more favourable for an effective spatial separation between the exciton population and the charge carriers. The availability of a third electrode to balance electron and hole currents and therefore to further reduce exciton–charge quenching is the other obvious advantage of OLETs.

For realising efficient ambipolar transport based ambipolar different approaches can be pursued: one can employ a single organic material capable of transporting electrons as well as holes (single component approach) or combine two unipolar transport materials (multicomponent approach).

In the single material approach, a single-layer device is fabricated using both small-molecules [8] or polymer [9] as active material (Fig. 1a). When the single-component ambipolar OFET is biased with a gate voltage value in between the source and the drain voltage values, an electron accumulation layer should form near one electrode coexisting with a hole accumulation layer near the other electrode. Normally this regime is defined as *truly ambipolar*.

Thus, electrons and holes are expected to recombine where the two accumulation layers meet, leading to light emission from a well-defined zone.

In polymer-based organic field-effect transistors (OTFTs), for a small number of materials, control of the electron-hole recombination region inside the device channel has been already demonstrated with high electroluminescence efficiency in correspondence of ambipolar transport [2]. One of the limiting drawback of polymer-based devices is the low value of charge carrier mobility that can be obtained.

In the multi-component approach, OLETs can be obtained superposing two layers of unipolar materials in bilayer structure [10] (Fig. 1b) or can be fabricated by simultaneous coevaporation of two unipolar materials realising a bulk heterojunction [11].

In bulk organic heterojunction exciton formation and charge transport are competitive processes due to the dispersed interface between the p-type and n-type transport materials. Clearly, the wider the interface surface is, the higher the probability that electrons and holes recombine in forming excitons. Nevertheless, connected percolative paths are needed for the charges to migrate by hopping so that interface can represent a physical obstacles for efficient charge transport.

Even if interface morphology is precisely controlled during vacuum sublimation, well-balanced ambipolar behaviour is almost impossible to achieve.

Rost et al. reported the first ambipolar light-emitting transistor based on coevaporated PTCDI-$C_{13}H_{27}$ (P13) and α-quinquethiophene (α-5T). Light emission was observed for several voltage conditions, and the light intensity was proportional to the drain current. However, the position of the emission zone was not reported. Loi et al. later found that light emission from this blend depends on the ratio of P13 to α-5T [12]. When there is an excess of α-5T, ambipolar transport takes place but no light is detected, which is attributed to quenching of P13 excitons upon interaction with α -5T. For an excess of PTCDI-$C_{13}H_{27}$, on the other hand, only n-channel behaviour is observed. Nevertheless, light is emitted from the transistor.

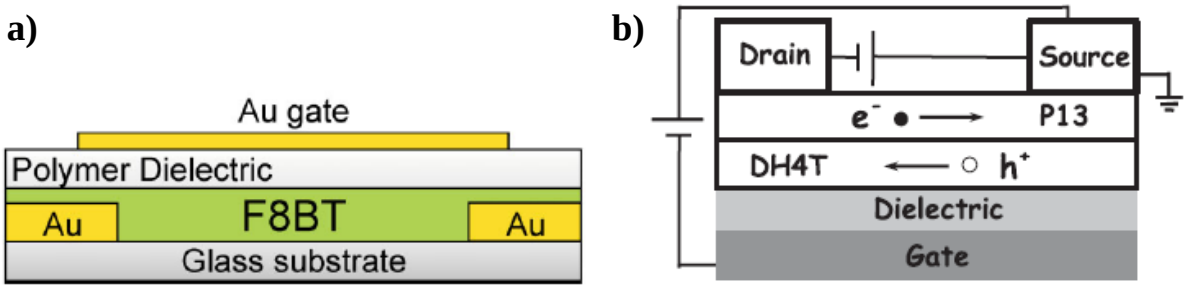

Figure 1. a) Schematic illustration of a bottom-contact/top-gate polymer OLET with gold source/drain electrodes, F8BT as the semiconducting and emissive polymer, a spin-cast insulating polymer as the gate dielectric, and an evaporated top-gate electrode [9]. b) Schematic of a bottom gate/top contac OLET based on a DH4T–P13 bilayer. The active layers are deposited by vacuum sublimation on a Si/SiO_2 substrate in sequence. The dielectric thickness is 300nm and the contacts are made of gold [10]

In the case of bilayer structures, a balanced ratio between hole and electron current density should guarantee the maximization of electroluminescence emission. However the physical separation between p-transport and n-transport material confines holes and electrons in the respective unipolar layers almost preventing exciton formation and light emission

Dinelli et al. reported that bilayers of α,ω-dihexylquarterthiophene (DH4T) and P13 show good ambipolar transistor behavior and light emission [10]. However, light emission took place only in the unipolar regime, which indicates that one should consider the pn-junction underneath the electrodes as the source of emission instead of a recombination zone arising from hole and electron channels in series.

TRI-LAYER HETEROJUNCTION OLET

In order to exploit completely the scientific and technological potentiality of OLET devices it is necessary to achieve the maximum of electroluminescence efficiency in the correspondence of the maximum of charge current density.

So, we propose a new approach in realizing ambipolar OLET based on a device architecture that can guarantee higher and well-balanced current density for both electrons and holes and the separation of the region of maximum charge accumulation from the region of exciton formation and light emission, thus preventing charge-exciton quenching.

We propose a tri-layer vertical heterojunction (Fig. 2) as active material in bottom gate/top contact ambipolar OFET in which two layers (the bottom and the top ones) are devoted to

the electron and hole transport (*n*- and *p-transport layers*) while the middle layer is for exciton formation and light emission (*recombination layer*).

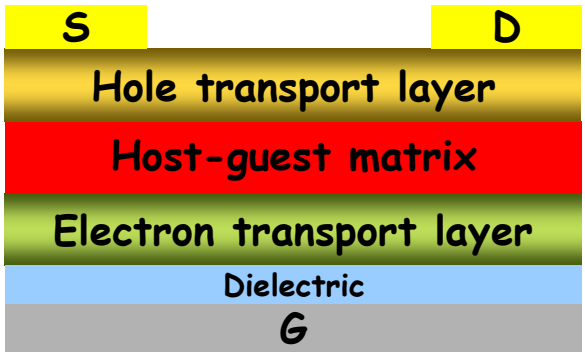

Figure 2. Schematic of a tri-layer vertical heterojunction-based OLET in a bottom gate/top contact configuration

The recombination layer is engineered as a molecular binary host-guest system with an efficient Förster energy transfer and ASE properties under optical pumping (see Chapter 4).

Thus, the tri-layer heterojunction configuration can be considered as an ideal platform for realizing micro-scale integrated multifunctional devices such as electrically-pumped organic laser. Indeed not only the high charge current density achievable in OFET and low charge-exciton interaction in tri-layer configuration, but also the easily implementation of a resonant cavity in a planar geometry make the ambipolar OLET device we propose a competitive structure for realizing electrically-pumped laser.

Hereafter the working principles of the tri-layer heterojunction based OLETs presented in Fig. 2 are described in more details. The first organic thin-film in contact with the device dielectric layer is devoted to the unipolar field-effect n-type transport. The second layer deposited onto it is the recombination layer which present high emission quantum efficiency and OLED-like vertical bulk mobility value. The third layer is devoted to unipolar p-type charge transport (complementary to that of the first layer).

So, in the first and top layers a planar field-effect transport of opposite charges take place, generating the ambipolar electrical characteristics of the device.

The vertical field created by the two opposite charge distributions in the field-effect accumulation regions enable a portion of the electrons and holes currents to percolate into the recombination layer. The bulk conducting properties of the recombination layer

guarantee that either both or one of the charge carriers can migrate (through hopping or diffusion) in that layer until the condition for excitons formation are energetically favourable. Indeed in the structure we present, the recombination layer is engineered so that exciton formation may take place by an energy transfer process in the host-guest system (see § 5.2).

The key idea of the vertical tri-layer heterojunction approach in realizing OFET is that each layer has to be optimised according to its specific function (charge transport, energy transfer, radiative exciton recombination…). Clearly, matching the overall device characteristics with the functional properties of the single materials composing the active region of the OFET, is a great challenge that requires a deep investigation of the morphological, optical and electrical features of the system.

In particular, functional interfaces play the predominant role in determining the performance of vertical tri-layer heterojunction. Since it is well-established that in OFET planar devices only the first few nanometers of the transport layer from the gate dielectric layer are fundamental in achieving good charge transport [13], it is clear that the interfaces between the dielectric and the bottom transport layer and between the recombination and the top transport layer are crucial for guaranteeing ambipolar field-effect electrical characteristics (even if the top layer is not in direct contact with the dielectric layer). Moreover interfaces between the bottom transport and the recombination layer and between the recombination and the top transport layer should provide the favourable conditions for the charge percolation to happen in he recombination layer.

As we will see in the next paragraph, another important issue to take into account when realizing the tri-layer heterojunction is the overall energetic level diagram of the system. Indeed, the HOMO and LUMO levels of the recombination layer should favourably align with those of the transport layers in order to allow the exiton formation in the appropriate molecular sites.

5.2 A model system for tri-layer vertical heterojunction OLETs

In Fig. 3 we report the diagram of the energy levels of the materials implemented for the realization of the first vertical tri-layer heterojunction OLET.

The guiding principle in choosing the materials of every layer is basically related to the optimisation of the opto-electronic characteristics of every layer.

As transport layers we implemented materials with performant electrical are real competitive and whose growth conditions and morphological features are well known. So, the end-substituted α-oligothiophenes we discussed in Chapter 3 are used: α,ω-diperfluorohexyl-quaterthiophene (DHF4T) as n-transport material (bottom layer) and α,ω-dihexyl-quaterthiophene (DH4T) as p-transport material (top layer).

The recombination layer is a lasing host-guest molecular system formed by blending aluminum tris(8-hydroxyquinoline) (Alq_3) with 5% in weight of 4-(dicyanomethylene)-2-methyl-6-(p-dimethylaminostyryl)-4H-pyran (DCM) dye molecules because this system is highly luminescent (PLQY ~ 90%) and widespread used in OLEDs realization. The 5% doping guarantees an efficient Förster energy transfer to take place between the Alq_3 matrix and the DCM molecules and very low ASE threshold for DCM emission.

As the energy diagram shows, the recombination of holes and electrons in the Alq_3:DCM layer is favored. In particular we suppose that holes after being trapped in Alq_3 in the proximity of the interface with DH4T can generate a local electric field able to attract the electrons inside the recombination layer. If the electric field is intense enough electrons can be transferred directly from DHF4T to Alq_3 LUMO overcoming the potential barrier. Since Alq_3 is a n-type material, electrons can diffuse inside the matrix towards holes trapped in Alq_3 in the proximity of the interface with DH4T. Then excitons can be formed in Alq_3 molecules and then be non-radiatively transferred to DCM dye molecules by means of Förster energy transfer.

Nevertheless in this scenario we cannot exclude *a priori* that excitons could be formed by other mechanisms, such as direct charge hopping in the emitting molecule that are energetically favorable (i.e. electrons from DHF4T to DCM LUMO and holes from Alq_3 to DCM HOMO). In any case the recombination layer should act as a *macroscopic* charge trap regardless the possible processes taking place, since once both the charges are in DCM molecules they cannot easily migrate or be transferred to other molecular sites due to the unfavorable energetic barriers they should overcome.

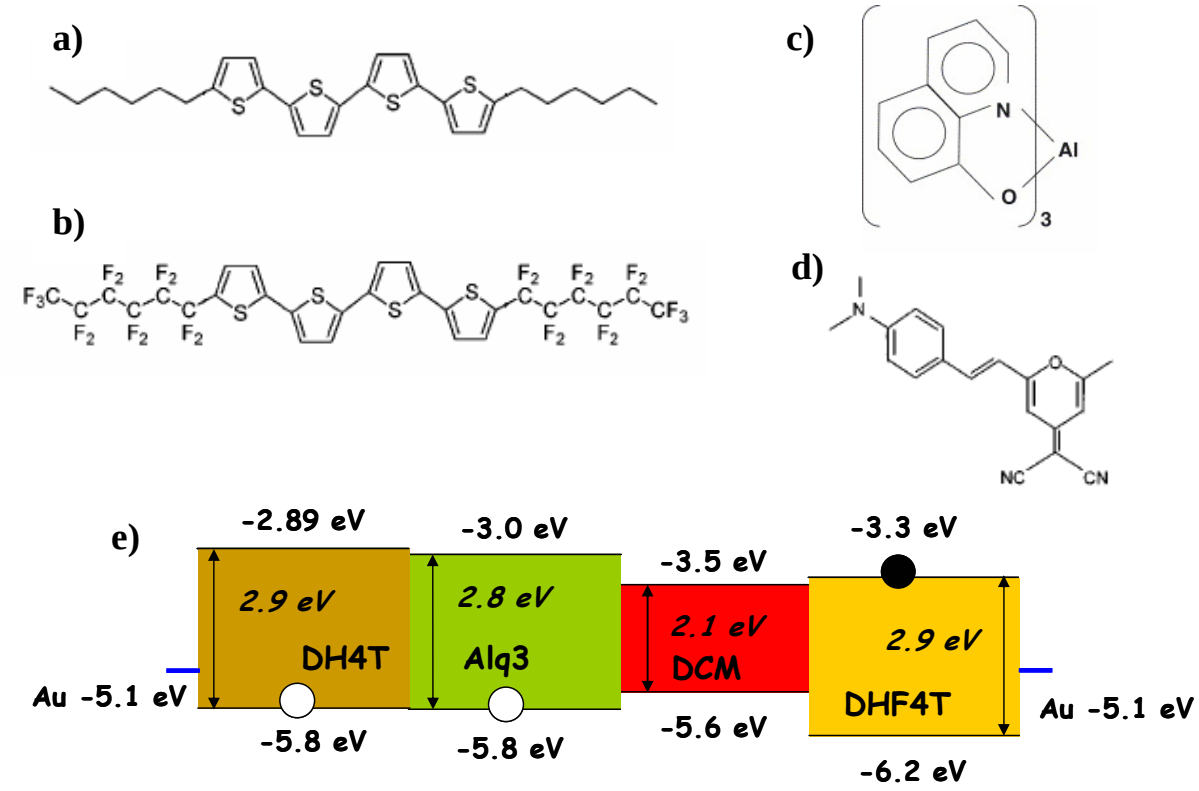

Figure 3. Chemical structure of a) α,ω-dihexyl-quaterthiophene (DH4T), b) α,ω-diperfluorohexyl-quaterthiophene (DHF4T), c) aluminum tris(8-hydroxyquinoline) (Alq_3) and d) 4-(dicyanomethylene)-2-methyl-6-(p-dimethylaminostyryl)-4H-pyran (DCM). e) Energy diagram of the tri-layer heterojunction system.

OPTO-ELECTRONIC CHARACTERISTICS

As the first step a test device based on the bilayer heterojunctions of DHF4T and DH4T are characterized in a top contact field-effect configuration. We first verify the electrical and opto-electronic properties of the bi-layer heterojunction before introducing the light emitting layer.

The thickness of the first layer is engineered to be the lowest that still presents good transport properties. The minimization of the first layer will ensure in the three-layer structure the optimal interaction between the electrons accumulated in the bottom layer and the holes accumulated in the

top layer to achieve exciton formation in the recombination layer. Using the bi-layer test device it is also possible to determine how the inclusion of the emitting layer affects charge transport and light

emitting characteristics of the devices.

Both the DHF4T and DH4T layers are grown at a rate of 0.2 Å/s with the substrate at room temperature. The DHF4T layer thickness is 7nm while that of DH4T is 20nm. We spin-coat a 100 nm-thick thin-film of polymethilmetacrilate (PMMA) on the top of the SiO_2 300 nm-thick dielectric in order to prevent electron trapping mechanisms [2]. The device configuration is a bottom gate/top contact with gold electrode contacts and the channel length is 600 μm.

The I-V p-type and n-type transfer and output curves of the DHF4T/DH4T bi-layer test device are reported in Fig. 4.

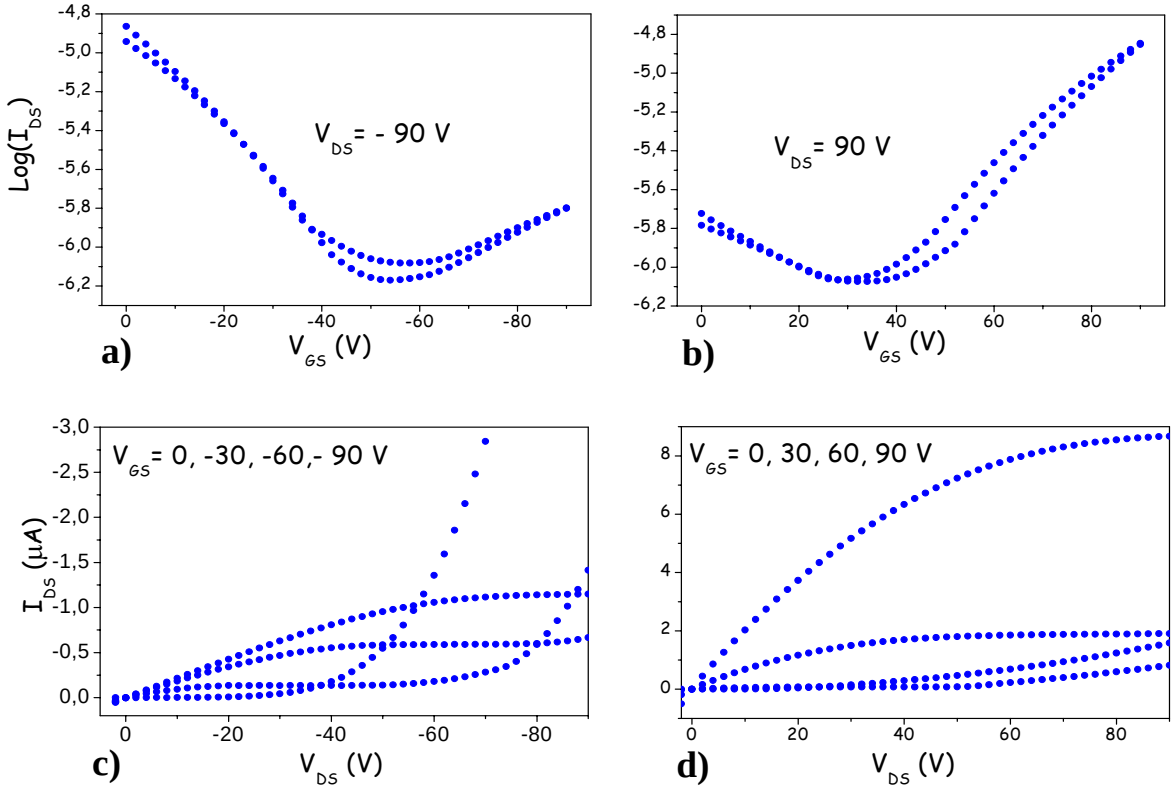

Figure 4. DHF4T/DH4T bi-layer device electrical characteristics: a) p-type transfer curve, b) n-type transfer curve, c) p-type output curve and d) n-type output curve.

The characteristic transfer and output curves exhibited by an ambipolar transistor can be understood easily, considering the potentials applied to the source, drain, and gate electrodes relative to one another.

Let us assume a transistor at a given positive drain voltage V_{ds} and start with a positive gate voltage with $V_{gs} = V_{ds}$. Just as in a unipolar transistor, the gate electrode is more positive than the source electrode and thus electrons are injected from the source into the accumulation layer and drift toward the drain, given that $V_{gs} > V_t{}^n$ (with $V_t{}^n$ the threshold

voltage for electron accumulation). Since only one polarity of charge carriers is present this regime is called unipolar.

When, on the other hand, V_{gs} is smaller than V_{ds}, the gate is more negative than the drain electrode by $V_{gs} - V_{ds}$ value. While, for $V_{gs} < V_t{}^n$, the source is not injecting electrons anymore, in an ambipolar transistor the drain electrode will inject holes into the channel if $V_{gs} - V_{ds} < V_t{}^p$ (with $V_t{}^p$ the threshold for hole accumulation). Thus, the drain electrode can be now regarded as a hole source. A hole current will flow in the channel, and differently from a unipolar n-channel transistor the ambipolar transistor is in on-state.

If the gate potential is between V_{ds} and V_s (which is grounded) so that it is bigger than $V_t{}^n$ but also $V_{gs} - V_{ds} < V_t{}^p$, both the source and drain electrodes will inject the respective charge carriers and thus both electrons and holes are accumulated in the channel. This regime is called the ambipolar regime, in contrast to the unipolar regime, where only one polarity of charges is present in the channel for any particular biasing condition.

The transfer curves of ambipolar transistors exhibit a characteristic V-shape with one arm indicating electron transport and the other indicating hole transport (see Fig. 4a and 4b). For positive (negative) applied voltages, the effective gate voltage for holes (electrons) depends on the applied source-drain voltage, which gives rise to the characteristic dependence of the transfer characteristics on the source-drain voltage.

The output curves are characterized by a superposition of standard saturated behaviour for one carrier at high V_{gs} and a superlinear current increase at low V_{gs} and high V_{ds} due to injection of the opposite carrier (Fig.4c and 4d).

The IV curves clearly show that the device exhibits an ambipolar behaviour of the device. The saturation of n-type and p-type mobilities are $\mu_n = 5 \times 10^{-2}$ cm^2/Vs and $\mu_p = 1 \times 10^{-3}$ cm^2/Vs. The gate threshold voltages for n-type and p-type operation are $V_t^n = 31$ V and $V_t^p = -2$ V.

We observe a slight degradation of the p-transport properties with respect the DH4T single-layer device we reported in § 3.1.1 which can be due likely to differences in growth modality on a surface different from PMMA in both chemical composition and morphology. As expected no electroluminescence emission could be detected from this device.

So we introduce the recombination layer by depositing by vacuum sublimation a 20 nm-thick layer of Alq_3:DCM blend between the transport layers. The DCM weight concentration with respect to Alq_3 is 5% and the deposition rate is 0.2 Å/s.

The thickness of the n-transport layer is 7 nm and the thickness of the p-transport layer is 28 nm; electrode contacts are made of gold as usual.

In Fig. 5 we report the n-type and p-type transfer characteristics of the tri-layer vertical heterojunction OLET together with the electroluminescent measurements.

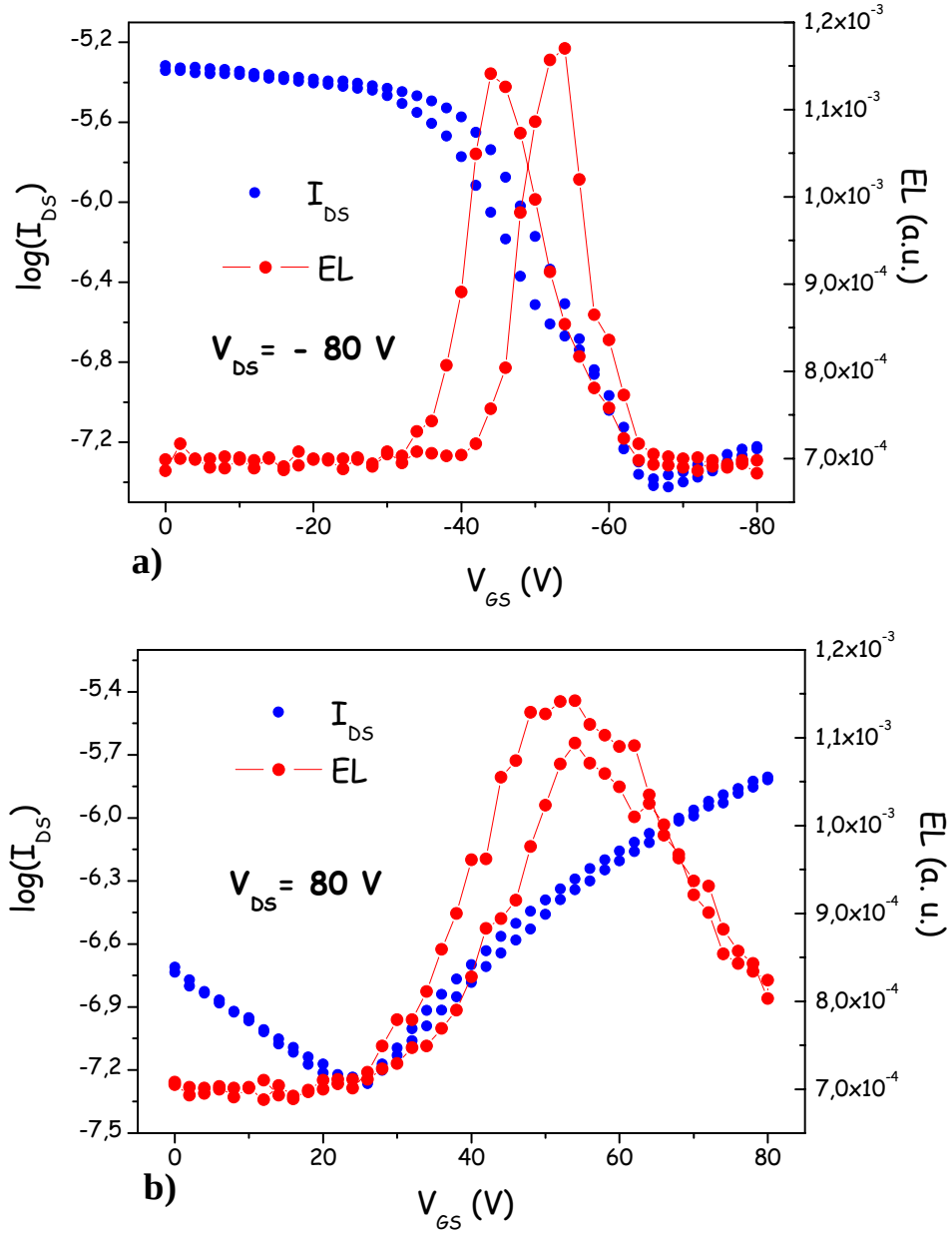

Figure 5. n-type (a) and p-type (b) transfer curves and electroluminescence emission (onward and backward voltage scans) of the tri-layer heterojunction device. The channel length is 150 μm and channel width is 10 mm.

As it can be seen, the device maintains the ambipolar electrical character observed for the bi-layer heterojunction one, and in addition electroluminescence is generated due to charge recombination in the host-guest emitting layer. The saturation mobility and the gate threshold voltage are $\mu_n=10^{-3}$ cm^2V/s and V_t^n = 10 V for electrons, and μ_p = 6.2×10-5 cm^2V/s and V_t^p = -20 V for holes. As expected the presence of the emitting layer induces a degradation of the p-type transport characteristics evidenced by a decrease in the hole mobility by more than one order of magnitude.

We note that the threshold voltages for electron and hole transport do not shift drastically during onward and backward measurements This can highlight that both the charge trapping is almost absent or the subsequent detrapping is efficient for holes and electrons.

However, the electroluminescence intensity is clearly observed at a relatively low voltage, which is an indication of preferential charge recombination in the intermediate emitting layer. Interestingly it is observed that the light generation occurs in the ambipolar region of the device operation, which suggests exciton formation and light emission in the central part of the channel active area. Even more important is the observation of an emission peak located in correspondence of a gate voltage within the range 45 - 55 V in both the n-type and p-type transfer curves. This indicates that the maximum of exciton recombination efficiency takes place when the electron and hole current are balanced within the device.

The current density in the active area of field-effect devices can be estimated considering that charge carriers in the transistor channel are accumulated in the first 2 nm close to the relevant interface, either with the dielectric or with the underneath organic layer.

The current density achieved in this device at the highest measured current values is about 8 A/cm^2 for electrons and 4×10^{-1} A/cm^2 for holes. Although the measured device characteristics are encouraging, it is clear that the electron and hole mobility values, as well as the current densities, need to be substantially improved.

By introducing B-staged bisbenzocyclobutene (BCB) as polymeric buffer layer during the device fabrication process, and in particular by decreasing the channel length to 85 μm, we find a substantial increase of the n- and p-type electrical currents.

The n-type mobility is enhanced to $\mu = 5 \times 10^{-2}$ cm^2/Vs with a gate threshold voltage for the electrons of V_t^n = 14.5 V. The p-type mobility also improves by two orders of magnitude and reaches $\mu = 4.5 \times 10^{-3}$ cm^2/Vs with a gate threshold voltage as low as V_t^p = 5 V. We underline that the ambipolar regime can be difficult to reach even if electron and hole accumulation layers can be induced separately at high positive and negative gate

voltages, respectively, because the coexistence of both carriers requires the threshold voltage difference for electron and hole accumulation to be sufficiently small.
We have determined that this last device affords n-type current densities of 1 kA/cm^2 and p-type current densities of 0.2 kA/cm^2, that are the highest reported current density values for field-effect light-emitting transistor devices to date.

So introducing this new approach in realizing ambipolar OLET we are able to achieve very high current density (~ 1 kA/cm^2), electroluminescence located preferentially in the ambipolar region and high electron and hole mobility values (~ 10^{-2} cm^{2}V/s).

FITTING TRI-LAYER HETEROJUNCTION OPTO-ELECTRONIC CHARACTERISTICS

In order to obtain high external EL quantum efficiency, not only the peak of the EL signal has to be in correspondence of the maximum of the current density (possibly for both the charge carriers) but also the exciton after being formed have to recombine radiatevely with the highest efficiency.
So a detailed study on how the exiton formation process takes place in a tri-layer vertical heterojunction is necessary for improving quantitatively the device emission properties.
In bulk heterojunction and single-layer OLET electrons and holes coexist in the same layer. When an ambipolar FET is biased with the gate voltage in between the source and the drain voltage, an electron accumulation layer should form near one electrode coexisting with a hole accumulation layer near the other electrode [9]. The electron-hole recombination takes place mainly where these two accumulation layers meet, so that light emission is localised in a portion of the device channel. The total current flowing in the device channel is so limited by the electron-hole recombination process since it can be only partly radiative.
In a multi-layer ambipolar OFET, electron and hole FET transport is achieved in different layers. In tri-layer heterojunction, the electron and hole accumulation regions are located either in the bottom or in the top layer. The total current flowing in the device channel can be considered as the sum of three different contributions: FET-like planar electron current in the n-transport layer, FET-like planar hole current in the p-transport layer and a LED-like vertical current due to the percolation or migration of the charges accumulated in the layer under- and overneath through the vertical heterojunction induced by the electron-hole attraction (Fig. 6a).
In principle the device channel can be considered a sort of vertical *pn* junction since the vertical percolating current can happen to form all along the device channel length. Thus,

the emission zone cannot be localised as in a single-layer OLET. Moreover in a multilayer OLET structure, light emission in the proximity of the contact region is always present due to the electrons tunnelling from the electrode into the channel region [14] (Fig. 6b).

Due to the effective pn-junction within the channel and complete recombination of holes and electrons, the quantum efficiency of ambipolar light-emitting FETs should also be much higher than that of unipolar light-emitting FETs.

So the emission profile will depend on the EL quenching at the electrodes and on the relative light intensity between the emission due to radiative recombination at the electrode and the emission due to exciton formation and recombination in the central part of the channel.

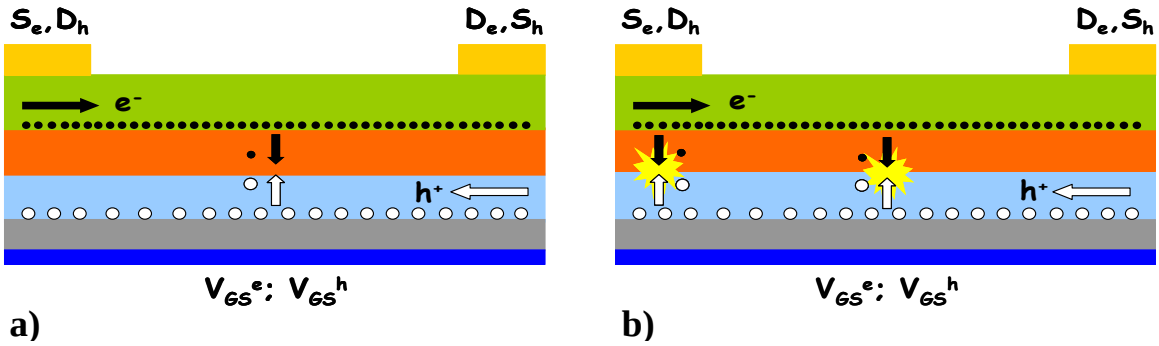

Figure 6. a) Schematics of the three current components present in a tri-layer heterojunction. b) Radiative recombination processes that contribute to the light emission profile of a tri-layer heterojunction. In both the panels *S* stands for source contact, *D* for drain contact and V_{GS} for the potential applied at the gate contact; the apexes refer to the ambipolar nature of the charge transport.

In order to verify the existence and the entity of the vertical current component, we implement a simple modelling for fitting the experimental tri-layer heterojunction electrical characteristics. Although more sophisticated models can be used [15], in a simple way we assume that (1) the transverse electric field induced by the gate voltage is largely higher than the longitudinal field induced by the gate bias (*gradual channel approximation*) and (2) the mobility is constant all over the channel (see § 1.4.3.2). Moreover the model considers the total of charges accumulated in the channel without taking into account the real charge spatial distribution. The electroluminescence emission profile is considered constant and the radiative recombination processes in the proximity of the electrodes are described according to the tunnelling modelling introduced by Capelli [14].

Here we will not treat in details all the results of the proposed fitting model, but just give some hints on the radiative recombination process in the middle of the channel

In Fig. 7a a comparison between fitting the experimental data with and without taking into account the LED-like vertical current is shown. As it can be seen the introduction of a vertical current is absolutely necessary for describing properly the electrical and electroluminescence characteristics of a vertical tri-layer heterojunction-based OLET, even if the restrictions and approximations imposed to the model are very severe.

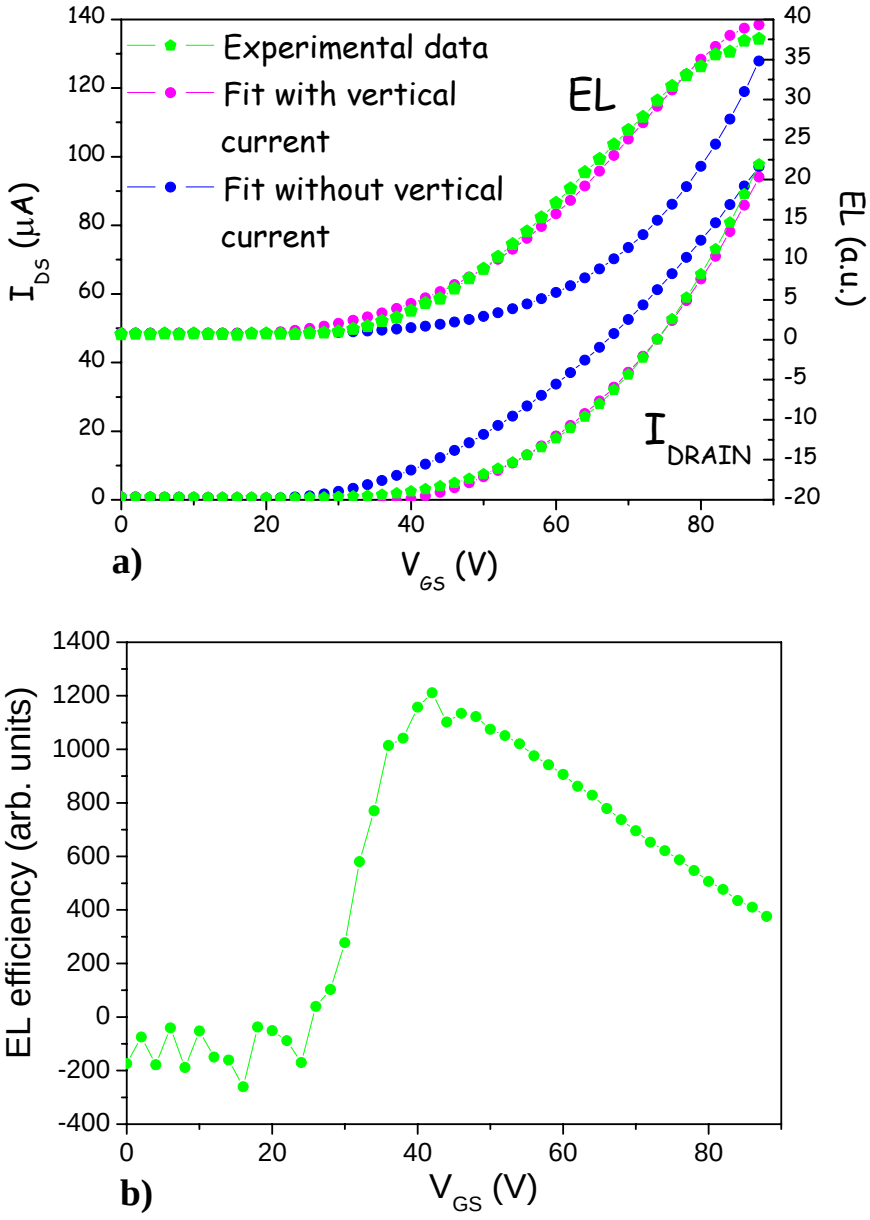

Figure 7. a) Fitting of a saturation n-type transfer curve with and without vertical recombination current in the tri-layer vertical heterojunction. b) Corresponding EL efficiency measurement. The channel length is 150 μm.

In Fig. 7b we report the electroluminescence efficiency obtained by dividing the electroluminescence intensity by the corresponding current value. The location of the maximum of the emission around the ambipolar region is clear visible, as well as the non negligible emission with the increasing gate potential due to radiative recombination at the electrode.

From the fitting it is possible estimate that the amount of the vertical hole and electron current that forms excitons and recombine radiatevely is only the 30%. Clearly for improving the opto-electonic performances of tri-layer heterojunction OLET it is necessary to enhance the efficiency of the exciton formation and recombination process.

Apart from the energetic of the system that seems quite favourable to the exciton formation in the recombination layer, the control of the morphology of the different layer interfaces play a fundamental role in determining the overall efficiency of the system.

Clearly only the EL emission spectrum will show on which molecular sites the recombination is happening and whether energy transfer process taking place in the recombination layer is efficient.

MORPHOLOGICAL STUDY ON HETEROJUNCTION LAYERS

As it is already been reported for bi-layer ambipolar OFET [10] the layer thickness and the growth conditions are crucial to define the interfacial characteristics between superimposed layers, thereby determining the overall electrical and optoelectronic device performances.

It is therefore extremely important to understand how the morphology of bottom layers affects the subsequent morphology of the upper layers and to determine the optimum growth conditions of each layer to be used for device fabrication.

So we performed an AFM morphological investigation on the layers composing the organic heterojunction investigated in relation to growth parameters used in the realization of the tri-layer vertical heterojunction that showed the more promising opto-electronic characteristics.

In Fig. 8 we report on the topological feature of a DHF4T thin-film grown on a 100-nm thick PMMA film with increasing the film thickness from 5 nm to 15 nm. The DHF4T deposition rate is 0.5 Å/s and the Si/SiO_2 is held at room temperature during the growth.

In the thicker sample a large amount of 3D rod-like aggregates with length around hundreds-of-nanometers covers the majority of the surface. Since the strong tip-surface interaction we are not able to give a reliable estimation of the aggregate heights.

By decreasing the film thickness from 15 nm to 5 nm, not only there is a significant decrease in the amount of 3D aggregates but also a 2D layer-by-layer islands underneath are quite visible.

As we already mentioned in § 1.3.2, DHF4T shows a good film connectivity and coverage in the first thin-film monolayer due to the coalescence of the islands at the round boundaries. We underline that a complete coverage of the dielectric surface is a necessary condition for obtaining good field-effect transport properties.

Layer thickness around 7 nm is a good compromise for achieving high electron mobility without increasing the film roughness which would prevent a smooth growth of the subsequent films.

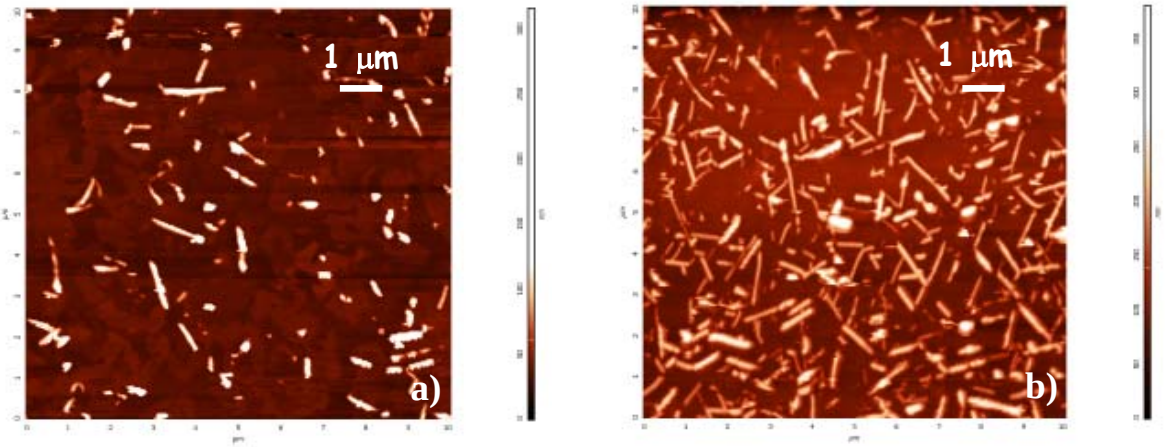

Figure 8. 10x10 μm^2 topological AFM images of
(b) DHF4T layer that is 15 nm thick, (c) DHF4T layer that is 5 nm thick. Both samples are grown on top of PMMA and had a growth rate of 0.5 Å/s at room temperature.

The recombination layer of the device that is grown on top of DHF4T is the host-guest layer made of an Alq_3:DCM 5% blend.

In Fig. 9a we report the morphology of a 20 nm-thick Alq_3:DCM 5% grown on a 7 nm-thick DHF4T layer with a 0.2 Å/s deposition rate at room temperature in order to reproduce the device fabrication conditions. As it can be seen from the AFM image, the surface on which the subsequent DH4T is going to be grown is formed by 3D globular aggregates and with variety of widths (ranging from 200-300 nm). The grains tend to coalesce into fiber-like structures.

Clearly the surface roughness and the presence of voids and protuberances in principle would prevent the layer-by-layer growth of a smooth surface onto the recombination layer.

Generally lower deposition fluxes favours the growth of wider size grains so reducing the density of grain boundaries which are well known traps for the charge migration or hopping [16].

However, because of Alq_3 is an amorphous material the aggregates grow isotropically (i.e. with a globular shape) without forming long-range crystalline domains that can cover homogeneously the underneath layer.

When the deposition rate is increased from 0.2 to 2 Å/s and the recombination layer is grown on 100 nm-thick PMMA film, the Alq_3:DCM 5% blend morphologiacal features are completely different (Fig. 9b). Indeed, the recombination layer covers completely and homogeneously the underneath layer and presents fewer voids whose dimensions are now reduced.

We can also recognise that the repeating motif in the morphology of the blend is invariant with respect increasing the deposition rate apart from the fact that the size of the globular aggregates is much reduced (~ 10 nm) and more monodispersly distributed.

Since the average roughness of the film is similar to the roughness of PMMA alone (2.8 nm), the film surface morphology obtained by increasing the deposition rate reveals to be much more suitable for multilayer structure.

Unfortunately, growing Alq_3:DCM 5% layer on a 7 nm-thick DHF4T layer with a 2 Å/s deposition rate does not affect significantly the dimensions of the aggregates probably because of the much higher average roughness and the different surface energy of the n-transport layer with respect the PMMA layer. Indeed the *wettability* of polar DHF4T layer surface has to be enhanced with respect the incoming Alq_3 molecules either by reducing the presence of the 3D rod-like aggregates on the DHF4T surface or by performing the blend layer deposition at high fluxes and temperature.

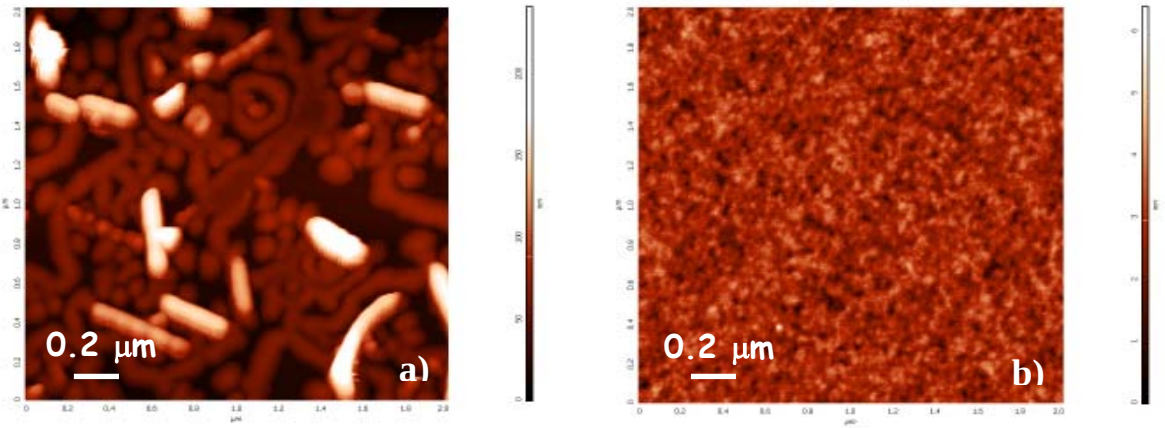

Figure 9. a) A 2x2μm AFM image of Alq3:DCM 5% grown on 7 nm-thick thin-film of DHF4T. Growth rate was 0.2 Å/s at room temperature and the total thickness was 20 nm. b) A 2x2μm AFM image of Alq3:DCM 5% mixture grown on PMMA. Growth rate was 2 Å/s at room temperature and the nominal thickness was 20 nm.

Finally an AFM investigation is carried out on the top DH4T top layer. The sample has the following structure: SiO_2/PMMA/DHF4T (0.2 Å/s, 7nm, RT)/Alq3:DCM 5%(0.2 Å/s, 20nm, RT)/DH4T (0.2 Å/s, 30nm, RT)/Au electrodes in order to reproduce the device fabrication conditions. The p-transport layer morphology is measured in the device channel, since this is the device active region. Comparing the images reported in Fig. 10 with the images of a DH4T grown on PMMA/SiO_2 substrate reported in § 1.3.1, we can infer that the underneath layers have modified the DH4T morphology. The layer grows only partly through a layer-by-layer mechanism and 3D protrusions are present on the surface. The jagged and high boundaries of the aggregates prevent the collection of a clear image of the DH4T morphology due to the strong interaction between the AFM tip and the sample surface. Nevertheless, the typical morphological features of DH4T thin-film are still partly visible: round shaped islands are buried under the pillar-like 3D aggregates. The islands are clearly reduced in size with respect to islands grown on a PMMA substrate.

Implementing AFM as a tool for characterizing the film morphology we cannot probe directly the interface between the recombination layer and the p-transport layer. However we can infer that the connectivity among DH4T polycrystalline domains has to be sufficient to guarantee long enough percolation paths for the charges, as the hole mobility value can show.

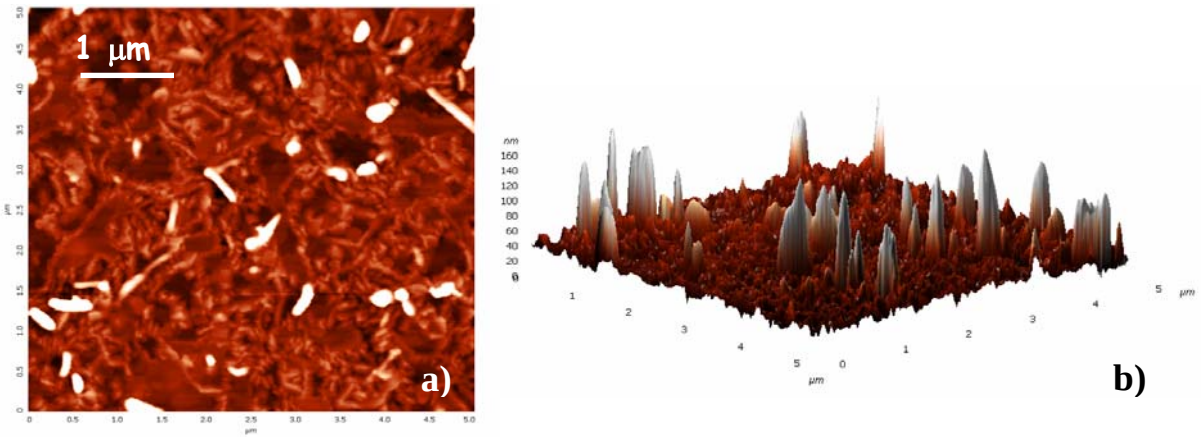

Figure 10. 5×5 μm^2 topological AFM image of a 30 nm-thick film grown on the top of 20 nm Alq_3:DCM/7 nm DHF4T bi-layer structure in 2D (a) and 3D (b) view.

By mean of this morphological study, we have shown the importance of controlling the layer interface morphology (in particular for the first layer) in order to enhance the opto-electronic performances of the tri-layer vertical heterojunction.

We propose to perform DHF4T deposition at 90 °C for increasing the long-range order in the crystalline domains and the smoothness of the monolayer surface as we discussed in Chapter 3. Moreover we do not exclude that the chemical interactions between the growing-up DHF4T and the solvent residuals present in the underneath PMMA buffer layer can induce some modification in the overall layer 3D architecture.

5.3 New materials combination for improving tri-layer heterojunction OLET opto-electronic performances

Given the versatility of the tri-layer vertical heterojunction, different strategies can be adopt for improving the overall device performances. Since every single layer is aimed to a specific function, it is possible to implement different materials which preserve the same functional properties but show molecular packing in thin-films more suitable for a multilayer structure.

Indeed, using the p-transport DH4T layer as first layer on top of the dielectric can guarantee a smooth and well-connected surface for the growth of the subsequent layers (see § 3.1.1).

Reversing the order of the transport layers, we prefer to implement *N*,*N*′-ditridecylperylene-3,4,9,10-tetracarboxylic diimide, $PTCDIC_{13}H_{27}$, P13) as n-transport material since bi-layer obtained by growing P13 layer onto DH4T layer have shown good balance in ambipolar transport and the highest electron and hole mobility values reported up to now in an OLET [10].

Moreover the doping dye 4-dicyanomethylene-2-methyl-6-(2-(2,3,6,7-tetra-hydro-1H,5H-benzo)[ij]quinolizin-8-yl)-4H-pyran (DCM2) is used in the recombination layer since it shows negligible absorbance at the emission wavelength and slight lower ASE threshold [17] with respect to DCM, even if it is less thermal stable.

A sketch of the OLET based on a tri-layer heterojunction implementing new material combination is reported in Fig. 11a. The chemical structures of P13 and DCM2 are reported n Fig. 11b and 11c.

In the recombination layer the percentage in weight of DCM2 molecules (guest material) with respect to Alq3 (host material) is 3% for guaranteeing an efficient Förster energy transfer to take place. The thickness of the recombination layer is 20 nm.

In this new configuration the tri-layer heterojunction is grown on a thick film of PMMA (~ 450 nm) that acts as the gate dielectric. The gate electrode is a thin-film of tin indium-oxide (ITO) deposited on a glass substrate and drain and source electrodes are made of gold.

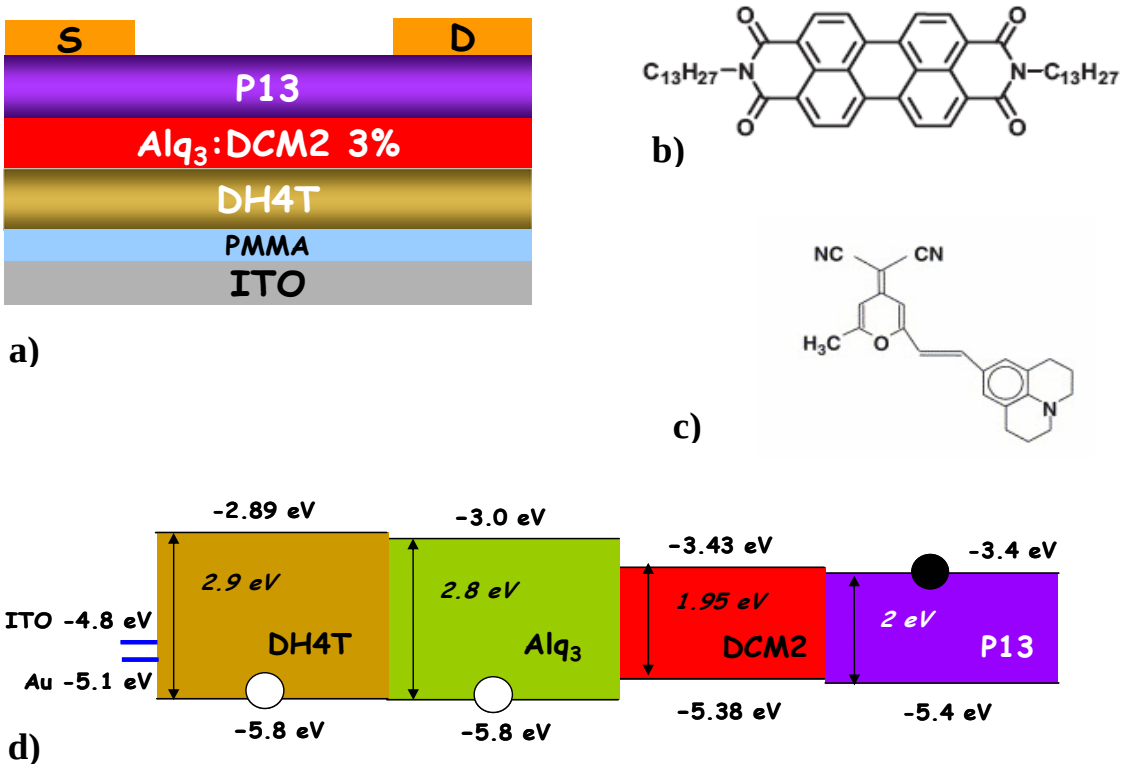

Figure 11. a) Sketch of the new OLET based on a tri-layer heterojunction. Chemical structure of *N*,*N*′-ditridecylperylene-3,4,9,10-tetracarboxylic diimide, $PTCDIC_{13}H_{27}$ (P13) (b) and of 4-dicyanomethylene-2-methyl-6-(2-(2,3,6,7-tetra-hydro-1H,5H-benzo)[ij]quinolizin-8-yl)-4H-pyran (DCM2) (c). d) Energy diagram of the new tri-layer heterojunction system.

So the new tri-layer heterojuncion-based OLET can be considered a fully optically transparent device in which light emission efficiency is maximized since the sources of light attenuation due to the presence of an opaque substrate (such as SiO_2 in the previous device structure) are almost negligible.

Moreover if we consider the energy diagram of the tri-layer heterojunction (Fig. 11c) the radiative recombination of holes and electrons in the Alq_3:DCM2 layer is likely to happen through a mechanism similar to what reported in the previous paragraph. In particular we suppose that holes after being trapped in Alq_3 in the proximity of the interface with DH4T can generate a local electric field able to attract the electrons inside the recombination layer. If the electric field is intense enough electrons can be transferred directly from P13 to Alq_3 LUMO overcoming the potential barrier. Since Alq_3 is a n-type material, electrons can diffuse inside the matrix towards holes trapped in Alq_3 in the proximity of the interface

with DH4T. Then excitons can be formed in Alq_3 molecules and then be non-radiatively transferred to DCM2 dye molecules.
Nevertheless in this scenario we cannot exclude *a priori* that excitons could happen to form by other mechanisms, such as direct charge hopping in the emitting molecule (i.e. electrons from P13 to DCM2 LUMO and holes from Alq_3 to DCM2 HOMO).

Since in this configuration we are dealing with the implementation of PMMA instead of SiO_2 as new dielectric material, as first step we fabricate single-layer OFET based on the charge transport materials. DH4T and P13 layers are sublimated with the substrate held at 90 °C and at room temperature respectively. As it can be seen in Fig. 12, the electrical behaviour of DH4T and P13 as active materials in field-effect devices is what expected from literature: the output curves show that at high applied drain voltage absolute values the saturation of the current intensity in the channel is achieved while at low applied drain voltage absolute values the curves can be interpolated by a lines passing through the same origin as expected from theory. Moreover electrical hysteresis is completely absent both in locus and output characteristics.
These evidences together with the fact that the dielectric does not break down for applied gate voltage values as high as 90 V allow us to consider a 450 nm-thick PMMA film as an almost trap-free good dielectric layer for OFET realization.
The electrical mobility values we can extract from the electrical characterization are 8×10^{-2} cm^2/Vs for the holes and 3×10^{-1} cm^2/Vs for the electrons while the threshold voltages are -18 V for the holes and 37 V for the electrons.

It is fundamental to perform also a morphological characterization on the active materials of the single-layer devices in order to be able to correlate the opto-electronic performances of the final tri-layer vertical heterojunction device with the modification of the molecular organization within every single layer due to the interaction with the others.
CLSM image of the 10 nm-thick DH4T layer (Fig. 13a) reveals very smooth and flat morphology of lamellar crystalline domains (see § 3.1.1). As reported elsewhere [18], DH4T growth with the substrate held at 90 °C can guarantee that the crystalline lamellae can extend over many tens of micrometers without showing multilayering. The only distinguishing feature is the presence of transverse cracks as the result of contraction during cooling.

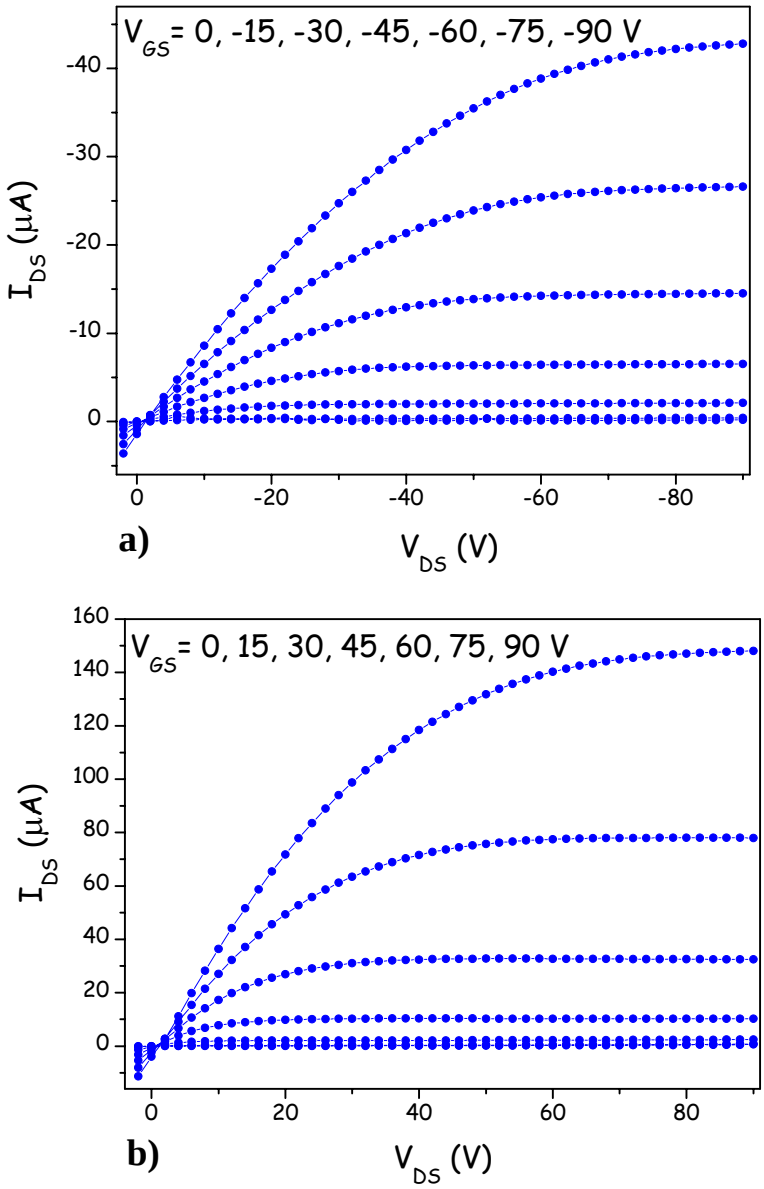

Figure 12. Output curve characteristics of 300 μm channel single-layer OFETs whose active material is (a) 10 nm of DH4T and (b) 15 nm of P13. The dielectric is a 450 nm-thick layer of PMMA. The gate contact is made of ITO while the source and drain contacts are made of gold.

In the case of the single-layer device implementing P13 as active material (Fig. 13b), the thin-film morphology is continuous and homogeneous covering completely the dielectric surface. Even if intense red PL emission does not show morphological features, a careful investigation reveals round-like grains with size around 1 μm^2 are present in the thin-film texture.

As it is well-known, perylene diimide end-substituted with alkyl chains tend to aggregate in grains whose dimensions increase with increasing the substrate temperature. At the proper temperature, depending on the length of the alkyl chain lamellar domains which are typical of crystalline organic semiconductors start forming [19]. It has been proposed that perylene diimide alkyl derivatives arranges in thin-film in crystalline domains which pack according to a triclinic lattice with the *c* axis parallel to the surface normal. In this packing scheme the long axis of the perylene diimide core is oriented roughly parallel to the substrate normal, meaning π-stacking occurs parallel to the substrate surface. This is the optimal packing scheme for charge transport in the OTFT structure [20].

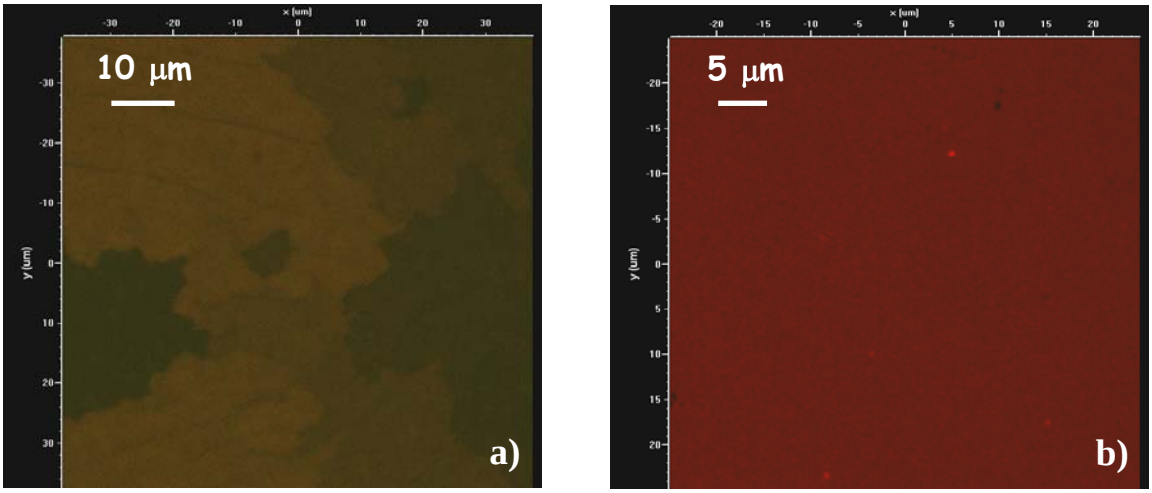

Figure 13. CLSM images of the channel region of single-layer devices whose active materials are (a) 10 nm of DH4T and (b) 15 nm of P13. The signal is excited by the Ar^+ 488 nm and collected through the glass substrate by a 60× dry panfluor objective. The PL signal is collected only by the green PMT channel in (a) and only by the red PMT channel in (b).

Given the electrical characteristics of the single layer OFET devices reported above, it is easily found out that DH4T/P13 bi-layer field-effect activity is almost invariant with respect the gate dielectric implemented, either silicon dioxide or PMMA.

Thus, also in this configuration the growth conditions of the recombination layer turn out to be the key parameters to control for achieving high performances tri-layer vertical heterojunction OLET. Indeed varying the evaporation rate of Alq3 molecules or diminishing the substrate temperature from room to liquid nitrogen temperature drastically

affects not only the typical morphological features of the recombination layer itself but also those of the electron transport layer.

Since in tri-layer heterojunction-based OLET electron transport is restricted inside the P13 layer to the first few nanometers at the interface with the recombination layer underneath, it is evident the correlation between the Alq_3:DCM2/P13 interface morphology and the opto-electronic performances of the overall device.

Differently from other scanning-probe techniques, laser scanning confocal microscopy reveals to be an extremely valuable tool for directly probing the interfaces buried between different layers, particularly in this multilayer OLET device configuration. Indeed, it is possible to excite selectively different materials composing the layers with different laser sources from the bottom of the device (through the ITO glass substrate) and to collect selectively PL emission in specific wavelength range by choosing the appropriate PMT channel.

So cross-correlating the overall opto-electronic characteristics with the CLSM morphological investigation on the tri-layer vertical heterojunction in function of the growth parameter variation during recombination layer vacuum sublimation can be a useful approach for understanding the charge transport mechanisms and emission processes in the multilayer device structure.

In Fig. 14 we report the saturation transfer curves for the p-type and n-type polarization of the tri-layer heterojunction-based OLET in which the charge transport layer are grown according to the parameters optimized in the unipolar single-layer devices and the recombination layer is grown with 0.5 Å/sec deposition rate holding the substrate at low temperature (~ 80 K).

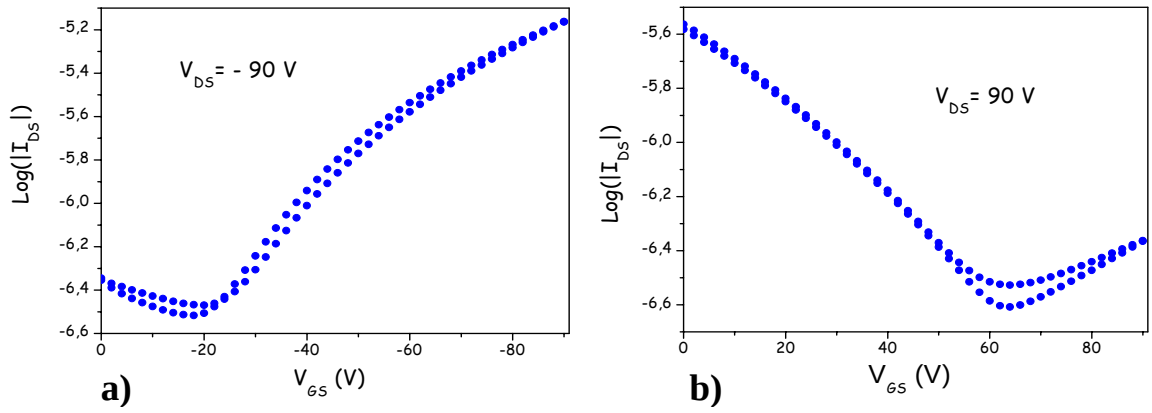

Figure 14. Saturation transfer curves for p-type (a) and n-type polarization of the tri-layer heterojunction-based OLET. The evaporation is held at liquid nitrogen temperature.

The overall electrical behaviour is unbalanced since the electron mobility is low with respect the single layer device value ($\mu_n \sim 8\times10^{-5}$ cm^2/Vs) while the hole mobility is only slightly less than what we expect.

As we can infer from the CLSM images obtained by exciting with Ar^+ 488 nm, P13 morphology (Fig. 15a) reveals to be discontinuous and not completely well-connected so that the deterioration of the electron transport properties can be explained by the lack of percolation paths long enough for the charges to reach the electrodes. Clearly using this excitation wavelength it is not possible to distinguish directly the P13 PL signal from that of DCM2 molecules dispersed in the Alq_3 matrix.

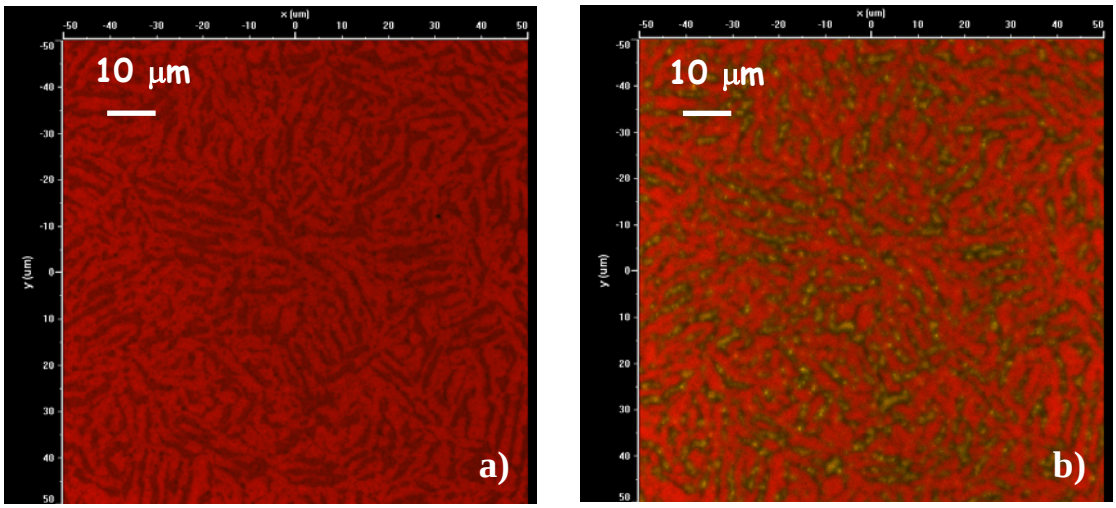

Figure 15. Tri-layer heterojunction-based OLET in which the recombination layer is grown at 0.5 Å/s at low temperature. LCSM images collected with a 60× dry objective exciting through the glass substrate. a) Image collected from the red PMT channel (> 600 nm) exciting at 488 nm. b) Image collected from the green (center at 515 ± 15 nm) and red PMT channels exciting at 405 nm.

However by changing the exciting wavelength from 488 to 408 nm (Fig. 15b), we can note that in the voids of the P13 morphology an underneath structure of globular grains is present. We guess that the prevalently green signal is due to the emission of Alq_3 molecules and not to the p-transport layer since DH4T is a poorly emitting molecule compared with Alq_3.

So we can deduce either that the number of DCM2 molecules we suppose to deposit on the substrate in our sublimation system cannot guarantee an efficient energy transfer to take place or that growing the recombination layer at low temperature can induce an

inhomogeneous dispersion of the guest molecules in aggregating host molecules. The latter hypothesis can be corroborated by the fact that lowering the temperature could prevent the very polar DCM2 molecules to orient in domains that minimize the overall energy of the host-guest system. The net effect of the inhomogeneous dopant distribution is therefore to increase the host and decrease the guest luminescence [21].

In any case micrometric spherical Alq_3 domains prevent the formation of a continuous and uniform P13 layer.

So we decide to deposit the recombination layer at room temperature maintaining constant the evaporation rate. We expect to reduce the tendency of the molecules to coalesce by endowing them with sufficient kinetic energy to start nucleation process in different positions. Indeed CLSM images (Fig. 16a) reveal that P13 growth on Alq_3:DCM2 layer resembles the one we observe in single layer device, i.e. uniform and homogeneous. At higher resolution a smaller and finer sub-structure ca be detected and plausibly ascribed to the emission of DCM2 molecules homogeneously dispersed in Alq_3.

By collecting the signal only from the green channel we clearly recognize that DH4T grows layer by layer, as expected in single layer device, also in the tri-layer heterojunction (Fig. 16b).

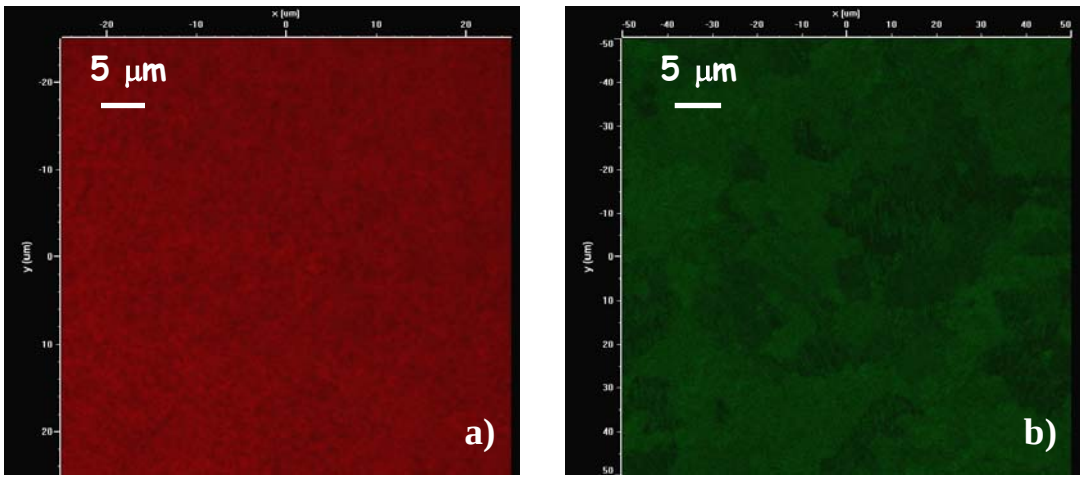

Figure 16. Tri-layer heterojunction-based OLET in which the recombination layer is grown at 0.5 Å/s at room temperature. LCSM images are collected with a 60× dry objective exciting through the glass substrate. a) Image collected from the red PMT channel (> 600 nm) exciting at 488 nm. b) Image collected from the green PMT channel (center at 515 ± 15 nm) exciting at 488 nm.

The main difference between the tri-layer vertical heterojunction configurations we presented here and in the previous paragraph is that the recombination layer is grown on surface with different chemical-physical and morphological features.

As we described in Chapter 3, linear end-substituted oligothiophenes such as DH4T and DHF4T tend to pack in polycrystalline thin-film according the herringbone structure with molecule long axis oriented normal to the surface so that thin-film surface energy is generally dominated by the chemical nature of the substituents . In our specific cases, since the alkyl chains in DH4T behave as weakly electron-donating groups while the fluoalkyl chains in DHF4T behave as electron-withdrawing groups, DH4T thin-film surface is much less polar than DHF4T one.

Thus, either the high hydrophobicity or the smoothness of the DH4T layer surface could be responsible for the reduced tendency of Alq_3 molecules to arrange in globular grains. Since the recombination layer growth conditions are invariant in the two vertical tri-layer heterojunction, we can conclude that the driving force in the molecular organization and film connectivity of the recombination layer is the incoming molecule-substrate interaction.

As it is expected the opto-electronic performances of the tri-layer heterojunction-based OLET with the recombination layer grown at room temperature are much more promising. As it can be seen from the saturation transfer curves reported in Fig. 17, the hole and electron mobilities ($\mu_p \sim 2\times10^{-1}$ cm^2/Vs and $\mu_n \sim 2\times10^{-2}$ cm^2/Vs) are well-balanced and comparable to the values of the corresponding single layer devices.

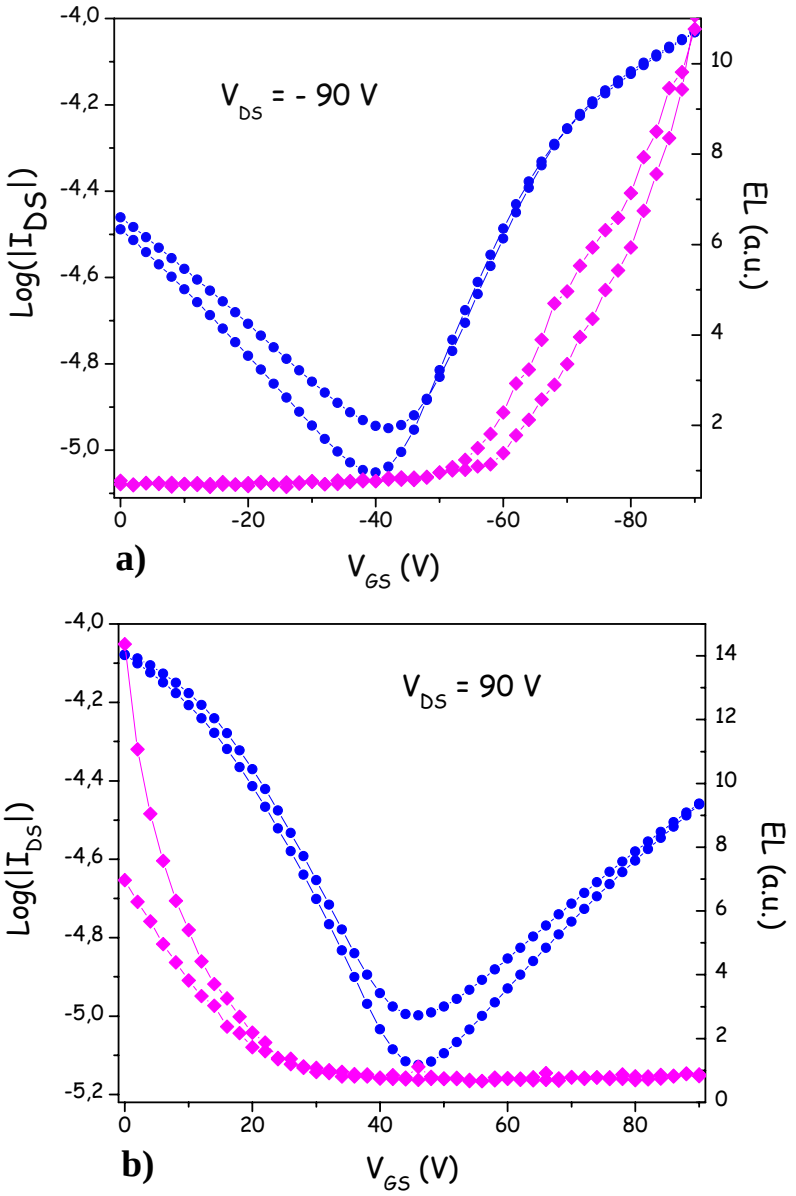

Figure 17. Saturation transfer and electro-luminescence curves for p-type (a) and n-type (b) polarization of the tri-layer heterojunction-based OLET. The evaporation of the Alq_3:DCM2 layer is held at room temperature.

Moreover we roughly estimate a value of charge carrier density around $10^{-1} \div 10^{-2}$ KA/cm^2 for both the electrons and holes. As mentioned above, this value in principle can guarantee a sufficient electrical pumping for achieving laser action [22].

Nevertheless we have to notice that even if we have increased light emission in absolute value with respect to the bi-layer approach, again the most part of EL is located in correspondence of the unipolar transport region. This means that when the current densities

are maxima for both carriers (in the ambipolar gate voltage region) the light emission is not maximized.

This is a clear evidence of the fact that the recombination layer is not working properly. As a first step we should collect a spectrum of the EL in order to understand which of the three layers contribute to light formation process. Moreover this would help us to discern if it is the energy diagram of the system or the morphology of the interfaces to play a fundamental role in light formation in the tri-layer heterojunction. Indeed at this stage we have to improve the performances of the tri-layer heterojunction grown on transparent substrate either by selecting and implementing new materials that facilitate exciton formation or by carefully controlling the molecular packing of the different layers.

5.4 Conclusions

Throughout this chapter we have presented a new approach for realizing ambipolar organic light emitting transistors (OLETs). OLETs represent a class of devices of particular interest for the future development of organic opto-electronics since their planar geometry can guarantee high charge mobility, high current density and ambipolar control of the recombination region.

OLETs can be considered an alternative structure with respect to OLEDs for achieving efficient radiative charge recombination because the emission is located away from the electrodes (ideally in the middle of the channel) so reducing the possible exciton quenching due to the proximity of metals. Charge-exciton quenching is also reduced thanks to the high charge carrier mobility.

Moreover the possibility of integrating a resonant optical cavity inside the active region makes the OLET device structure suitable for the realization of an electrically pumped organic laser. The planar geometry of OLETs imposes physical constraints in the molecular packing of charge transport layers and in the morphology of organic interfaces in order to achieve high charge transport in field effect conditions. This last requirement excludes most of the typical OLED materials from being used in FET heterojunction structure.

The device architecture we propose for obtaining balanced charge transport and efficient light emission is to realize a heterojunction using different materials each having a specific function. Clearly, matching the overall device characteristics with the functional properties of the single materials composing the active region of the OFET, is a great challenge that requires a deep investigation of the morphological, optical and electrical features of the system.

The specificity of the presented tri-layer based OLET is the intrinsic separation of the charge transport region from the exciton formation region thus preventing completely the exciton-carrier quenching.

Each layer is devoted to a single functionality and can be optimised by controlling the growth of the different organic/organic, organic/contact and organic/dielectric interfaces. The first layer and third layer are optimized for field-effect charge (electrons and holes) transport. The second layer is formed by a host-guest matrix with high emission efficiency and showing amplified spontaneous emission under optical pumping

We try to improve the performance of the OLETs by exploiting the feasibility of the vertical heterojunction approach. We realized devices changing substrates (silicon and glass), dielectric (SiO_2 and PMMA), the active materials and the their growth conditions.

Implementing confocal laser scanning microscopy as morphological probing tool especially in transparent devices allows to recognise directly the fundamental role played by different layer interfaces in determining the overall opto-electronic performances of the vertical tri-layer heterojunctions.

Moreover we can correlate the OLET electrical characteristics to the morphology of the interfaces and the charges recombination processes by a simple and effective theoretical model.

The optimization of the charge transport and light emission mechanisms allow the realization of a tri-layer heterojunction presenting balanced electron and hole mobility ($\sim 10^{-1}$-10^{-2} cm^2/Vs), high charge carrier density in correspondence of the maximum electroluminescence signal ($\sim$ 1 KA/cm^2) and intense light emission.

References

[1] J. Zaumseil, H. Sirringhaus, *Chem. Rev.*, **2007**, 107, 1296.

[2] L. L. Chua, J. Zaumseil, J. F. Chang, E. C. W. Ou, P. K. H. Ho, H. Sirringhaus, R. H. Friend, *Nature*, **2005**, 434, 194.

[3] R. Schmechel, M. Ahles, H. von Seggern, *J. Appl. Phys*., **2005**, *98*, 084511.

[4] A. Dodabalapur, H. E. Katz, L. Torsi, *Adv.. Mater.* **1996**, 8, 853.

[5] A. Hepp, H. Heil, W. Weise, M. Ahles, R. Schmechel, H. von Seggern, *Phys. Rev. Lett.*, **2003**, 91, 157406.

[6] M. Ahles, A. Hepp, R. Schmechel, H. von Seggern, *Appl. Phys. Lett.*, **2004**, 84, 428.

[7] M. Muccini, *Nature Mater.*, **2006**, 5, 605.

[8] R. Capelli, F. Dinelli, S. Toffanin, F. Todescato, M. Murgia, M. Muccini, A. Facchetti, T. J. Marks, *J. Phys. Chem. C*, **2008**, 112, 12993.

[9] J. Zaumseil, C. L. Donley, J. -S. Kim, R. H. Friend, H. Sirringhaus, *Adv. Mater.*, **2006,** 18, 2708.

[10] F. Dinelli, R. Capelli, M. A. Loi, M. Murgia, M. Muccini, A. Facchetti, T. J. Marks, *Adv. Mater.* **2006**, 18, 1416.

[11] C. Rost, S. Karg, W. Riess, M. A. Loi, M. Murgia, M. Muccini, *Appl. Phys. Lett.* **2004**, 85, 1613.

[12] M. A. Loi, C. Rost-Bietsch, M. Murgia, S. Karg, W. Riess, M. Muccini, *Adv. Funct. Mater.* **2006**, 16, 41.

[13] C. R. Newmann, C. D. Frisbie, D. A. Da Silva Filho, J. L. Bredas, P. C. Ewbank, K. R. Mann, *Chem. Mater.*, **2004**, 16, 4436.

[14] C. Santato, R. Capelli, M. A. Loi, M. Murgia, F. Cicoira, V. A. L. Roy, P. Stallinga,; R. Zamboni,; C. Rost,; S. E. Karg, M. Muccini, *Synth. Met.* **2004**, 146, 329.

[15] T. Lindner, G. Paasch, S. Scheinert, *J. Appl. Phys*., **2007**, 101, 014502.

[16] G. Horowitz, R. Hajlaoui, H. Bouchirha, R. Bourguiga, M. Hajlaoui, *Adv. Mater.*, **1998**,
10, 923.

[17] V. G. Kozlov, V. Bulovic, P. E. Burrows, M. Baldo, V. B. Khalfin, G. Parthasarathy, S. R. Forrest, Y. You, M. E. Thompson, *J. Appl. Phys.*, **1998**, 48, 4096.

[18] H. E. Katz, A. J. Lovinger, J. G. Laquindanum, *Chem. Mat.*, **1998**, 10, 457.

[19] C. W. Struijk, A. B. Sieval, J. E. J. Dakhorst, M. van Dijk, P. Kimkes, R. B. M. Koehorst, H. Donker, T. J. Schaafsma, S. J. Picken, A. M. van de Craats, J. M. Warman, H. Zuilhof, E. J. R. Sudhlter, *J. Am. Chem. Soc.*, **2000**, 22, 11057.

[20] R. J. Chesterfield, J. C. McKeen, C. R. Newman, P. C. Ewbank, D. A. da Silva Filho, J. –L. Brdas, L. L. Miller, K. R. Mann, C. Daniel Frisbie, *J. Chem. Phys. B*, **2004**, 108, 19281.

[21] R. Farchioni, G. Grosso, *Organic Electronic Materials* (Sprinter-Verlag Berlin Heidelberg 2001).

[22] H. Yamamoto, T. Oyamada, H. Sasabe, C. Adachi, *Appl. Phys. Lett*., **2004**, 84, 1401.

Conclusion

The work presented in this Ph.D. thesis aims at studying different classes of π-conjugated organic materials that present functional properties suitable for the realization of opto-electronic devices. In particular we focused our attention on the two specific properties that are deeply correlated to the molecular arrangement in the realization of nano-scale multifunctional devices: charge transport and light emission.

Indeed, the description of the solid state electronic properties of organic materials necessitates of taking into account the nature of intermolecular interactions which depends, among others, on the molecular arrangement in the solid state. In the technologically appealing thin films, the molecular arrangement is extremely sensitive to the deposition procedures and to the nature of the substrate.

Thus, of great interest is the understanding at the micro- and nano-scale of the molecular architecture and morphological features which favour charge transport and/or energy transfer, in order to enhance performances of opto-electronic devices based on thin films. Whereas it has been demonstrated that the molecular properties can be tuned by chemical tailoring, morphology and supramolecular arrangement are generally more difficult to control, and this appears to be one of the next challenges in the field of organic π-conjugated materials.

When organic materials are implemented as active layers in device realization, interfaces formed by different materials are intrinsically important. Organic based devices are composed by many different interfaces and OFETs in particular are considered *true interface* devices. The comprehension of the physics behind each interface is a crucial point to design new materials for device applications or to improve the performances of the existing ones.

The possibility of combining different functionalities in a single device is of great relevance for the further development of organic electronics in integrated components and circuitry. Organic light-emitting transistors (OLETs) have been demonstrated to be able to combine in a single device the electrical switching functionality of a field-effect transistor and the capability of light generation. With respect to light-emitting diodes, OLETs present some intriguing characteristics which overcome many physical and technical drabacks in the realization of nano-scale integrated electro-optical devices. In particular, these

characteristics include: control over the position of the emission zone, emission far away from injecting metal electrodes, high current densities, low charge concentration within the emission zone, and perfectly balanced hole and electron currents.

In Chapter 3 we have demonstrated that the highest mobility values in OFET device are shown by materials presenting unidimensionality of their elemental unit which results in anisotropic charge transport and optical properties. In general, linear α-oligothiophenes can organize advantageously in thin-films in so as to guarantee the *proper* overlap between molecular orbitals which enables efficient field-effect chrge transport.

End-substituted α-oligothiophenes seem to be the suitable materials that can provide good charge transport properties in field-effect devices together with the possibility of controlling their supramolecular organization in thin-film.

In the case of DH4T and DHF4T α-oligothiophenes, the substituted groups play a fundamental role in determining not only whether the α-oligothiophene molecule shows p- or n-type transport properties in the solid-state, but also all the chemical-physical interactions between the active material and the other layers in contact with it (such as those of the dielectric layer and metal electrodes).

Optimizing vacuum sublimation growth conditions allows one to obtain high mobility values for both the p-transport and n-transport materials (~ $10^{-2} \div 10^{-1}$ cm^2/Vs). Moreover using confocal laser scanning microscopy and atomic force microscopy as morphological investigation tools we found out that DH4T and DHF4T thin-films present sufficiently smooth and connected surfaces. Thus, these materials are very good candidate for being implemented in multilayer vertical heterostructures.

Controlling the material organization/molecular orientation during or after device fabrication represents a critical issue when device fabrication by solution-based processes is envisioned. The development of organic semiconductors with higher dimensionality and isotropic charge transport and optical properties could represent an exciting alternative strategy for avoiding all the device fabrication issues related to the specific control of molecular interactions and orientation

In this scenario we studied a new family of all-thiophene branched macromolecules denominated spider-like oligothiophenes (TX_n).

After performing a detailed photoluminescence spectroscopy study on all the molecules dispersed in dilute solution, we instigated how the molecular spectroscopic features are modulated by the solid-state aggregation in thin-films. Since dendrimers supramolecular

architecture can play a relevant role in enhancing light emission properties in small molecule-based OFET, we performed a morphological study on solution-deposited thin-films.

Spider-like oligothiophenes spectroscopic properties in solid state are determined by the balance between two molecular structural features: the long planar α-conjugated chain which is expected to promote π–π stacking (thus enabling efficient intermolecular electronic coupling) and the large molecular surface due to the pendant legs in β positions which enhance the 3D branching of the structure. So increasing the length and the number of β-substituted α-conjugated branches, different exciton intermolecular migration processes (hopping, energy transfer…) can take place in solid-state aggregates. In particular, the largest spider-like oligothiophene is likely to present intramolecular energy transfer also in solution.

Moreover molecular steric hindrance and different energetically-stable conformer configurations are responsible for the variation of the molecular aggregate morphological features upon depositing as thin-films. TX_n aggregates are deeply affected by the molecule-substrate interaction strength, thus displaying different shapes and substrate coverage.

The degree of intermolecular π-stacking overlap between the conjugated branches is a crucial parameter that at the same time determines the charge-transport and light emission properties of the device. So using branched oligothiophenes as active materials in OFET we aim at obtaining a balance between the long-range highly ordered structure required in field-effect transport and the suitable electronic structure that can afford high PLQY.

However, implementing vacuum-sublimed $T5_3$ thin-film as active layer in OFET devices promising ambipolar charge transport properties are obtained even without having optimised the dielectric-active material interface, but no light emission was detected.

In Chapter 4 we focussed on studying the light emission properties organic system in order to enhance its efficiency. We presented a host-guest lasing system obtained by co-evaporation of an oligo(9,9-diarylfluorene) derivative (host) with a well-known red-emitter dye (guest)

The use of a binary blend in which Förster energy transfer between an absorptive donor and an emissive acceptor takes place allows reducing the optical losses in the thin-film waveguides and decreasing the ASE threshold.

Moreover blending can assure strong absorption and broad emission spectra in host-guest systems. The strong absorption (and associated strong stimulated emission) enables extraordinarily compact lasers and optical amplifiers to be made. The broad spectra enable not only tuneable lasers to be made but also femtosecond pulse generation and broadband optical amplification.

The investigation of the photo-physical properties of the host-guest system T3:DCM highlighted that an efficient Förster energy transfer takes place from the T3 matrix to the DCM molecules. Indeed, we found out that the non-radiative energy transfer is Förster-like only for the lowest guest concentration sample. For higher guest concentrations the energy transfer becomes much faster and the overall dynamics is dominated by the guest-guest interaction and aggregation.

The mirroless lasing measurements performed on the blends, revealed that the lowest DCM ASE threshold is presented by the blend in which the guest aggregation is almost negligible and the energy transfer is incomplete.

We found out that the 2% DCM:T3 ASE threshold value is an order of magnitude lower than that of the 2% DCM:Alq_3 model system measured in the same experimental conditions.

In Chapter 5 we present vertical tri-layer heterojunction approach for realizing organic light-emitting transistor. The specificity of the presented tri-layer based OLET is the intrinsic separation of the charge transport region from the exciton formation region thus preventing completely the exciton-carrier quenching.

Each layer is devoted to a single functionality within the device and can be optimised by controlling the growth of the different organic/organic, organic/metal and organic/dielectric interfaces. Single functional properties have been extensively treated and discussed in the previous paragraphs.

In the heterostructure we propose the first layer and third layers are optimized for field-effect charge (electrons and holes) transport. The second layer is formed by a host-guest matrix with high optical performance and showing amplified spontaneous emission under optical pumping.

Implementing confocal laser scanning microscopy as morphological probing tool (especially in transparent) devices allows to recognise directly the fundamental role played by different layer interfaces in determining the overall opto-electronic performances of the vertical tri-layer heterojunctions.

The optimization of the charge transport and light emission properties allows the realization of a tri-layer heterojunction presenting balanced electron and hole mobility (~10^{-1}-10^{-2} cm^2/Vs), high charge carrier density in correspondence of the maximum electroluminescence emission (~ 1 KA/cm^2) and intense light generation

OLET planar structure is not only a convenient platform for investigating charge carrier recombination processes in organic semiconductors with spatially resolving probes, but it is also attractive for the realization of integrated electro-optical switches and, potentially, electrically pumped lasers.

Acknowledgments

First of all I would like to thank my supervisor Prof. Bozio at the University of Padova for giving me the possibility to start (and finish, hopefully) my Ph.D.
Then I thank my boss Dr. Michele Muccini at the ISMN-CNR in Bologna for trusting myself and my skills, just one minute before I starting doing it by myself. Michele, are you still sure it was a good idea?
I thank my *sensei* Raffaella Capelli: I really would not have finished my Ph.D. without your firm and friendly helping hand during *that* August. I just hope that I have been a good apprentice during these years.
I thank Maria Antonietta Loi for having taught me how a researcher should behave in a spectroscopic laboratory.
I thank Miguel Ramon for having taught me how a researcher should *not* behave in a spectroscopic laboratory.
I thank all the people involved in the work reported in this thesis: Franco Dinelli, Francesco Todescato, Prof. Francesco Sannicolò, Filippo De Angelis, Tobias Plötzing and Juan Cabanillas-Gonzales.
I thank all guys (well, I don't thank really everyone) at the ISMN-CNR in Bologna for having always been friendly and warm to me: Is not you, it's that I don't smile so frequently!...
I thank the science material crew in Padova (Luca, Marco, Cicci, Pol… and all the others): we are a pretty bizarre amount of people, worse than chemists and physicists but much more funny.
And since Life is not always inside dark spectroscopic labs, I thank Lara for singing during cold nights in the countryside when she is driving.
I thank Andrea for the chance he gave me to look beyond that wall.
I thank Simone for holding my hand when I cross the street.
I thank all the friends that I meet in the usual bars standing on the wall and looking at the people passing by.
I thank all my family and clan for having taught what drama and comedy really mean.
Mom and Dad, I know that you both don't have any idea about what I do when I go to work, but thanks for your support during all these years.

Thanks to my brother and my sister because they are my brother and my sister.
Finally thanks to my grandparents for having taught that studying and learning is emancipating from your limits.